



Universidad de Valladolid



**PROGRAMA DE DOCTORADO EN QUÍMICA: QUÍMICA DE
SÍNTESIS, CATÁLISIS Y MATERIALES AVANZADOS**

TESIS DOCTORAL:

**NUEVAS REDES DE POLÍMEROS POROSOS
PARA SEPARACIONES AVANZADAS;
MEMBRANAS MIXTAS DE MATRIZ POLIMÉRICA
PARA CAPTURA DE CO₂**

Presentada por Laura Matesanz Niño para optar al
grado de
Doctora por la Universidad de Valladolid

Dirigida por:
Ángel E. Lozano López
Cristina Álvarez Sancho
Laura Palacio Martínez

Por fin ha llegado el final de esta etapa. La preparación de esta Tesis ha llevado su tiempo, ha sido un trabajo largo y duro, pero que finalmente ha tenido sus recompensas, entre ellas la oportunidad de haber conocido a personas a quienes tengo muchas cosas que agradecer.

En primer lugar, me gustaría agradecer a Alfonso por enseñarme algo de todo lo que sabe y ayudarme y apoyarme siempre hasta en los peores momentos.

Gracias Ángel por todo el conocimiento de síntesis que he podido absorber de ti, ha sido muy enriquecedor. Por lo que me has enseñado a tu manera. Por estar siempre, cuando las cosas salían, y también cuando no salía nada. También te he de agradecer que gracias a los malos momentos ahora soy mejor investigadora.

Agradecer a Cristina todo, gracias por poner un poco de cordura siempre, por enseñarme a aprender, a preguntarme siempre el porqué de las cosas, a buscar soluciones, a escribir, comprender, investigar... Sin ti esta tesis no habría salido adelante, cada día te lo sigo agradeciendo.

Y por supuesto a Laura, por darme la oportunidad de hacer la tesis.

Sin duda, el desarrollo de esta tesis doctoral no la puedo catalogar como algo fácil, pero lo que sí puedo hacer es afirmar que durante este tiempo he aprendido, me he desarrollado tanto en lo personal como en lo profesional y he conocido a personas muy interesantes que, como a mí, nos apasiona la Ciencia. Por todo ello, gracias.

Especialmente agradezco las dotaciones económicas que hicieron posible que realizara las dos breves estancias, 5 meses en Oklahoma, pues considero que sin duda alguna fue, tanto a nivel profesional como personal, algo de lo más positivo de estos 5 años de Tesis. I would like to thank Prof. Michele Galizia, who gave to me the opportunity to learn and work with him in his group and Matthew who showed me how to understand plastification. Thanks to all the very nice and helpful people I found over there, Elena, Wen, Lucas, Jing, Will, Yafei...

Además, agradezco mi contrato predoctoral de la Universidad de Valladolid que me ha permitido realizar la tesis doctoral, los proyectos a los que he estado adscrita PID2019-109403RB-C21 y PID2019-109403RB-C22 y los laboratorios SMAP y ICTP-CSIC que me han permitido el desarrollo de la parte experimental de este trabajo.

Agradecer también a todas las personas que han hecho posible de manera directa o indirecta la realización de esta tesis doctoral. Gracias Mónica, sin ti no habría llegado a este punto.

Por supuesto, agradecer a mis amigos de la carrera, Cintya, David, Bea, Ana, Gaby, que, desde el primer día, hace 10 años, no nos hemos separado y sin duda han conseguido hacer esta tesis más llevadera, por escucharme siempre que no podía más y convencerme de lo contrario, no sé qué habría hecho sin vosotros.

Además, agradecer a Raquel, Marina, Bea, Alicia, Paula por tener siempre un consejo para mí, escuchar mis lloros, pero también por las historias vividas estos años juntas.

Gracias Víctor, por estar siempre.

Por último, gracias a mi familia, especialmente a mis padres, mi hermano, mis abuelos... Ellos han sido siempre el motor que impulsaba mis sueños, quienes estuvieron siempre a mi lado en los días más difíciles. Siempre son mis mejores guías. Hoy, cuando concluyo mi doctorado, os dedico a vosotros este logro, como una meta más conquistada. Agradecida de que todos estéis a mi lado en este momento tan importante.

ABSTRACT

Aromatic polyimides are polymers that have excellent thermal and chemical stability, mechanical robustness, easy processability, and when they are correctly designed are attractive materials for gas separation applications. However, gas-separation aromatic polyimide materials are susceptible to plasticization and physical aging, especially those with high-free volume polyimides, and thus exhibit poor long-term stability. In this context, the present Ph.D. thesis aims to develop new materials that not only provide a good gas selectivity/gas permeability balance but also an enhanced CO₂-induced plasticization and aging resistance, in particular using two main approaches: polymer blending, including mixed matrix membranes, and thermal crosslinking.

For this purpose, two different classes of materials have mainly been synthesized: aromatic-aliphatic polyimides capable of cross-linking thermally and porous organic polymers.

6FDA-6FpDA and 6FDA-TMPD are two aromatic polyimides that are easily processable as they are soluble in common organic solvents, and they have been widely studied for gas separation membrane applications due to their high free volume, good mechanical resistance, high thermal stability, and good permeability/selectivity balance for CO₂/CH₄ and CO₂/NH₂ gas pairs. However, they, especially 6FDA-TMPD polyimide, suffer from both plasticization and physical aging. To address these shortcomings, two series of aromatic-aliphatic copolyimides based on 6FDA-6FpDA and 6FDA-TMPD polyimides, which are derived from 4,4'-(hexafluoroisopropylidene) diphthalic anhydride (6FDA) and 2-2'-bis(4-aminophenyl)hexafluoropropane (6FpDA) or 2,4,6-trimethylphenyl diamine (TMPD), have been synthesized by incorporating different contents of 3,5-diaminobenzoic acid (DABA) and polyethylene oxide segments (PEO) into their main chains (6FDA-6FpDA-xDABA-yPEO) and (6FDA-TMPD-xDABA-yPEO). The membranes derived from these new aromatic-aliphatic copolyimides were subjected to high-temperature pyrolysis, which was previously optimized for each series of polymers (up to 350 or 450 °C), to cause the selective removal of PEO segments and thus form cross-linked membranes with high thermal stability and good mechanical properties. The presence of DABA moiety caused an additional cross-linking between DABA's carboxylic groups reducing the shrinkage during the thermal treatment; i.e., retaining the free volume created by the loss of PEO segments.

Regarding the gas separation properties, the cross-linked membranes obtained from aromatic-aliphatic copolyimides containing molar percentages of DABA between 10 and 20% by mol and PEO less than 5% by mol showed better selectivity/permeability balance relative to the reference polyimides (6FDA-6FpDA and 6FDA-TMPD). However, the most relevant result was that the cross-linking in these membranes successfully led to the suppression of CO₂ plasticization upon exposure to gas up to 30 bar.

On the other hand, a parallel study based on polymer blending, in particular of 6FDA-6FpDA and 6FDA-6FpDA-xDABA-yPEO mixtures, showed another possible strategy to prepare high-free volume polymer membranes with high plasticization resistance using analogous cross-linkable polymers as mere additives.

Another strategy to reduce physical aging and plasticization is to fabricate mixed matrix membranes (MMMs). For this, it is essential to have a high compatibility between the matrix and the porous filler. In this Ph.D. thesis, new porous organic polymers (POPs) were synthesized by combining multifunctional aromatic monomers with activated ketones through an aromatic electrophilic substitution reaction (EAS) in a superacidic media. Searching strategies to create tailor-made highly microporous materials possessing very rigid structures and excellent thermal stability, various tetra- tri- and bi-functional aromatic monomers showing different structural features have been used.

Thus, Ho-POPs were prepared by reacting tri-functional aromatic monomers such as 1,3,5-triphenylbenzene (TPB), 1,3,5-tri-(2-methylphenyl)benzene (TMB), 1,3,5-tri-(biphenyl)benzene (TBB), or triptycene (TR), or tetra-functional monomer such as 9,9'-spirobifluorene (SBF) with different cross-linkers: 2,2,2-trifluoroacetophenone (TF), 1H-indole-2,3-dione (I), or 1-methylindoline-2,3-dione (N-methylisatin, MI). These cross-linkers were chosen as they do not introduce flexibility in the molecular structure of the networks and they incorporate amide groups derived from lactam rings and fluor atoms that could increase the affinity with CO₂. Also, Co-POPs were prepared by combining the previous tri- or tetra-functional monomers with bi-functional monomers such as biphenyl (BP) and 9,10-dimethyl-9,10-dihydro-9,10-ethanoanthracene (DMHEA), with the main target of increasing the crosslinking length between the monomers.

After a thorough synthesis optimization, where different reaction conditions were tested to prepare porous materials in high reaction yield and with high surface areas, the POPs obtained were amorphous materials with moderate high surface area 577-1033 mmol g⁻¹ and excellent thermal stability (>450 °C). Moreover, they were highly microporous materials. In fact, the POPs obtained by combining SBF, TR or TPB with the rigid and

contorted DMHEA, using isatin as cross-linker, showed the narrowest micropore size distribution with pore sizes between 4-5 Å and CO₂ uptakes between 3.61-2.10 mmol g⁻¹ at 0 °C and 1 bar. The other POPs with a wider micropore size distribution exhibited CO₂ uptakes between 5.42 – 2.94 mmol g⁻¹ at 0 °C and 1 bar. Among all of the POPs prepared, triptycene-based POPs behaved as excellent molecular sieves for separation processes in Pressure Swing Adsorption (PSA) technologies.

Because the great enhancement in plasticization resistance was not accompanied by a parallel substantial improvement in the separation performance of cross-linked membranes relative to reference polyimides, mechanically robust MMMs were fabricated by adding 20% by weight of triptycene-isatin POP to the previous aromatic-aliphatic copolyimide derived from 6FDA-TMPD polyimide containing molar percentages of 20% for DABA and 1% for PEO. The high thermal stability of POPs prepared in this Ph.D. thesis allowed us to carry out a high-temperature pyrolysis to obtain cross-linked MMMs. To mitigate the effects of thermomechanical history before performing the plasticization studies, the membranes were aged in a controlled way. All of these membranes suffered from physical aging, but the values of permeability were much higher than that of the reference polyimide (6FDA-TMPD) without losing selectivity. The MMM plasticization was suppressed upon exposure to CO₂ up to 30 bar, even without the aid of any thermal crosslinking for copolyimides containing PEO. A possible interaction between the components of MMM was rationalized by molecular simulation assuming the formation of hydrogen bonds between the lactam groups of POP and oxygen of PEO molecules. Finally, the cross-linked MMM exhibited the best selectivity/permeability performance, with a permeability about 1.6 times higher for all gases tested, and without sacrificing selectivity relative to reference polyimide.

RESUMEN

Las poliimidas aromáticas son polímeros que presentan excelente estabilidad térmica y química, robustez mecánica, fácil procesabilidad y, cuando se diseñan correctamente, son materiales atractivos para aplicaciones de separación de gases. Sin embargo, los materiales de separación derivados de poliimidas aromáticas son susceptibles a la plastificación y al envejecimiento físico, especialmente para aquellos materiales de alto volumen libre, por lo que presentan escasa utilidad a largo plazo. En este contexto, la presente tesis doctoral pretende desarrollar nuevos materiales que no sólo proporcionen un buen balance selectividad/permeabilidad en separación de gases, sino también una mayor resistencia a la plastificación inducida por el CO₂ y al envejecimiento físico, en particular utilizando dos aproximaciones: mezclas de polímeros, incluidas membranas de matriz mixta, y procesos de entrecruzamiento térmico.

Para ello, se han sintetizado principalmente dos clases diferentes de materiales: un conjunto de poliimidas aromático-alifáticas capaces de entrecruzar térmicamente y unas redes de polímeros orgánicos porosos.

Particularmente, la 6FDA-6FpDA y la 6FDA-TMPD son dos poliimidas aromáticas fácilmente procesables ya que son solubles en disolventes orgánicos comunes, y que han sido ampliamente estudiadas para aplicaciones de membranas de separación de gases debido a su alto volumen libre, buena resistencia mecánica, alta estabilidad térmica y buen balance permeabilidad/selectividad para parejas de gases como CO₂/CH₄ y CO₂/NH₃. Sin embargo, éstas poliimidas, especialmente la poliimida 6FDA-TMPD, sufren procesos de plastificación y de envejecimiento físico. Para superar estas limitaciones, dos series de copoliimidas aromático-alifáticas basadas en las poliimidas 6FDA-6FpDA y 6FDA-TMPD, obtenidas mediante reacción del anhídrido diftálico 4,4'-(hexafluoroisopropilideno) (6FDA) y del 2-2'-bis(4-aminofenil)hexafluoropropano (6FpDA) o de la 2, 4,6-trimetilfenil diamina (TMPD), se han obtenido incorporando diferentes contenidos de ácido 3,5-diaminobenzoico (DABA) y de óxido de polietileno (PEO) a su cadena principal (6FDA-6FpDA-xDABA-yPEO y 6FDA-TMPD-xDABA-yPEO). Las membranas derivadas de estas nuevas copolimidas aromático-alifáticas se sometieron a pirólisis a alta temperatura, proceso que fue previamente optimizado para cada serie de polímeros (procesos térmicos desde 350 a 450 °C), para producir la eliminación selectiva de los segmentos PEO y formar así membranas entrecruzadas con alta estabilidad térmica y buenas propiedades mecánicas. La presencia de DABA provocó

un entrecruzamiento adicional entre los grupos carboxílicos del propio DABA, lo que redujo la contracción del volumen de la membrana durante el tratamiento térmico; es decir, se retuvo el volumen libre creado por la pérdida de segmentos PEO.

En cuanto a las propiedades de separación de gases, las membranas entrecruzadas obtenidas a partir de copolimidas aromático-alifáticas que contenían porcentajes molares de DABA entre el 10 y el 20% por mol y de PEO inferior al 5% por mol mostraron un mejor balance selectividad/permeabilidad en comparación con las poliimidas de referencia (6FDA-6FpDA y 6FDA-TMPD). Sin embargo, el resultado más relevante fue que el entrecruzamiento de estas membranas condujo con éxito a la supresión de la plastificación del CO₂ incluso bajo exposición al gas a una presión de 30 bar.

Por otra parte, un estudio paralelo basado en mezclas de polímeros, en particular de mezclas de 6FDA-6FpDA y 6FDA-6FpDA-xDABA-yPEO, mostró otra posible estrategia para preparar membranas poliméricas de alto volumen libre y con alta resistencia a la plastificación utilizando como meros aditivos polímeros análogos capaces de entrecruzar térmicamente.

Otra aproximación para reducir el envejecimiento físico y la plastificación consistió en fabricar membranas de matriz mixta (MMMs). Para ello, es esencial que exista una alta compatibilidad entre la matriz y el relleno poroso. En esta tesis doctoral, se sintetizaron nuevos polímeros orgánicos porosos (POPs) combinando monómeros aromáticos multifuncionales con cetonas activadas mediante una reacción de sustitución electrofílica aromática (EAS) en un medio superácido.

En este contexto, y con una idea centrada en la búsqueda de estrategias para obtener materiales altamente microporosos con estructuras muy rígidas y una excelente estabilidad térmica, se utilizaron diversos monómeros aromáticos tetra- tri- y bifuncionales con diferentes características estructurales. Así, los polímeros Ho-POP se prepararon por reacción de monómeros aromáticos trifuncionales como el 1,3,5-trifenilbenceno (TPB), el 1,3,5-tri-(2-metilfenil)benceno (TMB), el 1,3,5-tri-(bifenil)benceno (TBB), o con el tripticeno (TR), y otros monómeros tetrafuncionales como el 9,9'-espirobifluoreno (SBF) empleando diferentes entrecruzantes: 2,2,2-trifluoroacetofenona (TF), 1H-indol-2,3-diona (I), o 1-metilindolina-2,3-diona (N-metilisatina, MI). Estos entrecruzantes se eligieron porque no introducen flexibilidad en la estructura molecular de las redes e incorporan grupos amida derivados de anillos

lactama y átomos de flúor que podrían aumentar la afinidad por el CO₂. Asimismo, se prepararon copolímeros Co-POPs combinando los anteriores monómeros tri- o tetra-funcionales con monómeros bi-funcionales como el bifenilo (BP) y el 9,10-dimetil-9,10-dihidro-9,10-etanoantraceno (DMHEA), con el objetivo principal de aumentar la longitud de separación de los puntos de entrecruzamiento entre los monómeros. Tras una exhaustiva optimización de la síntesis, en la que se probaron diferentes condiciones de reacción para preparar materiales porosos con un alto rendimiento de reacción y con áreas superficiales elevadas, se determinó que los POPs obtenidos fueron materiales amorfos con un área superficial entre moderada y alta (577-1033 mmol g⁻¹) y una excelente estabilidad térmica (>450 °C). Además, estos materiales fueron altamente microporosos. De hecho, los POPs obtenidos combinando SBF, TR o TPB con el monómero de estructura rígida y contorsionada DMHEA, utilizando isatina como entrecruzante, mostraron una distribución de tamaño de microporo estrecha con tamaños de poro entre 4-5 Å y adsorciones de CO₂ entre 3,61-2,10 mmol g⁻¹ a 0 °C y 1 bar. Los otros POPs presentaron una distribución de tamaño de microporo más ancha y adsorciones de CO₂ entre 5,42 - 2,94 mmol g⁻¹ a 0 °C y 1 bar. Entre todos los POPs preparados, los POPs basados en triptíceno se comportaron como excelentes tamices moleculares para procesos de separación mediante tecnologías de adsorción por oscilación de presión (conocidas por su acrónimo en inglés PSA).

Dado que la mejora en la resistencia a la plastificación de las membranas entrecruzadas no fue acompañada de una mejora en sus prestaciones de separación en comparación con las poliimidas de referencia, se fabricaron MMMs mecánicamente robustas añadiendo un 20% en peso del POP de triptíceno-isatina a una de las anteriores copoliimida aromático-alifática derivada de la poliimida 6FDA-TMPD, con porcentajes molares del 20% para el DABA y del 1% para el PEO.

La elevada estabilidad térmica de los POPs preparados en esta tesis doctoral permitió llevar a cabo una pirólisis a alta temperatura para obtener MMMs entrecruzadas. Para mitigar los efectos de la historia termomecánica, antes de realizar los estudios de plastificación, se dejó envejecer a las membranas de forma controlada. Todas estas membranas sufrieron envejecimiento físico, pero los valores de permeabilidad fueron muy superiores a los de la poliimida de referencia (6FDA-TMPD) sin perder selectividad. La MMM no sufrió plastificación bajo exposición a presión de CO₂ de 30 bar, incluso sin la necesidad del entrecruzamiento térmico en el caso de la copoliimida que contiene PEO.

Una posible interacción entre los componentes de la MMM ha sido sugerida mediante simulación molecular, a través de la formación de enlaces de hidrógeno entre los grupos lactama del POP y el oxígeno de las moléculas de PEO. Por último, la MMM entrecruzada mostró el mejor rendimiento de selectividad/permeabilidad, con una permeabilidad aproximadamente 1,6 veces superior, al resto de membranas, para todos los gases medidos, y sin sacrificar la selectividad en comparación con la poliimida de referencia.

INDEX

1. Introducción.....	3
1.1.SOCIAL ISSUES ASSOCIATED WITH CLIMATE CHANGE	3
1.2.CAPTURE TECHNOLOGIES AND CHALLENGES	7
1.3.SEPARATION MEMBRANE TECHNOLOGY	11
1.4.GAS TRANSPORT MECHANISMS IN SEPARATION MEMBRANES	12
1.5.MEMBRANE EFFICIENCY AND EVALUATION OF POLYMERIC MEMBRANES.....	15
1.6.DRAWBACKS OF A GAS SEPARATION MEMBRANE.....	17
1.7.MIXED MATRIX MEMBRANES.....	18
2. Objectives	25
3. General methodology.....	33
3.1.SYNTHESIS OF POLYMERS	33
3.1.1. Preparation of polymer networks	35
3.1.1.1. Materials	35
3.1.1.2. Synthesis of monomers	36
3.1.1.3. Synthesis of porous organic polymers	39
3.1.2. Preparation of polymers	43
3.1.2.1. Materials	43
3.1.2.2. Synthesis of aromatic copolyimides	44
3.1.2.3. Synthesis of aromatic-aliphatic copolyimides	45
3.2. MEMBRANE FABRICATION	46
3.2.1. Neat polymer membranes	46
3.2.2. Polymer blend membranes	47
3.2.3. Mixed matrix membranes	47
3.2.4 Membranes conditioning in methanol	48
3.2.5. Thermal cross-linking protocol	49
3.3. CHARACTERIZATION TECHNIQUES.....	49
3.3.1. Characterization of monomers and polymers.....	49
3.3.2. Characterization of membranes	50
3.3.3. Characterization of porous polymer networks	51
3.4. GAS TRANSPORT PROPERTIES.....	53

3.4.1. Permeability measurements	53
3.4.2. Plasticization test	55
4. Gas Separation Membranes Obtained by Partial Pyrolysis of Polyimides	
Exhibiting Polyethylene Oxide Moieties	59
4.1. INTRODUCTION.....	59
4.2. RESULTS AND DISCUSSION.....	62
4.2.1. Synthesis and characterization of the copolyimides.....	62
4.2.2. Characterization of the membranes	65
4.2.3. Preparation of the cross-linked PIxEOy membranes	68
4.2.4. Gas transport properties	70
4.2.5. Blends of PIx and PIxEOy.....	75
5. Tuning the Porosity of Porous Organic Polymers for Carbon Capture	
Applications	81
5.1.INTRODUCTION.....	81
5.2.RESULTS AND DISCUSSION.....	83
5.2.1. Synthesis optimization of porous organic polymers	85
5.2.2. Characterization of POPs	87
5.2.3. Thermal properties of POPs.....	91
5.2.4. Textural properties of POPs.....	92
5.2.5. Low-pressure CO ₂ uptake.....	98
5.2.6. High-pressure gas uptake of CO ₂ , N ₂ and CH ₄	100
5.2.7. CO ₂ /N ₂ /CH ₄ separations.....	103
6. Plasticization-resistant gas separation membranes derived from polyimides	
exhibiting polyethylene-oxide moieties	109
6.1.INTRODUCTION.....	109
6.2.RESULTS AND DISCUSSION.....	111
6.2.1. Polymers synthesis and characterization	111
6.2.2. Membrane characterization	113
6.2.3. Mechanical properties	118
6.2.4. Physical aging analysis	120
6.2.5. Gas Separation Properties	121
6.2.6. Plasticization study.....	124
7. Conclusions.....	131

<i>Appendix 1</i>	141
<i>Appendix 2</i>	153
<i>Appendix 3</i>	177
<i>8. References</i>	197

Chapter 1

1. Introduction

1.1. SOCIAL ISSUES ASSOCIATED WITH CLIMATE CHANGE

“*Global warming*” is understood as the effect on the climate of human activities, in particular the burning of fossil fuels (coal, oil, and gas) and large-scale deforestation, which cause the emission of massive amounts of greenhouse gases (GHG), including carbon dioxide (CO₂), methane (CH₄), nitrous oxide and fluorinated gases [1]. One of the most pressing environmental problems of our time is the rapid increase of these GHG levels in the Earth’s atmosphere. Among these GHGs, CO₂ is the gas emitted in the highest amount, it has accumulated in the atmosphere over decades to centuries, and it dissolves in the sea resulting in ocean acidification. According to the National Oceanic and Atmospheric Administration (NOAA), “*2022 was the 11th consecutive year CO₂ increased by more than 2 ppm, the highest sustained rate of CO₂ increases in the 65 years since monitoring began. Before 2013, three consecutive years of CO₂ growth of 2 ppm or more had never been recorded*” [2]. Nowadays, atmospheric CO₂ has risen to 50% above its pre-industrial level (before 1750).

The “*enhanced greenhouse effect*” is the principal driver of climate change. It is explained simply by the increase of GHG, mainly CO₂ gas, which acts as a blanket over Earth’s surface that traps the sun’s heat and prevents it from escaping into space. When the energy leaving is less than the energy entering, the Earth warms until a new energy balance is established. The Earth’s temperature has increased more than 1.1 °C since the end of the XIX century until now, being this increase approximately half of that increase produced in the last thirty years. Thus, it is accepted that the 2011-2020 period has been the warmest decade recorded until now [3].

Most of the worst disasters in the world are related to the temperature increase, which is also responsible for ice melting from ice sheets, mainly contributing to the rise in sea level. In addition, on average, the precipitations have considerably increased on the planet, but some regions have suffered from severe droughts, increasing the risk of fires, harvest failures, and lack of fresh water. All of these disasters are becoming more and more common and, thus, a wide range of responses will need to mitigate damage to ecosystems and human societies.

The “*enhanced greenhouse effect*” affects everyone in the world, thus it can only be countered by global solutions. In the “*27th Conference of the Parties to the United Nations Frameworks Convention on Climate Change*” (COP27), that took place in Sharm el-Sheikh (Egypt), the participating countries have reached an agreement adopted through Decision-/CP27 (known as the Sharm el-Sheik Implementation Plan) [4]. This agreement seeks to renew solidarity among countries to accomplish the Paris Agreement [5], which was adopted for the benefit of people and the planet. Among the sixteen key goals, the following can be highlighted:

- Keeping the global warming temperature limited to 1.5 °C by reducing the global GHG emissions of 43% by 2030 relative to 2019 level. This will require expanding clean energy quickly enough by 2030, which will lead to a strong decline in fossil fuel demand too.
- Providing loss and damage funding for vulnerable countries hit hard by climate disasters.
- Holding businesses and institutions to account by ensuring the transparency of commitments, which will be a priority of UN Climate Change in 2023.
- Mobilizing more funding for developing countries so that they can combat climate change. On this crucial topic, COP27 created a pathway to align the broader finance flows towards low emissions and climate-resilient development.

The affordable fossil fuel energy that has facilitated the simultaneous growth in population and improvement in living standards over the last century is not easy to substitute at scale. However, the burning of fossil fuels for energy is not only harmful to the planet but also fossil fuels are unsustainability as finite resources. Thus, both the spread of climate change awareness and the necessity of a sustainable energy supply have led to propose some approaches to mitigate the anthropogenic carbon dioxide emissions, which are schematized in Figure 1.1. These approaches are based either on reducing CO₂ production (lowering the usage of fossil fuels and using clean and renewable energy) or on capturing it at the emission source and then storing it or using it to produce valuable products or on extracting the produced CO₂ from climate balance [6].

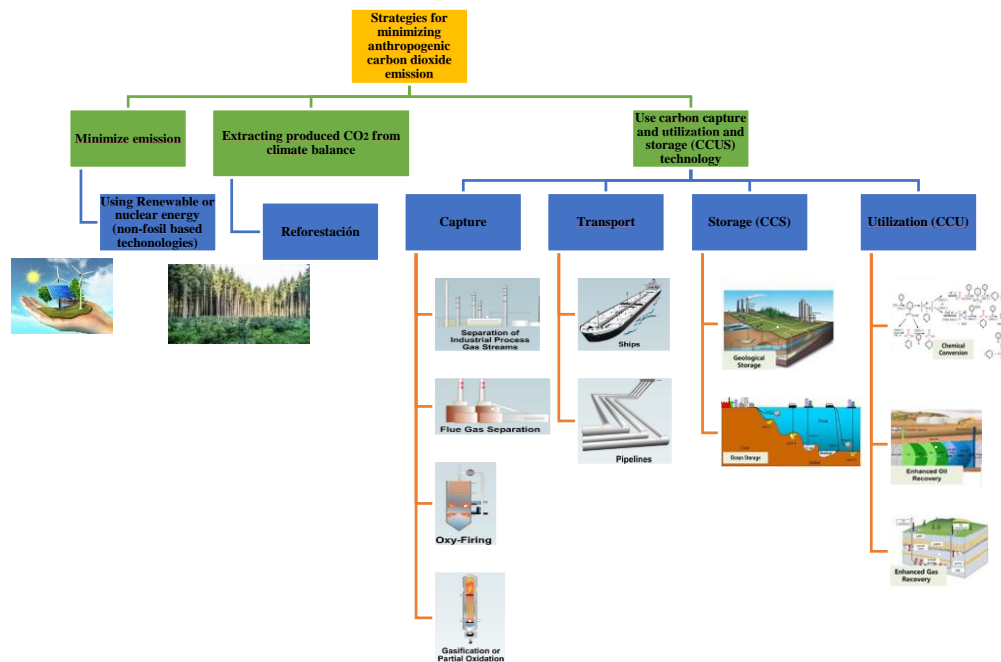


Figure 1.1. Approaches to mitigate CO₂ emissions.

By choosing sustainable energy resources, such as wind, solar, water (hydropower), and geothermal, and committing to clean energy the world's societies can effectively slow down the acceleration of climate change. Considerable efforts are being made to achieve a sustainable path, but carbon emissions have risen every year since the Paris Goals were agreed, except in 2020 due to the COVID-19 pandemic. According to the *BP's Statistical Review of World Energy 2022* [7], the global primary energy in 2021 increased by almost 6%, more than reversing the sharp fall in energy consumption in 2020, due to high demand for energy by the rapid recovery in economic activity. The primary energy consumption in 2021 was 1.3% above 2019. Encouragingly, the share of renewables in global power generation continued to increase and now accounts for 17.7% (including hydroelectricity and nuclear energy), as shown in Figure 2. The primary energy consumption in the European Union and Spain is also shown in Figure 1.2. Therefore, despite the speed of maturity in renewable technologies, the country's transition to a low-carbon economy is still far away, at least in the coming decades.

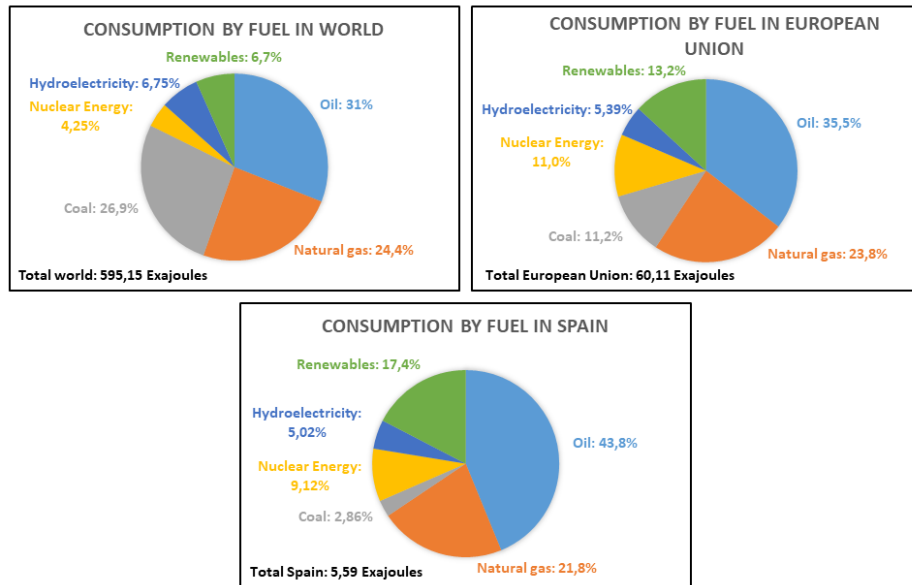


Figure 1.2. Contribution of different energy resources in global power generation in 2021. Data taken from [7]

In this scenario, the world still needs to invest in fossil fuels to meet global energy demand. While waiting for renewable energy technologies can lead to the replacement of fossil-based fuels, it is essential to develop the emerging carbon capture, utilization, and storage (CCUS) technology to prevent the release of CO₂ emissions into the atmosphere and, thus, to mitigate the climate change in the short and medium term [8]. CCUS (Figure 1) refers to the suite of technologies including the CO₂ removal from relevant emission sources by using capture systems, then transporting it to the storage site and isolating it from the atmosphere for a long time (so-called carbon capture and storage, CCS, chain) or using it to produce valuable products (so-called carbon capture and utilization, CCU, chain).

The development of energy-efficient CO₂ capture processes from industrial gas streams as well as directly from air is the key to the whole CCUS technology. An overview of CO₂ capture technology will be given in Section 1.2.

In the transport stage, which links industrial facilities and storage sites, the continuous transport of large CO₂ volumes as compressed gas or liquid or liquid/dense-phase fluid is done via pipeline, while modular transport of liquefied CO is done by ship, truck, or railroad. The choice of transport mode mainly depends on economic considerations. Although pipelining is the most common mode of transportation, pipeline CO₂ potentially contains hazardous contaminants, such as hydrogen sulfide, which poses a public safety

risk if pipeline corrosion and pipeline leakage take place [9]. Shipping is an attractive alternative for CO₂ transport, but today it still occurs on a much smaller scale; the optimal conditions for transporting CO₂ on a large scale are still not defined, especially concerning transport pressure [10]. Transport by truck and railroad is carried out just for small quantities of CO₂.

In the CCS chain, the captured CO₂ is stored in appropriate geological storage sites, including depleted oil and gas field reservoirs, saline aquifers, and non-exploitable coal seams [8]. Geological storage is the main storage method of CO₂ at present. Depleted oil and gas field reservoirs are considered the best storage sites because they already have an infrastructure that can be used and the reservoirs themselves have a good sealing property and can store gas for a long time. Moreover, the CO₂ injection can help enhance oil recovery efficiency.

In the CCU chain, the captured CO₂ is widely used in a variety of applications [11], among others, for the production of beer and carbonated beverages, for fresh frozen food, for enhanced oil recovery, as well as, for the synthesis of diverse products such as salicylic acid, urea, organic fuels (e.g. methanol and formic acid) and polymer materials (e.g. polycarbonate and polyurethane). In addition, CO₂ utilization is now receiving huge interest from the scientific community, because not only it will allow mitigating climate change, but also the CO₂ could be able to be used as feedstock resulting in a cheaper or cleaner production process when compared with conventional hydrocarbons [12,13].

Both CCU and CCS chains allow for reducing CO₂ emissions, but today the amount of CO₂ used is much smaller than the amount of CO₂ stored. Furthermore, the CO₂ used will be re-released at the end of the product life cycle. Thus, in the near future, CO₂ storage will still be the main strategy to reduce CO₂ emissions. However, it will also be necessary for a long-term integrity assessment of storage sites to avoid leakages or contamination of subsurface resources [14].

1.2. CAPTURE TECHNOLOGIES AND CHALLENGES

There are three basic CO₂ capture technology routes [11,15], which are schematically shown in Figure 1.3:

- *Pre-combustion CO₂ capture*: it consists of converting the primary fuel to hydrogen-rich synthesis gas that is used to run the turbine generator to produce power. Briefly, the gas produced from gasification (*usually known as syngas*) is

converted to CO_2 (25%-35%) and H_2 (30%-50%) at high pressures (5-40 bar) and the CO_2 is then extracted from the syngas stream before the combustion of H_2 rich gas to produce power. The CO_2 capture usually operates at pressures around 30 bar and temperatures around 40 °C with adsorbent bed.

- *Post-combustion CO_2 capture*: this process involves the separation of CO_2 from N_2 after combustion of fossil fuels before it enters the atmosphere. The flue gas stream mainly contains CO_2 (15-16%) and N_2 (70%-75%). After the removal of SO_x (about 800 ppm), the separation of CO_2 from CO_2/N_2 mixtures operates at near atmospheric pressures and temperatures between (40-80 °C).
- *Oxy-fuel combustion*: the fuel is burned in an O_2 -enriched atmosphere and the gaseous product obtained contains mainly CO_2 (55%-65%) and water (25%-35%) that can be easily separated to produce a high-purity CO_2 stream.

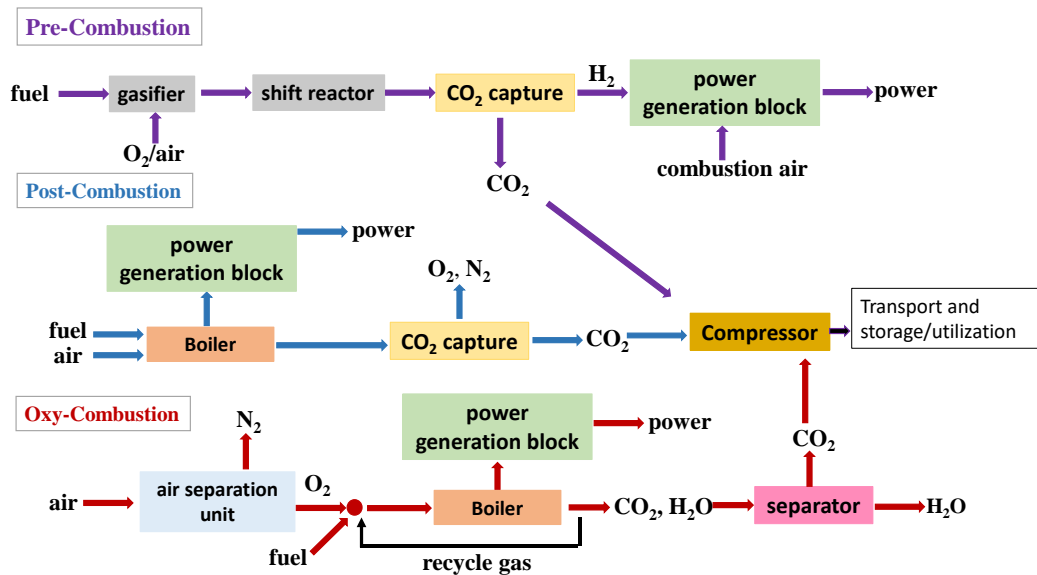


Figure 1.3. Scheme of main CO_2 capture technology routes.

The selection of the strategy for CO_2 capture depends on economic and reliability considerations. *Pre-combustion CO_2 capture* benefits from CO_2 at high partial pressure and concentrate gas streams leading to efficient absorption, but its principal limitation is the need for gasification adding complexity and cost to the process. *Oxy-fuel combustion* benefits from a concentrated CO_2 stream facilitating CO_2 absorption, but the energy-intensive air separation process required considerably increases the investment in carbon capture. As for *post-combustion CO_2 capture*, it is considered to be the most feasible to reduce CO_2 emissions on a short time scale since many of the proposed technologies can

be retrofitted to the existing fossil fuel power plants [11]. However, the main difficulty of post-combustion capture is represented by the need to produce a highly concentrated CO₂ stream matching the purity requirement for transportation and storage from flue gas streams where the CO₂ is highly diluted.

According to the principle of the capture process, there are different types of separation techniques to separate CO₂ from the flue gas stream, including absorption by solvents, adsorption by solid materials, membranes, and cryogenics, each of which has advantages and limitations. Some of the main ones are summarized in Table 1.1 [15].

Among these types of separation techniques, amine-based absorption is the most commercially mature option and is applied for the separation of CO₂ in real industrial processes, such as natural gas sweetening and the production of hydrogen and ammonia. However, high energy consumption, especially in the regeneration of absorbent, prevents amine-based solvents from being commercialized at the industrial level [16,17].

The membrane separation process has been considered to be an energy-efficient process because it does not require a thermal driven force to separate mixtures. Moreover, it has been extensively studied due to its remarkable industrial prospects [18]. Here, in this work, our interest is going to be focused on gas separation membranes, especially in the development of new low-cost and efficient materials.

Table 1.1. *Advantages and limitations of CO₂ separation techniques.*

Technique	Advantages	Limitations
<i>Absorption by solvents</i>	<ul style="list-style-type: none"> • Versatility and adaptability to various process • High CO₂ capture efficiency • Matured technology 	<ul style="list-style-type: none"> • High-energy intense regeneration of solvent • Possibility of solvent degradation and toxicity
<i>Adsorption by solid materials</i>	<ul style="list-style-type: none"> • High adsorption rate • Low regeneration energy • Can be used in temperature (TSA) and pressure (PSA) swing operations 	<ul style="list-style-type: none"> • Need of developing low-cost and efficient adsorbent materials • Materials sensitive to the presence of moisture in the flue gas stream • Require regeneration material
<i>Cryogenic separation</i>	<ul style="list-style-type: none"> • High CO₂ recovery and purity • Low energy consumption of pressurization for transport • Commercially matured and proven technology 	<ul style="list-style-type: none"> • Highly energy-intensive process • Expensive and often cost-effective in niche applications requiring high-purity CO₂ process • Large equipment
<i>Membrane separation</i>	<ul style="list-style-type: none"> • Less energy-intensive • Compact and modular design. Easy to scale up • Simple operation • Coupled with other separation techniques 	<ul style="list-style-type: none"> • Achieve good permeability/selectivity balance • Long working life time: fouling, swelling, plasticization, etc • High cost of membranes • Defect-free production of membranes

1.3. SEPARATION MEMBRANE TECHNOLOGY

The separation membrane technology is based on the intrinsic ability of a membrane to separate selectively one or more components in a mixture while retaining others, as schematically illustrated in Figure 1.4. The components pass through the membrane by applying a driving force such as a pressure gradient, temperature gradient, electrochemical gradient, etc.

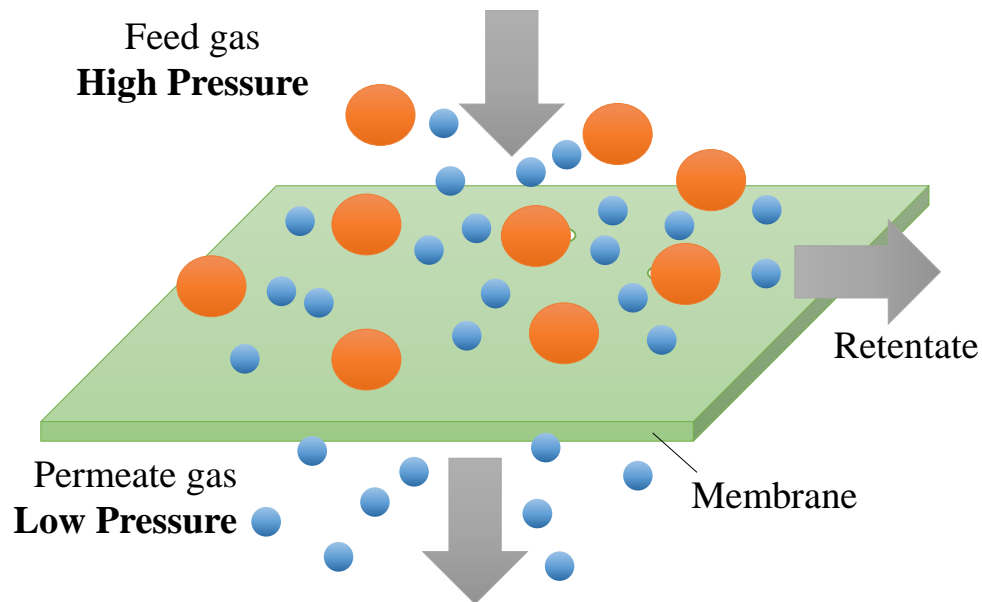


Figure 1.4. Schematic membrane-based gas separation process.

Over the last few decades, membrane-based separation technologies have gained worldwide recognition in numerous applications such as in wastewater treatment, desalination, gas separation, etc [19,20]. Separation membrane technology is presented as an alternative to other conventional separation technologies, such as distillation, adsorption, and absorption, due to their simplicity, cost-effectiveness, high selectivity, ease of scaling up, and the ability to conjugate with other processes.

Even though the gas diffusion and mass transfer principles through membranes are known since more than one century ago, only in the last four decades, membranes have been applied on industrial scale in gas separation membranes (GS). The breakthrough of membrane-based GS took place in 1980 with the first commercial application of Prism[®] membranes by Permea (Monsanto) for hydrogen separation. Since then, industry needs have generated significant academic and industrial research activity, which has been reflected in the exponential growth of commercially available membrane systems; by the

mid-1980s, Cynara, Separex, and Grace Membrane Systems commercialized membrane plants to remove carbon dioxide from methane in gas natural. At about the same time, Dow launched Generon[®] develop the first separation system to separate nitrogen from air. More recently, other systems have been launched to separate nitrogen and volatile organic compounds from the air, to remove hydrogen sulfide from methane, to purify natural gas in the refineries by removing acid gases, to adjust the hydrogen-monoxide ratio in syngas, etc [20]. The most recent commercial successes for polymeric gas separation membranes include its application for onboard inert gas generation systems (OBIGGS), which generate a dry nitrogen-enriched air blanket to cover the interior of the fuel tanks, to improve safety and reduce the risk of in-flight explosions, and also for the purification of biogas [21]. The main milestones in the development of membrane gas separation technology are shown in Figure 1.5.

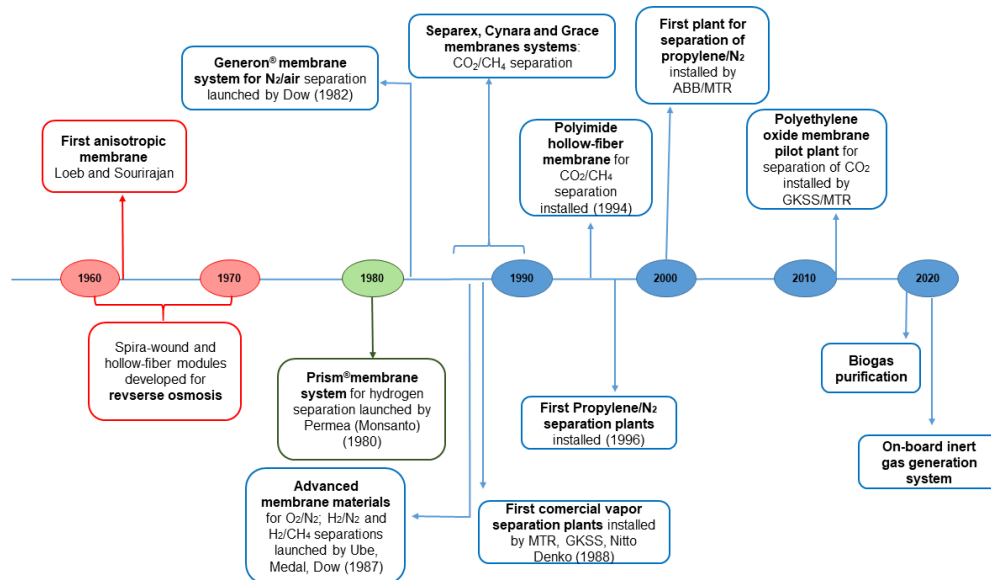


Figure 1.5. Main milestones in the development of membrane gas separation technology.

1.4 GAS TRANSPORT MECHANISMS IN SEPARATION MEMBRANES

The membranes can be classified according to two main criteria [22]:

- By nature of the material from which they are made: natural or synthetic (organic, inorganic, or hybrid).
- By morphology or structure of membrane: symmetrical ones that can be porous or non-porous (dense) or asymmetrical ones in which the membrane is supported or

integrated on a material. As examples, schematic representations of morphologies of dense and porous membranes, as well as of thin film composite (TFC) membranes are shown in Figure 1.6.

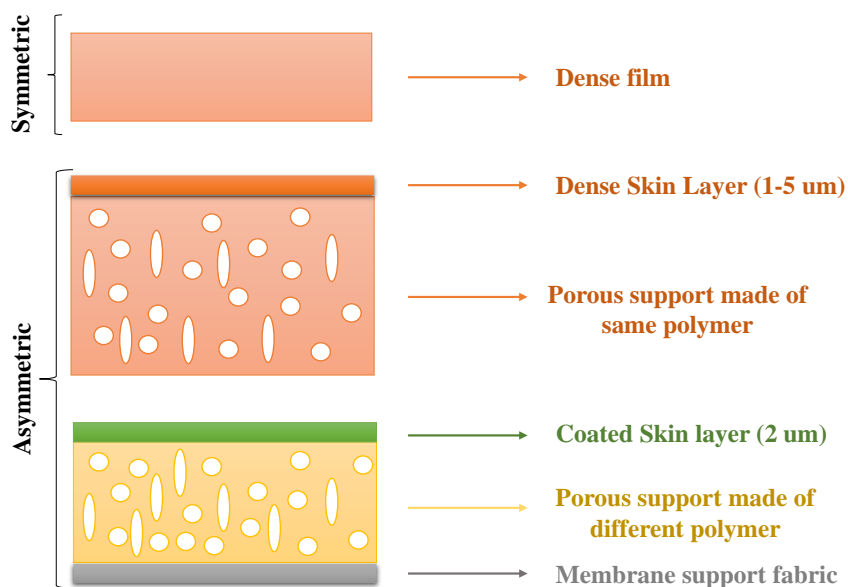


Figure 1.6. Schematic representation of three different types of membrane morphology: homogenous symmetric (above), asymmetric membrane (middle), and TFC membrane (below)

According to the morphology of the membrane, different separation mechanisms take place [19]. Regarding porous membranes, if the pore size is in the range of 0.1-10 μm , gases permeate the membrane by convective flow; i.e. no separation occurs. If the pores are smaller than 0.1 μm , the gas diffusion through such pores is ruled by Knudsen diffusion, and the transport rate of gas is inversely proportional to the square root of its molecular weight (Graham's law of diffusion); and if the pores are extremely small (0.5-20 nm), gases are separated by molecular sieving effect. In the case of dense membranes, the gas separation through the membrane is described by the solution-diffusion mechanism.

Almost all of the current commercial gas separations are based on dense polymeric membranes which are the main target of this thesis. Thus, the solution-diffusion model is going to be briefly introduced below.

The solution-diffusion model considers that permeating gas (A) dissolves into the membrane at the feed side (upstream side), diffuses across the membrane, and then desorbs at the permeate side (downstream side), as illustrated in Figure 1.7.

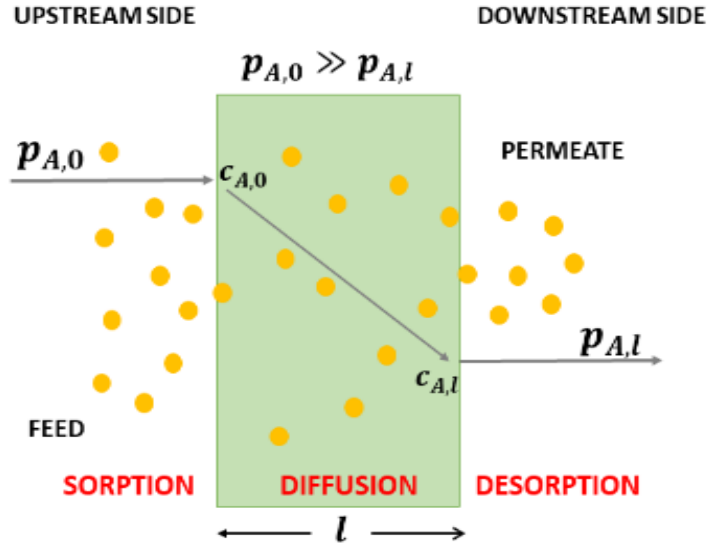


Figure 1.7. Scheme of gas transport across a dense polymer membrane based on the solution-diffusion model.

The permeability coefficient is defined as the amount of permeating gas (A) across the membrane per unit time and unit area (J_A) scaled on the pressure drop and the membrane thickness (l):

$$P_A = \frac{J_A \cdot l}{p_{A,0} - p_{A,l}} \quad [\text{Eqn. 1.1}]$$

Where $p_{A,0}$ and $p_{A,l}$ are the partial pressures of the gas A on the upstream and downstream sides, respectively. Within the context of the solution-diffusion model and Fick's law in the limit when the downstream pressure is much lower than the upstream pressure, the permeability (P_A) can be expressed as the product of the gas solubility (S_A) in the upstream side of the membrane and the average effective gas diffusion coefficient (D_A) in the membrane [23,24].

$$P_A = D_A \times S_A \quad [\text{Eqn. 1.2}]$$

The ability of a membrane to separate two gases (A and B) is characterized by the ideal selectivity or permselectivity (α_{AB}), which can be divided into two components: the diffusivity selectivity (D_A/D_B), and the solubility selectivity (S_A/S_B).

$$\alpha_{AB} = \frac{P_A}{P_B} = \frac{D_A}{D_B} \times \frac{S_A}{S_B} \quad [\text{Eqn. 1.3}]$$

The permeability of each of the gases A and B depends on the product of solubility and permeability in a particular polymer membrane. Thus, if gas A is much more permeable

than gas B can be due to the following reasons: 1) gas A has a higher diffusion, 2) gas B is more soluble in the membrane (i.e., higher gas/polymer interaction), or 3) both 1 and 2. In general, the gas separation in polymer membranes is based on differences in either gas diffusivity (diffusivity-selective or size-sieving materials) or gas solubility (solubility-selectivity materials).

The current work is focused on gas separation membranes made from glassy amorphous polymers. Because the polymer chains cannot pack efficiently, free spaces (holes or so-called free volume elements) are created. The total volume of all of these free-volume elements is the so-called fractional free volume (FFV). The gas diffusion through glassy polymers proceeds by a jumping mechanism, whereby molecules located inside holes move to neighbor holes through channels, which are occasionally opened by thermal fluctuations of local to short-scale cooperative segmental motions, such as chain bending, bond rotation or phenyl ring flips [25]. Therefore, the molecular mobility of polymer chains is a crucial factor to be considered in gas diffusion.

1.5. MEMBRANE EFFICIENCY AND EVALUATION OF POLYMERIC MEMBRANES

An optimal membrane for gas separation processes must show high permeability (that is, the membrane productivity) and high selectivity (that is, the membrane's ability to discriminate a specific component in a mixture) at the same time, as well as high chemical and thermal stability, superior mechanical resistance under operating conditions, long working lifetime, cost-effective and defect-free production. Glassy polymer membranes are mostly used due to their desirable combination of size-sieving ability and mechanical properties. However, they exhibit a well-known trade-off between the permeability of membrane and its selectivity; i.e., membranes show a balanced behavior, in such a way that more permeable materials tend to be less selective and *vice versa*.

The trade-off of separation membranes was evidenced by Robeson in 1991 [26]. Since then, the state of the art for a given gas pair is identified by a linear “upper bound” fit to the top performing materials on a double-logarithmic plot of selectivity *versus* permeability of the faster gas (also so-called Robeson plots); i.e., above the upper bounds that are empirically determined no data exist. Accordingly, the position of the gas permeability data of membranes relative to the upper bounds on the Robeson plot allows

us to estimate their potential for gas separation applications. However, the continuous development of membrane materials with enhanced performances means that the upper bounds move as shown in Figure 1.8. Thus, Robeson updated the database in 2008 [27], Pinnau et al. in 2015 [28], and McKeown et al. in 2019 [29] proposed new upper bounds for some relevant gas pairs from the permeability data of a series of ultrapermeable polymers synthesized by them.

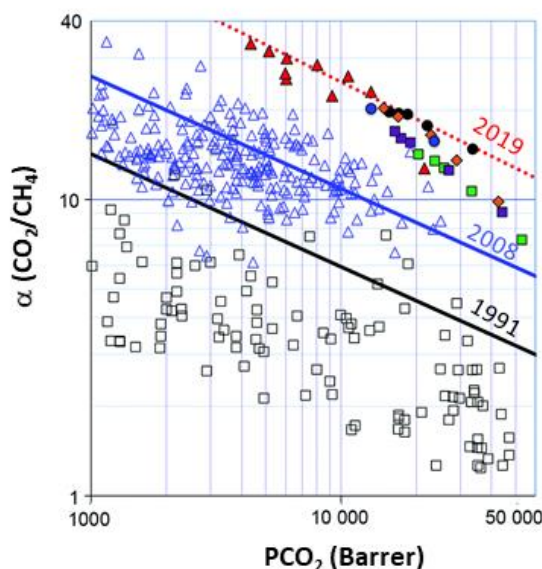


Figure 1.8. Robeson plot for CO₂/CH₄ separation [29]

In 1999, Freeman provided the fundamental theoretical basis for the gas separation upper bound [30]. Briefly, he concluded that the most fruitful pathway for the development of high performance polymeric membranes for separation consists of simultaneously increasing the interchain spacing (i.e., high FFV) and the backbone stiffness (i.e., molecular mobility restriction of polymer chains) to achieve both higher permeability and higher selectivity. However, increasing interchain spacing to increase permeability will not be effective if the gas separation is no longer governed by diffusion; because permselectivity would be reduced. Therefore, the trade-off relationship has been assumed as a consequence of the dependence of gas diffusion coefficients on the molecular diameter of the gases to be separated. Later, Robeson et al. [31] compiled a large database of permeability, diffusion, and solubility of glassy polymers to study the correlation between solubility coefficient and FFV, which had been observed in some specific families of glassy polymers. They found that solubility selectivity for the AB gas pair (S_A/S_B , Eqn. 1.3) usually decreases with increasing permeability of A gas (and FFV)

when the diameter of gas molecule B is larger than that of gas A; i.e., larger molecules have less access than smaller molecules to the sorption sites when FFV decreases due to a higher packing density. However, they concluded that FFV contribution to the solubility selective, and then to changes in permeability, is modest. Moreover, they showed that the slope of the upper bound in terms of diffusivity (D_A/D_B vs D_A), was modestly different from the upper bound in terms of permeability.

1.6. DRAWBACKS OF A GAS SEPARATION MEMBRANE

Following Freeman's approach, the simultaneous increase in polymer chain stiffness and FFV is an effective strategy to improve solubility and gas permeability. In this context, microporous organic polymers including polymers of intrinsic microporosity (so-called PIMs) and thermally rearranged (TR) polymers have attracted strong interest because of their highly rigid macromolecular structures, which prevent space-efficient packing of the chains in the solid state, and thus they show high FFV. These sets of polymers are considered the most promising candidates for the next generation of membranes since they have superior permselectivity properties [32,33]. In fact, PIMs have been used since 2008 to update the Robeson upper bounds for some gas pairs (2015 and 2019 upper bounds) [28,29].

Other polymeric membrane materials for gas separation that have also attracted attention are glassy polyimides (PIs). They have high chemical resistance, large thermal stability, and good mechanical strength, as well as good performance as gas separation properties. The most effective method and widely used to improve PI membrane performance is to introduce non-coplanar structures (spiro, cardo, and kink units), and bulky groups ($-\text{CF}_3$ and $-\text{CH}_3$) [34].

Also, the properties of glassy polymers depend on the polymer processing history. For example, exposure to highly soluble penetrants and thermal treatments can influence the gas transport properties. Thus, plasticization and physical aging phenomena are challenging issues for long-term industrial applications [35]. Both phenomena and their effect on permeability and selectivity will be briefly introduced below. More detailed information about glassy polymers in membrane separation applications can be found elsewhere [36].

Plasticization induced by CO_2 remains a problem commonly found in gas separation involving aggressive feed streams, such as in natural gas processing, which requires

membranes with high selectivity for CO₂ to CH₄ [37]. A typical effect of plasticization is that the permeability versus pressure curves go through a minimum [38–40]. The pressure corresponding to the minimum permeability is called plasticization pressure. The plasticization is produced because the polymer matrix swells due to the high sorption of CO₂ at high-pressure conditions increasing the polymer free volume (i.e. higher FFV) and chain mobility. As a result, the permeability of both components of the gas mixture increases, but the increase is higher for the slower permeating component and thus simultaneously the selectivity decreases.

Physical aging in glassy polymers is due to that they are in non-equilibrium states and their structure can evolve towards equilibrium conditions due to the local-scale segmental motions of polymer chains that take place in the glassy state [41]. Although physical aging occurs without any external influence, its rate is dependent on factors such as temperature, polymer structure, membrane thickness, etc. In fact, even in polymers with very high intra-chain rigidities, such as PIMs, rapid physical aging occurs [39]. The physical aging leads to a densification of chain packing that affects some macroscopic polymer properties, such as density, refractive index, mechanical strength, and transport properties of small molecules. For gas transport properties, the densification (i.e., producing a decrease in FFV) causes a decrease in the permeability of the membrane. The effect of physical aging can be determined by measuring the changes in permeability of membrane with operating time [42].

Several approaches have been proposed to overcome selectivity/permeability trade-off, physical aging, and/or plasticization issues covering, among others, post-synthetic modification (e.g., chemical or physical cross-linking), addition of porous nanoparticles to polymer matrix (mixed matrix membranes), incorporation of chemical groups in the polymer structure that can interact with one of the permeating species (facilitated transport), etc. [18].

1.7. MIXED MATRIX MEMBRANES

There is a wide variety of inorganic (e.g., zeolites and carbon molecular sieves) and hybrids (e.g., metal organic frameworks) materials that can offer efficient ways to achieve narrow pore size distributions that lead to high permeability and/or high selectivity. In particular, metal organic frameworks (MOFs), which are made by linking inorganic and organic units by strong bonds, have well-defined pore sizes, high porosity (~50% of the

crystal volume), and exhibit high surface areas (range from 1000 to 10000 m²g⁻¹), [43]. They exceed the traditional surface areas of zeolites and carbon molecular sieves (CMS), but they have lower chemical and hydrothermal stability. Despite their advantages of offering an excellent selectivity/permeability balance, MOFs films are not mechanically robust enough to form large surface area membranes and they must be fabricated on porous supports, and thus it is difficult to obtain defect-free thin films [44].

Whereas traditional membranes for gas separation are largely based on polymers and are subjected to permeability-selectivity trade-off, mixed matrix membranes (MMMs) offer the possibility of controlling the pore size and size distribution, which can break the conventional upper bound; i.e., membrane performance close or above the 2018 upper bound. MMMs consist of a dispersed micro-or nanoparticles (inorganic or hybrid) phase and a continuous polymer matrix phase. These MMMs have the potential to combine synergistically the high intrinsic gas separation performance of porous filler material with the easy processability of polymers [45,46]. Most studies involving MMMs have incorporated molecular sieving particles such as zeolites, carbons, and MOFs [47,48] to prepare symmetric dense films due to the simplicity of the fabrication process.

Despite the promising separation performance of MMMs, the dispersed phase may cause undesirable effects that can lead to different morphologies of the membrane that exhibit overall separation performance much worse than that expected (Case 0), as schematically shown in Figure 1.9 [49]. Among other effects are polymer rigidification at the matrix-filler interface (Case I) and pore blockage (Case II) and, in the case of a poor matrix-filler adhesion, interfacial voids can be created resulting in increased permeability (case III), or increased permeability and decreased selectivity (case IV). The last case occurs when the effective void thickness is about the gas molecule size ($\sim 5 \text{ \AA}$). In addition, the aggregation of filler particles hinders the achievement of homogenous dispersions at high loading levels.

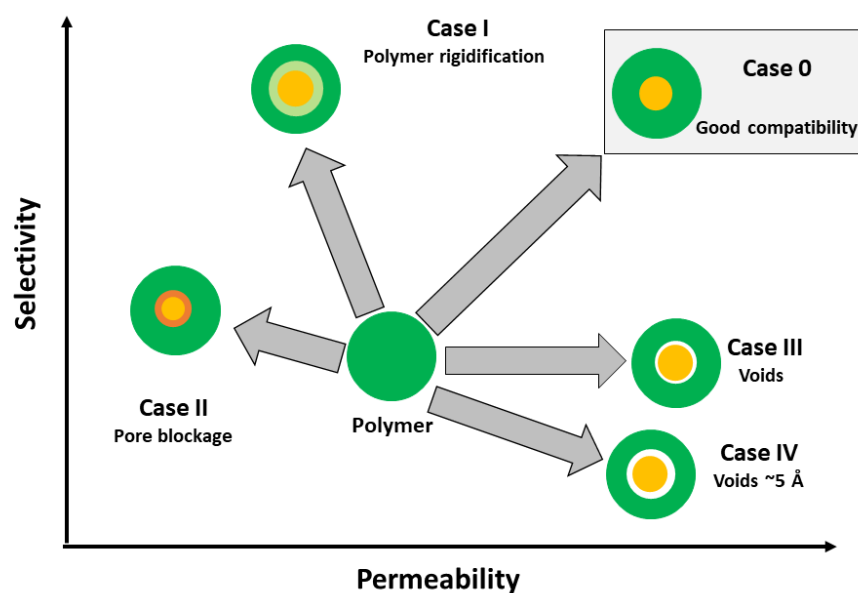


Figure 1.9. Schematically representation of the relationships between mixed matrix membranes morphologies and transport properties.

Porous organic polymers (POPs) are an interesting class of new emerging filler since they offer better adhesion and compatibility with polymer matrix than inorganic fillers. In addition, they also exhibit low density, robust structure, high thermal and chemical stability, and excellent hydrothermal stability, among other important characteristics. The wide range of optional rigid building blocks (mainly aromatic monomers) and rigid linkers as well as the flexibility of synthetic routes allow preparing materials with tunable characteristics [50]. Thus, POPs can be designed at the molecular level with large specific surface areas, adjustable porosity, and tailorable functionalization for the desired application. POPs have received different names based on either their synthetic route or building block, as shown in Figure 1.10. Moreover, they can be also classified into two sub-classes: crystalline POPs formed via reversible bond-forming chemistry, which have well-ordered structures and uniform pore sizes, such as COFs, and disorder amorphous POPs with interconnected hierarchical pore structures.

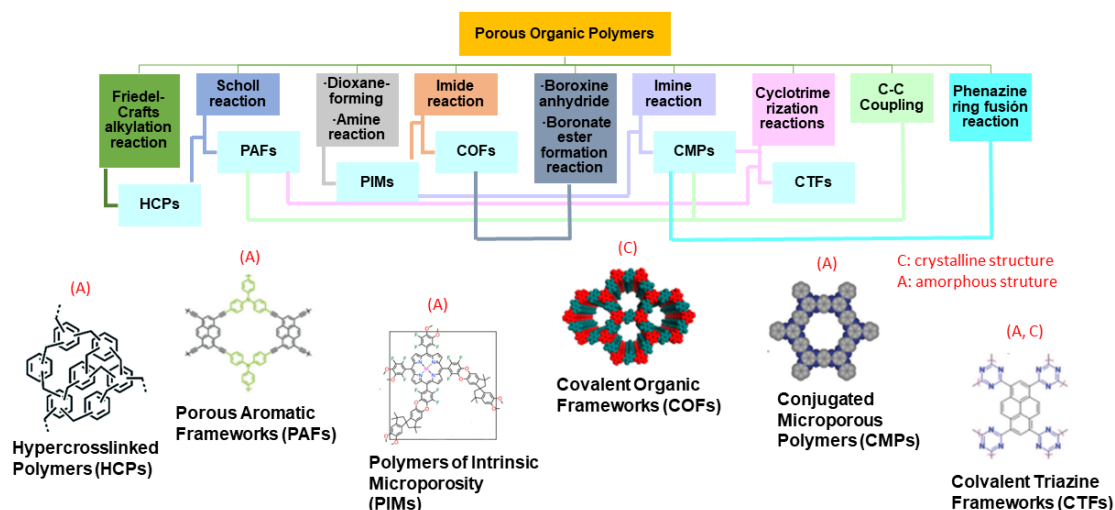


Figure 1.10. Classification of porous organic polymers based on the synthetic methodology.

POPs are attracting considerable scientific interest and showing promising applications in gas adsorption and separation, energy storage, heterogeneous catalysis, water treatment, electrochemical application, and so on [51–55].

Despite well over a decade of sustained efforts to develop MMMs, their use in large-scale gas separation processes for industrial applications remains restricted. Today, although they show outstanding properties in the laboratory, they are far from replacing conventional glassy polymers. Thus, the current work is focused on the preparation of MMMs using a new class of amorphous POPs that ensure an excellent compatibility with the polymer matrix, in particular with high-free volume polyimides, so that materials can achieve the best gas separation membrane performance. In addition, an appropriate design of the polyimide matrices has allowed post-modification of the MMMs by controlled high-temperature crosslinking to be carried out aimed to improve the long-working life of membranes by enhancing the resistance to CO₂ plasticization and mitigating the physical aging associated with high-free volume polymers.

Chapter 2

2. General objectives and work plan

The main motivation of this Ph.D. thesis titled *New porous polymeric networks for advanced separations; mixed polymeric matrix membranes for CO₂ Capture* has been the design and the obtaining of new high-performance polymeric materials for use in gas separation applications, mainly CO₂ separation. This Ph.D. has been development in the framework of the SMAP-Uva-CSIC research unit supported by the Spanish Research Agency (AEI) through a coordinate project (PID2019-109403RB-C21 and PID2019-109403RB-C22 projects).

Based on the research group's knowledge of how to obtain polymer materials with advanced gas separation properties, this Ph.D. thesis aims to *design and develop polymer materials to obtain neat membranes and mixed matrix membranes, easily processed as defect-free films, where the filler is a microporous polymer network, and the matrix is a linear polymer capable of being thermally-treated at medium-high temperatures to ultimately produce cross-linked materials with improved gas separation properties.*

The design of gas separation materials was carried out taking into account that the incorporation of certain chemical groups can produce an increase in the rigidity of the macromolecular chain and, at the same time, can lead to a separation among chains, which increases the internal free volume of material. In addition, the increase in polymer chain rigidity is a very adequate strategy to overcome typical drawbacks of polymer membranes such as plasticization and physical aging. For this purpose, the synthesis of a great variety of polymer materials has been carried out, which, moreover, has required the search for improved processability methodologies.

The **specific objectives** of this Ph.D. thesis can be mainly divided into three blocks:

- 1) Synthesis and characterization of polyheterocyclic polymers including linear polymers capable of undergoing a thermal cross-linking under a controlled partial degradation process at high temperatures, generating very rigid stable structures, and porous polymer networks.
- 2) Evaluation of previous materials as gas separation membranes including neat membranes and mixed matrix membranes.
- 3) Studies aimed at eliminating physical aging and plasticization.

Additionally, due to the highly microporous nature of porous polymer networks, these materials were parallel evaluated as efficient adsorbents for selective separation of CO₂ from CO₂/N₂ and CO₂/CH₄ mixtures.

To achieve these objectives, the **work plan** can be summarized in the following sections:

- Synthesis of new high-performance materials:
 - i. Synthesis and purification of new trifunctional aromatic monomers having D_{3h} and C_{3v} symmetry, which have bulky groups in their structure providing rigidity and pore stability to the polymer network.
 - ii. Optimization of the synthetic routes to obtain difunctional monomer compounds with high yield and high purity.
 - iii. Synthesis of porous polymer networks having high inherent microporosity.
 - iv. Synthesis of high molecular weight aromatic polyimides copolyimides, and aromatic-aliphatic copolyimides.
- Characterization of the chemical structure of monomers and polymers by common organic and macromolecular techniques such as Fourier-transform infrared spectroscopy (FTIR), and nuclear magnetic resonance (NMR) in solution and solid state. Moreover, in particular, the molecular weight of polymers was estimated by inherent viscosity measurements.
- Analysis of the textural properties of porous polymer networks from low-pressure isotherm measurements using N₂ at -196 °C and CO₂ at 0 °C.
- Preparation and characterization of membranes manufactured from polymer materials synthesized.
 - i. Neat membranes were prepared from the synthesized linear polymers by a deposition-evaporation (casting) procedure.
 - ii. Mixed matrix membranes were prepared by incorporating different loadings of microporous polymer networks as filler. A deposition-evaporation (casting) procedure was also employed.
 - iii. Thermally cross-linked membranes were prepared subjecting precursor membranes to a thermal treatment previously optimized by isothermal thermogravimetric analysis (TGA) to generate materials with high FFV and rigidity.

- iv. Morphology of membranes was explored by wide-angle X-ray scattering (WAXS) and scanning electronic microscopy (SEM).
- v. Thermal stability of membranes was determined by TGA.
- vi. Fractional free volume (FFV) of membranes was determined from their bulk density.
- vii. Study of mechanical properties.
- Evaluation of gas separation performance of neat membranes and mixed matrix membranes by measuring pure gas permeability.
- Study of membrane physical aging and plasticization resistance.
- Evaluation of porous polymer networks as efficient adsorbents for selective separation of CO₂/N₂ and CO₂/CH₄ mixtures from low- high-pressure adsorption isotherms at room temperature.

In order to satisfactorily frame the research carried out in the bibliographical context of the subject and systematize the results obtained, the memory has been divided into a Summary section, 8 chapters, and 3 appendix, with this distribution.

SUMMARY

CHAPTER 1. Introduction

CHAPTER 2. General Objectives and Work Plan

CHAPTER 3. General Methodology: Materials and Methods

CHAPTER 4: Gas Separation Membranes Obtained by Partial Pyrolysis of Polyimides Exhibiting Polyethylene Oxide Moieties

CHAPTER 5: Tuning the Porosity of Porous Organic Polymers for Carbon Capture Applications

CHAPTER 6: Plasticization-resistant Gas Separation Membranes Derived from Polyimides Exhibiting Polyethylene-oxide Moieties

CHAPTER 7. Conclusions

APPENDIX 1

APPENDIX 2

APPENDIX 3

CHAPTER 8. Bibliography

This Ph.D. thesis has been completed through the financial support obtained from grants dedicated to the hiring of research personnel for the period 2020-2023. These grants were

co-funded by the University of Valladolid. Additionally, during the period 2017-2019, funding was provided by the Junta de Castilla y León as well as the following AEI research projects (PID2019-109403RB-C21 and PID2019-109403RB-C22) to which we are grateful for their funding.

In addition, the Ph. Student has completed two stays abroad in the research group of professor Dr. Michele Galizia (Sarkeys Energy Center, Norman, Oklahoma, United States), which were financed by the University of Valladolid. These stays have allowed her to carry out studies of plasticization at high pressures.

It is noteworthy that the outcomes achieved in the course of this thesis have resulted in the publication of two articles, corresponding to chapters 4 and 6, respectively.

L. Matesanz-Niño, C. Aguilar-Lugo, P. Prádanos, A. Hernandez, C. Bartolomé, J.G. de la Campa, L. Palacio, A. González-Ortega, M. Galizia, C. Álvarez, Á.E. Lozano, Gas separation membranes obtained by partial pyrolysis of polyimides exhibiting polyethylene oxide moieties, *Polymer*. 247 (2022). <https://doi.org/10.1016/j.polymer.2022.124789>.

L. Matesanz-Niño, M. T. Webb, A. González-Ortega, L. Palacio, C. Álvarez, Á.E. Lozano, M. Galizia; Plasticization resistant gas separation membranes derived from polyimides exhibiting polyethylene-oxide moieties; *Polymer* (2023) <https://doi.org/10.1016/j.polymer.2023.126535>.

Besides, the results of Chapter 5 are also being prepared for publication:

L. Matesanz-Niño, A. G. del Campo, A. Martínez-Gómez, L. Palacio, A. González-Ortega, F. Suárez-García, Á.E. Lozano, C. Álvarez, Tuning the Porosity of Porous Organic Polymers for Carbon Capture Applications.

It is important to highlight that, although not explicitly detailed in this report, the Ph.D. student has actively contributed to the synthesis, evaluation of gas transport properties writing and organization of three other research works, which are related to mixed matrix membranes derived from new polymers and porous polymer networks that have been prepared during this Ph. D. thesis. Moreover, she has contributed to another work related to new aromatic polyimides with improved gas separation properties.

L. Matesanz-Niño, N. Esteban, M.T. Webb, A. Martínez-Gómez, F. Suárez-García, A. González-Ortega, J.A. Miguel, L. Palacio, M. Galizia, C. Álvarez, Á.E. Lozano, Polymer materials derived from the SEAr reaction for gas separation applications, *Polymer*. 267 (2023). <https://doi.org/10.1016/j.polymer.2022.125647>.

L. Matesanz-Niño, J. Moranchel-Pérez, C. Álvarez, Á.E. Lozano, C. Casado-Coterillo, Mixed Matrix Membranes Using Porous Organic Polymers (POPs)—Influence of Textural Properties on CO₂/CH₄ Separation, *Polymers*. 15 (2023) 4135. <https://doi.org/10.3390/polym15204135>.

L. Matesanz-Niño, D. Cuellas, C. Aguilar-Lugo, L. Palacio, A. González-Ortega, J.G. de la Campa, C. Álvarez, Á.E. Lozano, Isomeric Aromatic Polyimides Containing Biphenyl Moieties for Gas Separation Applications, *Polymers*. 15 (2023) 1333. <https://doi.org/10.3390/polym15061333>.

Finally, she is working on two new publications related to polymers of intrinsic microporosity (PIMs) and fluorinated polyimides.

S. Rico-Martínez, M. Rojas-Rodríguez, N. Esteban, **L. Matesanz-Niño**, M. Juan y Seva, L. Alexandrova, B.D. Freeman, C. Alvarez, A.E. Lozano, C. Aguilar-Lugo, Fluorinated biphenyl aromatic polyimides for gas separation applications. Real gas mixture study. Under review, *Industrial & Engineering Chemistry Research*. Manuscript ID: ie-2023-041206

L. Matesanz-Niño, A. González-Ortega, Á.E. Lozano, L. Garrido, C. Álvarez, Effect of Porous Polymer Networks Loads in the Gas Separation Properties of Polymers of Intrinsic Microporosity.

Chapter 3

3. General methodology

3.1 SYNTHESIS OF POLYMERS

To obtain polymer membranes with good mechanical properties able to be evaluated as materials for gas separation, it is essential to have previously synthesized high molecular weight polymers.

Polymerization is the process of converting an initial chemical substance, called monomer, into a long-chain molecule, polymer. An important parameter in the definition of a polymer is the degree of polymerization, DP, which determines the number of repeating units that make up the final structure of the polymer. The relationship between DP and molecular weight, M_w , is straightforward being $M_w = DP \times SU$ (where SU is the molecular weight of the repeating structural unit).

For step-growth polymerization, DP is a function of the conversion of the polymerization reaction (p) as determined by Carothers [56–58]:

$$DP = \frac{1}{(1-p)} \quad [\text{Eqn. 3.1}]$$

This equation when there is a stoichiometric imbalance, r , becomes:

$$DP = \frac{r+1}{r+1-2pr} \quad [\text{Eqn. 3.2}]$$

where r is the ratio of the monomer in stoichiometric defect to the one in excess.

Due to the Carothers equation, the purity of the monomers must be very high as a condition to obtain polymers of high molecular weight [59]. For example, partial oxidation of diamines gives rise to monofunctional monomers or non-reactive molecules, which leads to stoichiometric disproportionation. Also, water presents in the solvent can react with the functional groups of monomers, giving rise to non-reactive compounds. Therefore, the use of an inert atmosphere, pure reactives, and anhydrous solvents is essential in this type of polymerization.

In this memory, the polymeric materials have been obtained by step-growth polymerization. In particular, the polymers that have been employed are:

- Aromatic polyimides
- Aliphatic-aromatic polyimides
- Polymer networks made by electrophilic aromatic substitution reaction (EAS) (here called porous organic polymers, POPs)

The preparation of aromatic polyimides usually involves the use of a polycondensation method carried out at low temperatures, mainly to avoid side reactions that could limit the growth of macromolecular chains. In particular, the synthesis of polyimides consisted of two steps involving the formation of poly(amic) acid and posterior thermal or chemical cyclation to obtain the sought polyimide, as shown in Figure 3.1.

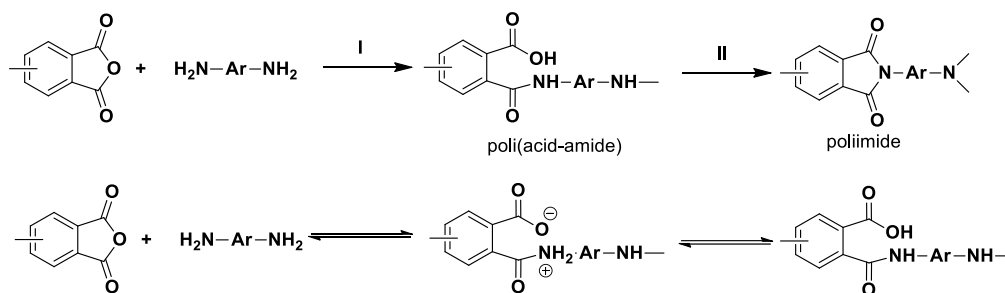


Figure 3.1. Above: Two-step synthesis of polyimides, down: Reaction mechanism for obtaining poly(amic-acid).

Over the years, reaction improvements have been made in polycondensation chemistry through the utilization of activated monomers. The activation of these monomers can be achieved by either activating the electrophile, primarily using organophosphorus reagents, or activating the nucleophilic diamines. Studies of our group [60–62] have reported that for the synthesis of aromatic polyimides by the *in-situ* formation of silylated diamines, the use of a tertiary base such as pyridine (Py) as an activating agent, and the use of a non-stoichiometric amount of a high pKa base (higher pKa than pyridine, for instance 4-dimethylamino pyridine, DMAP), significantly improves their molecular weight. This activation method has demonstrated remarkable efficacy, particularly for sterically hindered amines and amines possessing strong electron-withdrawing groups. Moreover, it was demonstrated that the use of N,N-dimethylacetamide (DMAc) as an aprotic polar solvent instead of N-methylpyrrolidone (NMP) resulted in an additional enhancement of the reaction that consequently led to higher viscosity.

The synthesis of the aromatic polyimides of this work involved the reaction between dianhydride and diamine, facilitated by base-assisted *in-situ* silylation of the diamine with the assistance of a mixture of tertiary bases. The silylation of diamine was achieved by dissolving it and then adding a precise quantity of trimethylchlorosilane (TMSCl, usually 1 mol/mol of amine), the corresponding base (usually Py, 1 mol/mol of amine), and a co-

base (DMAP, 0.05-0.5 mol/mol of Py). Finally, the appropriate stoichiometric amount of dianhydride was added to the reaction mixture.

The preparation of microporous polymer networks (POPs) was carried out using a relatively modern synthetic methodology developed by us [63]. This methodology is based on several Olah's studies about the protonation of activated aldehydes or ketones when subjected to highly acidic conditions. This protonation gives rise to high reactive intermediates, known as superelectrophiles, which exhibit a doubly electron-deficient nature. Notably, the reactivity of these superelectrophiles surpasses that of their parent monocations under traditional reaction circumstances, as stated through various studies [64–66]. This super-electrophilic entity can subsequently engage in successive condensation reactions with diverse nucleophiles, enabling interactions even with deactivated aromatic rings, as depicted in Figure 3.2.

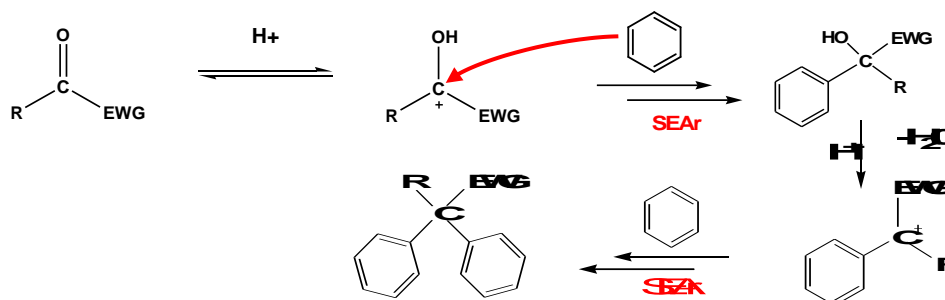


Figure 3.2. Methodology of the formation of Hydroxylalkylation polymers.

The synthesis of the polymer networks of this Ph.D. memory (POPs) was carried out using multifunctional aromatic (more than two aromatic groups) monomers with activated ketones. Reaction was promoted by using superacids like trifluoromethanesulfonic acid (TFSA), methanesulfonic acid (MSA), trifluoroacetic acid (TFA), or mixtures thereof.

3.1.1. Preparation of polymer networks

3.1.1.1. Materials

Most of the commercially available reagents were used without further purification, if not mentioned otherwise. Isatin (1H-indole-2,3-dione or I, 98% purity), 2,2,2-trifluoroacetophenone (TF, 98% purity), biphenyl (BP, 99% purity), methanesulfonic

acid (MSA, 98% purity), and chloroform (CHCl_3 , $\geq 99\%$ purity) were purchased from Sigma-Aldrich. Isatin was dried at $40\text{ }^\circ\text{C}$ for 2 h under vacuum prior to use. 1,3,5-triphenylbenzene (TPB, 99% purity) was purchased from Tokio Chemical Industry, triptycene (TR, 98% purity) from ABCR GmbH, and trifluoromethanesulfonic acid (TFSA, $>99.5\%$ purity) from Apollo Scientific.

3.1.1.2. Synthesis of monomers

3.1.1.2.1. 9,9'-spirobifluorene monomer (SBF)

The scheme of reaction is shown in Figure 3.3. Under a nitrogen atmosphere, a 500 mL three-neck flask equipped with a reflux condenser, a magnetic stir bar, and an addition funnel, was charged with a dispersion of magnesium turnings (1.69 g, 69.40 mmol) in the quantity required of anhydrous diethyl ether (Et_2O) to cover the magnesium turnings. Then, 1 mL of 2-bromobiphenyl was added to the magnesium dispersion to initiate the formation of Grignard reagent. The addition funnel was charged with a solution of 2-bromobiphenyl (11.09 g, 64.35 mmol) in 45 mL of anhydrous Et_2O . Afterwards, the solution was added dropwise and the mixture was allowed to reflux for 3 h until homogeneous. Next, a solution of fluorenone (11.36 g, 63.08 mmol) in 110 mL of anhydrous Et_2O was slowly added, and the mixture was allowed to reflux for a further 3 h. Finally, 100 mL of acetic acid (AcOH) was slowly added. The Et_2O solvent was stripped off by distillation under reduced pressure and the residue was washed and filtered with cold ethanol to afford the desired product 9,9'-spirobifluorene (SBF) monomer (reaction yield of 93%) as a white solid, mp: $206\text{ }^\circ\text{C}$. The chemical structure was confirmed by ^1H - and ^{13}C - NMR, as seen in section S2.1.1, Appendix 2.

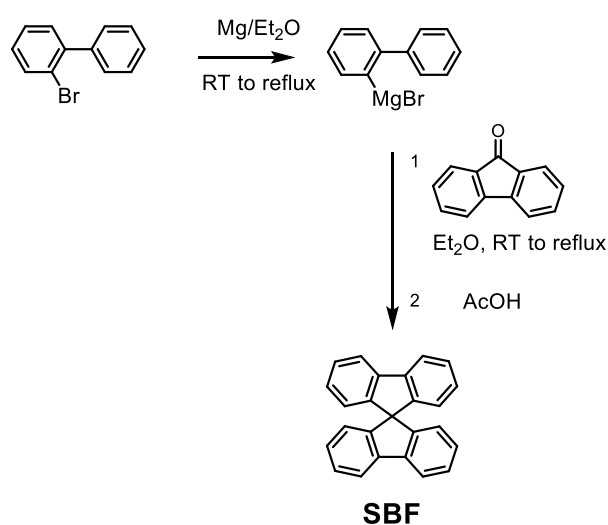


Figure 3.3. Synthesis of 9,9'-spirobifluorene.

3.1.1.2.2. Synthesis of 9,10-Dimethyl-9,10-dihydro-9,10-ethanoanthracene monomer (DMHEA)

The synthesis of DMHEA consisted of the preparation of 2,5-diphenylhexane-2,5-diol through a Grignard reaction and its ulterior cyclization by a Friedel-Crafts alkylation [53,67], as shown in Figure 3.4.

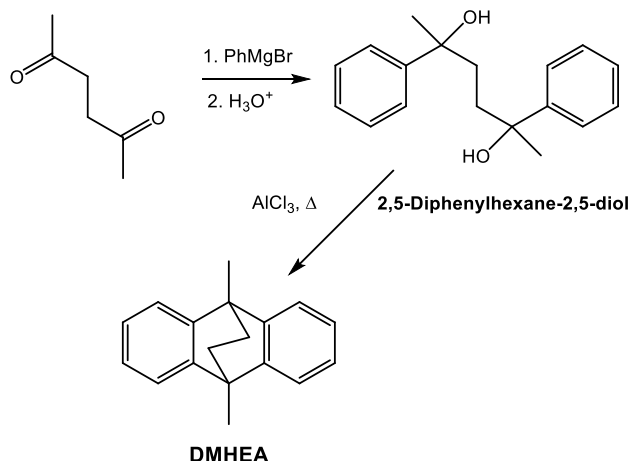


Figure 3.4. Synthesis of 9,10-dimethyl-9,10-dihydro-9,10-ethanoanthracene.

3.1.1.2.2.1 Synthesis of 2,5-diphenylhexane-2,5-diol

In a 1 L two-neck flask equipped with a reflux condenser, a dropping funnel, and a magnetic stir bar, a solution of phenylmagnesium bromide was prepared from magnesium (17.2 g, 720 mmol), bromobenzene (76 mL, 720 mmol) and 350 mL of dry ether. After, the solution was cooled with an ice-water bath, and 2,5-hexanedione (24 mL, 205 mmol) with 50 mL of dry ether was slowly added with the addition funnel. The reaction was maintained at room temperature for 12 h and at the reflux temperature of dry ether for a further 3 h. Next, the reaction was cooled with an ice-water bath and hydrolyzed with a very dilute solution of hydrochloric acid. The precipitate was quickly filtered, washed with abundant water, and dried under vacuum at room temperature. The 2,5-diphenylhexane-2,5-diol was obtained as a white solid (mp: 122 °C). The reaction yield was 86%. The chemical structure was confirmed by ¹H- and ¹³C- NMR, as seen in section S2.1.2.1, Appendix 2.

3.1.1.2.2.2. Synthesis 9,10-dimethyl-9,10-dihydro-9,10-ethanoanthracene

1 L three-neck flask blanketed by nitrogen was charged with 2,5-diphenylhexane-2,5-diol (27.0 g, 99.9 mmol) and 600 mL of anhydrous toluene. Afterward, it was cooled in an ice bath, and aluminum trichloride (15.0 g, 110 mmol) was slowly added in portions and the reaction suspension was stirred at room temperature for 6 h. Next, water was added to the

mixture and the toluene was decanted. The aqueous layer was extracted with Et₂O. The organic layer was washed with water, dried with MgSO₄, filtered, and concentrated under vacuum at 35 °C. The 9,10-dimethyl-9,10-dihydro-9,10-ethanoanthracene was crystallized from n-hexane (mp:121 °C). The yield reaction was of 46%. The chemical structure was confirmed by ¹H- and ¹³C-NMR, as shown in section S2.1.2, Appendix 2.

3.1.1.2.3. 1,3,5-tri-(2-methylphenyl)benzene (TMB)

The scheme of reaction is shown in Figure 3.5. A 50 mL two-neck Schlenk flask equipped with a reflux condenser and magnetic stir bar was charged with 2-methyl acetophenone (9.81 mL, 75 mmol) and trifluoromethanesulfonic acid (TFMSA) (0.66 mL, 7.50 mmol) under a nitrogen atmosphere, and heated at 130 °C. The reaction was maintained at this temperature for 24 h. The final product was concentrated in a rotary evaporator and purified by a chromatographic column using hexane as eluent. The 1,3,5-tri-(2-methylphenyl)benzene (TMB) was dried at 120 °C for 3h under vacuum, (mp:135-137 °C). The reaction yield was 82%. The chemical structure was confirmed by ¹H- and ¹³C-NMR, as shown in section S2.1.3, Appendix 2.

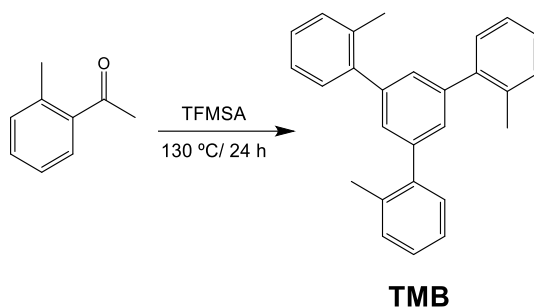


Figure 3.5. Synthesis of 1,3,5-tri-(2-methylphenyl)benzene.

3.1.1.2.4. 1,3,5-tri-(4-biphenyl)benzene (TBB)

The scheme of reaction is shown in Figure 3.6. A 100 mL three-neck flask equipped with a reflux condenser, mechanical stirring, and nitrogen flow, was charged with 4-acetylbiphenyl (23.24 g, 118.4 mmol) and dodecylbenzenesulfonic acid (DBSA) (7.50 mL, 23.69 mmol), which was heated at 50 °C. The reaction was maintained at 130 °C for 10 h. Next, 50 mL of methanol was added to the reaction, and the solid obtained was filtered and sequentially washed with cold methanol, a saturated solution of sodium bicarbonate, and water. The solid was then purified by percolation with dichloromethane (DCM) in a short silica-gel column. The pure product was dried at 120 °C for 3 h under vacuum, (mp: 235-237 °C). The reaction yield was 92%. The chemical structure was confirmed by ¹H- and ¹³C-NMR, as shown in section S2.1.4, Appendix 2.

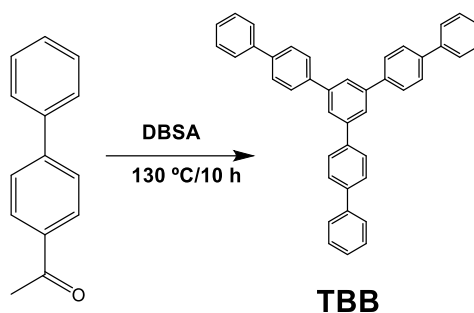


Figure 3.6. Synthesis of 1,3,5-tri-(biphenyl)benzene.

3.1.1.2.5. 1-methylindoline-2,3-dione (*N*-methyl isatin, MI)

The scheme of reaction is shown in Figure 3.7. A 250 mL two-neck flask equipped with a magnetic stir bar and a nitrogen blanket was charged with isatin (8 g, 54.4 mmol), potassium carbonate (K_2CO_3) (8.28 g, 59.8 mmol), iodomethane (CH_3I) (3.38 mL, 54.4 mmol) and 110 mL of *N,N*-dimethylformamide (DMF) under mechanical stirring and nitrogen flow. The reaction was maintained at room temperature for 12 h. Then, water was added to the mixture and the aqueous layer was decanted. The product was extracted with DCM, purified by recrystallization in toluene, and dried at room temperature under vacuum (mp: 131-139 °C). The reaction yield was 97%. The chemical structure was confirmed by 1H - and ^{13}C -NMR, as shown in section S2.1.5, Appendix 2.

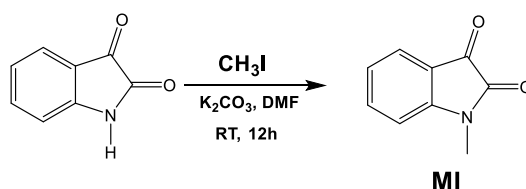


Figure 3.7. Synthesis of 1-methylindoline-2,3-dione.

3.1.1.3. Synthesis of porous organic polymers

The porous polymer networks (POPs) were synthesized by reacting a trifunctional monomer (TR, TPB, TMB, or TBB) or a tetrafunctional monomer (SBF) with an activated ketone (I, MI, or TF) in super acidic conditions using TFSA as the catalyst (Figure 3.8). Analogous networks were also synthesized by adding a mixture of the tri- or tetrafunctional monomer and a bifunctional comonomer (DMHEA or BP).

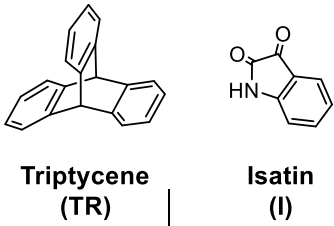


Figure 3.8. Example of scheme of the synthesis of the POP.

For simplicity, we will refer to networks derived from just one nucleophilic monomer as Ho-POPs and to those from 2 nucleophilic ones Co-POPs. The functional group stoichiometry was maintained by using an adequate amount of bi and tri or tetrafunctional reactants. In addition, different reaction conditions were used for the synthesis optimization of these materials, by varying the solvent (CHCl_3 or MSA) and the reaction temperature (room temperature (RT) or 60°C). The reaction conditions employed are summarized in the four methods that are listed in Table 3.1, where the number (1 and 2) refers to the solvent (CHCl_3 and MSA, respectively) and the letter (a and b) to temperature/reaction time (RT/120 h and $60^\circ\text{C}/96$ h, respectively). The number and letter of each method will be added to the acronyms of Ho-POPs bifunctional-activated ketone) and Co-POPs (tri (or tetra) functional/bifunctional monomer-activated ketone) to identify them, as shown in Tables 3.2 and 3.3.

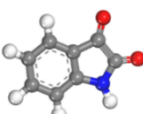
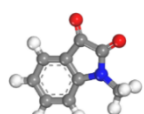
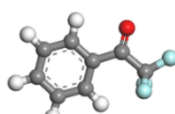
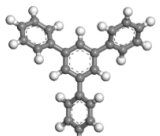
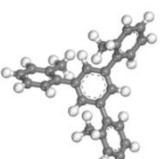
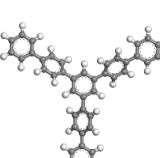
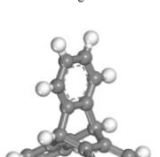
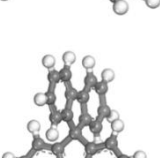
As an example, a general procedure for the synthesis of TR/DMHEA_I number (n) letter (l) is the following: an oven-dried, 50 mL, three-necked Schlenk flask equipped with a mechanical stirrer and nitrogen inlet and outlet was charged with TR (1.78 g, 7.0 mmol), DMHEA (2.46 g, 10.5 mmol), I (3.09 g, 21.0 mmol) and CHCl₃ or MSA (15 mL). The mixture was stirred at RT under a nitrogen blanket, cooled to 0 °C, and TFSA (30 mL or 20 mL according to catalyst/solvent ratio in Table 1) was then added dropwise for 15-20 min. Finally, the reaction mixture was allowed to warm to RT and held at that temperature for 120 h with stirring (method 1a and 2a) or held at RT for 1 h and at 60 °C for 96 h

(method 1b or method 2b). Once it was cold, the product was poured into a water/ethanol mixture (3/1), filtered, and consecutively washed with water (2x200 mL), CHCl_3 (2x200 mL), and acetone (1x200 mL). The powder obtained was dried at 180 °C for 12 h in a vacuum oven.

Table 3.1. *Reaction conditions used for the preparation of POPs*


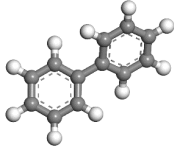
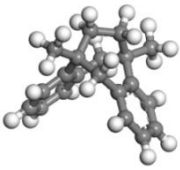
	Catalyst/Solvent (ratio)	Temperature, °C /reaction time, h
Method 1a	TFSA/ CHCl_3 (2/1)	RT /120
Method 1b	TFSA/ CHCl_3 (2/1)	RT/1, 60/96
Method 2a	TFSA/MSA (3/2)	RT/120
Method 2b	TFSA/MSA (3/2)	RT/1, 60/96

Table 3.2. Composition of *Ho-POPs* synthesized for this work

<i>Ho-POPs</i>		<i>I</i>	<i>MI</i>	<i>TF</i>
				
<i>TPB</i>		TPB-I nl	TPB-MI nl	TPB-TF nl
<i>TMB</i>		TMB-I nl	TMB-MI nl	TMB-TF nl
<i>TBB</i>		TBB-I nl	TBB-MI nl	TBB-TF nl
<i>TR</i>		TR-I nl	TR-MI nl	TR-TF nl
<i>SBF</i>		SBF-I nl	SBF-MI nl	SBF-TF nl

n and *l* refer to reaction conditions according to Table 1

Table 3.3. Composition of Co-POPs synthesized for this work

<i>Co-COPs</i>		<i>I</i>
		
<i>TPB</i>		TPB/BP-I
<i>TR</i>		TR/BP-I nl
<i>SBF</i>		SBF/BP-I
<i>TPB</i>		TPB/DMHEA-I
<i>TR</i>		TR/DMHEA-I nl
<i>SBF</i>		SBF/DMHEA-I

n and *l* refer to reaction conditions according to Table 1

3.1.2. Preparation of polymers

3.1.2.1. Materials

2-2'-Bis(4-aminophenyl)hexafluoropropane (6FpDA) was purchased from Chriskev (USA), 2,4,6-trimethylphenyldiamine (TMPD), 4,4'-(hexafluoroisopropylidene) diphtalic anhydride (6FDA) and 3,5-diaminobenzoic acid (DABA) were purchased from Apollo Scientific (UK). These monomers were purified by high vacuum sublimation

before use. Bis(2-aminopropyl) poly(ethylene oxide) (Jeffamine ED 2003), named here for simplicity as PEO, with a mean molecular weight of 1942 g/mol, was a gift from Huntsman International Europe. The PEO was dried to 40 °C for 5 h in a vacuum oven before being used.

Anhydrous 1-methyl-2-pyrrolidone (NMP), anhydrous N, N'-dimethylacetamide (DMAc), anhydrous pyridine (Py), 4-dimethylaminopyridine (DMAP) and trimethylchlorosilane (TMSCl), together with the other solvents and commercial reagents, such as acetic anhydride, were purchased from Sigma-Aldrich (Merck, Spain) at their highest level of purity.

3.1.2.2. Synthesis of aromatic copolyimides

Aromatic copolyimides containing carboxyl groups were prepared by a two-step polycondensation reaction of equimolecular amounts of the 6FDA dianhydride and a mixture of the 6FpDA and DABA diamines in a mole ratio of 1/0.1 or 1/0.2 (6FpDA/DABA), or 6FDA dianhydride and a mixture of the TMPD and DABA diamines in a mole ratio of 1/0.2 (TMPD/DABA). The reaction was carried out using the base-assisted *in-situ* silylation method [61,62] following the procedure described in [68], to obtain high-molecular weight polymers. Quantitative yields, well above 97%, were obtained for all of the copolymers.

As an example, the synthesis of the 6FDA-6FpDA-DABA copolyimide using a 6FpDA/DABA molar ratio of 1/0.1 is described below:

A 100 mL three-neck flask equipped with a mechanical stirrer and gas inlet and outlet was charged with 7.50 mmol (2.50 g) of 6FpDA, 0.75 mmol (0.114 g) of DABA, and 8 mL of NMP. Under a blanket of nitrogen, the mixture was stirred at room temperature until the solid was completely dissolved, was cooled to 0 °C, and 18.1 mmol (2.30 mL) and 18.1 mmol (1.46 mL) of Py were added dropwise for 30 min. The solution was then stirred for 5 min and allowed to warm to room temperature to ensure the silylation of diamines. Next, the solution was cooled again to 0 °C, and 8.25 mmol (3.65 g) of 6FDA and 1.80 mmol (0.221 g) of DMAP were added together with 8 mL more of NMP. The mixture was stirred for 15 min, the temperature was raised up to room temperature and the reaction was left overnight to form the poly(amic acid) solution. Afterward, 65.8 mmol (6.2 mL) of acetic anhydride and 65.8 mmol (5.3 mL) of Py were added and the mixture was stirred at room temperature for 6 h and at 60 °C for 1 h to promote the whole cyclization of poly(amic acid) to polyimide. Finally, the copolyimide

was precipitated in distilled water, collected, and consecutively washed with cold water, hot water, and a water/ethanol mixture (1/1). Finally, the polyimides were dried in a vacuum oven at 60 °C for 12 h, at 120 °C for 1 h, and at 180 °C for 12 h.

For comparative purposes, the 6FDA-6FpDA(PI) and 6FDA-TMPD (PI*) homopolyimides were also prepared from an equimolecular amount of 6FDA dianhydride and the corresponding diamine (6FpDA or TMPD). The copolyimides containing 6FpDA diamine will be named PI_x and TMPD PI*_x, where x is the molar percentage of DABA (x=10 and 20).

3.1.2.3. *Synthesis of aromatic-aliphatic copolyimides*

A series of aromatic-aliphatic copolyimides were prepared by a conventional two-step polycondensation reaction of equimolecular amounts of the 6FDA dianhydride and a mixture of the 6FpDA, DABA, and PEO diamines or 6FDA dianhydride and a mixture of the TMPD, DABA, and PEO diamine. For the preparation of these copolyimides, mixtures with weight ratios (y/1) between the aromatic diamines (6FpDA, and DABA) and the aliphatic diamine (PEO) of 1/1, 2/1, and 4/1 were used. In addition, an equimolecular amount of 6FDA was reacted with a mixture of TMPD, DABA, and PEO diamines in a molar ratio of 1:0.2:0.01 (TMPD:DABA:PEO). Quantitative yields, well above 97%, were obtained for all of the copolymers.

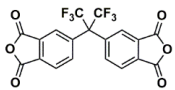
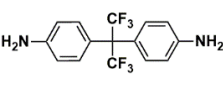
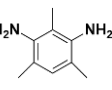
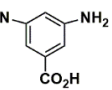
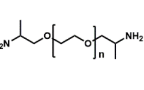
As an example, the synthesis of the copolyimide using a 6FpDA/DABA molar ratio of 1/0.1 and a (6FpDA/DABA)/ PEO weight ratio of 1/1 is described below:

A 100 mL three-neck flask equipped with a mechanical stirrer and nitrogen inlet and outlet was charged with 2.09 g (1.08 mmol) of dry PEO and 10 mL of NMP. When the PEO diamine was completely dissolved, 2.0 g (6.00 mmol) of 6FpDA and 0.091 g (0.60 mmol) of DABA were added together with 2 mL more of NMP. Once the diamines were dissolved, the flask was immersed in an ice-water bath and 7.68 mmol (3.40 g) of 6FDA dianhydride (in amount equimolar to the sum of the three diamines) and 10 mL more of NMP were added. The mixture was left stirring at room temperature for 12 h to form the poly(amic acid). Afterward, 60 mmol (5.65 mL) of acetic anhydride and 60 mmol (4.83 mL) of Py were added and the mixture was stirred at room temperature for 6 h and 60 °C for 1 h to promote the whole cyclization of poly(amic acid). Finally, the resulting copolyimide was precipitated into water and thoroughly washed in water and in ethanol-water 1/2 mixtures several times, dried at 60 °C for 12 h, 120 °C for 1h, and 180 °C for 12 h under vacuum.

The aromatic-aliphatic copolyimides will be hereinafter referred to as PI_xEO_y or PI*_xEO_y, where x is the molar percentage of DABA (x=10 and 20) and y is the weight ratio of aromatic diamine/aliphatic diamine mixture (y= 1, 2, 4 or 8).

As a summary, Table 3.4 shows all of the polymers synthesized for this work.

Table 3.4. *Molar composition of polymers*

	6FDA	6FpDA	TMPD	DABA	PEO
					
PI0	1	1	0	0	0
PI10	1.1	1	0	0.1	0
PI20	1.2	1	0	0.2	0
PI10EO4	1.15	1	0	0.1	0.05
PI10EO2	1.19	1	0	0.1	0.09
PI10EO1	1.28	1	0	0.1	0.18
PI20EO4	1.25	1	0	0.2	0.05
PI20EO2	1.29	1	0	0.2	0.09
PI20EO1	1.39	1	0	0.2	0.19
PI*	1	0	1	0	0
PI*20	1.2	0	1	0.2	0
PI*20EO1	1.21	0	1	0.2	0.01

3.2. MEMBRANE FABRICATION

3.2.1. Neat polymer membranes

Copolyimide films were prepared by the solution casting method. 10% (w/v) copolyimide solutions in tetrahydrofuran (THF) or DMAc were filtered through a 3.1 μ m fiberglass Symta[®] syringe filter, poured onto a glass ring placed on a leveled glass plate, and left at 30 °C for 12 h and 60 °C for 12 h to remove most of the solvent (Figure 3.9). The films were peeled off from the glass plate and subjected to the following thermal treatment

under vacuum conditions: 60 °C/1 h, 80 °C/30 min, 120 °C/1 h, 150 °C/30 min, and 180 °C/12 h (c.f. figure y). Transparent films with thickness ranging from 40 to 60 μm were obtained.

The copolyimide films will be referred to as the copolyimides.

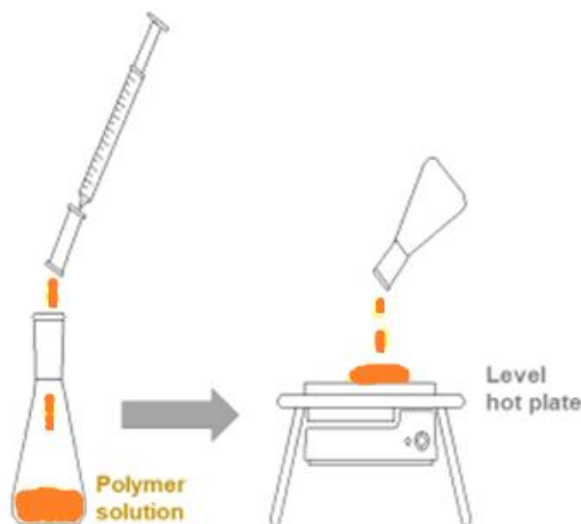


Figure 3.9. Solution casting method.

3.2.2. Polymer blend membranes

A series of polymer blends were prepared using different weight ratios of PI_x/PI_xEO_y copolyimides (z/1): 2/1 and 1/1. The required amounts of PI_x and PI_xEO for each blend were dissolved at 10% (w/v) in THF by stirring at room temperature. Next, the films of the blends were obtained using the solution casting method and the thermal treatment above described. The final thickness of the blend films ranged from 40-60 μm .

The blend films will be hereinafter referred to as PI_x/PI_xEO_y (z/1), where (z/1) is the weight ratio of PI_x to PI_xEO_y.

3.2.3. Mixed matrix membranes

Free-standing, flat sheet mixed matrix membranes (MMMs) were prepared by incorporating 20 wt.% of POP into PI*, PI*20, or PI*20EO1, using the procedure described in Figure 3.10. A suspension of POP (120 mg in 4 mL of DMAc) was stirred for 24 h at room temperature, followed by ultra-sonication (US) for 20 min using a 130 W ultrasonic probe (Vibra Cell 75186) operating at 50% maximum amplitude. The US procedure consisted of 40 cycles, each consisting of 20 s of US followed by 10 s of non-

US, to ensure proper particle dispersion. Next, one-third of a filtered polymer solution (600 mg of polymer in 4.0 mL of DMAc) was added to the suspension while stirring. Subsequently, the suspension was sonicated for a further 2 min (4 cycles: 20s on / 10s off) before adding the remaining polymer solution. The resulting mixture was magnetically stirred for 10 min. MMM films were cast from this suspension and subjected to the same drying procedure described in Section 2.1. The final thickness of the MMM films ranged from 45-65 μm .

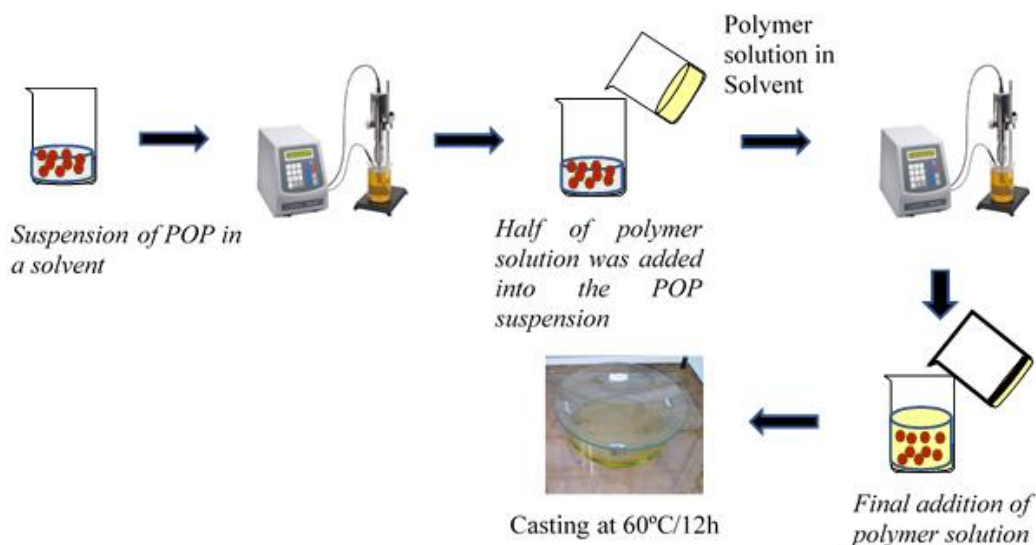


Figure 3.10. Procedure for the preparation of mixed matrix membranes.

The MMMs were named following the same convention as the pristine membranes but with the addition of POP at the end. Therefore, the corresponding MMM abbreviations will be PI*POP, PI*20POP, and PI*20EO1POP.

3.2.4 Membranes conditioning in methanol

Neat polymer membranes, as well as MMMs, were soaked in methanol for 24 h, followed by drying them at 30 °C for 3 h under high vacuum conditions. The samples were stored at room temperature and left to age. The physical aging of the samples was monitored at three time points: immediately after the conditioning and drying process ($t=0$, referred to as point 0), as well as at 12 (point 1) and 18 months (point 2). At this point, it is important to clarify that pure membranes and MMMs, aged at 18 months, were the materials used for this work. The objective of the methanol conditioning was to restore the permeability

of the membranes to a point close to $t=0$ (eliminating the differences that could occur in their processing and drying [69–72]) and then the films were stored for a long time at room temperature to physically make the aging to the membranes before performing the characterization and plasticization studies.

3.2.5 Thermal cross-linking protocol

Circle membrane coupons of copolyimides and polymer blends were cut into 3 cm² pieces, sandwiched between ceramic plates to avoid film rolling at high temperatures, and placed in a quartz tube furnace in a high-purity nitrogen atmosphere (0.3 L min⁻¹). Samples were heated to 275 °C at 10 °C min⁻¹ and held for 10 min, then to 375 °C at 5 °C min⁻¹ and held for 10 min, and finally to 450 °C at 5 °C min⁻¹ for 5 min. Then, the samples were cooled as fast as the device allowed (average cooling rate around 15 °C min⁻¹).

For the sake of simplicity, the thermally treated membranes were named the same as pristine membranes and MMMs, with the addition of -TT at the end.

3.3. CHARACTERIZATION TECHNIQUES

3.3.1. Characterization of monomers and polymers

Chemical structures of monomers and polymers were characterized by proton (¹H) and carbon (¹³C) nuclear magnetic resonance (NMR). The spectra were recorded on a Bruker Avance 400 spectrometer using deuterated solvents, such as dimethyl sulfoxide (DMSO-d₆), tetrahydrofuran (THF-d₈), or chloroform (CDCl₃). In particular, polymer networks (POPs) were characterized by Solid state ¹³C cross-polarization magic angle spinning. NMR spectra (CP-MAS ¹³C NMR) were recorded on a Bruker Avance 400 spectrometer equipped with an 89 mm wide bore and a 9.4 T superconducting magnet. The spectrometer operated at a Larmor frequency of 100 MHz using a contact time of 1 ms and a delay time of 3 s. All samples were spun at 11 KHz.

Polymer solubility tests were conducted in test tubes, using 1-2 mg of polymer and 1 mL of solvent. Each polymer sample was stirred at room temperature for 24 h. If the sample did not dissolve, it was heated to the boiling temperature of the solvent and then allowed to cool to observe if the polymer precipitated.

Inherent viscosities of polymers were measured at 30 °C with an Ubbelohde viscometer using DMAc as solvent at 0.5 g dL⁻¹ concentration.

The thermal stability of POPs was measured by thermogravimetric analyses (TGA), which were performed on a TA Q-500 thermobalance under a nitrogen atmosphere (60 mL min⁻¹). High-resolution dynamic thermogravimetric analyses (Hi-ResTM TGA) at 20 °C min⁻¹ from 30 to 850 °C, with sensitivity and resolution parameters of 1 and 4, respectively.

3.3.2. Characterization of membranes

The chemical structure of membranes was characterized using attenuated total internal Reflectance-Fourier transform infrared analysis (ATR-FTIR). Spectra were registered on a Perkin Elmer Spectrum RX1 FTIR spectrometer.

The thermal stability of membranes was also measured by TGA using the same protocol described above. In particular, isothermal TGA measurements by holding the sample at a temperature for a given time were carried out to optimize the thermal treatment needed for obtaining cross-linking membranes.

Morphology of membranes was studied by wide-angle X-ray scattering (WAXS). WAXS patterns were recorded in the reflection mode at room temperature, using a Bruker D8 Advance diffractometer provided with a Goebel Mirror and a PSD Vantec detector. CuK_α (wavelength, λ= 1.54 Å) radiation was used. A step-scanning mode was employed for the detector, with a 2θ step of 0.024° and 0.5 s per step. In particular, the cross-sectional morphology of mixed matrix membranes was analyzed by Field emission scanning electron microscopy (FE-SEM). FE-SEM images were taken with a Quanta 200 FEG ESEM on Au-metallized samples operating at an acceleration voltage of 15 kV in a high vacuum, using the secondary electron detection method.

The membrane density (ρ) was determined based on Archimedes' principle using a top-loading electronic XS105 Dual Range Mettler Toledo balance coupled with a density kit. The samples were sequentially weighed in air and then in high-purity isooctane at room temperature. The density was calculated from Equation (3.3).

$$\rho = \rho_{\text{liquid}} \times \frac{w_{\text{air}}}{w_{\text{air}} - w_{\text{liquid}}} \quad [\text{Eqn. 3.3}]$$

where ρ_{liquid} is the density of isooctane, *w_{air}* is the sample weight in air, and *w_{liquid}* is the sample weight in isooctane. The average value and standard deviation of the density were obtained from six measurements for each sample.

The fractional free volume (FFV) was estimated from density data using Equation (3.4):

$$FFV = \frac{V_e - 1.3V_w}{V_e} \quad [\text{Eqn. 3.4}]$$

where V_e is the polymer specific volume (i.e., $1/\rho$) and V_w is the polymer van der Waals volume. V_w was calculated through molecular modeling of the polymer repeating units using the semiempirical Austin Model (AM1) [73] in the Biovia Materials Studio program [74]. The optimized repeating units were used to calculate the molecular volume by constructing a 20-unit polymer structure using the Builder Polymers, and Atom Volumes and Surface algorithms.

The gel fraction of cross-linked samples was estimated using eqn. (3.5):

$$\text{Gel fraction (\%)} = \frac{W_{\text{final}}}{W_{\text{initial}}} \times 100 \quad [\text{Eqn.3.5}]$$

where W_{initial} is the weight of cross-linked sample and W_{final} is the weight of the cross-linked sample after extracting the soluble fraction. W_{final} was determined by immersing the cross-linked samples in DMAc at room temperature for 24 h and at 60 °C for 4 h under stirring. Then the sample was washed four times with ethyl ether and dried at 60 °C for 4 h and at 180 °C under vacuum for 12 h and weighed again.

Mechanical properties of membranes were evaluated under uniaxial tensile tests at room temperature using an MTS Synergie-200 testing machine equipped with a 100 N load cell. Rectangular pieces of 5 mm width and 30 mm length were subjected to a tensile load applied at 5 mm min⁻¹ until fracture.

3.3.3. Characterization of porous polymer networks

The surface area and pore texture of POPs were determined by physical adsorption using N₂ and CO₂ as adsorptive at low pressures (up to 1 bar) to obtain a thorough characterization of these materials. POPs synthesized for this work are highly microporous (pore widths less than 2 nm), and no mesoporosity (pore widths between 2 and 50 nm) and/or macroporosity (pore widths greater than 50 nm) were observed [75]. In addition, micropores can be classified according to their width as: narrow micropores, also called ultramicropores (width less than 0.7 nm), micropores (width between 0.7 nm and 1.4 nm), and supermicropores (width between 1.4 and 2.0 nm) [76]. N₂ at -196 °C (77K) is the most widely used adsorptive since it covers a wide range of relative pressure from 10⁻⁶ to 1, and thus its use is very useful for the characterization of porous materials. However, it is well-known that diffusion of N₂ molecules into narrow micropores is very slow at cryogenic temperature [77]. Despite the similar minimum kinetic dimensions for

N₂ (0.36 nm) and CO₂ (0.33 nm) molecules, there is a better accessibility of CO₂ molecules into narrow micropores due to the higher adsorption temperature (0 °C). In summary, the CO₂ adsorption at 0 °C covers a relative pressure range up to 0.03, and thus provides the volume of narrow micropores (V_{nmicro}), whereas the N₂ adsorption at -196 °C (77K) provides the total volume of micropores (V_{micro}).

Low-pressure N₂ adsorption–desorption isotherms measured at -196 °C (77 K) in a volumetric device ASAP 2010 (Micromeritics) in the 10^{-6} to 0.995 relative pressure (p/p_0) range. The minimum equilibrium time (both for the adsorption and desorption cycle) was 300 s. Samples were previously degassed at 125 °C for 18 h under a high vacuum to eliminate humidity traces and any other adsorbed gases. The CO₂ adsorption capacities of the POPs up to 1 bar were measured at 0 and 25 °C (273 and 298 K) in a volumetric device Nova 4200 (Quantachrome). The system was exposed to high vacuum and the sample was heated at 125 °C for 18 h to degas it before measuring gas adsorption.

From the N₂ adsorption branch, three relevant textural parameters of POPs were determined [78]. The surface area by applying the Brunauer–Emmett–Teller (BET) method (S_{BET}) in the 0.01 to 0.2 p/p_0 range, which is the model most widely used for the determination of surface area of porous materials. At low temperatures, the N₂ molecules tend to fill the entire porosity, with packing only depending on the N₂ molecule, independent of the adsorbent structure making this the optimum adsorptive for determinate S_{BET} . The total pore volume (V_{total}) was defined as the volume of liquid nitrogen adsorbed at 0.975 relative pressure. The total available micropore volume (V_{micro}) by applying the Dubinin–Radushkevich (DR) equation in the 0.001 to 0.2 range, which is based on the Dubinin theory of the volume filling of micropores and is widely used for assessing the volume of micropores in microporous materials, especially carbonaceous materials.

From the CO₂ adsorption isotherm at 0 °C, the narrow micropore surface area (S_{nmicro}) and the narrow micropore volume (V_{nmicro} , pore width less than about 0.7 nm) were determined by applying the Dubinin–Radushkevich (DR) equation in the 10^{-4} to 0.03 p/p_0 range. The pore size distribution (PSD) is another important property when designing porous materials for gas storage and separation applications. Experimentally, one of the current standards for determining PSD is using the nonlocal density functional theory (NLDFT) and N₂ isotherms at -196 °C. The NLDFT method is based on calculating model isotherms assuming an ideal pore geometry (e.g. slit pore) that is used to determine the PSD in the entire range of pore sizes accessible to the adsorptive molecule. However, in

this work, due to the highly microporous nature of POPs, NLDFT PSD was obtained from the CO₂ adsorption isotherms of POPs using the SAIEUS (solution of adsorption integral equation using splines) software [79].

The binding affinity of POPs to CO₂ was assessed by determining the isosteric heat of adsorption, Q_{st} , which was calculated with the ASiQwin[®] by applying the Clausius-Clayperon equation (Eq. 3.6) to the adsorption isotherms measured at 0 °C and 25 °C at various CO₂ coverages (θ).

$$\left[\frac{\delta(\ln P)}{\delta\left(\frac{1}{T}\right)} \right]_{\theta} = \frac{Q_{st}}{R} \quad [\text{Eqn. 3.6}]$$

Where P, T, and R are the pressure, temperature, and the universal gas constant, respectively.

Finally, The adsorption selectivity of CO₂ over N₂ and CH₄ was estimated from the pure high-pressure CO₂, N₂, and CH₄ adsorption isotherms at 25 °C by applying the Ideal Adsorbed Solution Theory (IAST) proposed by Myers and Prausnitz [80] and revised in other articles [81,82]. High-pressure adsorption/desorption isotherms up to 30 bar for N₂ and CO₂, and 70 bar for CH₄ were measured volumetrically at 25 °C in a high-pressure device iSorb (Anton Paar). The samples were degassed in situ in the balance, at 120 °C under vacuum for 12 h.

3.4. GAS TRANSPORT PROPERTIES

3.4.1. Permeability measurements

Pure gas permeability of membranes was measured by a custom-made constant volume/variable pressure apparatus at 35 °C and with an upstream pressure of 3 bar. The purities for CH₄ and O₂ were greater than 99.95% and for He, N₂, and CO₂ were higher than 99.99%. The scheme of the permeation device is shown in Figure 3.11. Prior to each measurement, the membranes were placed in the system and maintained under a high vacuum overnight to remove possible traces of humidity and other sorbed species. The permeate pressure was recorded as a function of time until the steady state was reached, as shown in Figure 3.12. Before measuring the other gases, helium permeation tests at three upstream pressures (1, 3, and 5 bar) were carried out to verify the absence of pinholes in the membrane.

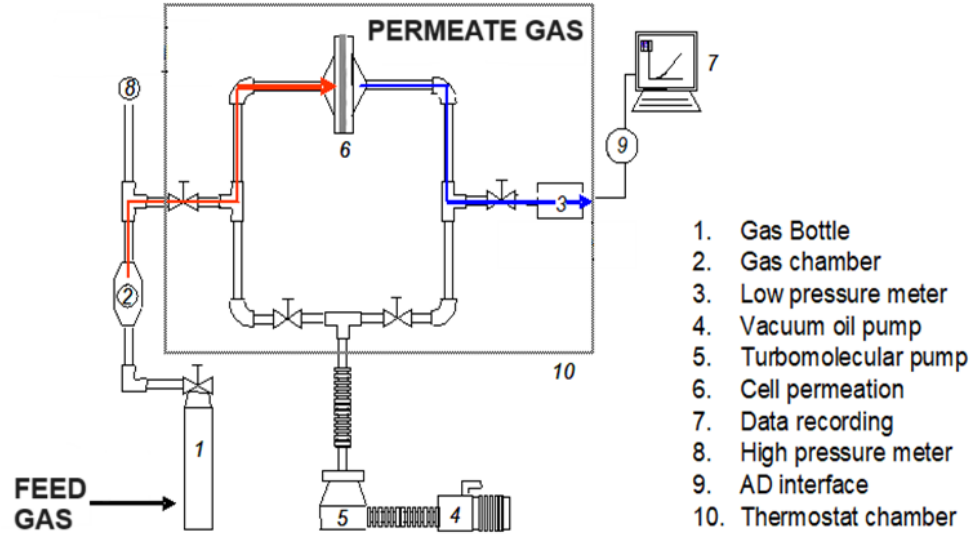


Figure 3.11. Scheme of permeation device

The gas permeability coefficient, P , was calculated as follows:

$$P = \frac{273.15Vl}{76ATp_0} \times \left[\left(\frac{dp(t)}{dt} \right)_{ss} - \left(\frac{dp(t)}{dt} \right)_{leak} \right] \quad [\text{Eqn 3.7}]$$

Where V is the downstream volume (cm^3), T is the temperature (K), l is the membrane thickness (cm), A is the effective area (cm^2) of the membrane, p_0 is the upstream pressure (mbar), $(dp(t)/dt)_{ss}$ is the steady-state rate of the permeate pressure (mbar s^{-1}), and $(dp(t)/dt)_{leak}$ is the system leak rate (mbar s^{-1}), which was less than 1% of $(dp(t)/dt)_{ss}$, 76 cmHg and 273.15 K are standard conditions for pressure and temperature, respectively. The permeability coefficient was expressed in Barrers [$1\text{Barrer} = 10^{-10} (\text{cm}^3 (\text{STP}) \text{cm cm}^{-2} \text{s}^{-1} \text{cm Hg}^{-1})$].

The ideal selectivity between two gas pairs ($\alpha_{A,B}$), A and B, is the ratio of the pure gas permeabilities (Equation (3.8)).

$$\alpha_{A,B} = \frac{P_A}{P_B} \quad [\text{Eqn. 3.8}]$$

Additionally, to further compare each material, permeability was broken into its diffusion (D) and sorption (S) components via the solution-diffusion model.

$$P = DS \quad [\text{Eqn. 3.9}]$$

To do so, the diffusivity coefficient was estimated through permeation experiments via the time lag method [Eqn. 3.10].

$$D = \frac{l^2}{6\theta} \quad [\text{Eqn. 3.10}]$$

Where θ is the time lag value.

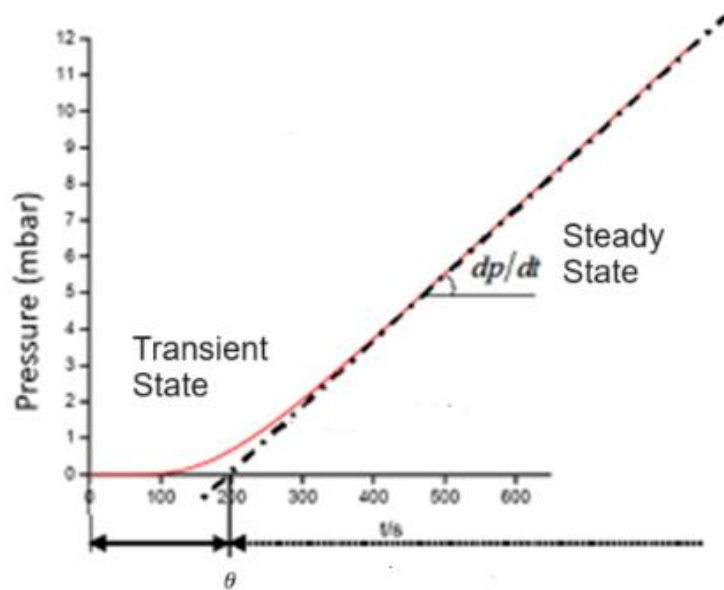


Figure 3.12. Typical permeation curve

3.4.2. Plasticization test

Plasticization tests were carried out by measuring CO₂ permeability under varying feed pressures (ranging from 1 to 30 atm) and temperatures (25, 35, and 50 °C). The pressure increments were either 5 atm (at 35 °C) or 10 atm (at temperatures other than 35 °C). Two consecutive cycles were performed as follows:

1. The membrane was mounted inside the permeation cell and the system was exposed to a high vacuum overnight to degas the membrane.
2. The feed pressure was adjusted to the desired value and then the permeate pressure was recorded as a function of time. Each pressure step was run for 6 times the time lag (θ), followed by a depressurization step for approximately the same time.
3. At the end of cycle 1, the membrane was kept at the conditioning pressure (30 atm) for a minimum of 6 θ . Subsequently, the system was degassed overnight.
4. Finally, the two first steps were repeated for the second cycle.

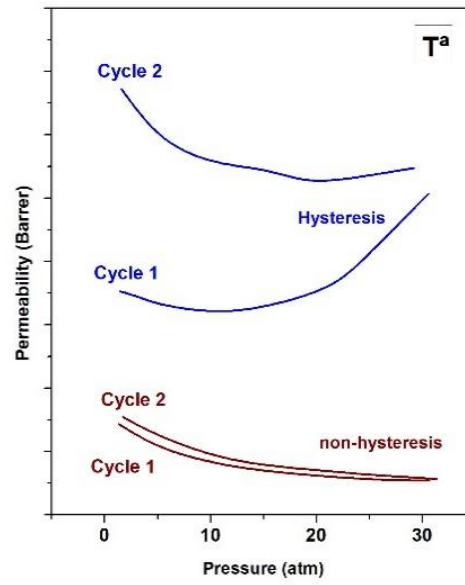


Figure 3.13. Plasticization experiment curves

Chapter 4

4. Gas Separation Membranes Obtained by Partial Pyrolysis of Polyimides Exhibiting Polyethylene Oxide Moieties

4.1 INTRODUCTION

Nowadays it is mandatory to develop energy-efficient separation processes exhibiting mild environmental fingerprints. Energy consumption in chemical separation processes in all industrialized countries is enormous and it must be corrected as soon as possible to improve social welfare. For example, in the US, it accounts for 50% of the chemical industry's energy consumption and 15% of the total national energy needs [83]. Therefore, it is a priority to integrate or replace traditional thermal separation processes, such as distillation, with better energy-efficient separations based on membranes [18,84,85]. Membrane gas separation offers interesting potential advantages over conventional separations (e.g., absorption, distillation, adsorption), including energy efficiency, small footprint, compact design, and mechanical integrity [21,86–90]. The search for membrane materials exhibiting enhanced gas separation properties is being increasingly explored to improve existing applications (e.g., air separation, hydrogen recovery, and CO₂/CH₄ and CO₂/N₂ separations), and develop new ones (e.g., olefin/paraffin separations, CO₂ separations, H₂S removal from natural gas, gas separation at high temperatures, etc.) [18,44,91–93].

The key factors determining the membrane performance for industrial gas separation applications are high selectivity (that is, the membrane's ability to discriminate a specific component in a mixture) and permeability (that is, the membrane productivity; i.e. flux of a certain gas through the membrane), adequate chemical, thermal and mechanical resistance under operating conditions, long working lifetime, cost-effective and defect-free membrane production. Glassy polymer membranes are mostly used in gas separations due to their desirable combination of size-sieving ability and mechanical properties. However, polymer membranes exhibit a well-known permeability/selectivity trade-off, based on which highly permeable membranes are often poorly selective, and vice versa. This behavior was first evidenced by Robeson in 1991 [26], updated in 2008

[27], and revised recently [31,94,95], due to the progress in the area of membrane materials science. In general, the knowledge acquired during the last years has allowed for establishing some basic rules to overcome the permeability/selectivity trade-off [44,96]. Today, highly permeable membranes capable of surpassing the 2008 upper bound have been developed, such as well-designed aromatic polyimides [97], polymers of intrinsic microporosity (PIMs) [98,99], perfluoropolymers [100,101], and thermally rearranged (TR) polymers [102]. However, the issues of easy processability, mechanical stability, and long-term stability are not yet solved.

Glassy high fractional free volume polymers suffer from physical aging and plasticization, which limits their potential for industrial gas separation membranes. At temperatures below the glass transition temperature, short-range cooperative motions of polymer chains allow the system to slowly relax the excess free volume, to approach the final equilibrium state. Physical aging results in polymer densification and, therefore, in a reduction of its internal free volume, which causes a decrease in gas permeability [41,103]. Plasticization is the consequence of polymer swelling upon sorption of highly condensable and soluble species, which translates to higher permeability and lower selectivity [38,39], which, analogous to physical aging, is related to chain mobility. Several approaches have been exploited to improve the resistance to plasticization and physical aging of high-free volume polymers including, among others, molecular tailoring of polymers [104], polymer blending [105–107], chemical and thermal cross-linking [108–110], and addition of nanoparticles [72,111].

Cross-linking is one of the most cost-effective and easy-to-apply strategies for reducing molecular mobility by increasing interchain rigidity and, thus, mitigating physical aging and plasticization effects. However, cross-linked membranes commonly exhibit high selectivity but reduced permeability relative to the original, non cross-linked materials [112,113].

Carbon molecular sieve (CMS) membranes are commonly derived from the controlled pyrolysis of aromatic polymeric precursors [114]. Because of the carbonization process, CMS membranes possess a bimodal pore size distribution consisting of micropores (0.7–2 nm), which provide a high gas permeability, and ultramicropores (< 0.7 nm), which allow selective discrimination of gases by size molecular (high permselectivity). This particular porous structure, which primarily depends on temperature, time of pyrolysis, gas atmosphere, and precursor polymer, makes them ideal materials to separate gas pairs

such as CO₂/CH₄, CO₂/N₂, and C₃H₆/C₃H₈ [115–117]. Several studies have shown the preparation of CMS membranes derived from blends of thermally stable and thermally labile polymers as an alternative to obtain higher permeability membranes, with better mechanical resistance, by controlled pyrolysis [118,119].

In a recent study [120], our group developed a strategy that consisted of blending a high-free volume aromatic polyimide with block aromatic-aliphatic copolymers, which derived from the same polyimide but having poly(ethylene oxide) (PEO) moieties. 6FDA-6FpDA polyimide was chosen as the aromatic polyimide because of its high free volume, good mechanical resistance, and good permeability/selectivity balance for CO₂/CH₄ gas pair; however, this material suffers from plasticization. Blends of 6FDA-6FpDA polyimide and 6FDA-6FpDA-PEO copolyimide yielded cross-linked materials after selectively removing the PEO units upon thermal treatment below the degradation temperature of the aromatic polyimide. The cross-linked membranes exhibited better plasticization resistance to CO₂ relative to neat 6FDA-6FpDA polyimide. However, cross-linking caused a significant decrease in gas permeability, which was likely due to a volume shrinkage of membrane (i.e., producing a decrease in the fractional free volume (FFV)).

In this work, we propose a new strategy to eliminate the membrane volume shrinkage, consisting of the incorporation of an additional aromatic diamine, 3,5-diaminobenzoic acid (DABA), capable of producing interchain cross-linking [110,121,122]. Thus, during the thermal treatment to selectively remove the PEO units, an additional cross-linking due to the carboxylic groups takes place, which prevents, or minimize the membrane shrinkage, leading to a much improved permeability/selectivity balance.

To support this hypothesis, a series of aromatic copolyimides, 6FDA-6FpDA-DABA (PIx), and aromatic-aliphatic copolyimides, 6FDA-6FpDA-DABA-PEO (PIxEOy), has been prepared by varying both the content of PEO and DABA. In this work, the content of PEO in the PIx/PIxEOy blends has been reduced to less than 10 wt.%. These blends have been evaluated as gas separation membranes before and after a thermal treatment to remove the PEO units.

The final goal of this work is to use analog cross-linkable materials as a mere additive that can be mixed with high fractional free volume glassy polymers, to improve or maintain their gas separation properties, while enhancing their plasticization resistance.

4.2 RESULTS AND DISCUSSION

4.2.1. Synthesis and characterization of the copolyimides

A set of aromatic copolyimides (PI_x) and aromatic-aliphatic copolyimides (PI_xEO_y) were prepared by a two-step condensation reaction as described in sections 3.1.2.2 and 3.1.2.3 in Chapter 3. The chemical structure of the starting monomers and the synthetic scheme of the copolyimides are shown in Figures 4.1 and 4.2. The activation of diamines by the *in-situ* silylation method was not used in the synthesis of PI_xEO_y, because it yielded copolyimides having lower molecular weights than those obtained by the classical two-step polycondensation. The compositions of all the copolyimides and the corresponding acronyms, which will be used throughout this work, are shown in Table 3.4 in section 3.1.2.3 Chapter 3.

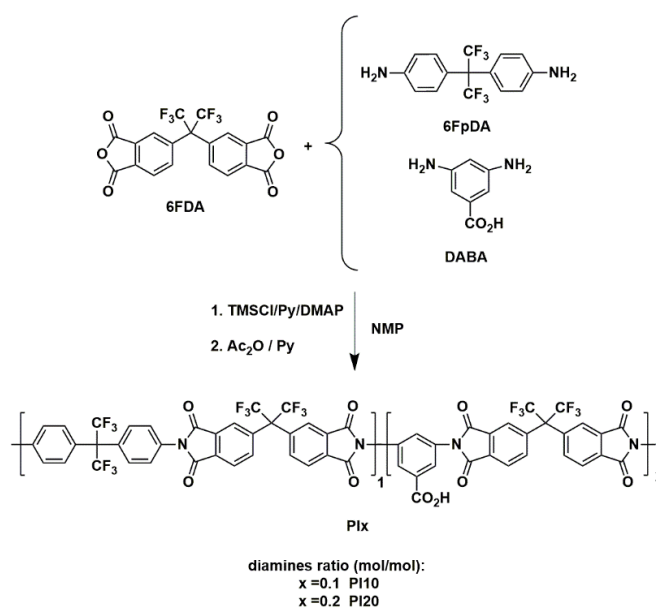


Figure 4.1. Scheme of synthesis of the aromatic copolyimides (PI_x).

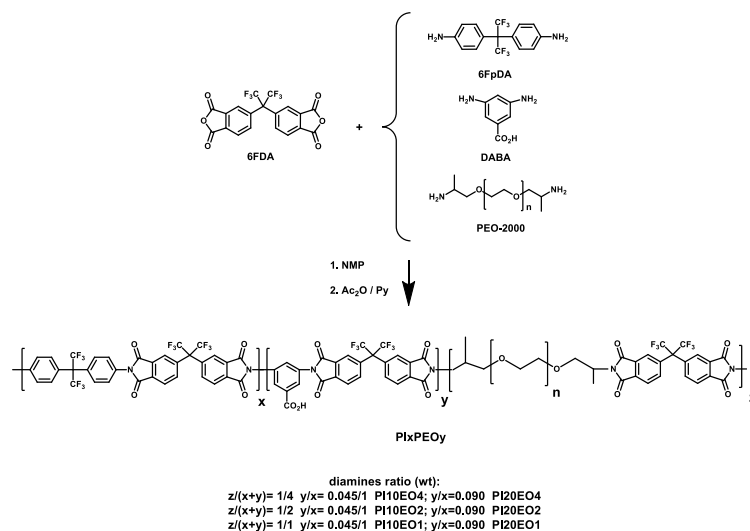


Figure 4.2. Scheme of synthesis of aromatic-aliphatic copolyimides (PIxEOy).

All of the copolyimides were soluble in polar aprotic media and even in a solvent like THF, as shown in Table S1.1, section 1.1 in Appendix 1, which allowed them to be easily processed into films using the casting method. Moreover, the use of THF as the casting solvent greatly simplified the removal of solvent at low temperatures.

The chemical structure of PIx and PIxEOy was confirmed by ^1H NMR and ATR-FTIR. As an example, the ^1H -RMN spectrum of PI20EO2 is shown in Figure 4.3. The characteristic peaks for aromatic protons appeared between 7.50 and 8.50 ppm. The protons of DABA moiety appeared at 8.22 (H7) and 7.95 ppm (H6). All the aromatic signals were consistent with the ones observed in the PI20 spectrum (Figure S1.1, section 1.1 in Appendix 1). The protons of methylene groups appeared at 3.52 ppm (H9, H10, and H12-H14) and the one of methyl groups between 1-1.5 ppm (H15 and H16). The composition of the copolyimides could not be accurately determined from the ratio of areas of the peaks at 8.22 and 7.95 ppm (of the DABA moiety) to the peak at 3.52 ppm (of the PEO fraction) because the integrated area under the aromatic peaks was considered too small to give a reliable value.

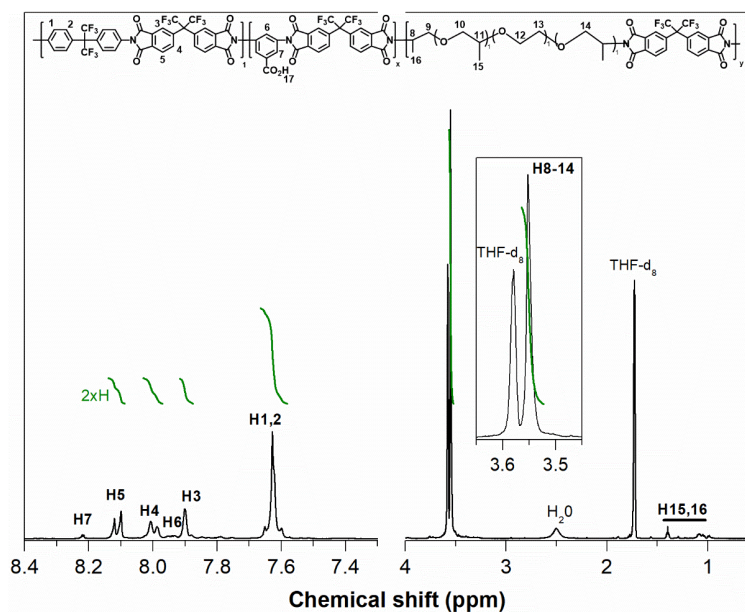


Figure 4.3. ^1H NMR spectrum of PI20EO2 in THF- d_8 .

The molecular weight of copolyimides was estimated by measuring their inherent viscosities, and the values are listed in the first column of Table 4.1. It must be pointed out that the viscosities of PI x were not compared to those of PI x EO y because they have different chemical structures. For PI x , the viscosity and molecular weight decreased with increasing the DABA content. A possible explanation is the low reactivity of the amino groups from the DABA monomer due to the electron-withdrawing effect of the carboxyl group, despite using the *in-situ* silylation method during the polyamic acid formation. For PI x EO y having comparable PEO percentages, the viscosities were similar, and thus similar molecular weights could have been achieved.

All of the copolyimides and the reference polyimides were processed as films, whose properties were thoroughly characterized to optimize the cross-linking protocol.

Table 4.1. *Inherent viscosity (η_{inh}) and thermogravimetric results of PI0 polyimide and PIx and PIxEOy copolyimides.*

Sample	η_{inh}^a	T_{d1}^b	PEO content ^d	$T_{d2}^{b,c}$	R_{800}^e
PI0	0.703±0.005		0	514	52.7
PI10	0.63±0.01		0	512	53.0
PI10EO4	0.415±0.004	394	9.93 (9.66)	nd ^b	46.9
PI10EO2	0.54±0.01	383	19.0 (17.3)	nd ^b	42.2
PI10EO1	0.367±0.006	376	30.8 (28.6)	nd ^b	36.0
PI20	0.363±0.006		0	508	51.0
PI20EO4	0.472±0.006	397	11.2 (9.45)	nd ^b	46.3
PI20EO2	0.508±0.008	386	18.9 (17.0)	nd ^b	41.6
PI20EO1	0.40±0.01	381	28.7 (28.1)	nd ^b	36.8

^a measured in DMAc at 30 °C (dL g⁻¹), ^b the onset degradation temperatures (°C) of first (1) and second (2) weight loss steps, ^c the onset degradation temperature cannot be accurately determined by the overlap between the two steps (nd: not detected), ^d the parenthetical values correspond to the theoretical PEO content (wt.%), and ^e the char yield at 800 °C (wt.%).

4.2.2. Characterization of the membranes

ATR-FTIR spectra of PIx and PIxEOy membranes are shown in Figure 4.4 and Figure S1.2, section 1.1 in Appendix 1. The characteristic absorption bands of imide groups appeared at 1785 and 1720 cm⁻¹ (C=O asymmetric and symmetric stretching, respectively) and 1360 (C-N stretching). The typical aliphatic C-H absorption bands just below 3000 cm⁻¹ were also detectable. Moreover, the intensity of the band centered at 1085 cm⁻¹, which was assigned to the C-O stretching mode of aliphatic ether moieties, and the bands around 810 cm⁻¹, which were related to the CH₂ rocking vibrations, increased with higher PEO content.

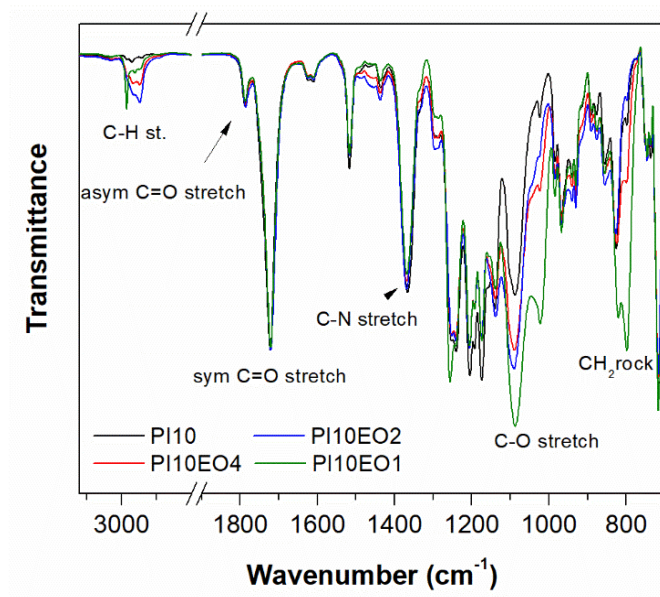


Figure 4.4. ATR-FTIR spectra of PI10EOy copolyimides. The spectra were normalized to the band at 1720 cm^{-1} (sym C=O stretch).

The thermal stability of the copolyimide membranes was evaluated by TGA. The thermograms of PI0, PI10, PI20, and PIxEOy are shown in Figure 4.5. In all of the copolyimides, a small weight loss below $300\text{ }^{\circ}\text{C}$ ($< 3\text{ wt.}\%$) was observed, which was attributed to residual solvent, indicating that the thermal treatment at $180\text{ }^{\circ}\text{C}$ for 1 h was not enough to efficiently remove it. The degradation onset of PIx was found to be lower than that of PI0 (c.f. Table 4.1), which was attributed to the thermal decarboxylation of DABA prior to the generalized polymer degradation. This thermal behavior has been already reported for other polymers containing DABA [121][122]. The thermograms of PI0 and PI100 (6FDA-DABA) were compared with those of PI10 and PI20 to support this fact, as shown in Figure S1.3 in Appendix 1. It was observed that the weight loss by thermal decarboxylation for PI100 (6FDA-DABA) covered the same temperature range, between 350 and $500\text{ }^{\circ}\text{C}$, as in PIx. The decarboxylation mechanism over a wide temperature range would be consistent with the removal of the carboxylic groups through a two-step mechanism including the formation of interchain anhydride linkages and eventually cross-linking through decarboxylation (from dianhydride moieties and free carboxylic groups) at high temperature [122,123].

Two main weight losses were observed in the PIxEOy thermograms: the first one was associated with the degradation of the PEO segments in the range between 350 and $450\text{ }^{\circ}\text{C}$ -the higher the PEO content the higher the weight loss- and the second one was caused

by the generalized degradation of the remaining polymer above 450 °C. In these copolyimides, the decarboxylation of the DABA moieties would occur at the last stage of degradation of the PEO segments.

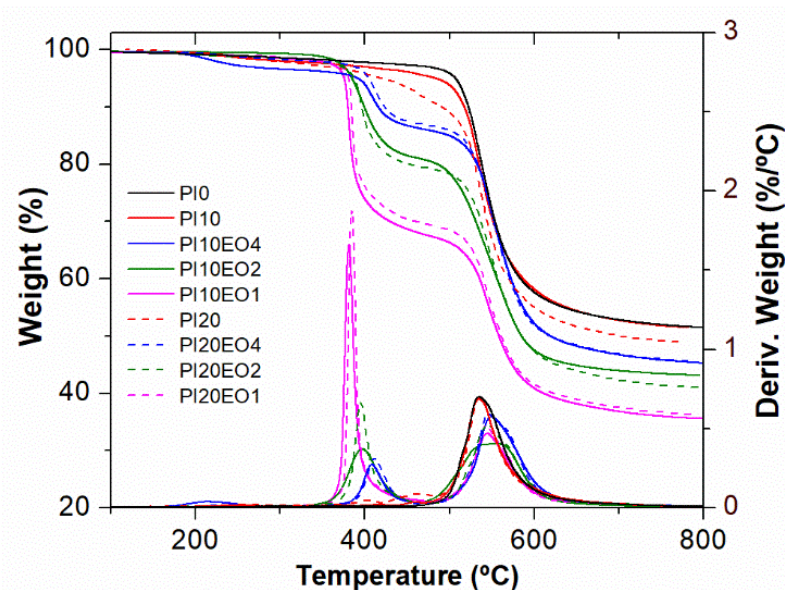


Figure 4.5. Hi-Res TGA scans of PI0, PI_x, and PI_xEO_y under nitrogen atmosphere.

The PEO content of PI_xEO_y was estimated by TGA from the weight loss of the first step. The percentage by weight of PEO, the onset degradation temperatures, T_{d1} and T_{d2} , which correspond to the PEO loss and the generalized degradation of the polymer, respectively, and char yield at 800 °C of all the copolyimides are listed in Table 4.1. The calculated percentages of PEO weight loss were somewhat higher than the theoretical ones because the existence of an overlap between the first and second stage of weight loss (due to the loss of carboxylics coming from the DABA groups) did not allow a more accurate value to be obtained. As expected, the char yield of PI_xEO_y was lower than that of PI_x because of the additional weight loss of PEO; thus, the higher the PEO content, the lower the char yield. Moreover, for the same content of DABA, T_{d1} was found to be lower when the PEO content was higher.

WAXS was used to evaluate the effect of the PEO content on the membrane packing density. All of the patterns of PI_x and PI_xEO_y exhibited amorphous halos indicating the amorphous nature of the membranes. The patterns of PI0, PI_x, and PI_xEO_y were compared in Figure 4.6 and Figure S1.4, section 1.1 in Appendix 1. The patterns of PI_x were similar to that of PI0 exhibiting a high-intense well-defined scattering peak centered

at 15.5° and three additional lower intensity peaks at 21.5 , 26.5 , and 40.0° (2Θ). According to Bragg's law ($d\text{-spacing} = \lambda/\sin\Theta$, where Θ is the scattering angle), the maxima's positions corresponded to preferential intersegmental distances ($d\text{-spacing}$) of 5.7 , 4.1 , 3.3 , and 2.3 Å, respectively. This is in contrast to the patterns of PIxEOy that showed a slight shift of the highest intensity peak towards higher angles, for example from 15.5° for PI0 to 16.5° for PI10EO1, and a strong increase in the intensity of the other three peaks. This increase in the intensity of the peaks was attributed to a higher contribution of the shorter $d\text{-spacing}$, especially those around 4.1 and 3.3 Å, to the global scattering pattern, indicating that PEO segments caused a higher packing density relative to that of PI0 and PIx.

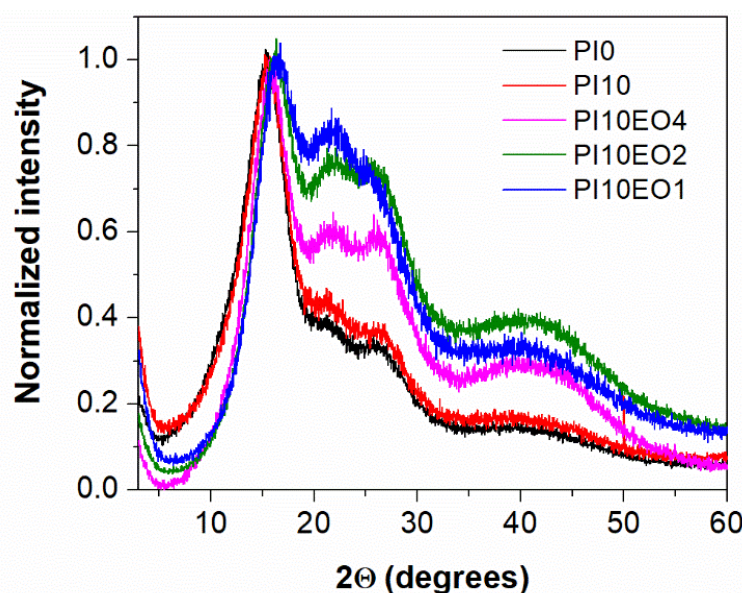


Figure 4.6. WAXS patterns of PI0, PI10, and PI10EOy. For comparative purposes, the patterns were normalized to the intensity of the large scattering peak around 15.5° (2Θ).

4.2.3. Preparation of cross-linked PIxEOy membranes

The thermal treatment to prepare the cross-linked membranes, PIxEOy-TT, was performed in a quartz tube furnace under a nitrogen atmosphere, and it was previously optimized by isothermal TGA measurements due to the wide temperature range where the removal of PEO took place (see Figure 4.5). PIxEOy was crosslinked using a three-step thermal treatment, which is detailed in Figure 4.7(a), along with the corresponding thermograms of the PIxEOy in Figure 4.7(b). The residual solvent was removed in the first step, while the cross-linking of the samples took place in the other two ones. During

the second step at 375 °C, the PEO weight loss, relative to the total PEO loss, for PIxEO1 was higher than 70%, while for PIxEO2 and PIxEO4 was lower because they seem to need a higher temperature to remove the PEO, as shown in Figure 4.5. Thus, the temperature was raised at 400 °C and the sample was held at that temperature for 1 min. With this last step, PEO weight losses of 80% or more were achieved for all the PIxEOy, as seen in Table 4.2. Moreover, according to the decarboxylation mechanism of DABA commented on above, it was expected that the additional cross-linking between adjacent acid groups would be due to the intermolecular anhydride formation, not by their loss, which would occur at higher temperatures (Figure S1.3, section 1.1 in Appendix 1) [121–124].

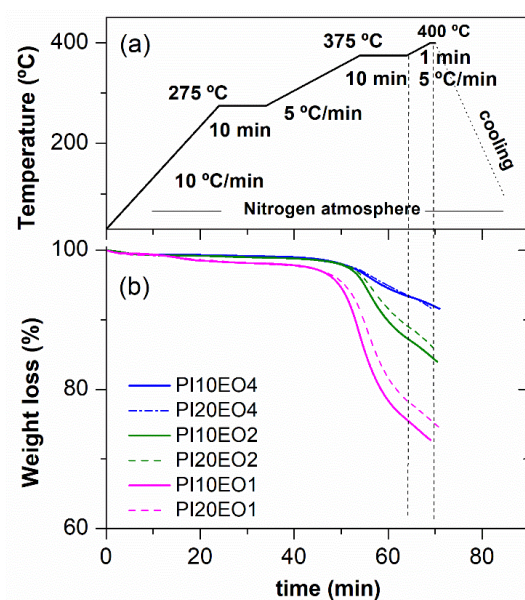


Figure 4.7. (a) Scheme of the thermal treatment of cross-linking and (b) isothermal TGA curves for PIxEOy.

The PEO removal was confirmed in addition to TGA by ATR-FTIR and WAXS, as an example seen in Figures S1.5 and S1.6, section 1.1 in Appendix 1. It was observed that the aliphatic C-H absorption bands around 2950 cm^{-1} disappeared and the intensity of the C-O stretching band aliphatic ether moieties at 1085 cm^{-1} was significantly reduced. Thus, the spectra of the thermally treated were found to be similar to those of the corresponding PIx. The WAXS patterns of PIxEOy-TT were consistent with this result; similar WAXS patterns for PIxEOy-TT and PIx were observed.

The cross-linking of the PIxEOy after thermal treatment was checked by determining the gel fractions of PIxEOy-TT. The values are listed in the last column of Table 4.2. It was found that the PIxEO1, having the highest PEO content, showed the lowest gel fractions (< 80%), indicating a lower cross-linking degree than those of the PIxEO4 and PIxEO2 membranes. Therefore, a higher PEO content seems to hinder the cross-linking of the chains.

Table 4.2. *Weight loss of PEO and gel fraction of PIxEOy-TT*

Sample	Exp. loss ^a	Exp. loss /Theor. loss ^b	Gel fraction
PI10EO4-TT	7.73	80	90
PI10EO2-TT	14.7	85	92
PI10EO1-TT	25.4	89	68
PI20EO4-TT	7.92	84	85
PI20EO2-TT	13.5	80	82
PI20EO1-TT	23.4	83	77

^a *Experimental weight loss of PEO (%) after thermal treatment by TGA,* ^b *experimental loss/theoretical loss ratio (%)*

The mechanical properties of PIxEOy and PIxEOy-TT are listed in Table S1.2, section 1.1 in Appendix 1. In general, the mechanical properties of PIxEO4 and PIxEO2 were similar to those of PI0, with Young's moduli about 2.0 GPa, tensile strengths higher than 85 MPa, and moderate elongations at break from 7 to 12%. In particular, the mechanical properties of PE20EO1 were poorer than PI0, having a Young modulus of 1.0 GPa and a tensile strength of 65 MPa. After thermal treatment, the mechanical properties of all the films decreased; especially for PIxEO1-TT and PI20EO2-TT, which could not be tested as gas separation membranes due to their poor mechanical properties.

4.2.4. Gas transport properties

Pure gas He, O₂, N₂, CH₄, and CO₂ permeability in PIx, PIxEOy and their cross-linked analogs, PIx-TT and PIxEOy-TT, as well as the ideal selectivity for O₂/N₂ and CO₂/CH₄ gas pairs are listed in Table S1.3, section 1.2 of Appendix 1. For the sake of comparison,

Figure 4.8 shows the change in permeability of PIx and PIxEOy at 35 °C, before (a) and after (b) the thermal treatment at 400 °C, relative to the neat PI0 polyimide.

The gas permeability in PIx and PIxEOy before thermal treatment was significantly lower than that of PI0, to which the value of 1 was assigned, (cf. Figure 4.8(a)). The decrease in permeability in PIx was associated with the formation of hydrogen bonds between carboxylic acids [124]; for example, the permeability was reduced by 50% in PI20. The reduction in permeability was considerably higher when the PEO content increased; thus, this reduction was even higher in the membrane having the highest content of DABA, PI20EOy. The behavior of PIxEOy was consistent with the WAXS results where a higher packing was observed for PIxEOy than for PI0, as shown in Figure 4.6.

After the thermal treatment (cf. Figure 4.8(b)), the permeability of the PIxEOy materials increased. However, only the permeability of PI10EO4-TT and PI10EO2-TT were higher than those of PI0. Although these cross-linked membranes showed similar WAXS patterns, the increase in He permeability was 1.72 times for PI10EO4-TT and 1.47 times for PI10EO2-TT relative to that of PI0, which was associated with an increase in the FFV due to the elimination of PEO during the thermal treatment. On the other side, the permeability of PI10EO4-TT was significantly higher than that of PI20EO4-TT, indicating that the presence of a higher DABA content in the pristine membrane led to a lower FFV after the thermal treatment. This behavior was opposite to that observed in PIx, where the permeability of PI20 was higher than that of PI10 after thermal treatment.

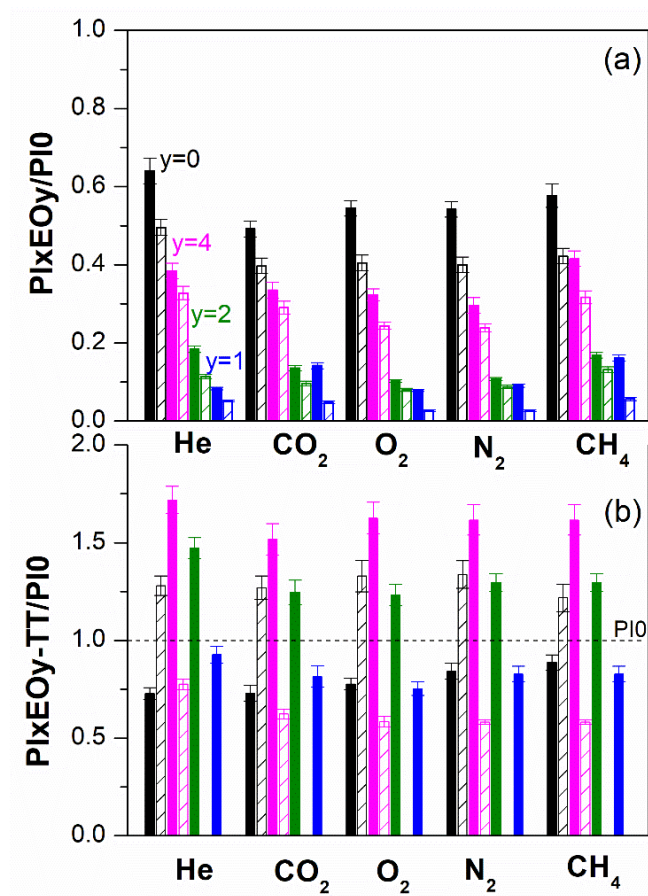


Figure 4.8. Changes in permeability for PIx and PIxEoy, before (a) and after thermal treatment at 400 °C (b) relative to the neat PI0 (6FDA-6FpDA), which has been given a value of 1, for every tested gas at 35 °C. The solid column corresponds to $x=10$ and the cross-hatched column to $x=20$. The standard deviations from repeated measurements are shown as error bars.

Figure 4.9 shows the normalized permeability behavior of CO₂ and N₂ as a function of feed pressure for PI10EO4 and PI10EO2 and their cross-linking analogs, as well as for PI0. The permeability to CO₂ of PI0 started to increase from a feed pressure about 12 bar due to the plasticization. Moreover, after holding the membrane to a feed pressure about 30 bar for a sufficient time (section 3.4.2 Chapter 3), the permeability exhibited significant hysteresis when the feed pressure decreased. In contrast, N₂ did not induce plasticization or conditioning and, consistently with the dual mode picture [125], N₂ permeability slightly decreased as the feed pressure increased and no hysteresis was observed. PI10EO4 and PI10EO2 showed a similar behavior to that of PI0.

After cross-linking, PI10EO4-TT and PI10EO2-TT exhibited resistance to CO₂-induced plasticization up to 30 bar.

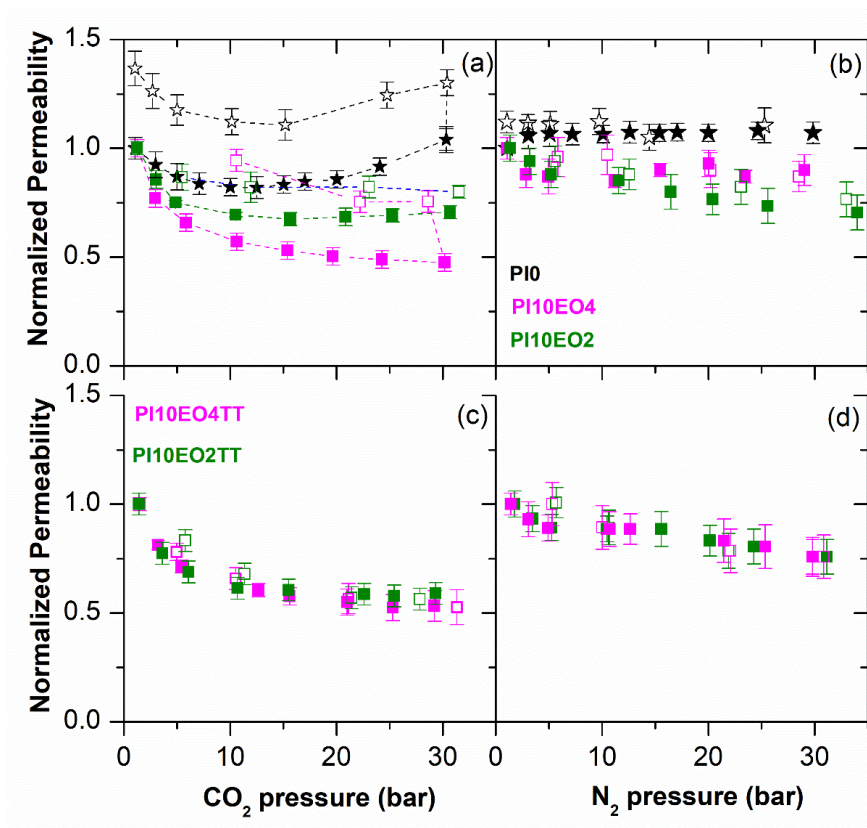


Figure 4.9. Effect of CO₂ (a) and N₂ (b) pressure at 35 °C in reference polyimide (PI0) and precursor membranes (PI10EO_y), and (c) and (d), respectively, in cross-linked membranes (PI10EO_y-TT). The permeability was normalized to the initial value measured to a pressure of 1 bar. The standard deviations from repeated measurements are shown as error bars.

To put these results in perspective, the O₂/N₂ and CO₂/CH₄ separation performance of our membranes were compared with those of standard polymers used in membrane gas separation (cf. Figure 4.10). The 1991 and 2008 upper bound lines were also included in the graph [26,27]. After the thermal treatment, the O₂/N₂ and CO₂/CH₄ separation performance of membranes shifted to the right, closer to the 1991 upper bound. PI10EO_y-TT exhibited a higher O₂ permeability relative to PI10, without relevant O₂/N₂ selectivity loss. For example, O₂ permeability increased by 1.6-fold for PI10EO1-TT and by 2.9-fold for PI10EO4-TT.

Interestingly, PI10EOy surpassed the 1991 CO₂/CH₄ upper bound. The CO₂/CH₄ separation performance for PI10EO4-TT and PI10EO2-TT was superior to that of PI10. Thus, for these two membranes, the permeability increased 2.5- and 3.0-fold, and the selectivity between 1.1 and 1.2, respectively, compared to PI10.

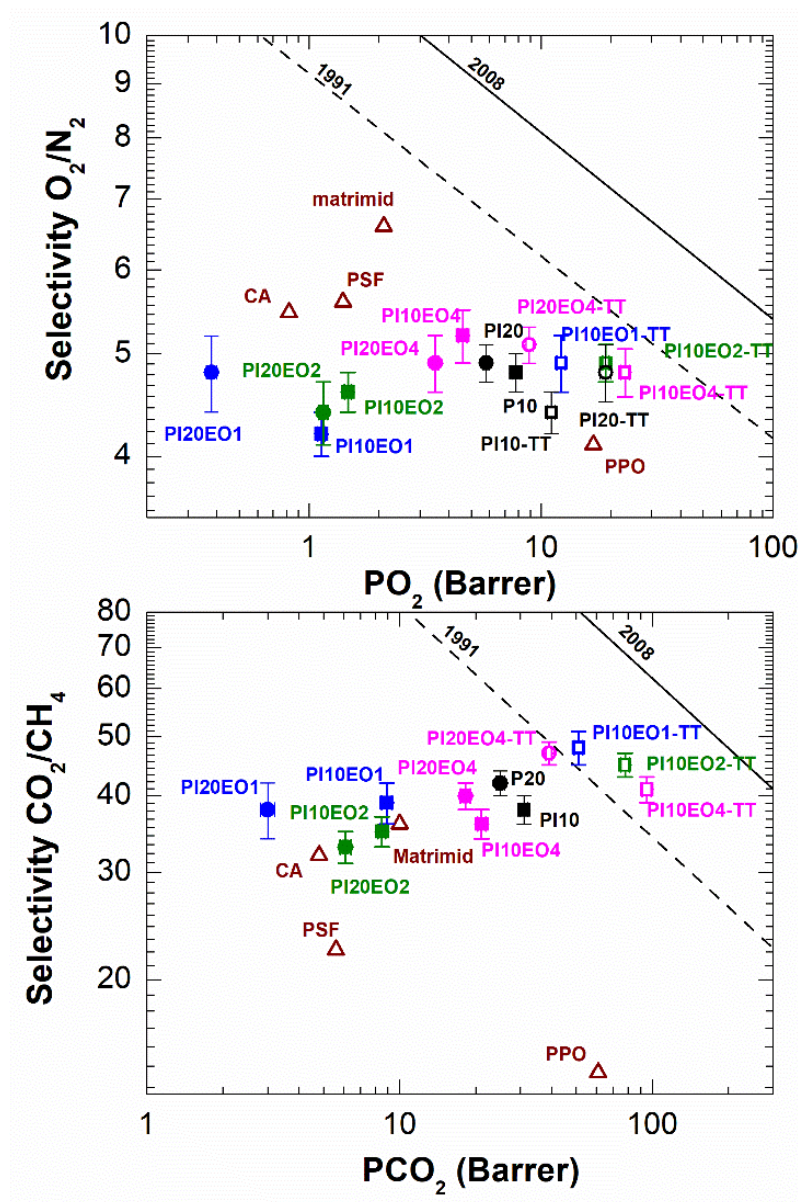


Figure 4.10. O₂/N₂ (up) and CO₂/CH₄ (down) Robeson diagrams for PI_xEO_y and PI_xEO_y-TT. The continuous line represents the 2008 upper bound, and the dashed line represents the 1991 upper bound. Data for relevant polymers used in gas separation were taken from ref. [89] PSF: polysulfone (PSF); PPO: poly(phenyl oxide); CA: cellulose acetate, and Matrimid. The standard deviations from repeated measurements are shown as error bars.

4.2.5 Blends of PIx and PIxEOy

Considering that the PI10EOy-based cross-linked membranes showed the best separation performance for CO₂/CH₄, a series of membranes were prepared blending PI10 and PI10EOy at different weight ratios. The PI10/PI10EOy ratios were chosen such that the amount of PEO in the blends was between 3 and 10% (by weight). The blend films, PI10/PI10EOy(z/1), were obtained by solution casting and, then, they were subjected to the same thermal treatment described above (cf. Figure 4.7(a)). The removal of PEO in the polymer blends was confirmed by TGA (cf. Figure S1.7, section 1.3, in Appendix 1). The cross-linking degree was determined by measuring the gel fraction, which was higher than 90%. The composition of the blends and their acronyms, the percentage of PEO loss by weight after thermal treatment, and the gel fraction are listed in Table S1.4, section 1.3 in Appendix 1.

The single gas permeability of the blends was measured at 30 °C and 3 bar before and after thermal treatment, and the data are shown in Table S1.5, section 1.4 in Appendix 1. Figure 4.11 shows the variations in gas permeability of the cross-linked membranes relative to the pristine PI10.

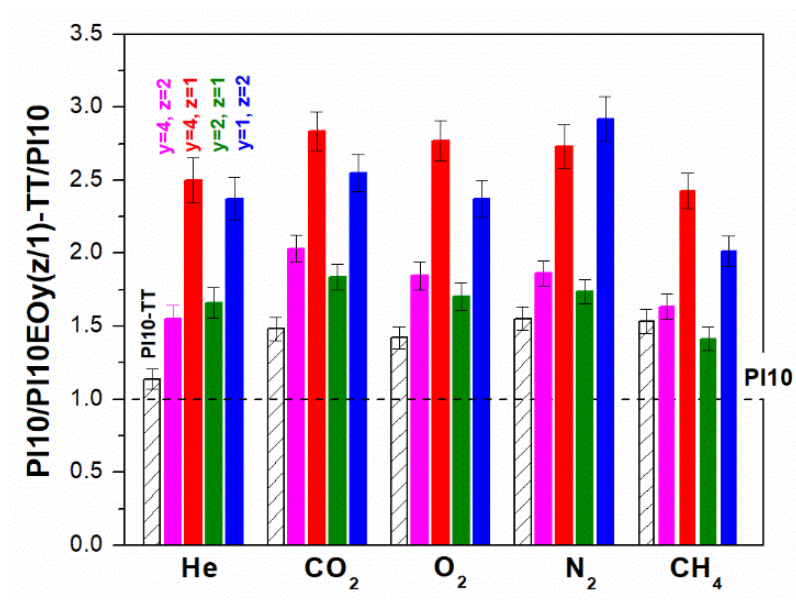


Figure 4.11. Changes in permeability for PI10/PI10EOy(z/1) after thermal treatment at 400 °C relative to the neat polyimide, PI10, which was given a value of 1, as a function of tested gas at 35 °C. The solid column corresponds to x=10 and the cross-hatched column to PI10-TT. The standard deviations from repeated measurements are shown as error bars.

The relative gas permeability was higher in the cross-linked membranes derived from PI10-based blends than in the PI10-TT. It has to be pointed out that the thermal treatment on the PI10/PI10EO2(1/1), with a PEO content of about 9.5 wt.%, resulted in a less permeable membrane than that obtained from PI10/PI10EO1(2/1), which contained a higher percentage of PEO (about 10.5 wt.%). This result seems to demonstrate that the PEO content in the blend is not the key point in determining the separation characteristics, but that the composition of PIxEOy, i.e., the PEO and DABA content, is a crucial point to be considered when designing new materials employing this methodology.

The CO₂/CH₄ separation performance of PI10/PI10EOy(z/1)-TT is shown, in the Robeson plot, in Figure 4.12. For the sake of comparison, the data for cross-linked membranes were compared to those of PI0-based analogous ones, which were reported in a previous work [120], and of their pristine PI10 and PI0. Because the composition of the precursor membranes (i.e., before the thermal treatment) was similar in both PI10- and PI0-series, analogous acronyms will be used to designate them.

The cross-linking improved the CO₂/CH₄ separation performance of PI10/PI10EOy(z/1)-TT; both the permeability and selectivity of these membranes considerably increased relative to that of their reference polyimide, PI10. The performance of all the PI10/PI10EOy(z/1)-TT surpassed the 1991 upper bound. This behavior contrasted with that of PI0/PI0EOy(z/1) derived from the reference polyimide PI0; the PI0/PI0EOy(z/1)-TT showed similar, or even lower, separation performance to that of PI0. For example, the CO₂ permeability of PI10/PI10EO4(1/1)-TT increased by 2.8-fold and its CO₂/CH₄ selectivity by 1.16-fold relative to PI10, while that of the analog PI0/PI0EO4(1/1)-TT decreased by 0.8-fold and its selectivity barely varied relative to PI0. Therefore, the additional cross-linking from the carboxylic groups of DABA moieties in the PI10/PI10EOy(z/1) helps to minimize the shrinkage exhibited by the PI0/PI0EOy(z/1) blends, while enhancing the selectivity/permeability balance relative to that of PI10.

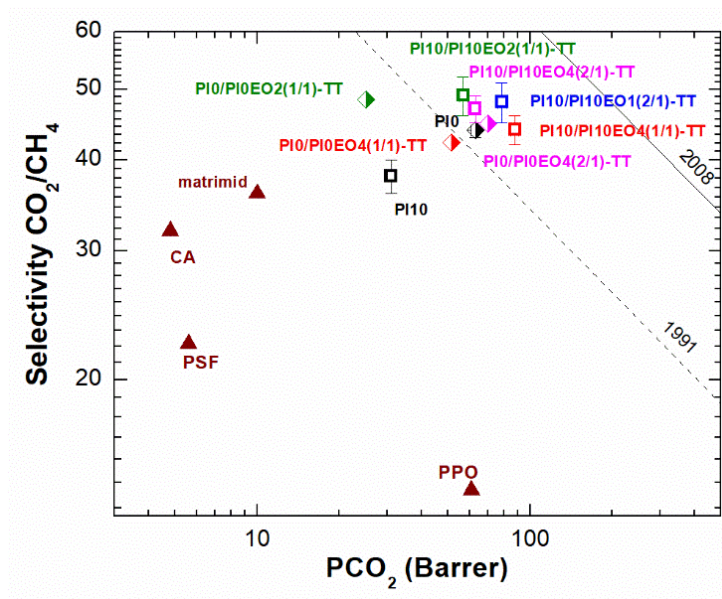


Figure 4.12. CO₂/CH₄ Robeson diagram for PI10/PI10EO_y-TT and PI0/PI0EO_y-TT. The dashed line represents the 1991 upper bound and the continuous line represents the 2008 one. Data for relevant polymer used in gas separation were taken from ref.[89]: polysulfone (PSF); poly(phenyl oxide) (PPO); cellulose acetate (CA), and Matrimid. The standard deviations from repeated measurements are shown as error bars.

Chapter 5

5. Tuning the Porosity of Porous Organic Polymers for Carbon Capture Applications

5.1. INTRODUCTION

The disproportionate carbon dioxide (CO₂) emission, released from the burning of fossil fuels (coal, petroleum, and natural gas) and industrial activities (such as steel production, cement manufacturing, and many others), is one of the main causes of global warming and ocean acidification. Thus, research seeks the most efficient ways to diminish emissions to the atmosphere until renewable energies such as wind, solar and biomass energy can be extensively incorporated into the energy sector worldwide [126]. Until then, *Carbon Capture and Storage* (CCS) technologies have emerged as a promising technique for reducing CO₂ emissions while continuing to use fossil fuels for power generation [127–129]. CCS technologies pursue to reduce CO₂ emitted directly from emission sources, before entering the atmosphere, and are classified according to the CO₂ capture process: post-combustion, pre-combustion, and oxy-fuel combustion [130,131]. The gas stream from these CCS technologies varies from 3–20% (post-combustion) to over 50% CO₂ (pre-combustion and oxy-fuel combustion) by volume. However, the considerable cost of the carbon capture process slows down the integration of CCS technologies to commercial scale [132]; nearly two-thirds of the total cost includes the three steps: CO₂ capturing, transporting, and storing the gas underground.

Over the last two decades, amorphous *Porous Organic Polymers* (POPs) have emerged as a new category of porous materials mainly derived from highly crosslinked polymeric materials, which are formed from aromatic monomers to prevent the space-effective packing and create a large free volume excess, which generically leads to permanent microporosity [133,134]. The chemistry to prepare these POPs is highly diverse and ranges from metal-catalyzed couplings to metal-free condensation reactions. Thus, they have been named in many different ways: *Hyper-Crosslinked Polymers* (HCPs) [135–137]; *Porous Aromatic Frameworks* (PAFs) [138,139]; *Hyper-Cross-linked Polymers of intrinsic microporosity* (PIMs) [140], *Azo-Linked Porous Polymers* (ALPs) [141]; *Benzimidazole-, Benzoxazole-, and Benzothiazole- Linked Polymers* (BILPs, BOLPs and BTLPs) [142–145] etc. The versatility of the chemistry to prepare amorphous POPs

allows for the design of materials exhibiting high surface areas, and different pore size distributions. Besides, these materials can incorporate functional groups, making them potentially useful in areas such as gas storage, separation, and catalysis [133,146,147].

Recently, our research group has developed a feasible and low-cost synthetic protocol to prepare high-thermal and chemically stable POPs by reaction of rigid tri-functional aromatic monomers with activated ketones having electron-withdrawing groups through a reaction of *Electrophilic Aromatic Substitution* (EAS, polyhydroxyalkylation reaction) in a super acidic media following Olah's methodology [148]. These materials are highly microporous polymers with moderate area surface of up to $800 \text{ m}^2 \text{ g}^{-1}$ and CO_2 uptakes of up to 207 mg g^{-1} ($105 \text{ cm}^3(\text{STP}) \text{ g}^{-1}$) at 273 K and 1 bar. The wide diversity of nucleophilic and electrophilic monomers that can be used has allowed the preparation of well-designed POPs to be studied in a variety of potential applications ranging from gas separation membranes [149–152] to catalysis [153,154].

So far, POPs have been prepared by combining one trifunctional aromatic monomer (having a required symmetry), such as 1,3,5-triphenylbenzene (TPB) and triptycene (TR), with one or two activated ketones, such as 1H-indole-2,3-dione (here named isatin or I), 2,2,2-trifluoroacetophenone (TF) and 4,5-diazafluoren-9-one (DAFO) [148,153], which act as cross-linkers in the polyhydroxyalkylation reaction. The choice of monomers to prepare these POPs depends on the desired applications; for example TR-I (POP made from TR and I) and TR-TF (POP made from TR and TF) are good CO_2 adsorbent solids, while TPB-DAFO (POP made from TPB and DAFO) and TPB-DAFO-I (POP made by copolymerization of TPB and a mixture of DAFO and I) are excellent heterogeneous catalysts for C-C heterocoupling reactions due to that the DAFO monomer has a rigid bipyridine moiety in its structure, which is able to complex a wide variety of metal cations, such as Pd and Ag [151,153].

Recently, we have prepared new POPs looking for strategies to create high surface area microporous polymers by incorporating other various nucleophilic monomers into their networks. The evaluation of these porous materials looks to establish relationships between their structure and their porous characteristics, which will allow to design in a rational way new microporous materials conceived for a specific application. Thus, three main strategies have been followed in the synthesis of new POPs as described below;

- 1) POPs made by using new nucleophilic monomers with triarylbenzene structures similar to TPB; thus, two new monomers as a more rigid monomer possessing a methyl group on the side benzenes, 1,3,5-tri-(2-methylphenyl)benzene (TMB), and another

where the side groups are biphenyl groups, 1,3,5-tri-(biphenyl)benzene (TBB), have been obtained.

2) POPs containing nucleophilic monomers that included a tetrafunctional aromatic monomer, 9,9'-spirobifluorene (SBF).

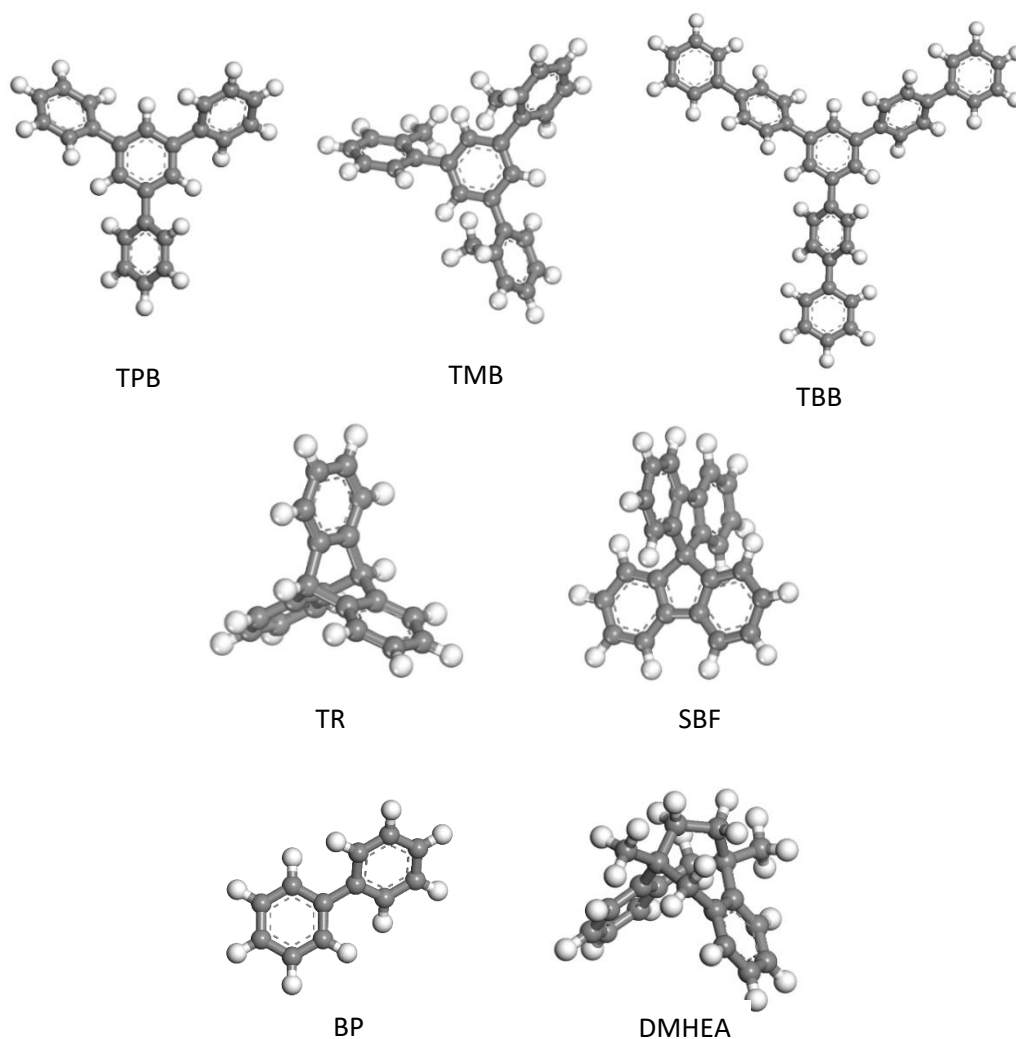
3) POPs where in addition to the multiaromatic monomers, bifunctional aromatic ones have been incorporated as comonomers; biphenyl (BP) and the rigid and contorted 9,10-dimethyl-9,10-dihydro-9,10-ethanoanthracene (DMHEA).

In particular, the second strategy seeks to produce a greater amount of crosslinking, and the third to increase the cross-linking length between the multifunctional monomers. On the other hand, in addition to the cross-linkers TF and I, an extra electrophilic ketone derived from isatin, 1-methylindoline-2,3-dione (1-methyl isatin, MI), has also been used. In this work, the optimization of the synthesis of these POPs were performed. In addition, the effect of the proposed strategies to design specific POPs on textural properties, such as surface area and pore size distribution, has been studied. Finally, the CO₂ adsorption of the POPs at low and high pressures and the CO₂ separation performance over N₂ under atmospheric conditions (post-combustion process conditions) have been evaluated and compared with other microporous materials. Finally, the CO₂ separation performance of these POPs over CH₄ from a methane-rich mixture has been tested for the first time.

5.2. RESULTS AND DISCUSSION

Ho-POPs were prepared from tri- or tetrafunctional aromatic monomers having different geometries: (a) TPB, TMB, TBB (which have C₃ symmetry structure), (b) TR (which has a D_{3h} symmetry and 3D paddle wheel structure), or (c) SBF (which has a spiranic carbon that induces a C₄ tetrahedral symmetry), using I, MI or TF as cross-linkers and a super-acidic media as reaction promotor. In addition, Co-POPs were prepared by adding an extra bifunctional aromatic comonomer, BP or DMHEA. The optimized DFT geometry (B3LYP/6-31G**) of all of the nucleophilic and electrophilic monomers were calculated and they are shown in Figure 5.1. Details about the synthesis of the monomers can be found in section 3.1.1.2 in Chapter 3. Moreover, the chemical structure of monomers was determined by nuclear magnetic resonance (NMR) and spectra are shown in Figures S2.1-S2.14, section S2.1, Appendix 2.

Nucleophilic monomers



Electrophilic monomers

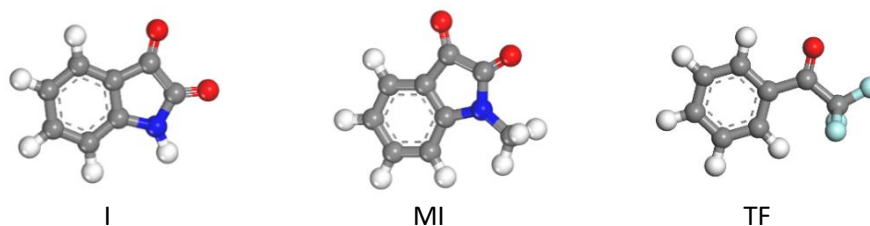


Figure 5.1. Optimized DFT geometry of multifunctional nucleophilic monomers and electrophilic monomers (cross-linkers).

Both BP and DMHEA were used as additional nucleophilic monomers in an attempt to study how their incorporation into the network could affect the porosity of the materials. Unlike the BP monomer, which has a linear structure, the DMHEA monomer has a very

rigid, highly shape-persistent structure, which is induced by the ethane bridge over the middle ring inducing an angle bending of 105° . DMHEA crystallizes in orthorhombic structure (space group Pccn), as determined by X-ray diffraction (Table S2.1 in section S2.2, Appendix 2). DFT molecular modeling of DMHEA was carried out to get insight into their electronic and geometrical features. Details about the molecular modeling are described in Appendix 2 (section S2.3). The DFT (DFT B3LYP/6-31G**) HOMO orbital molecular energy modeling of the three-dimensional structure (Figure S2.15, section S2.3) shows that there are two positions on each aromatic ring having equivalent electronic properties and so the electrophilic attack is then plausible on any of these two positions. Thus, the addition of DMHEA should lead to a higher irregularity in the network structure. In addition, the rigid contorted geometry of DMHEA should introduce a higher intrinsic microporosity in the network than the lineal geometry of BP.

Ho-POPs and Co-POPs were prepared by combining the monomers shown in Figure 5.1 *via* electrophilic aromatic substitution in super-acidic media, as seen in Figure 5.2.

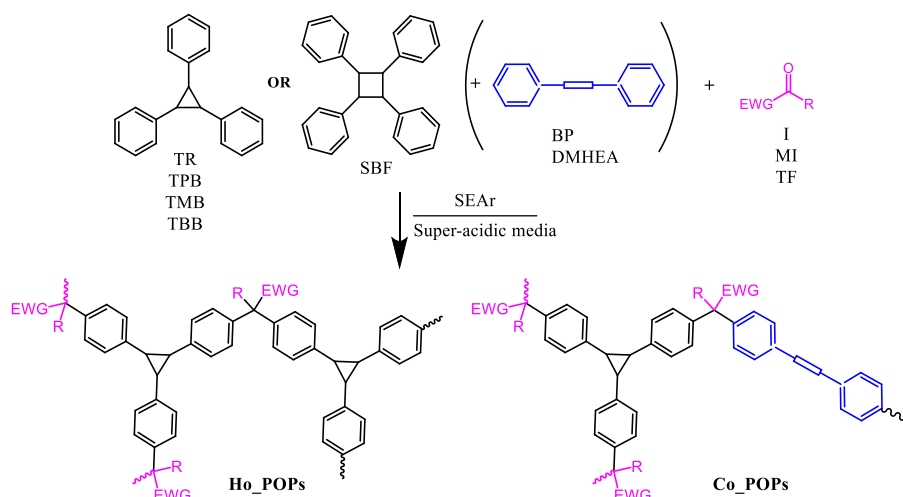


Figure 5.2. Synthesis of Ho-POPs and Co-POPs from monomers described in Figure 5.1

5.2.1. Synthesis optimization of porous organic polymers

The materials derived from TR or TPB trifunctional monomers and I cross-linker, as well as those also containing BP or DMHEA bifunctional monomers, were obtained by applying the methods that are described in Table 3.1, section 3.1.1.3, Chapter 3. During the process of synthesis optimization, the use of MSA, which is an easy-to-handle liquid, less corrosive, and with lower cost than TFSA, was tested as an alternative co-solvent to CHCl_3 . Thus, a TFSA/MSA (3/2) mixture (instead of TFSA/ CHCl_3 (2/1) one) was chosen because its use: 1) reduces the amount of TFSA by an equivalent of POP and 2)

avoids the employment of chlorinated solvents; both points would make the strategy for preparing the POPs, in a greener and more suitable scale-up synthesis.

With the target of finding out which of these methods gives the best porosity results, the Ho-POPs and Co-POPs were compared in terms of reaction yield and characteristic porosity parameters such as specific surface area (S_{BET}), total pore volume (V_{total}), and micropore volume (V_{micro}), which were obtained from low-pressure N_2 adsorption isotherms at $-196\text{ }^\circ\text{C}$. The low-pressure N_2 adsorption/desorption isotherms are shown in Figures S2.16 – S2.18, and the textural parameters are listed in Table S2.2 and S2.3 in Appendix 2 (section S2.4).

Most POPs were obtained in high yield ($>90\%$) using a TFSA/ HCCl_3 (2/1) mixture, but they showed significant differences when the porosity parameters were compared (c.f. Table S2.2, section S2.4.2). For example, the S_{BET} of the Co-POPs containing BP and DMHEA were very low, especially for those derived from the TPB monomer (32 and $2\text{ m}^2\text{ g}^{-1}$, respectively), when the reaction was carried out at room temperature (method 1a). In general, the reaction temperature had to be raised to $60\text{ }^\circ\text{C}$ and held for 96 h (method 1b) to increase the S_{BET} of the POPs, except for those Co-POPs containing DMHEA that yielded the same S_{BET} by both methods. According to the textural parameters, the incorporation of DMHEA in the network seems to result in very low porosity materials. The TR-based POPs were also prepared using a TFSA/MSA (3/2) mixture at room temperature (method 2a) or $60\text{ }^\circ\text{C}$ (method 2b). The reaction yields for Co-POPs obtained by method 2a were much lower, close to 75%, relative to those for the analogous Co-POPs obtained by method 1a (c.f. Table S2.3). We consider that the decrease in reaction yield was due to a lower solubility of the growing chains, which could precipitate from the reaction medium before reaching a sufficient degree of crosslinking. Indeed, this supposition was supported by the increase in the reaction yield of TR/BP-I (94%) when the reaction was carried out heating at $60\text{ }^\circ\text{C}$ following method 2b. However, although the reaction yield was 1.27 times higher, the S_{BET} of TR/BP-I_2b is 0.81 times lower than that of TR/BP-I_2a. Contrarily, the heating at $60\text{ }^\circ\text{C}$ did not increase the reaction yield of TR/DMHEA-I_2b, which was much lower (23%) than that of TR/DMHEA_2a (73%). Following method 2a, the S_{BET} of TR/DMHEA-I was much higher than that of the analogous Co-POPs obtained by 1a and 1b (c.f. Table S2.2), but the reaction yield was much lower.

From the above findings, we assume that method 1b was the best one to provide materials with the highest reaction yields (above 90%) and, in general, showing the highest

microporosity. Thus, all of the POPs presented in this work, which are summarized in Figure 5.2, were prepared using a TFSA/CHCl₃ (2/1) mixture and heating at 60 °C for 96 h, and hereafter the suffix 1b will not be added to the name of the POP to simplify.

5.2.2. Characterization of POPs

The acronyms of the POPs, along with the reaction yields, are summarized in Table S2.4 of section S2.5, Appendix 2. The yields of POPs in most cases were superior to 90%. All of the materials were insoluble in organic solvents and low pK_a acids. The chemical structure of POPs was checked by CP/MAS ¹³C-NMR and ATR-FTIR.

Some of the POPs CP/MAS ¹³C NMR spectra are shown in Figure 5.3 to point out the main characteristic peaks of these materials based on their starting co-monomers. All of the POPs showed intense peaks in the 160-100 ppm range, as they are highly aromatic networks, and the peak at about 63 ppm was assigned to the quaternary carbon, which was formed during the cross-linking reaction (peak 2 in the spectra). Furthermore, the POPs derived from I or MI showed an additional peak of around 180 ppm corresponding to the carbonyl group of the lactam ring.

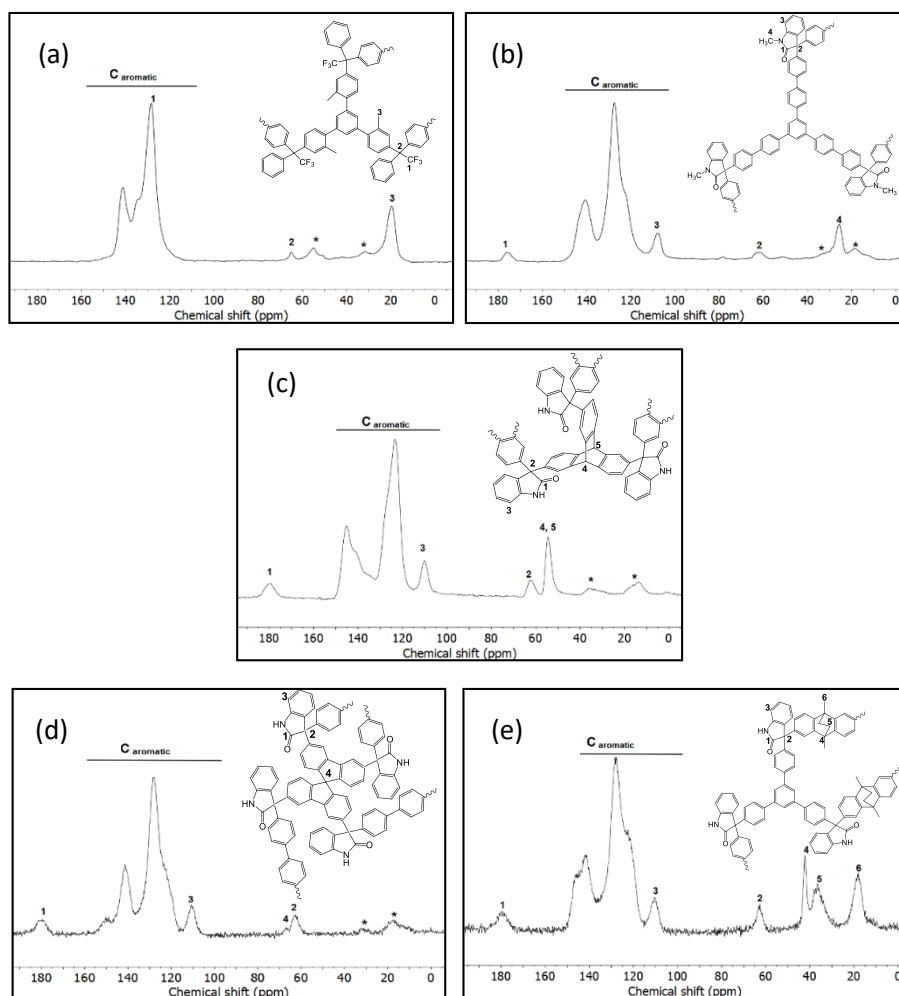


Figure 5.3. Solid-state CP/MAS ^{13}C NMR spectra of POPs: (a) TMB-TF, (b) TBB-MI, (c) TR-I, (d) SBF/BP-I, and (e) TPB/DMHEA-I. Asterisks denote spinning side bands.

The ATR-FTIR spectra of the previous POPs are shown in Figure 5.4 to point out the main absorption bands based on the cross-linkers. POPs derived from isatin exhibited the characteristic bands of the 5-member lactam ring at 3390 cm^{-1} (N-H st), 1710 cm^{-1} (C=O st), and 1620 cm^{-1} (N-H δ), and the typical bands at 1600 , 1495 and 1470 cm^{-1} were assigned to stretching vibrations of aromatic carbons ($\text{C}_{\text{ar}}\text{-C}_{\text{ar}}$ st). In the case of POPs derived from MI monomer, only the C=O stretching band of the lactam ring appeared and the $\text{C}_{\text{ar}}\text{-C}_{\text{ar}}$ stretching band at 1490 cm^{-1} increased in intensity due to the overlapping with the asymmetric bending band of methyl group ($\text{CH}_3\text{ }\delta$). Furthermore, the symmetric $\text{CH}_3\text{ }\delta$ band at 1375 cm^{-1} appeared next to an intense band at 1340 cm^{-1} , which was assigned to the C-N stretching vibration. POPs derived from the TF cross-linker showed two strong bands at 1145 and 1106 cm^{-1} associated with C-F stretching vibrations of the CF_3 group.

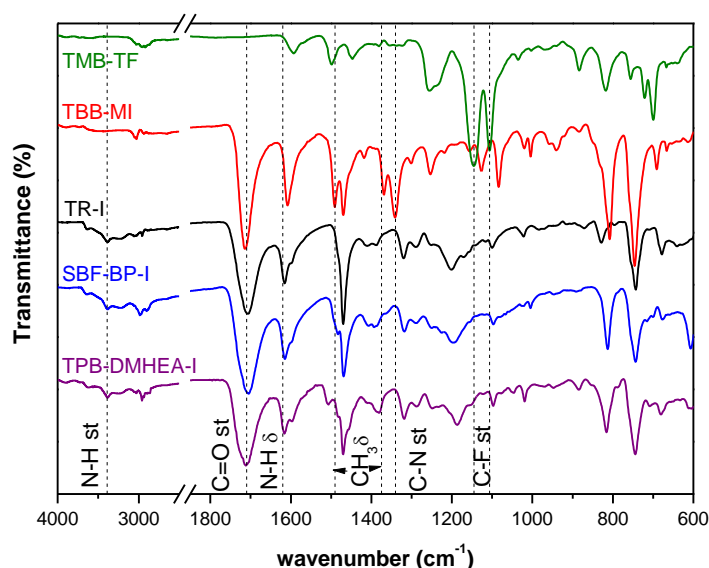


Figure 5.4. ATR-FTIR spectra of POPs. The dashed lines indicate the characteristic bands associated to cross-linkers (I, MI and TF)

The amorphous nature of the networks was confirmed by WAXS. The patterns of the materials are plotted by comparing those that share the same cross-linker (I, MI, and TF), as shown in Figure 5.5 and Figures S2.19 and S2.20 in section S2.6, Appendix 2. All of the Ho-POPs showed amorphous halos with two or three well-defined maxima as a function of scattering angle (Θ). Comparing the patterns, it was found that the shape of the amorphous halo changed with the chemical structure of POPs, especially concerning the maxima positions. According to Figure 5.5(up) and Figure S2.19, the changes in the position seem to be due to the tri- or tetra-functional monomers (TR, TPB, TMB, TBB, and SBF) rather than the cross-linkers (I, MI, and TF). The maxima positions have been usually related to the preferential intersegmental distances (d) existing in the chain's packing, as calculated from Bragg's equation ($d = \lambda / (2 \sin \Theta)$). Thus, the patterns of TR-based Ho-POPs showed preferential intersegmental distances at about 0.60 (14.5°), 0.38 (23°), and 0.20 nm (43°), while those of TPB-, TMB- and TBB-based-Ho-POPs exhibited a new distance at about 0.46 nm (19.3°) that became more preferential than that at about 0.38 nm (23°), which now appeared as a shoulder. In addition, the amorphous halos of TPB-, TMB- and TBB-based Ho-POPs also showed a contribution on the lower-angle side ($3\text{--}10^\circ$) that was not observed in those of TR- and SBF-based Ho-POPs. This contribution seems to indicate the presence of larger intersegmental distances (2.94–0.88 nm) in the networks derived from TPB, TMB, and TBB.

The patterns of the Co-POPs containing BP and DMHEA are displayed in Figure 5.5(down) and Figure S2.20. The Co-POPs patterns showed differences when they were compared to those of their analog Ho-POPs, and thus changes in the distribution of intersegmental distances were observed. For example, in the TR-based Ho-POPs (Figure 5.5(up)), the maximum at about 23° disappeared in the pattern of TR/DMHEA-I while another maximum at about 31° appeared, indicating the presence of smaller intersegmental distances (about 0.29 nm) in the network. In contrast to that, the pattern of TR/BP-I showed the same maxima as that of TR-I, but an additional shoulder at 12° was observed, revealing the existence of larger intersegmental distances (about 0.74 nm) in the network. Nevertheless, the presence of both DMHEA and BP in the other Co-POPs, TPB- and SBF-based ones, seems to lead to a higher presence of small intersegmental distances about 0.38 nm (23°) in the networks, relative to TPB-I and SBF-I, as shown in Figure S2.20.

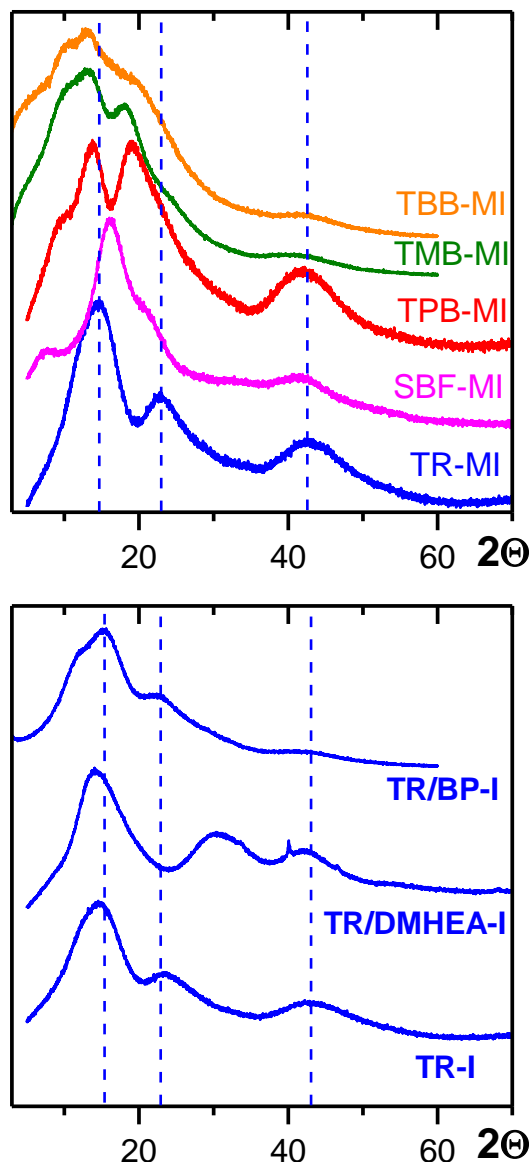


Figure 5.5. WAXS patterns of POPs containing MI (up) and those derived from TR-based POPs (down). The patterns were normalized to the intensity maximum at about 15° and shifted for clarity sake. The dashed lines are guides to the eye.

5.2.3. Thermal properties of POPs

The thermal resistance of POPs was determined by dynamic TGA measurements. The TGA curves of some POPs are shown in Figure 5.6 as examples of thermal behavior. The degradation onset temperature (T_d) and the char yield at 800 °C of all of the materials studied are listed in Table S2.5 in section S2.7, Appendix 2.

All of the POPs exhibited high thermal stability with T_d above 450 °C, except for the Co-POPs containing DMHEA monomer that showed an additional weight loss at about 310

°C due to the loss of the ethylene bridge (Figure 5.6(c)). After this weight loss, the generalized degradation of the polymer took place above 480 °C. The Ho-POPs derived from the TF cross-linker showed the lowest thermal stability ranging from 480 to 505 °C (Figure 5.6(b)) compared to that of the other Ho-POPs ranging from 515 to 565 °C (Figure 5.6(a)).

The highly aromatic structures of POPs provided materials with char yields above 60% at 800 °C. The Ho-POPs prepared from the nucleophilic monomer TMB showed the lowest values of char yield relative to the other POPs presumably due to the loss of the methyl groups present in their structure.

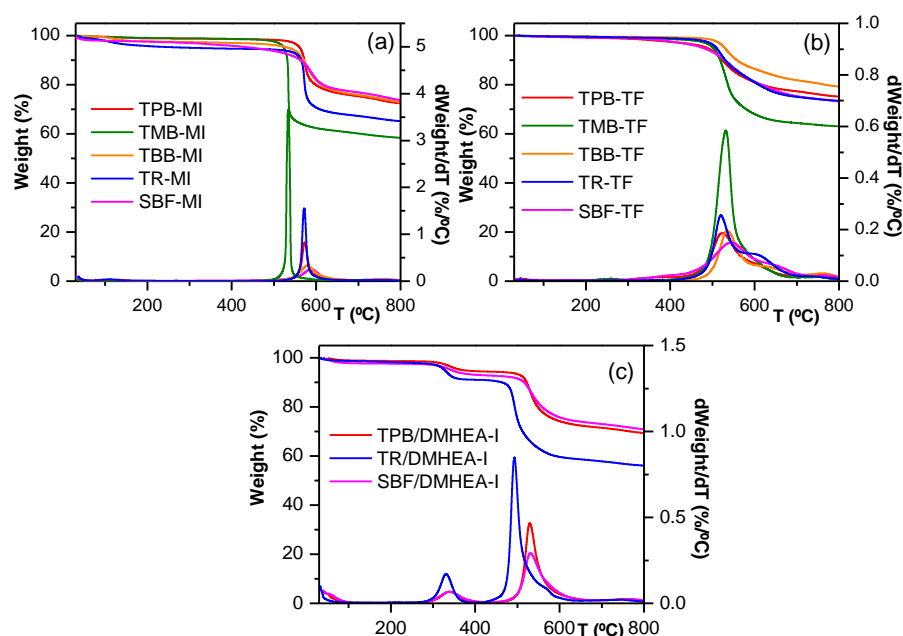


Figure 5.6. TGA curves of POPs: (a) Ho-POPs derived from MI cross-linker, (b) Ho-POPs derived from TF cross-linker, and (c) Co-POPs containing DMHEA nucleophilic monomer.

5.2.4. Textural properties of POPs

The textural properties of POPs were studied by low-pressure sorption measurements using nitrogen at -196 °C and CO₂ at 0 °C. The adsorption/desorption isotherms of the materials are shown in Figures 5.7 and 5.8. For the sake of comparison, the main textural parameters of POPs obtained from the N₂ and CO₂ adsorption isotherms are listed in Table S2.6 in section S2.8, Appendix 2.

Most of the N₂ adsorption isotherms of Ho-POPs in Figures 5.7(a-c) showed a rapid uptake (up to 150 or 250 cm³g⁻¹) at low relative pressure ($p/p_0 < 0.01$), revealing the presence of micropores, and then the N₂ uptake increased with increasing p/p_0 . The increase in N₂ uptake at $p/p_0 < 0.01$ was much less pronounced for TMB-I and TMB-TF (up to 50 and 6 cm³g⁻¹, respectively), suggesting that both POPs have either very low microporosity relative to the other ones or micropores with gate (entrance) sizes less than 5 Å, through which the diffusion of N₂ would be restricted at -196 °C. On the other hand, the desorption isotherms of Ho-POPs evidenced a remarkable low-pressure hysteresis, which has already been observed in analogous microporous materials [148]. This hysteresis is explained by a swelling phenomenon that occurs by the growth in the size of pre-existing pores and by the occurrence of diffusional restrictions of N₂ molecules in the molecular-size pore entrance in these materials.

The low-pressure N₂ adsorption/desorption isotherms of Co-POPs (Figures 5.7(d) and (e)) showed similar behavior to that observed in Ho-POPs. However, the uptake at $p/p_0 < 0.01$ was lower for Co-POPs relative to the corresponding Ho-POPs (i.e., TR-I and TPB-I and SBF-I): TR/BP-I and TPB/BP-I showed a rapid uptake up to 160 and 120 cm³g⁻¹, respectively, while the other Co-POPs barely adsorbed N₂ (less than 10 cm³g⁻¹). By analogy with the similar behavior of TMB-I and TMB-TF, the N₂ adsorption data of Co-POPs seem to suggest that the incorporation of BP and DMHEA bifunctional monomers to the networks either yields materials with lower microporosity than the analogous Ho-POPs or creates a higher number of micropores with entrance sizes less than 5 Å.

The values of specific surface area (S_{BET}), total pore volume (V_{total}), and micropore volume (V_{micro} , micropore sizes up to 20 Å) of POPs, which were calculated by applying the DR equation [155], are listed in Table S2.6. Overall, the POPs exhibited moderate/high surface areas ($S_{\text{BET}} = 540 - 1000 \text{ m}^2 \text{ g}^{-1}$), except for those that showed a very low N₂ uptake ($S_{\text{BET}} = 150 - 0 \text{ m}^2 \text{ g}^{-1}$). Furthermore, as expected, the larger the S_{BET} , the higher the value of V_{micro} .

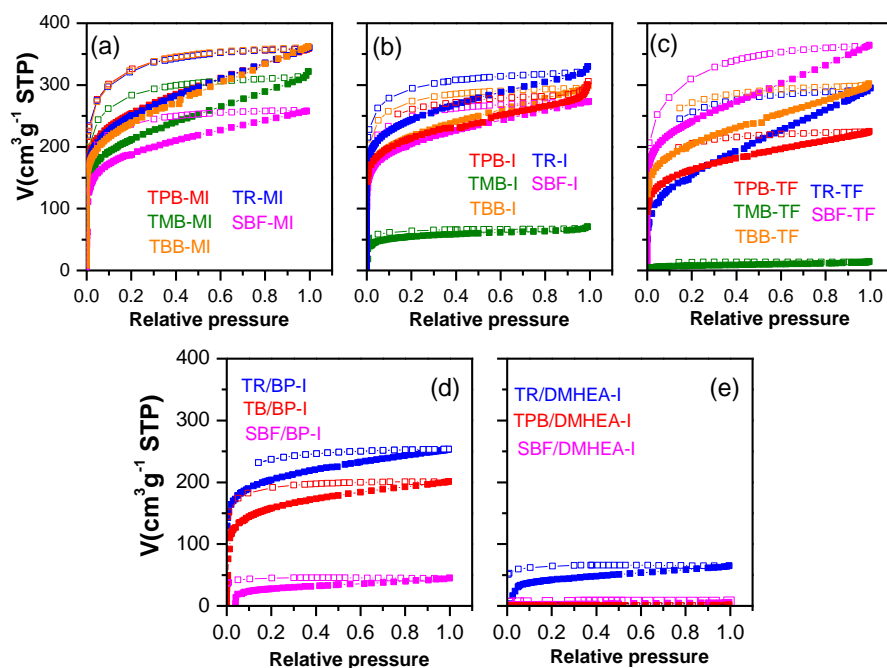


Figure 5.7. Low-pressure N₂ adsorption (solid symbols)/desorption (empty symbols) isotherms at – 196 °C of POPs.

The narrow microporosity (micropores size up to 7 Å) [156] features of the POPs were studied by measuring CO₂ adsorption/desorption isotherms at 0 °C and pressures up to 1 bar (pressure relative up to 0.03). Under these conditions, the CO₂ only fills the narrow micropores and, thus, CO₂ adsorption data at 0 °C is commonly used as a complement to nitrogen adsorption data at -196 °C for a complete characterization of the microporosity structure of materials [77,157].

The CO₂ adsorption isotherms of Ho-POPs (Figures 5.8(a-c)) showed that the CO₂ uptake increased with increasing pressure and no hysteresis was observed between the adsorption and desorption isotherms. The effect of chemical structure on the CO₂ uptake was visible in those POPs formed from the isatin monomer (Figure 5.8(b)); the CO₂ uptake (cm³ g⁻¹) at 0.03 p/p₀ followed the order: TR-I (121)>TPB-I (92)>TBB-I (70)>SBF-I (62)>TMB-I (44). Besides, the materials formed from the TF cross-linker (Figure 8(c)) showed the lowest CO₂ uptakes, especially for TMB-TF (20 cm³ g⁻¹ at 0.03 p/p₀).

The corresponding CO₂ isotherms of Co-POPs showed a similar behavior to that of Ho-POPs (Figure 5.8 (d) and (e)). Furthermore, when BP and DMHEA monomers were combined with TR, TPB, or SBF monomers using the isatin cross-linker, the CO₂ uptakes of TR/BP (or DMHEA)-I and TPB/BP (or DMHEA)-I significantly decreased in comparison to those of TR-I, TPB-I (about 50% and 30%, respectively). In the case of

SBF/BP-I and SBF/DMHEA-I, the CO₂ uptakes decreased by about 20 and 8%, respectively, relative to SBF-I.

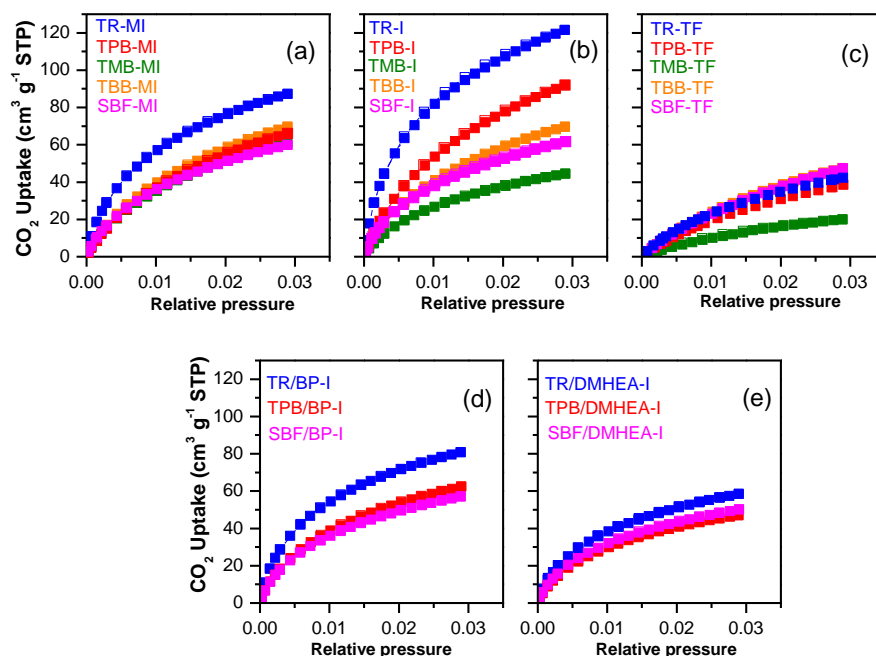


Figure 5.8. Low-pressure CO₂ adsorption (solid symbols)/desorption (hole symbols) isotherms at 0 °C of POPs.

From CO₂ adsorption data, the DR equation was applied to estimate the narrow micropore volume (V_{nmicro}). The V_{nmicro} values are listed in Table S2.6. It was found that those POPs in which the N₂ adsorption was null or negligible, such as DMHEA-based Co-POPs ($V_{\text{micro}} < 0.07 \text{ cm}^3 \text{ g}^{-1}$), exhibited V_{nmicro} values between 0.18 and 0.21, supporting the presence of micropores with entrance sizes lower than 5 Å.

The percentage of narrow microporosity of POPs was estimated from the ratio of V_{nmicro} to the total pore volume (V_{total} obtained from N₂ adsorption data). From the values shown in Table S2.6, it was found that the percentages were mostly superior to 60%, revealing that these materials show a high narrow microporosity. In particular, the incorporation of DMHEA bifunctional monomer to the networks (TPB/DMHEA, TR/DMHEA, and SBF/DMHEA-I) yielded materials having 100% of narrow microporosity. When they were compared to the analogous Ho-POPs, it was observed that TR-I also presented a high percentage of narrow microporosity (84%), but with much higher S_{BET} than TR/DMHEA-I. For the Co-POPs containing BP, the percentage of narrow microporosity was also high, but it depended on the tri- (TPB or TR) or tetra-functional (SBF)

nucleophilic monomer; i.e., the use of TPB or TR monomers yielded networks with 75% of narrow microporosity while with SBF monomer was of 100%.

The correlation between V_{nmicro} and S_{BET} of POPs is shown in Figure 5.9(a). For POPs with S_{BET} larger than $500 \text{ m}^2 \text{ g}^{-1}$, the V_{nmicro} tended to increase with the increase of S_{BET} , whereas, for those POPs with S_{BET} less than $200 \text{ m}^2 \text{ g}^{-1}$, no linear correlation between both parameters was observed. Unexpectedly, it was found that POPs with very different S_{BET} exhibited similar V_{nmicro} ; for example, SBF/DMHEA-I ($0 \text{ m}^2 \text{ g}^{-1}$, $0.18 \text{ cm}^3 \text{ g}^{-1}$) with TR-TF ($557 \text{ m}^2 \text{ g}^{-1}$, $0.19 \text{ cm}^3 \text{ g}^{-1}$), or TR/DMHEA-I ($151 \text{ m}^2 \text{ g}^{-1}$, $0.21 \text{ cm}^3 \text{ g}^{-1}$) with SBF-TF ($856 \text{ m}^2 \text{ g}^{-1}$, $0.21 \text{ cm}^3 \text{ g}^{-1}$).

The cumulative narrow micropore volume (V_{NLDFT}) and the narrow micropore size distribution (PSD) were determined from the CO_2 adsorption isotherms of POPs by using the NLDFT method using the 2D-NLDFT-Het surface Kernel with SAIEUS program. As examples, several comparative plots of the distribution of pores vs diameter (dp) of 3.0-16 Å of POPs are displayed in Figures 5.9(b-d).

The PSD curves of TPB-based POPs, which exhibited S_{BET} values ranging from 2 to $1033 \text{ m}^2 \text{ g}^{-1}$ (cf. Table S2.6), are shown in Figure 5.9(b). The shape of distribution changed with the chemical composition of the POPs, and it appeared to be more asymmetric when the S_{BET} of the materials decreased. For the TPB-based Ho-POPs, the contribution of the narrowest micropores volume (V_{NLDFT} for $\text{dp} < 5 \text{ Å}$ to which the N_2 gas could not access) to total V_{NLDFT} was 15% for TPB-I, 12% for TPB-MeI and 7% for TPB-TF. For the two TPB-based Co-POPs, TPB/BP-I and TPB/DMHEA-I, this contribution (about 22%) was higher than that for TPB-I.

In another comparative plot, the PSD curves of TF-based Ho-POPs are shown in Figure 5.9(c). These materials exhibited the lowest contribution of the narrowest micropores volume (V_{NLDFT} for $\text{dp} < 5 \text{ Å}$) to total V_{NLDFT} . The contribution was about 7% for all of these POPs, except for TR-TF (11%). Furthermore, they exhibited the highest value of average pore diameter (around 6 Å) relative to the other POPs (cf. Table S2.6).

Finally, the PSD curves of DMHEA-based Co-POPs having very small S_{BET} (between 0 and $150 \text{ m}^2 \text{ g}^{-1}$) are compared in Figure 5.9(d). It was found that the contribution of the narrowest micropores volume (V_{NLDFT} for $\text{dp} < 5 \text{ Å}$) to total V_{NLDFT} for those Co-POPs containing TR or SBF was similar to that of the corresponding Ho-POPs, TR-I (32%) and SBF-I (23%), while that for TPB/DMHEA-I (23%) was superior to that of TPB-I (15%).

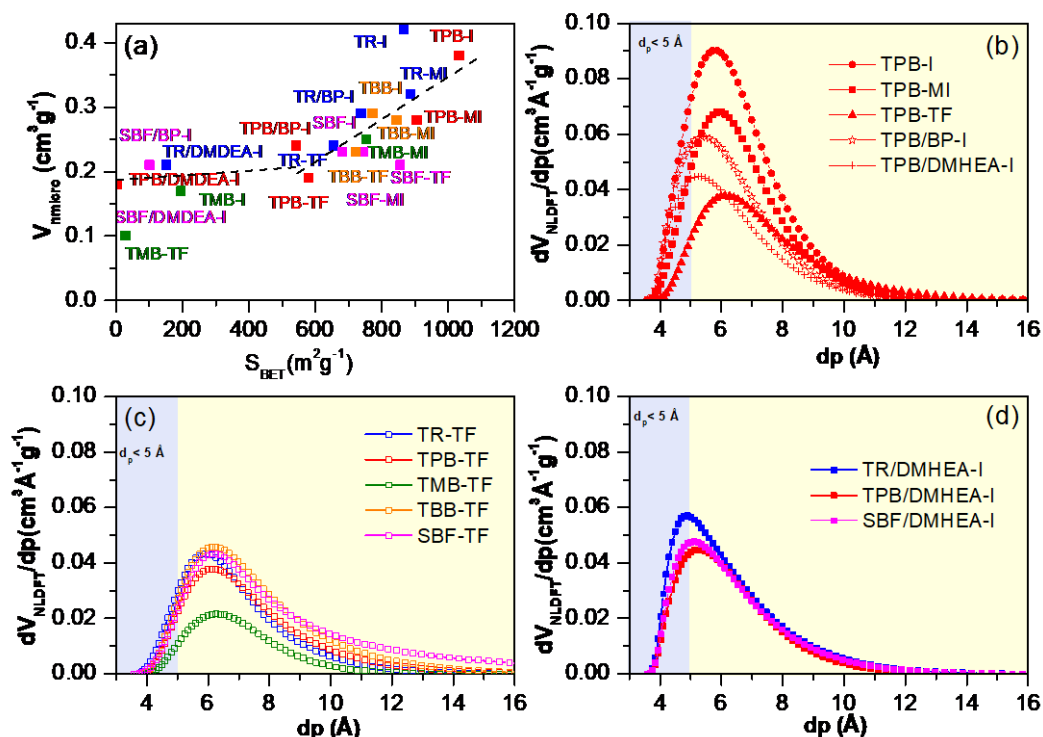


Figure 5.9. (a) Narrow micropore volume as a function of specific surface area. NFLDT pore size distribution of: (b) TPB-based POPs, (c) POPs derived from TF cross-linker, and (d) POPs containing DMHEA.

To explain these findings, we hypothesized that our materials were polymer networks consisting of irregular void sizes that were formed by an inefficient packing of the polymer chains, in agreement with their amorphous nature (cf. Figure 5.5), in which the gas molecules were accessible through entrances of small sizes. Thus, the null or very low N_2 adsorption of some POPs could be attributed to the presence of holes with entrance sizes close to the kinetic diameter of N_2 gas (3.6\AA). In the case of CO_2 (3.3\AA), the highest accessibility to the narrowest micropores ($< 5 \text{\AA}$) was due to the highest adsorption temperature employed for the measurements (0°C).

This microporous structure of POPs was supported by comparing the V_{nmicro} (obtained from CO_2 adsorption data) and V_{micro} (obtained from N_2 adsorption data). Figure 5.10 shows the correlation between both volumes (c.f. Table S2.6, section S2.8, Appendix 2). Most POPs showed a very narrow distribution of entrance sizes in the range of narrow micropores. Thus, those POPs that exhibited $V_{\text{nmicro}} \gg V_{\text{micro}}$ were formed by holes with entrances ranging from 4 to 5\AA in size (e.g., DMHEA-based Co-POPs, TMB-TF), whereas for those with $V_{\text{nmicro}} \sim V_{\text{micro}}$, the entrances were ranging from $5\text{--}8 \text{\AA}$ in size (e.g.

TPB-I, TBB-I, TR-MI, TPB-TF). Moreover, other POPs exhibited $V_{\text{nmicro}} < V_{\text{micro}}$, indicating the formation of other entrances having sizes of $> 8 \text{ \AA}$ (e.g., SBF-TF, TPB-MI), as well.

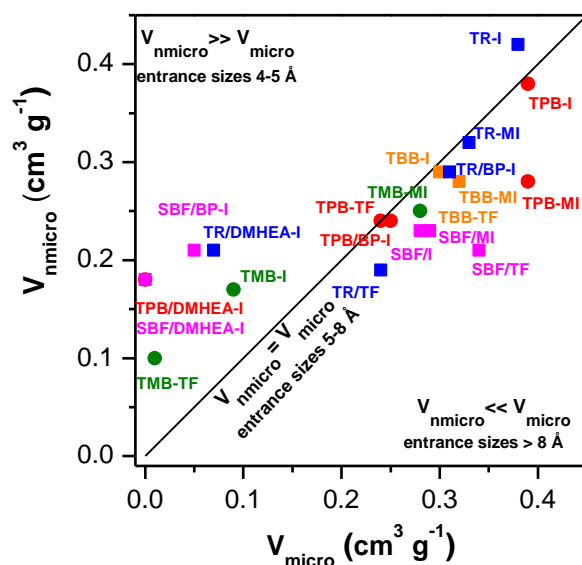


Figure 5.10. Correlation between V_{nmicro} (obtained from CO_2 adsorption data) and V_{micro} (obtained from N_2 adsorption data)

5.2.5. Low-pressure CO_2 uptake

CO_2 uptakes of POPs obtained from low-pressure adsorption isotherms at 0 and 25 °C, as well as the isosteric heat of adsorption (Q_{st}) values, are listed in Table S2.7 in section S2.9, Appendix 2. All of the isotherms showed an increase in gas uptake with increasing pressure (As an example see Figure 5.8). The reversibility of the CO_2 adsorption-desorption process at subatmospheric pressures for all of the POPs supported a physisorption nature. This fact is key for the easy recovery of the CO_2 adsorbed and the regeneration of porous material without applying a heat treatment. CO_2 uptakes at 0 °C ranging from 39 to 239 mg g^{-1} (0.89 – 5.43 mmol g^{-1}) were found for these materials. As expected in physisorption processes, a pronounced decrease in CO_2 uptakes at 25 °C (-60% on average) was observed relative to the 0 °C data.

To put the findings into a broader perspective, the CO_2 uptakes of our POPs as a function of total pore volume (V_{total}) were compared to those of other POPs containing TR, TPB, and SBF in their structures, as shown in Figure 5.11; these materials included azo-linked polymers (ALPs, 3.50-5.34 mmol g^{-1}) [141], polybenzimidazole networks (BILPs, TBILPs, BOLPs, BTLPs, and TBIs, 2.70-5.30 mmol g^{-1}) [142–145,158] porous aromatic

frameworks (PAFs, 3.30-4.70 mmol g⁻¹) [139], triazole-linked polymers (TNPs, 1.60-4.45 mmol g⁻¹) [159], triptycene-based microporous polymers (STPs, 3.70-4.14 mmol g⁻¹) [160], Hyper-cross-linked polymers of intrinsic microporosity (PIMs, 3.28-5.00 mmol g⁻¹) [140].

The comparison of our microporous materials with other ones showed that the V_{total} (that is directly related to S_{BET}) was not the key factor in the CO₂ adsorption capacity. For example, the hyper-cross-linked polymers of intrinsic microporosity PIMs having high V_{total} (0.84-1.3 cm³ g⁻¹) exhibited gas uptakes (3.28-5.00 mmol g⁻¹) comparable to those of some POPs of this work having lower V_{total} (0.39-0.64 cm³ g⁻¹), such as TR-MI (3.88 mmol g⁻¹), TPB-I (4.09 mmol g⁻¹), TR/BP-I (3.61 mmol g⁻¹) and TR-I (5.43 mmol g⁻¹). Zhou et al.[140] showed that the functionalization of these PIMs with NH₂ and HSO₃ groups considerably decreased V_{total} (0.303-0.852 cm³ g⁻¹), but the gas uptake of these functionalized PIMs was comparable to those of their precursors due to a better affinity for CO₂. Thus, the high CO₂ uptakes of TR-I (5.43 mmol g⁻¹), TPB-I (4.09 mmol g⁻¹), and SBF-I (3.00 mmol g⁻¹), when they were compared to PIM-TR (3.77 mmol g⁻¹), PIM-TPB (5.00 mmol g⁻¹) and PIM-SBF (3.27 mmol g⁻¹), could be due to the favorable interaction between CO₂ and the lactam moieties [148]. However, for these three Ho-POPs derived from isatin, the highest contribution of narrow microporosity to V_{total} led to a higher CO₂ uptake; for example, TR-I (84% of narrow microporosity, 5.43 mmol g⁻¹ of gas uptake) compared to TPB-I (60% of narrow microporosity, 4.09 mmol g⁻¹) and SBF-I (55% of narrow microporosity, 3.00 mmol g⁻¹ of gas uptake). Moreover, TR-I showed a remarkable CO₂ uptake (5.43 mmol g⁻¹) that was comparable, or even superior, to other porous organic polymers [140,161].

Considering DMHEA-based Co-POPs ($V_{\text{total}} \sim 0$ cm³ g⁻¹), which exhibited 100% of narrow microporosity due to the narrow distribution of entrance sizes (4-5 Å) to the volume units, they were found to have CO₂ uptakes between 2.11-2.61 mmol g⁻¹, which were values comparables to other POPs with higher V_{total} , such as BOLP5 (2.93 mmol g⁻¹) [145] and TNP3 (2.64 mmol g⁻¹) [159].

The data compared in Figure 5.11 also showed that the Ho-POPs derived from TF had the lowest uptakes relative to other Ho-POPs. For example, comparing the TR-I, TR-MI, and TR-TF polymer networks, it was found that the uptakes of TR-I and TR-MI were 3.1 and 2.2 times higher than that of TR-TF. In previous work, it was shown that the affinity for CO₂ is lower for TF-based POPs than for I-based POPs [148].

The Q_{st} values at zero coverage for our POPs (c.f. Table S2.7. section S2.9, Appendix 2) fell in a range between 17.8 and 36.4 kJ mol⁻¹. In general, the trend observed was similar; i.e., the POPs derived from the isatin cross-linker exhibited the highest Q_{st} values, especially the Co-POPs containing DMHEA, and the Ho-POPs derived from the TF cross-linker the lowest ones.

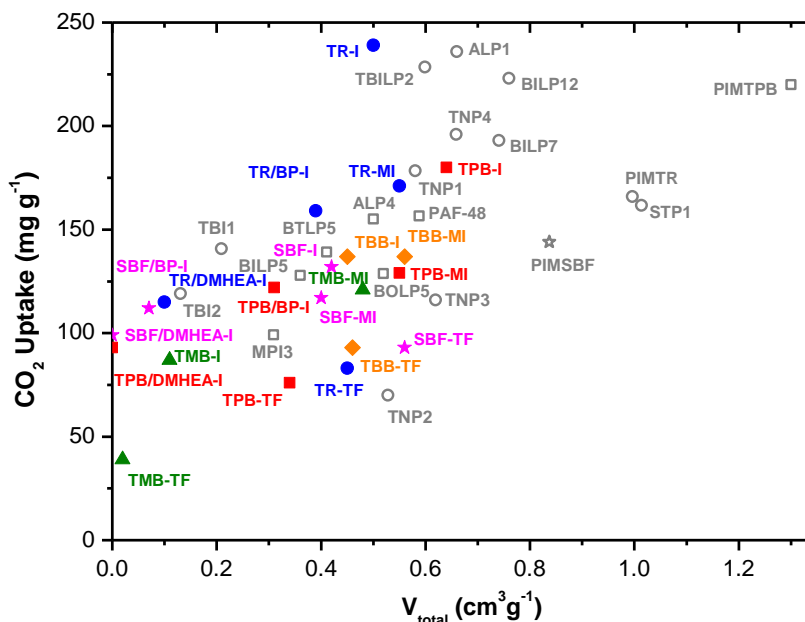


Figure 5.11. Relationship between CO₂ uptake and V_{total} of POPs

5.2.6. High-pressure gas uptake of CO₂, N₂ and CH₄

The adsorption/desorption isotherms of POPs for CO₂, N₂ and CH₄ at 25 °C and pressures up to 30 bar for CO₂, and N₂ at pressures up to 70 bar for CH₄, were measured. As an example of the behavior of POPs, the adsorption/desorption isotherms of Ho-POPs and Co-POPs derived from isatin crosslinker are shown in Figure 5.12.

The high-pressure adsorption isotherms of the POPs for the three gases tested showed an increase in adsorption capacity over the entire pressure range, although the adsorption slope decreased with increasing pressure. However, the saturation level of the materials was not reached at 30 bar, nor was it reached for CH₄ when pressures up to 70 bar were applied to the POPs, indicating that pore volume filling was not complete in this pressure range. Moreover, all of the adsorption/desorption isotherms of the POPs for CO₂ experienced a hysteresis loop, while those for N₂ and CH₄ did not present hysteresis since the measurements were performed well above their critical temperature (critical temperature of 126.2 (N₂) and 190.6 K (CH₄)). However, the CO₂ adsorbed was easily

released when returning to 0 bar, indicating the possibility of regeneration of these materials by applying a vacuum without temperature.

The excess adsorption at 30 bar for the three gases of all of the POPs studied are listed in Table S2.7, section S2.9, Appendix 2. The gas uptakes followed the order: $\text{CO}_2 > \text{CH}_4 > \text{N}_2$, as expected from the solubility coefficient of the gas as a function of its critical temperature: CO_2 (304 K) $>$ CH_4 (191 K) $>$ N_2 (126 K). Furthermore, the CO_2 adsorption of POPs was higher than those of N_2 and CH_4 adsorptions, thus CO_2/N_2 and CO_2/CH_4 ratios were about 7 and 8 at 25 °C and 30 bar for all of the POPs.

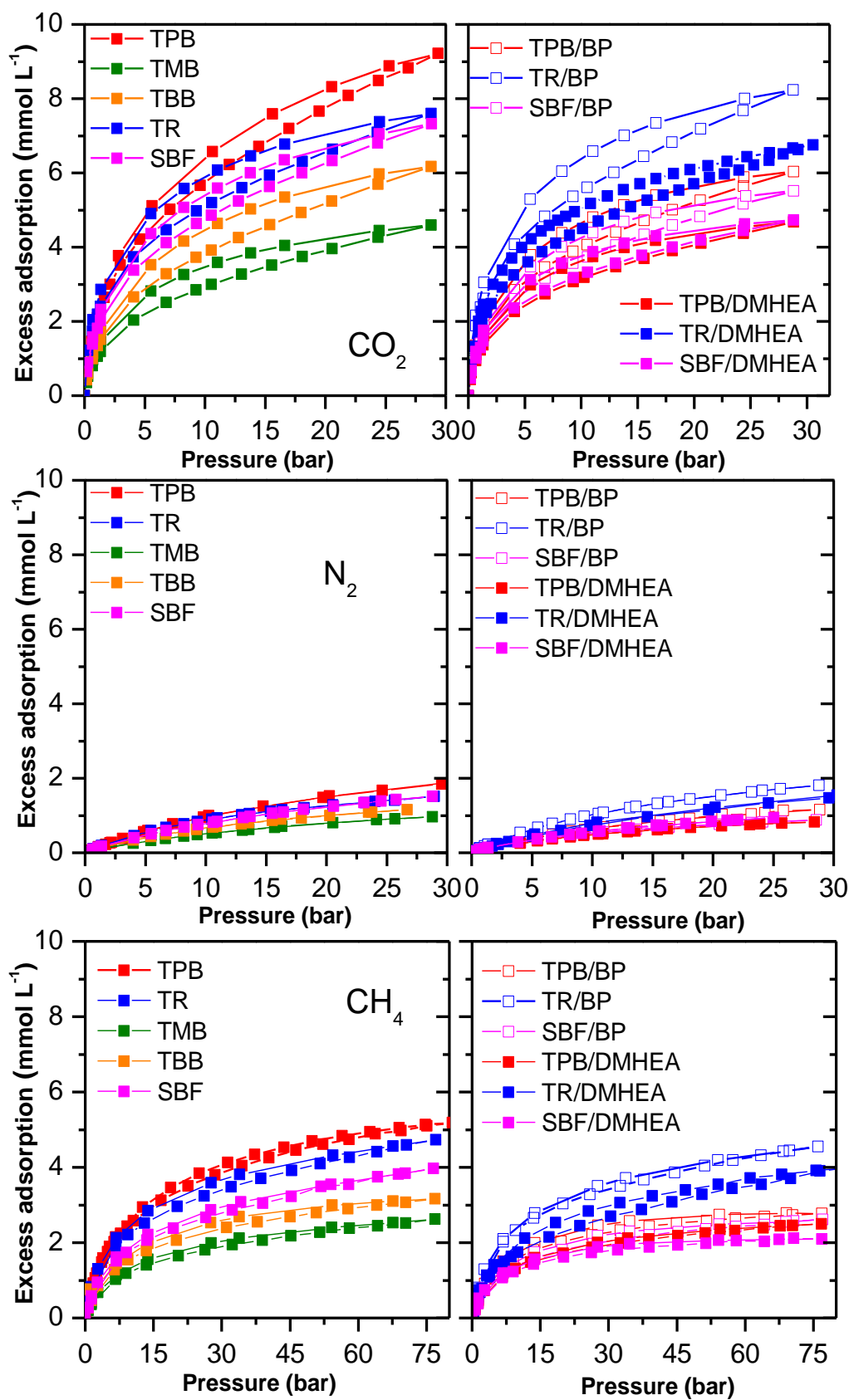


Figure 5.12. Excess CO₂, N₂, and CH₄ uptake of POPs derived from isatin cross-linker.

5.2.7. CO₂/N₂/CH₄ separations

In addition to the high thermal stability of POPs, due to their relatively good CO₂ adsorption and their easy regeneration, the selectivity of CO₂ over other gases is another important factor when the materials are designed to separate potential gas mixtures in industrial processes. For example, the capture of CO₂ from a CO₂/N₂ mixture in a post-combustion process of flue gas [134] or the removal of CO₂ from a CO₂/CH₄ mixture using pressure swing adsorption (PSA) technology to improve the quality of biogas [162,163].

The adsorption selectivity of CO₂ over N₂ and CH₄ was estimated from the pure high-pressure CO₂, N₂, and CH₄ adsorption isotherms at 25 °C by applying the Ideal Adsorbed Solution Theory (IAST) proposed by Myers and Prausnitz [80] (and revised in other articles [81,82]). As an example, Figure 5.13 shows the change of the selectivity factor of CO₂ over N₂ ($S_{\text{CO}_2/\text{N}_2}$) or CH₄ ($S_{\text{CO}_2/\text{CH}_4}$) of TR-based POPs as a function of the pressure from two binary mixtures: one with 0.15 molar fraction of CO₂ in N₂ (e.g., flue gas composition) and another with 0.50 molar fraction of CO₂ in CH₄ (e.g., biogas upgrade).

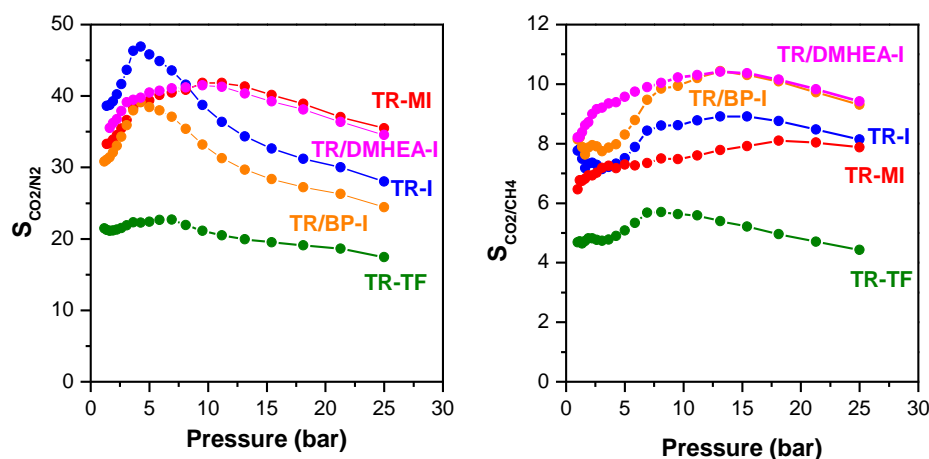


Figure 5.13. Selectivity factor of CO₂ over N₂ (right) and CH₄ (left) as a function of pressure at 25 °C for two binary mixtures of molar ratio: 0.15/0.85 for CO₂/N₂ and 0.50/0.50 for CO₂/CH₄.

The CO₂/N₂ selectivity of POPs increased with increasing pressure until a certain value was reached at which the selectivity decreased more or less significantly due to material saturation, except for the POPs derived from TF cross-linker, which did not show significant changes in selectivity over the pressure range. For example, TR-I showed a high selectivity of 47 at about 4 bar and then a strong decrease in selectivity was observed (28 at 25 bar), while the selectivity of TR-MI was from 39 at about 4 bar to 35 at 25 bar.

In contrast to CO₂/N₂ selectivity, the CO₂/CH₄ selectivity of POPs increased with increasing pressure over the pressure range; observing that the highest selectivity values were achieved above 5 bar. No significant saturation of materials was observed for this separation.

To put in perspective the adsorption selectivity data of CO₂ over N₂ and CH₄ at 25 °C, we compared the selectivity factors, S_{CO₂/N₂} and S_{CO₂/CH₄}, of our POPs with those of other materials reported in the literature that were calculated by applying IAST at similar temperature and pressure employing mixtures with the same molar composition. For that, S_{CO₂/N₂} and S_{CO₂/CH₄} values were shown as a function of CO₂ uptake, which was taken from low-pressure adsorption isotherms at 1 bar and 25 °C, in Figures 5.14 and 5.15.

Regarding the separation of CO₂ adsorption selectivity for flue gas composition (0.15/0.85 CO₂/N₂) (Figure 5.14), it was observed that TR-based Ho-POPs mostly yielded materials with both higher CO₂ uptake and S_{CO₂/N₂}, while TMB-based Ho-POPs showed the lowest CO₂ uptake values; for example, TR-I (3.60 mmol g⁻¹, 38.6) and TMB-I (1.21 mmol g⁻¹, 21) or TR-MI (2.45 mmol g⁻¹, 33.3) and TMB-MI (1.59 mmol g⁻¹, 4.51). Regarding the cross-linker units, the Ho-POPs formed from isatin showed the highest gas uptake and S_{CO₂/N₂} values, followed by those formed from MI and then from TF, which showed the lowest separation performance in selectivity and uptake; for example, TR-I (3.60 mmol g⁻¹, 38.6), TR-MI (2.45 mmol g⁻¹, 33.3) and TR-TF (1.05 mmol g⁻¹, 21.5). On the other hand, the separation performance of Co-POPs relative to Ho-POPs was lower in terms of CO₂ uptake, but not in selectivity. For example, TPB-I (CO₂ uptake of 2.29 mmol g⁻¹, selectivity of 25.5), TPB/BP-I (CO₂ uptake of 2.36 mmol g⁻¹, selectivity of 30.8), and TPB/DMHEA-I (CO₂ uptake of 1.73 mmol g⁻¹, selectivity of 35.5).

The selectivity factor and gas uptake were comparable to other POPs having TR, TPB, or SBF in their structure, as shown in Figure 5.14, except for a benzoxazole-linked porous polymer, BOLP5, which has a S_{CO₂/N₂} of 78, but a lower gas uptake than some of our POPs, such as TR-I, TR-MeI, TPB-I, and TR/BP-I. The separation performance of our POPs was relatively good and comparable, if not superior as TR-I was, to other reported porous organic polymers [134].

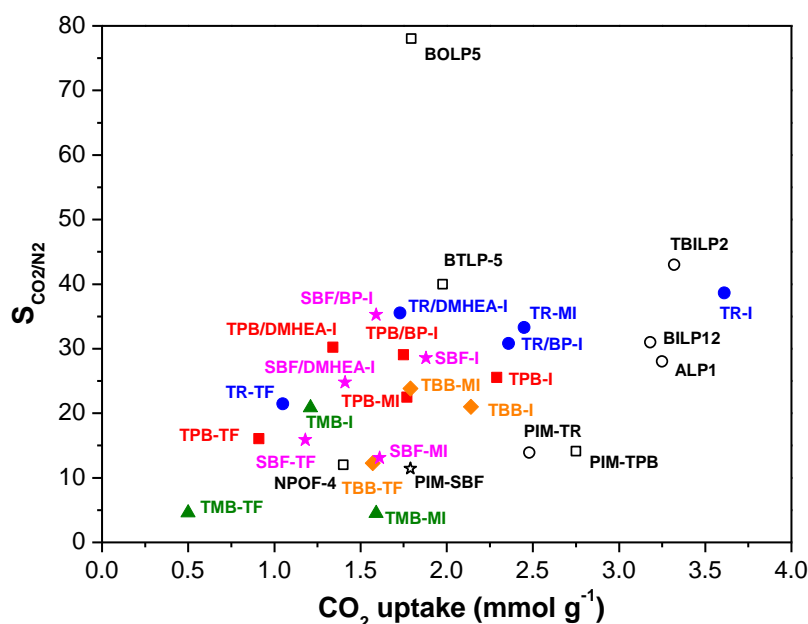


Figure 5.14. Comparison of CO₂/N₂ selectivity as a function of CO₂ uptake (1 bar and 25 °C) of the POPs prepared in this work and others taken from literature having TR (circle), TPB (square), and SBF (star) in their structures [140,141,143,145,158,164]. The selectivity factor, $S_{\text{CO}_2/\text{N}_2}$, was calculated from IAST for 15/85 CO₂/N₂ mixture at 1 bar and 25 °C.

As mentioned before, the separation CO₂ adsorption selectivity for an equimolecular mixture of CO₂/CH₄ has been studied for the first time in our POPs. As far as I know, little values about this particular separation in porous organic materials are available in the literature [135,140,145,164,165]. In Figure 5.15, the CO₂/CH₄ selectivity of our POPs at 1 bar (also values at 10 bar for TR-based POPs) and 25 °C are displayed as a function of CO₂ uptake taken at 1 bar, and 25 °C from low-pressure adsorption isotherms (c.f. Figure 5.8). The separation performance was compared to a few selectivity values for an equimolecular CO₂/CH₄ mixture at 25 °C and 1 bar of other POPs having TR and TPB in their structure [140,145,164].

Most TR-based POPs exhibited a good CO₂ adsorption capacity, with values above 2 mmol g⁻¹ (100 mg g⁻¹), and selectivities at 1 bar between 6 and 8. On the other hand, the Co-POPs exhibited lower adsorption capacity (1.3 - 1.8 mmol g⁻¹), but they were regarding selectivity comparable to those of TR-based POPs. Thus, in the case of Co-POPs containing DMHEA, the narrow distribution of very small entrance sizes, between 4 - 5 Å, seemed to be the key to good selectivity, while a wider distribution of entrance pores of POPs such as TR-I, TR-MI, and TR/BP-I, between 5 and 8 Å, improved

separation performance in terms of both selectivity and adsorption capacity. On the other hand, the selectivity factors at 10 bar for the TR-based POPs are also shown in Figure 5.15 to point out that these materials could be used in CO₂/CH₄ separation processes at higher pressures as the selectivity factor increases. Finally, it is to be also mentioned that most of the POPs exhibited CO₂/CH₄ selectivities, comparable to that of the excellent BOLP-5 and higher than many other POPs reported in the literature, as shown in Figure 5.15.

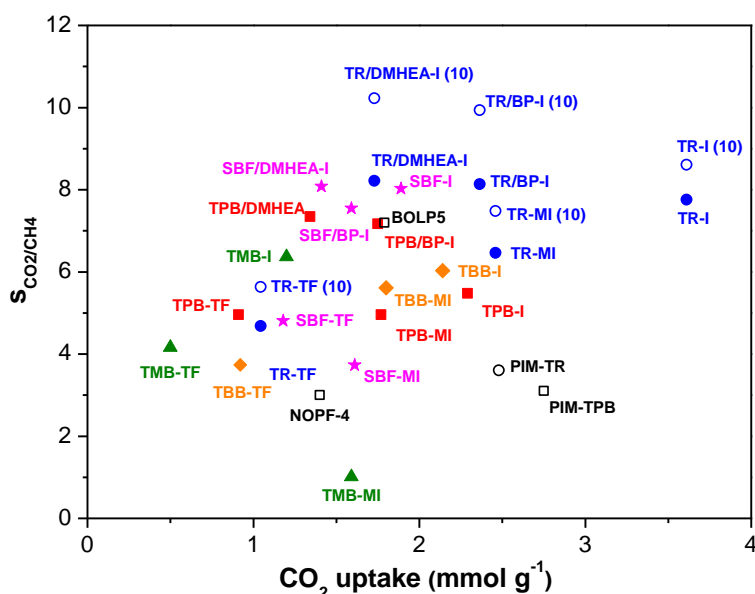


Figure 5.15. Comparison of CO₂/CH₄ selectivity as a function of CO₂ uptake (taken from CO₂ isotherms at 1 bar and 25 °C) of the POPs prepared in this work and others taken from literature having TR (circle) and TPB (square) in their structures [140,145,164]. The selectivity factor, $S_{\text{CO}_2/\text{CH}_4}$, was calculated from IAST for an equimolecular CO₂/CH₄ mixture at 1 bar and 25 °C. Selectivity data at 10 bar for TR-based POPs are indicated by adding to the name (10).

Chapter 6

6. Plasticization-resistant gas separation membranes derived from polyimides exhibiting polyethylene-oxide moieties

6.1. INTRODUCTION

Gas separation *via* dense polymer materials is a mature technology, with well-established emerged applications [18,93]. Despite recent progress in the field, new polymeric materials exhibiting higher levels of productivity, selectivity, and long-term durability are sought to make membrane separations competitive with conventional thermal separation techniques. Over the past three decades, aromatic polyimides have been extensively investigated as potential polymeric membrane materials for gas separation [34,89,166–168]. In particular, polyimides containing hexafluoropropylene bridges, that is, 6F moieties, exhibit excellent gas separation characteristics [149,169–172], although their susceptibility to physical aging and plasticization remains a drawback issue for their industrial application [173,174]. The overarching goal of this study is to address this long-standing issue, removing relevant roadblocks towards a more mature application of these materials.

Another issue that hampers membranes in real-world applications is that they are often tested only at low pressures (i.e., <10 bar). In the case of high-pressure tests, gas-polymer interactions may lead to conditioning, swelling, and plasticization, which adversely affect long-term membrane performance [175,176].

The concept of plasticization of polymer materials can be considered an extreme case of polymer swelling by a highly condensable (i.e., soluble) gas [105,106,110,177–180]. When this phenomenon occurs, polymer chains are pulled apart, which causes a significant increase in gas diffusion and permeability coefficients, according to the solution-diffusion model [5]. Moreover, plasticization may induce hysteretic behavior in gas sorption, diffusion, and permeation coefficients as a function of pressure or fugacity [124,181]. However, it should also be noted that, depending on the application, plasticization can also benefit both permeability and selectivity simultaneously. Therefore, any time a new membrane is synthesized, it is imperative to investigate its plasticization behavior in

realistic conditions [6].

In this study, we provide a synthetic strategy to mitigate plasticization and create materials exhibiting enhanced long-term stability. Multiple approaches have been proposed, over the years, to achieve better plasticization and physical aging resistance, such as polymer blending, chemical and/or thermal crosslinking [178,182], and mixed matrix membranes (MMMs), just to mention a few materials [183–185]. When these methodologies are carefully designed and properly implemented from the synthetic point of view, it is possible to achieve better membrane durability without sacrificing selectivity.

In previous works, we synthesized and studied aliphatic-aromatic copolyimides featuring sacrificial polyethylene oxide chains (PEO) and carboxylic groups derived from 3,5-diaminobenzoic acid (DABA) units [68,121,186,187]. After a controlled thermal treatment, which stripped off the PEO units, membranes exhibited enhanced permeability with minimal changes in selectivity [187]. Following this concept, the main idea of this study consists of the design, synthesis, and testing of novel gas separation materials exhibiting enhanced plasticization resistance and separation performance relative to previously reported polyimide PI-DABA-PEO materials [68]. Specifically, to achieve higher gas permeabilities relative to DABA-PEO-based polyimides, we replaced the aromatic diamine 2,2'-bis(4-aminophenyl)hexafluoropropane (6FpDA) with 2,4,6-trimethylphenyldiamine (TMPD), which produces polymers presenting higher fractional free volume [97,149]. Furthermore, we hypothesize that thermal elimination of the PEO chains provides extra free-volume elements and that crosslinking among DABA's carboxyl groups enhances plasticization resistance [68,121,187]. To test these hypotheses, a comprehensive plasticization study was carried out in this work. Since high-free volume polymers, such as polyimide 6FDA-TMPD (PI*), are prone to physical aging, all prepared membranes were aged for 18 months [188]. The physical aging of these membranes was monitored by measuring pure N₂ and CO₂ permeability throughout this time.

Recently, well-designed blends of microporous materials with polymeric matrices have attracted considerable interest, as their gas separation performance may exceed the permeability/selectivity trade-off [189,190]. Thus, with the idea of improving permeability, MMMs were fabricated by blending the newly synthesized aromatic-aliphatic polyimides, PI*-DABA-PEOs, with porous organic polymers (POPs), which are porous organic materials exhibiting excellent chemical and thermal stability [148]. POPs were synthesized

using a highly efficient Friedel-Crafts process reaction between ketones and polyaromatic compounds, such as triptycene, resulting in the formation of a new class of porous polymeric networks exhibiting high microporosity, good compatibility with a diverse set of polymer materials and excellent chemical and thermal stability. The resulting materials offer exciting avenues of exploration for catalysis [153,154], CO₂ capture [148], and gas separation applications [149,150].

6.2.RESULTS AND DISCUSSION

6.2.1 Polymers synthesis and characterization

Two aromatic polyimides, PI* and PI*20, were prepared through a two-step polycondensation, using the base-assisted *in-situ* silylation method (Figure 6.1) [61,62]. However, for the aromatic-aliphatic polyimide, PI*20EO1, the *in-situ* silylation method was not used as it produced polymers with lower molecular weights than those obtained when classical polycondensation was employed (Figure 6.2) [68]. Details about the synthesis are shown in section 3.1.2.2 and 3.1.2.3, Chapter 3.

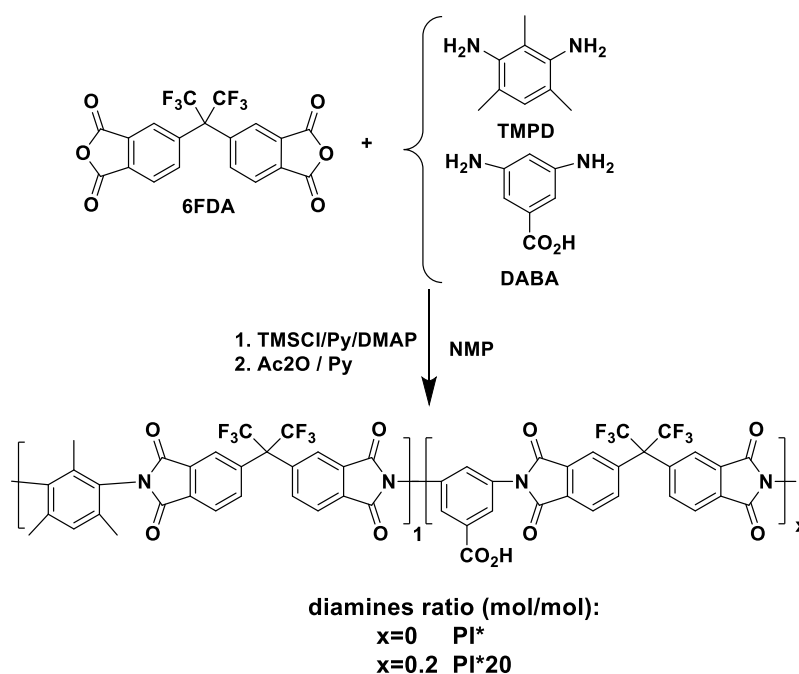


Figure 6.1. Scheme of synthesis of the aromatic polyimides: 6FDA-TMPD (PI*) and 6FDA-TMPD-DABA (PI*20). X denotes the DABA/TMPD molar ratio.

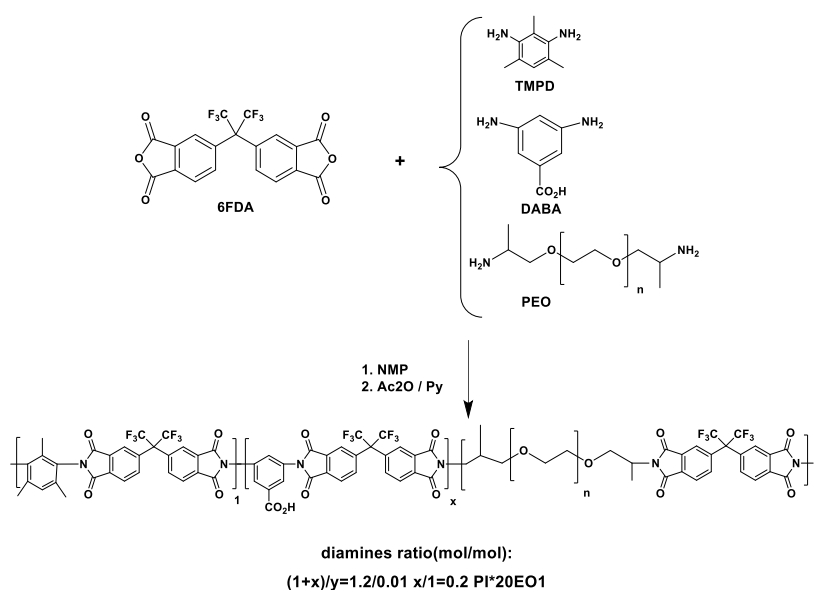


Figure 6.2. Scheme of synthesis of the aromatic-aliphatic copolyimide: PI*20EO1. X denotes the molar ratio of DABA to TMPD and Y denotes the molar ratio of PEO to TMPD.

All polymers were soluble in polar aprotic solvents as shown in Table S3.1 (section S3.1.1, Appendix 3).

The $^1\text{H-NMR}$ spectrum of PI*20EO1, PI*, and PI*20 are shown in Figures S3.1, S3.2, and S3.3, respectively, in section S3.1.2, Appendix 3. Peaks associated with the aromatic protons appeared in the region between 8.50 and 7.00 ppm, while aliphatic PEO protons (H10-14) appeared at 3.57 ppm, indicating the presence of methylene groups. Additionally, methyl group signals from TMPD were observed at 1.96 ppm (H1) and 2.18 ppm (H2).

The content of the DABA moiety in PI*20 was determined by analyzing the $^1\text{H-NMR}$ spectrum in Figure S3.2, section S3.1.2, Appendix 3. The area ratio of the aromatic proton peak at 8.24 ppm (H7, from DABA moiety) to 7.24 ppm (H3, from TMPD moiety) roughly agreed (99%) with the theoretical ratio (TMPD/DABA=1/0.2 mol/mol). Unfortunately, the composition of PI*20EO1 could not be determined from $^1\text{H-NMR}$, even though different deuterated solvents (such as $\text{CHCl}_3\text{-d}$, DMSO-d_6 , and THF-d_8) were tested. As an example, the spectrum of PI*20EO1 (theoretical ratio TMPD/DABA/PEO=1/0.2/0.01 mol/mol/mol) in THF-d_8 is shown in Figure S3.3, section

S3.1.2, Appendix 3. It can be observed that the aliphatic proton peaks from PEO (H10-H14) appear to overlap with the peak at 3.59 ppm assigned to the solvent. Alternatively, the PEO content was estimated to be about 90 wt.% of the theoretical value from isothermal thermogravimetric analysis (TGA), as commented below in section 6.2.2.

6.2.2. Membrane characterization

Other than neat polymer membranes, mixed matrix membranes were fabricated by incorporating 20 wt.% of POP in PI*, PI*20, and PI*20EO1. The POP chemical and physical characterization are summarized in section S3.2, Appendix 3 (Figures S3.4 and S3.5 and Table S3.2). Further information about the POPs employed in this Ph.D. memory can be found in the literature [148].

ATR-FTIR spectra of the MMMs show typical absorption bands of imide groups from the polymer matrix, as shown in Figure S3.6 in section S3.3.1, Appendix 3. However, the characteristic absorption bands of POP at 1708 cm^{-1} (sym C=O st), 1470 cm^{-1} (N-H stretching), and 1320 cm^{-1} (C-N st) could not be distinguished by overlapping with the typical polyimide's IR bands.

Figure 6.3(a) shows the TGA thermograms of all non-treated membranes (PI*, PI*20, and PI*20EO1). A minor weight loss (about 3.5 wt.%) below $300\text{ }^{\circ}\text{C}$ was associated with residual solvent loss (the solvent normal boiling point is $165\text{ }^{\circ}\text{C}$). Before polymer degradation, PI*20 and PI*20EO1 exhibited another minor weight loss between 350 and $450\text{ }^{\circ}\text{C}$. For PI*20, this weight loss was due to the decarboxylation process from the DABA comonomer unit. For PI*20EO1, the weight loss in this temperature range also included the removal of PEO segments present in the copolyimide structure [68].

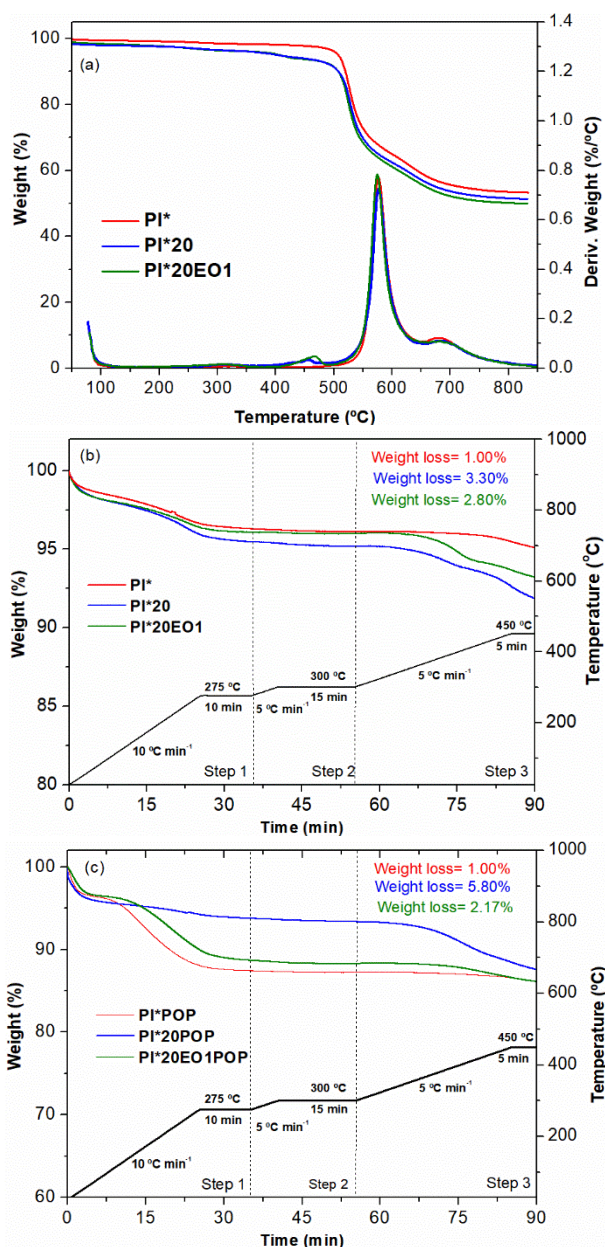


Figure 6.3. (a) TGA thermograms of polymer membranes, (b) isothermal TGA analysis of polymer membranes and (c) isothermal TGA analysis of MMMs.

Isothermal TGA analysis was performed to quantify the weight loss happening during the thermal protocol used to prepare cross-linked membranes (c.f. section 3.2.5, Chapter 3). The isothermal thermograms are shown in Figure 6.3(b). During the first isothermal steps at 275 and 300 °C, the residual solvent was removed from the samples. Subsequently, membrane cross-linking occurred during the final step (between 300 and 450 °C).

The removal of carboxylic groups from DABA arises through a two-step mechanism [191]: the formation of interchain anhydride linkages from adjacent carboxylic groups, and cross-linking by decarboxylation (from both dianhydride moieties and free carboxylic groups) at high temperature (above 450 °C). Therefore, the weight loss in PI*20 (3.30% during the final step) could be attributed to either the loss of H₂O due to the formation of dianhydrides or the total decarboxylation (theoretical loss weight= 4.48% (H₂O) and 1.3 (CO₂) or 1.07% (CO₂ and CO)).

For PI*20EO1, the weight loss during the final step was 2.80%. This weight loss was mainly attributed to the removal of PEO segments, as observed in analogous polyimides reported previously [68]. Furthermore, it was noted that the weight loss in the final step of the thermal treatment appeared to be 90% of the total PEO weight (theoretical weight loss = 3.15%).

The cross-linking degree of the thermally treated membranes, PI*20-TT and PI*20EO1-TT was estimated by calculating the gel fraction (c.f. Eqn. 3.5, section 3.3.2, Chapter 3), and values are listed in Table 6.1. The gel fraction of PI*20-TT was determined to be 68%, which is 2.6 times higher than that of PI*20EO1-TT. This indicates that the removal of PEO (about 90% in PI*20EO1-TT) appears to hinder the cross-linking process. The gel fraction of PI*20EO1-TT was determined to be 75%, which is 1.1 times higher than that of PI*20-TT. It is worth noting that analogous copolyimides derived from 2-2'-bis(4-aminophenyl)hexafluoropropane diamine (6FpDA) instead of TMPD exhibited higher gel fractions (above 70%). However, those copolyimides had a much higher content of PEO (between 9-28% w/w) [68].

The FFV of the thermally treated (TT) membranes was determined based on their bulk density according to Equation 3.4 (section 3.3.2, Chapter 3), and is reported in Table 6.1. It was observed that the FFV increased by 22% in PI*20-TT and by 28% in PI*20EO1-TT relative to the neat PI* membrane.

Table 6.1. Gel fraction, density, and fractional free volume (FFV) of the neat PI* and cross-linked copolyimides membranes.

Membrane	Gel fraction ^a	Density ^b	FFV ^c
PI*	0	1.32 ± 0.01	0.218 ± 0.002
PI*20-TT	68	1.35 ± 0.06	0.27 ± 0.02 ^d
PI*20EO1-TT	75	1.330 ± 0.004	0.278 ± 0.001 ^d

^a Gel fraction (%) determined from Eqn. 3.5; ^b bulk density (g cm^{-3}) calculated from Eq. 1; ^c FFV was estimated from Eqn. 3.4; ^d it was assumed that the Van der Waals volume was similar to that of PI*20 ($V_w = 218.83 \text{ cm}^3 \text{ mol}^{-1}$).

Previous studies demonstrated that POP derived from triptycene and isatin exhibits large thermal stability at elevated temperatures (weight loss of 5% after heating to 450 °C for 180 min) [150]. The degradation onset temperatures of POP (560 °C) and PI*POP were 55 °C and 45 °C higher than that of PI*, respectively, as shown in Figure S3.7 in section S3.3.2, Appendix 3. This indicates that the presence of POP imparts thermal stability to the MMM. Isothermal TGA thermograms of MMMs are shown in Figure 6.3(c). Similar to the behavior of the neat membranes, the two first steps of the thermal treatment involved the removal of residual solvent. The weight loss in the last step for PI*POP was 1%, which is the same as that observed in PI* (Figure 6.3(b)). For PI*20POP, the weight loss was 1.8 times higher than that of PI*20, while for PI*20EO1POP, the weight loss was 0.77 times lower compared to PI*20EO1. These results were unexpected, as it appears that the presence of POP affects both the decarboxylation of the DABA moiety and the removal of PEO. In the case of PI*20EO1POP, the presence of POP seems to hinder the PEO removal, while in the case of PI*20POP, it seems to facilitate the decarboxylation of the DABA moiety.

WAXS patterns of the membranes, before and after thermal treatment, are shown in Figure 6.4. All the polymer materials were amorphous. Thus, PI* displayed an intense peak at 15.2° along with two shoulders at 27 and 40.5°. By applying Bragg's equation ($\lambda = d\text{-spacing} \sin\Theta$, where d-spacing represents the intersegmental distance and Θ is the scattering angle), the most probable d-spacings were calculated to be approximately 0.57, 0.31, and 0.20 nm, respectively. The WAXS patterns of PI*20 and PI*20EO1 were similar in shape to PI*, but with a higher contribution of the d-spacings at 27° (0.31 nm) and 40.5° (0.20 nm). After

thermal treatment, the patterns of the PI*20-TT and PI*20EO1-TT membranes did not show significant differences with that of PI*.

The WAXS patterns of the MMMs were similar to those of neat membranes, as shown in Figure S3.8 in section S3.3.3, Appendix 3. No significant differences in the patterns of MMMs, before and after thermal treatment, were observed.

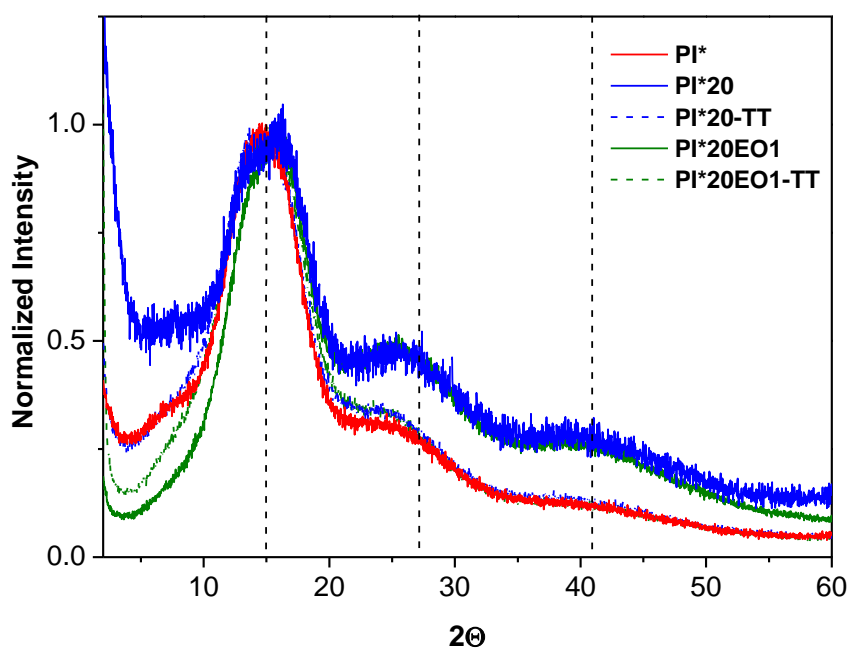


Figure 6.4. Comparison of WAXS patterns of PI*, PI*20, and PI*20EO1 membranes before and after thermal treatment

The morphologies of the MMMs were examined using FE-SEM. The cryogenically fractured cross-sectional surfaces of MMMs are shown in Figure 6.5. PI*POP showed a poorer matrix-filler adhesion than PI*20POP and PI*20EO1POP, as suggested by the presence of cavities containing agglomerates of POP particles after the fracture. PI*20POP and PI*20EO1POP exhibited a more homogeneous POP dispersion. After thermal treatment, PI*20POP-TT and PI*20EO1POP-TT showed a smooth surface without any cracks or plastic deformation.

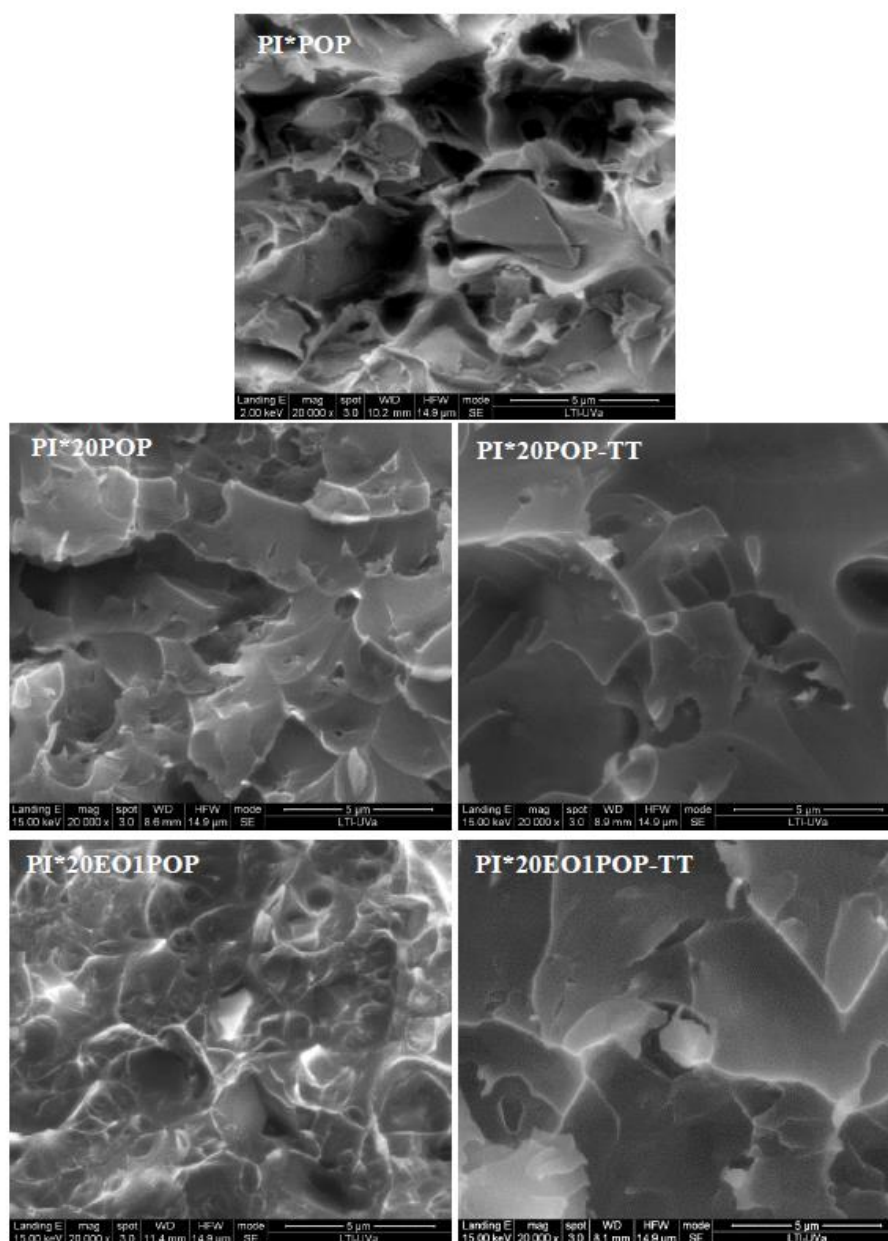


Figure 6.5. Cross-sectional FE-SEM micrographs of MMMs before and after thermal treatment

6.2.3 Mechanical properties

The Young's moduli, tensile strengths, and elongations at break of all of the materials were measured at room temperature, and the results are summarized in Table S3.3 in section S3.4, Appendix 3.

Generally speaking, the thermal treatment produced a modest, if not negligible, increase in the Young's modulus (+5.4% on average), and a decrease in the elongation at break (-37.6% on average) for the neat polyimides. This indicates that thermally treated samples

tend to be slightly more brittle relative to their untreated counterparts. In the case of MMMs, the incorporation of POP led to a decrease in the overall tensile strength and elongation at break (~50% in both cases). However, Young's modulus did not drastically change, demonstrating that the materials do not exhibit a drop in the ability to resist stresses. Subsequently, upon thermal treatment of MMMs, a pronounced increase in Young's modulus (+42.5% on average), along with a parallel increase in the tensile strength (+31.5% on average), was observed relative to the untreated MMMs.

To put our results in a broader perspective, the mechanical properties of a series of our polymer materials are compared to those of standard gas separation materials in Table 6.2.

Table 6.2. *Tensile Strength and elongation at break for popular commercial polymers, as well as previously studied thermally-rearranged polymers, compared to those for PI*20EO1, PI*20EO1TT, PI*20EO1POP, and PI*20EO1POP-TT. HAB-6FDA TR 450 stands for the thermally rearranged analog of the HAB-6FDA polyimide.*

Material	Tensile Strength (MPa)	Elongation at break (%)	Reference
Polysulfone	52.4	48.0	[192]
Matrimid	87.1	21.1	[193]
Cellulose Acetate	14.0	17.0	[194]
PI*20EO1	77 ± 5	7.3 ± 0.9	This Study
PI*20EO1-TT	58 ± 18	7 ± 2	This Study
PI*20EO1POP	40 ± 7	3.9 ± 0.7	This Study
PI*20EO1POP-TT	61 ± 11	3.1 ± 0.9	This Study
HAB-6FDA PI	153	7.1	[195]
HAB-6FDA TR 450	62	4.0	[195]

The polyimides/MMMs considered in this study are more brittle than commercial materials (see Table 6.2 and Table S3.3, section S3.4, Appendix 3), but possess similar tensile strength. For example, the elongation at break for PI*20EO1POP-TT was 3.1 ±

0.9%, which is 94% and 85% less than a commercial polysulfone and Matrimid, respectively, while the tensile strength (61 ± 11 MPa) was within the range presented from commercial materials (14 – 87.1 MPa). On the other hand, if we compare our materials with other reported polyimides, specifically those derived from 6FDA and 3,3'-dihydroxy-4,4'-diaminobiphenyl (HAB) [195], that have also undergone high-temperature treatments (up to 450°C), similar trends in the tensile strength are observed for neat materials. For example, the tensile strength of the neat polyimide HAB-6FDA decreased by 60% after thermal treatment (up to 450 °C, referred to as HAB-6FDA TR 450). The final values for the tensile strength (62 MPa) and elongation at break (4%) for HAB-6FDA TR 450 are comparable to most materials presented in this study. Overall, the thermal treatment can affect the mechanical nature of the materials, but positively benefits the mechanical properties of the POP-containing membranes. Despite mechanical differences when compared to commercial polymers, similarities drawn to thermally rearranged membranes show that the polyimides/MMMs presented in this study still offer comparable and reasonably high tensile strength.

6.2.4 Physical aging analysis

Before discussing the gas separation properties of neat PI* membranes and MMMs, it is important to recall that both neat membranes and MMMs were conditioned in methanol and stored at room temperature for 18 months to minimize changes in gas permeability due to physical aging during the plasticization studies. The pure gas permeability for CO₂ and N₂ at 3 bar and 35 °C was measured at 0, 12, and 18 months. For the sake of brevity, changes in CO₂ and N₂ permeability coefficients over time, as well as CO₂/N₂ selectivity, are shown in Figures S3.9 and S3.10 in section S3.5, Appendix 3.

When comparing the permeability of neat membranes (PI*, PI*20, and PI*20EO1) aged at 0 and 12 months, it was observed that upon 12 months of aging, the CO₂ and N₂ permeability in PI* both decreased by 40%, while that of PI*20EO1 decreased by 47% for CO₂ and 30% for N₂. Unexpectedly, the permeability of PI*20 increased by 25% for CO₂ and 70% for N₂ after the same aging time. The CO₂/N₂ selectivity of both PI*20 and PI*20EO1 decreased by 25%, while that of PI* remained unchanged. Between 12 and 18 months, the CO₂ and N₂ permeability coefficients changed little (about 3%), indicating that the membrane properties were pretty stable at that aging time. This is the reason why we decided to use all neat and mixed matrix membranes after 18 months of aging.

For the MMMs, it was found that the CO₂ and N₂ permeabilities of PI*POP and PI*20POP decreased by about 55% when the membranes were left to age for 12 months, while those of PI*20EO1POP only decreased by about 12%. The CO₂/N₂ selectivity remained unchanged over time. The permeabilities of MMMs barely changed (up to 4%) after 18 months. Therefore, in the case of PI*20EO1POP, the addition of POP to the PI*20EO1 matrix substantially mitigated the propensity for physical aging. Interestingly, the permeability was reduced by 75% and 60% less for CO₂ and N₂, respectively, compared to that of PI*20EO1.

6.2.5 Gas Separation Properties

Pure gas permeability coefficients for He, O₂, N₂, CH₄, and CO₂ in neat PI*, PI*20, and PI*20EO1, before and after thermal treatment, along with ideal selectivity values for O₂/N₂ and CO₂/CH₄ pairs, are shown in Table S3.4 in section S3.6, Appendix 3. The corresponding permeability coefficients and ideal selectivity values in MMMs, before and after thermal treatment, are also shown in Table S3.4.

For the neat, non-thermally treated membranes (i.e., PI*20 and PI*20EO1), each gas permeability coefficient was lower than that of the reference polyimide membrane, PI*. Specifically, the highest decrease in permeability in PI*20 and PI*20EO1 was observed for CH₄ and CO₂ (about 50% and 40%, respectively) compared to that for O₂ and N₂ gases (about 25%). The change in permeability may be related to a higher presence of small intersegmental distances in the chains' packing of these copolyimides, as shown by the WAXS data (c.f. Figure 6.4).

Interestingly, although gas permeability in PI*20 and PI*20EO1 increased after thermal treatment, the values remained lower than those seen in the neat PI* membrane. Specifically, permeability in both membranes was about 10% lower for O₂ and N₂, 25% for CH₄, and between 10% and 18% for CO₂, respectively. This behavior may be related to the disappearance, in the WAXS patterns, of the small intersegmental distances (0.31 and 0.20 nm) observed when comparing the amorphous halos of untreated and thermally treated membranes (cf. Figure 6.4). The disappearance of these distances is in agreement with the higher FFV exhibited by PI*20-TT and PI*20EO1-TT relative to PI* (cf. Table 6.1).

Let us now analyze the effect of POP on the transport properties, with emphasis on the individual and synergistic effect of POP incorporation and thermal treatment. For the non-

thermally treated MMMs, the effect of POP on the permeability depends on the polymer matrix. That is, the addition of POP to the PI* matrix decreased permeability of the corresponding MMM by approximately 27% for all gases, while the addition of POP to the PI*20 matrix increased CH₄ and CO₂ permeability by 40% and 54%, respectively. Blending POP with PI*20EO1 also increased permeability, but such an increase was considerably lower, particularly for CH₄ and CO₂ gases, whose permeability enhanced by only 8% and 19%, respectively. Relative to the PI*POP membrane, the permeability coefficients of PI*20POP increased by 25-35%, while those of PI*20EO1POP remained essentially unchanged. Interestingly, gas permeability in PI*20POP was similar to that observed for PI*.

In the case of the thermally treated MMMs, the permeability of PI*20POP-TT exhibited a reduction of approximately 50-60% for all gases compared to PI*POP. On the other hand, the permeability of PI*20EO1POP-TT was considerably higher; for example, the permeability of He increased by 132%, while that of other gases increased by 160% when compared with PI*20EO1POP.

For the sake of comparison, the Robeson plot for CO₂/CH₄ is shown in Figure S3.11 in section S3.6, Appendix 3. PI*20EO1POP-TT exhibited the best separation performance in terms of permeability relative to the reference PI* and PI*POP membranes (by 40 and 50%, respectively). The CO₂/CH₄ ideal selectivity was similar for all three membranes (i.e., selectivity of 20). In addition, after thermal treatment, it was observed that the CO₂ permeability of PI20POP-TT was 72% lower than that of PI20EO1POP-TT. Isothermal TGA data (Figure 6.3), suggests that the presence of POP might facilitate the decarboxylation of DABA in PI*20POP during the thermal crosslinking treatment, which is consistent with a collapse of voids within the membrane. This effect ultimately caused the observed decrease in permeability. In addition, after thermal treatment, the gas permeability values of PI*20-TT and PI*20EO1-TT were higher than those of their precursor membranes (by 30% for CO₂ and around 25% for CH₄). We hypothesize that the highest gas permeability exhibited by PI*20EO1POP-TT might be ascribed to some type of interaction between PEO and the lactam ring within POP, although effects of the crosslinking and pyrolysis process are also expected to play a role. This hypothesis will be tested and discussed in section 6.2.6.

The diffusivity and solubility coefficients were estimated by the lag time method [197], and their values are listed in Tables S3.5 and S3.6 in section S3.6, Appendix 3. Figure 6.6

shows the bar diagrams of the permeability (up), diffusivity (middle), and solubility (bottom) coefficients of neat membranes and MMMs, before and after thermal treatment, for CO₂ and CH₄. After thermal treatment, the CO₂ and CH₄ diffusivities of PI*20EO1POP-TT were higher than those of PI*20EO1-TT and PI*20POP-TT (1.80-2.74 times for CO₂ and 1.73-3.00 times for CH₄, respectively). On the other hand, the CO₂ and CH₄ solubilities of PI*20EO1POP-TT increased less than the diffusivity coefficients (1.04-1.3 times for CO₂ and 1.2-1.6 times for CH₄). Therefore, the increase in permeability in PI*20EO1POP-TT, caused by the removal of PEO and the presence of POP, was essentially ascribed to an increase in the gas diffusion coefficient.

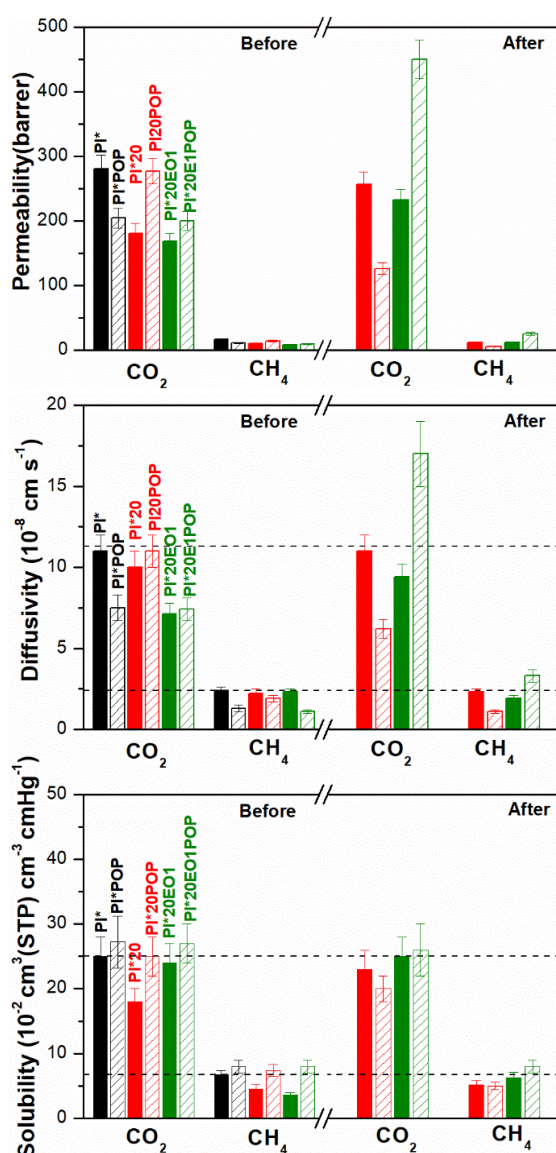


Figure 6.6. Permeability (up), diffusivity (middle) and solubility (bottom) coefficients of PI*, PI*20, PI*20EO1 and MMMs for CO₂ and CH₄ before and after the thermal treatment. Dashed lines are provided to guide the eye.

6.2.6 *Plasticization study*

CO₂ plasticization tests were run up to 30 atm and in the temperature range of 25–50 °C. The plasticization behavior of PI*20, PI*20POP, and their corresponding thermally treated membranes, PI*20-TT and PI*20POP-TT is shown in Figure 6.7. In both PI*20 and PI*20POP, the permeability at low pressures (i.e., <10 atm) decreased with increasing pressure, which is consistent with the typical dual-mode behavior of glassy polymers. However, at high pressures (i.e., >10 atm), an upturn was observed, which defines the plasticization onset. For instance, CO₂ permeability at 30 atm and 25 °C increased by 55% and 36% for PI*20 and PI*20POP, respectively, relative to their values at 1 atm. After conditioning both membranes at 30 atm for at least 6 h, hysteresis in permeability was observable in the second run, which is a consequence of the plasticization observed during the first run. Additionally, hysteresis decreased with increasing temperature, which is related to changes in the sorption behavior. It is well known, indeed, that gas sorption decreases with increasing temperature [198–200]. The plasticization propensity followed the same solubility trend. However, at the highest temperature measured (i.e., 50 °C), CO₂ permeability of PI*20 at 1 atm did not change significantly between runs, while PI*20POP at 1 atm experienced a 29% increase between runs.

In contrast, the thermally treated membranes, PI*20-TT and PI*20POP-TT, did not plasticize at any of the measured temperatures after conditioning, indicating that thermal cross-linking of the carboxyl groups of DABA was an effective method to suppress plasticization.

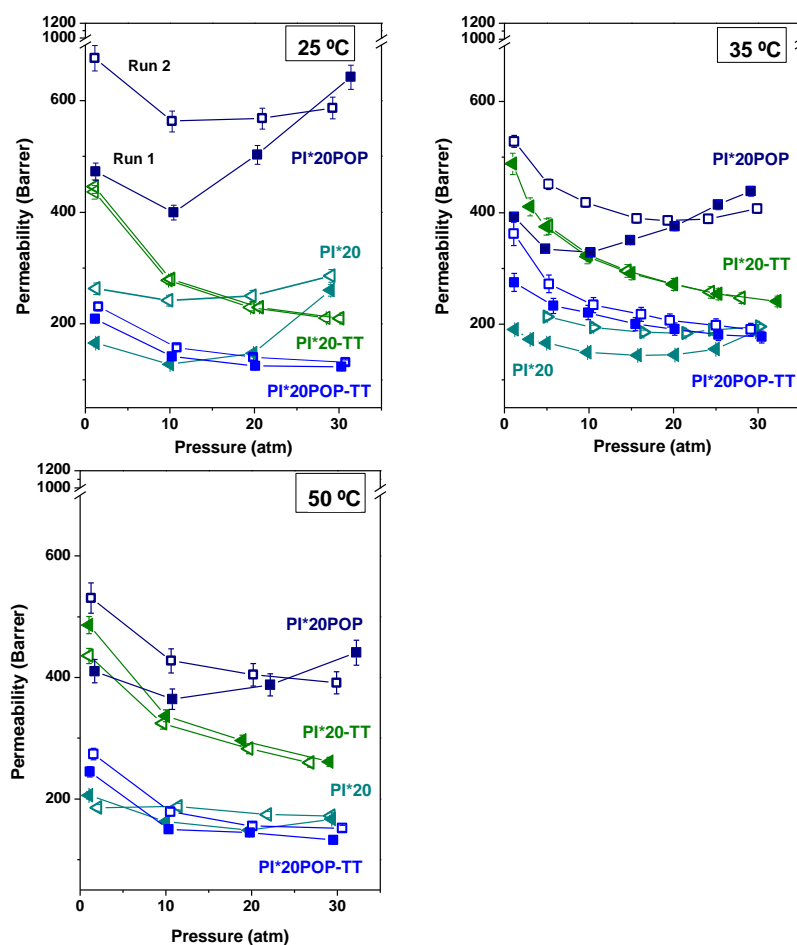


Figure 6.7. CO₂ plasticization curves at 25, 35, and 50 °C for PI*20 and PI*20POP before and after thermal treatment.

Figure 6.8 shows a similar plot for PI*20EO1 and PI*20EO1POP, both before and after thermal treatment. PI*20EO1 exhibited strong plasticization below 35 °C, and as a result, the full permeability isotherm was only measurable at 40 °C and 50 °C. The extent of plasticization for PI*20EO1 at 30 atm and 35 °C was relevant, as permeability in those conditions exceeded, by 127%, the value at 1 atm. Since it is possible that significant deviations exist due to a non-ideal behavior of CO₂, especially at higher pressures, it was decided to calculate and represent the permeability vs. fugacity instead of pressure [201–203]. However, as shown in Figure S3.12 in section S3.7, Appendix 3, using fugacity instead of pressure did not change the plasticization point, nor the overall shape and features of the permeation curve, and thus the use of pressure was retained.

At higher temperatures, PI*20EO1 experienced hysteresis, with an increase in permeability at 1 atm, between runs, of 14% and 8%, at 40 °C and 50 °C respectively. On

the other hand, after the thermal treatment, the permeability of PI*20EO1-TT at 30 atm was reduced by approximately 50% (at all measurement temperatures) relative to the permeability observed at 1 atm. In addition, no significant hysteresis was found over the measured pressure range.

The Arrhenius dependence of permeability on temperature was verified, as shown in Figure S3.13, section S3.8, Appendix 3. Upon thermal treatment, the activation energy of permeation at 1 atm for PI*20EO1 reduced from 55.2 ± 2.0 kJ/mol to 8.1 ± 0.5 kJ/mol in PI*20EO1TT, that is, by 86%. This decrease is most likely due to a decrease in the activation energy of diffusion, as was evidenced by an increase in the CO₂ diffusivity after the thermal treatment (cf. Figure 6.6). This behavior is consistent with the overall picture of the simultaneous partial pyrolysis/cross-linking process.

For PI*20EO1POP, the permeability at 30 atm was reduced below 40% relative to that at 1 atm, and no hysteresis was observed. After thermal treatment, the behavior of PI*20EO1POP-TT was similar to that of PI*20EO1-TT, except for the observed increase in permeability.

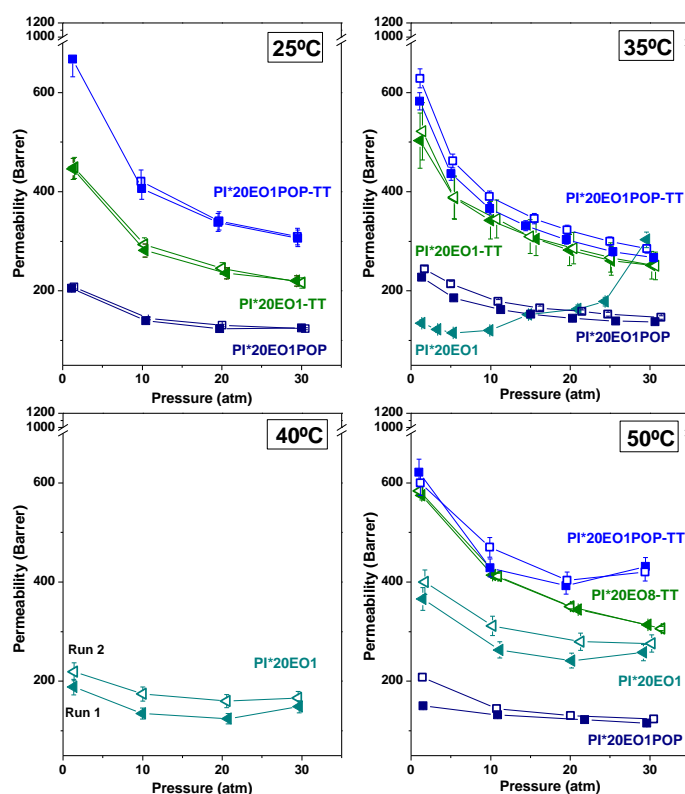


Figure 6.8. CO₂ plasticization pressure curves at 25, 35, 40, and 50 °C for PI*20EO1, PI*20EO1POP before and after thermal treatment.

An additional experiment was performed with PI*POP to compare its behavior with that of PI*20POP and PI*20EO1POP. The plasticization pressure curves of PI*POP, PI*20POP, and PI*20EO1POP, shown in Figure 6.9, indicate that the addition of POP to the PI* and PI*20 matrices did not avoid the matrix swelling. As a result, hysteresis was higher in PI*POP at 25 °C and 35 °C, where the increase in permeability at 1 atm after conditioning (i.e., during the second run) was about 135 % at both temperatures. For PI*20POP, this increase was 43% at 25 °C and 35% at 35 °C. Unexpectedly, a significant reduction in hysteresis exhibited by PI*POP was observed at 50 °C. After conditioning, it was observed that the increase in permeability of PI*POP at 1 atm was about 50% lower than that of PI*20POP. In contrast, PI*20EO1POP exhibited no hysteresis as commented above.

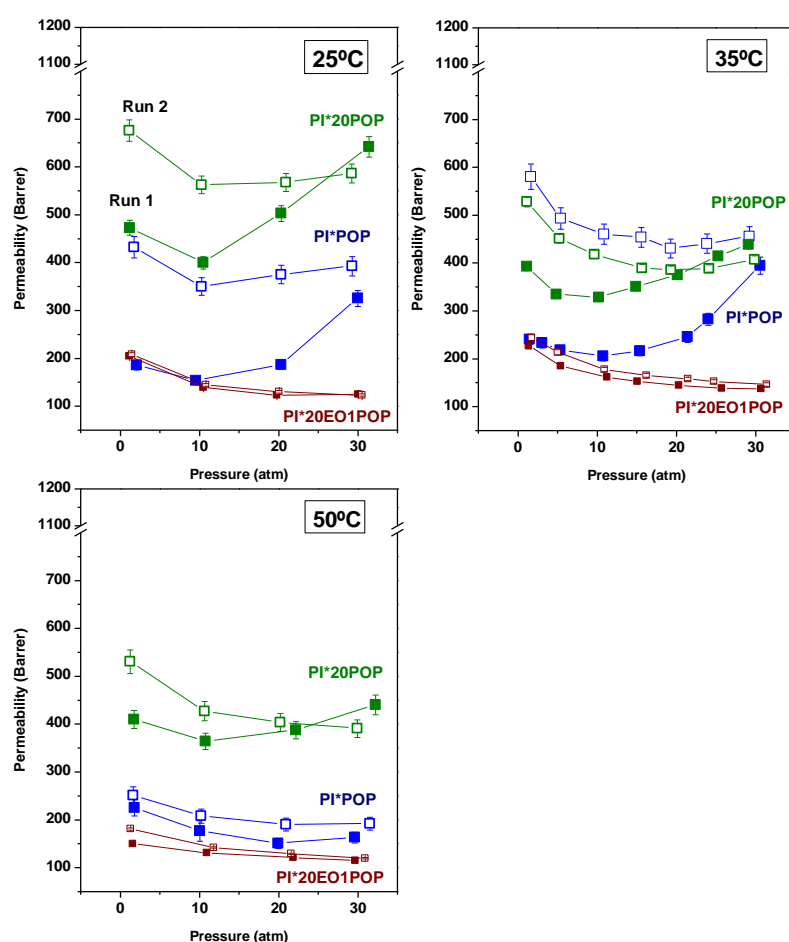


Figure 6.9. CO₂ plasticization curves at 25, 35, and 50 °C for PI*POP, PI*20POP, and PI*20EO1POP.

The difference in behavior between PI*20EO1 and PI*20EO1POP could be ascribed to a possible interaction between the POP and PEO segments. Thus, a quantum-mechanical study to determine the existence of an energy interaction between a POP model and a PEO model, based on density functional theory (DFT), was carried out. Details about the employed computational methods are summarized in section S3.9, Appendix 3. The electronic energy of the optimized geometries of the POP model and PEO model and the POP-PEO structure are listed in Table S3.7, section S3.9, Appendix 3. Figure 6.10 shows the optimized geometry of the corresponding POP model-PEO model adduct structure. The DFT simulation revealed a strong hydrogen bonding interaction (10 Kcal/mol) between the hydrogen of the lactam ring of the POP and the oxygens of the PEO chains. This interaction could modify the interface between the POP surface and the PI*PEO chains to some extent, causing changes in their rigidity and, ultimately, affecting the plasticization behavior.

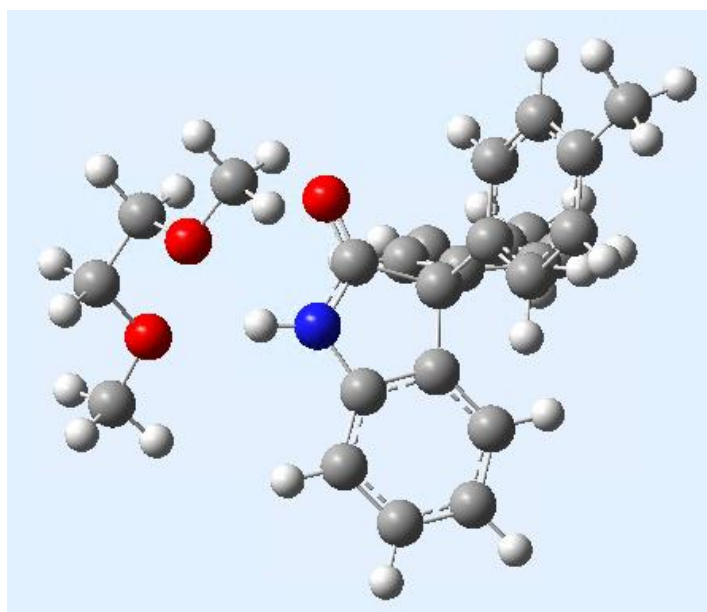


Figure 6.10. Molecular modeling of the interaction of a POP-model with a PEO-like structure model.

Chapter 7

7. Conclusions

The work described in this Ph.D. thesis memory aims to design, optimize, and develop polymeric materials, including linear polymers and microporous organic polymers (POPs), for preparing efficient gas separation membranes. In particular, this Ph.D. thesis focused on the obtaining of polymer membranes and mixed matrix membranes (MMMs) susceptible to thermally induced cross-linking. The design of both cross-linked membranes and MMMs searches materials with high fractional free volume (FFV) showing a good gas selectivity/gas permeability performance and, on other hand, having low physical aging and high plasticization resistance.

The main conclusions of this Ph.D. thesis are presented in three blocks that corresponds to chapters 4, 5 and 6.

Chapter 4 reports a new strategy to obtain cross-linked membranes, with improved gas separation performance, derived from copolyimides based on the 6FDA-6FpDA polyimide, which incorporate different molar percentages of PEO moieties (5%-20%) and DABA diamine (10% and 20%) (PIxEOy). The selective removal of the PEO segments from PIxEOy copolyimides under a controlled partial degradation process was successfully implemented and discussed. The incorporation of DABA in a molar percentage of 10% relative to 6FpDA diamine helped minimize the shrinkage of the membrane during the thermal removal of PEO. This effect was confirmed by observing a substantial improvement in O₂/N₂ and CO₂/CH₄ gas separations for the thermally treated membranes. In addition, the thermal cross-linking produced during the partial pyrolysis process greatly improved the plasticization resistance upon exposure to CO₂ up to 30 atm. Based on the results obtained, and with the aim of achieving more efficient membranes, PI10/PI10EOy(z/1) blends were prepared and their gas separation properties were compared with blends obtained from aromatic polyimides where the DABA comonomer was not included PI0/PI0EOy(z/1). The results showed that the presence of a small amount of DABA (molar percentage of 10% in both components of the blend) and PEO (less than 10 wt.% relative to the total weight of the blend) significantly improved the gas separation performance relative to that of PI0 after the selective removal of PEO. In particular, the PI10/PI10EO4 (z/1) blends showed a good permeability/selectivity balance and thus, this material could have significant potential for industrial application in CO₂/CH₄ separation.

Chapter 5 focused on the synthesis of a new class of porous polymer networks from different rigid and bulky aromatic buildings linked through cross-linkers that incorporate functional groups with affinity to CO₂ into the network structure. The idea was to use these porous materials as fillers that present good compatibility with specific polymer matrixes to increase, in CO₂ separations, the gas permeability without sacrificing the selectivity. On the other hand, the highly microporous nature of these materials led to the study of their potential application as adsorbents for selective separation of CO₂ from CO₂/N₂ and CO₂/CH₄ gas mixtures.

For this purpose, highly microporous POPs were prepared from tetra (SBF) and trifunctional (TPB, TMB, TBB, and TR) bulk aromatic rigid monomers that were combined (or not) with bifunctional aromatic monomers (named Ho-POPs or Co-POPs, respectively) using three different activated ketones (I, MI and TF) as cross-linkers. All of the POPs were successfully obtained in quantitative yield by using a cost-effective and feasible methodology.

The textural properties of POPs showed a strong dependence on the chemical structure. Thus, the specific surface area, S_{BET} , of Ho-POPs ranged from 577 to 1033 mmol g⁻¹, except for TMB-TF which was unexpectedly low (28 mg g⁻¹), while in most of the Co-POPs was very low (ranging from 0 to 101 mg g⁻¹), except for TR/BP-I and TPB/BP-I that showed values comparable to those of Ho-POPs. Despite the low S_{BET} values of some POPs, low-pressure CO₂ adsorption isotherm measurements at 0 °C revealed that these POPs were microporous materials. Thus, no clear relationship was found between S_{BET} and narrow micropore volume (V_{nmicro}), since some POPs with very different S_{BET} values presented similar V_{nmicro} .

From the data obtained from low-pressure CO₂ adsorption isotherms at 0 °C, the structure of POPs can be envisioned as macromolecular chain-packed materials, which form pores with different cavity sizes and entrance sizes ranging from 5 - 8 Å, except for Co-POPs containing DMHEA that have smaller cavities with entrance sizes between 4 - 5 Å, which was supported by their null N₂ adsorption at -196 °C.

For I and MI cross-linkers, the POPs formed from TR and TPB showed the best CO₂ uptakes (5.42 – 2.94 mmol g⁻¹ at 0 °C and 1 bar), while those from SBF showed lower uptakes (2.75 – 2.11 mmol g⁻¹ at 0 °C and 1 bar) due to presumably to a higher cross-linking of the macromolecular chains. POPs containing TF cross-linker showed the lowest CO₂ uptakes (2.12 – 0.89 mmol g⁻¹ at 0 °C and 1 bar). On the other hand, the

incorporation of BP and DMHEA into the networks yielded Co-POPs with good CO₂ uptakes (3.61 – 2.10 mmol g⁻¹ at 0 °C and 1 bar) compared to analog Ho-POPs.

TR-based POPs showed the best separation performance of CO₂ from binary mixtures of CO₂/N₂ (15/85) and CO₂/CH₄ (50/50) at 25 °C and 1 bar, comparable to other porous organic polymers reported in the bibliography. However, all Co-POPs showed lower CO₂ adsorption capacity, but comparable selectivities for each gas mixture tested. In addition, the separation of CO₂ over CH₄ improved at 10 bar, in contrast to CO₂ separation over N₂ where the selectivity decreased due to the gas saturation of the material. The good selectivities along with the excellent thermal stabilities and easy regeneration of these POPs (release of the gas under vacuum) made them potential candidates to use as molecular sieves in gas separation processes by using PSA technologies.

Finally, Chapter 6 reports two strategies to suppress CO₂ plasticization in high FFV polyimide membranes. The first one focused on the preparation of cross-linked membranes according to results obtained in Chapter 4. Thus, two 6FDA-TMPD-based copolyimides were prepared, one containing a DABA percentage of 20% by mol (PI*20) and another one having the same amount of DABA and a PEO percentage of 1% by mol (PI*20EO1). Using a, judiciously selected, thermal treatment, the selective removal of PEO was carried out. The presence of carboxyl groups coming from DABA moieties in the polymeric structure was essential to create efficient cross-links among the polymeric chains during the thermal treatment. This cross-linking process effectively locked the free volume created by the removal of PEO in the membrane (FFV increased by approximately 25 % relative to the reference membrane, 6FDA-TMPD or PI*), while suppressing plasticization.

However, the membranes did not show improved separation performance relative to the reference membrane. Therefore, a second strategy was proposed to prepare MMMs, by adding 20 % by weight of a triptycene-isatin POP, which was one of the microporous polymer networks obtained in Chapter 5, to the cross-linkable copolyimide matrices (PI*20POP and PI*20EO1POP). All membranes exhibited a homogeneous dispersion of the filler, excellent compatibility between matrix and filler, and good mechanical properties. The thermally treated MMMs, PI*20POP-TT and PI*20EO1POP-TT, exhibited an opposite behavior in gas permeability relative to precursor membranes. In particular, the PI*20EO1POP-TT membrane exhibited the best selectivity-permeability performance, with a permeability increase about 1.6 times higher for all the gases, without having a decrease of selectivity, relative to PI*. Besides, the thermal treatment

significantly improved the plasticization resistance of both neat membranes and MMMs upon exposure to CO₂ up to 30 atm, except for PI*20EO1POP, which did not show any plasticization process even before the thermal treatment, likely due to the presence of a hydrogen bonding interaction between the PEO segments and the POP lactam groups. Finally, it was also observed that the incorporation of POP decreased the membranes' physical aging tendency in the case of PI*20EO1POP.

As the conclusion of this Ph.D. thesis, the developed thermally cross-linking strategy was very effective in enhancing membranes' long-term stability and less effective in enhancing gas separation performance relative to reference membranes. However, when this strategy was applied to MMMs incorporating highly thermal stable POPs, a substantial improvement in gas permeability was observed, although it was less effective in enhancing selectivity. Research efforts are underway to address this shortcoming. One great advantage of the proposed approach is that it can be extended to other polymer materials, which is a key point in suppressing plasticization while simultaneously improving permeability and selectivity. Future work needs to investigate how defect-free thin-film composite membranes can be produced based on these materials, which is a necessary step for the extension of this approach to large-scale and industrial separation.

Conclusiones

El trabajo descrito en esta memoria de tesis doctoral tiene como objetivo el diseño, optimización y desarrollo de materiales poliméricos, incluyendo polímeros lineales y redes de polímeros orgánicos microporosos (POPs), dirigido a la preparación de membranas eficientes de separación de gases. En particular, esta tesis doctoral se ha centrado en la obtención de membranas poliméricas y membranas de matriz mixta (MMMs) susceptibles de sufrir entrecruzamiento inducido térmicamente. El diseño tanto de membranas entrecruzadas como de MMMs busca materiales con una alta fracción de volumen libre (FFV) que muestren un buen rendimiento en su balance selectividad/permeabilidad al gas y, por otro lado, que tengan un bajo envejecimiento físico y una alta resistencia a la plastificación.

Las principales conclusiones de esta tesis doctoral se presentan en tres bloques principales que corresponden a los capítulos 4, 5 y 6.

En el capítulo 4 se presenta una nueva estrategia para la obtención de membranas entrecruzadas, con mejores prestaciones en la separación de gases, derivadas de copolimidas (PIxEOy) basadas en la poliimida 6FDA-6FpDA, que incorporan diferentes porcentajes molares de segmentos de PEO (5%-20%) y DABA diamina (10% y 20%). Se implementó y discutió con éxito la eliminación selectiva de los segmentos PEO de las copolimidas PIxEOy mediante un proceso controlado de degradación parcial mediante temperatura. La incorporación de DABA en un porcentaje molar del 10% respecto a la 6FpDA diamina ayudó a minimizar la contracción de la membrana durante la eliminación térmica del PEO. Este efecto se confirmó al observar una mejora sustancial en las separaciones de gases O_2/N_2 y CO_2/CH_4 en las membranas tratadas térmicamente. Además, el entrecruzamiento térmico producido durante el proceso de pirólisis parcial mejoró considerablemente la resistencia a la plastificación tras la exposición a CO_2 hasta 30 atm.

A partir de los resultados obtenidos, y con el objetivo de conseguir membranas más eficientes, se prepararon mezclas de polímeros, PI10/PI10EOy(z/1), y se compararon sus propiedades de separación de gases con mezclas obtenidas a partir de poliimidas aromáticas y copoliimidas aromáticas-alifáticas, PI0/PI0EOy(z/1), en las que no se incluyó el comonomero DABA. Los resultados mostraron que la presencia de una pequeña cantidad de DABA (porcentaje molar del 10% en ambos componentes de la

mezcla) y PEO (menos del 10 % en peso en relación con el peso total de la mezcla) mejoraba significativamente el rendimiento de separación de gases en relación con la membrana de PI0 tras la eliminación selectiva de PEO. En particular, las mezclas PI10/PI10EO4 (z/1) mostraron un buen equilibrio permeabilidad/selectividad y, por tanto, este material podría tener un potencial significativo para su aplicación industrial en la separación CO₂/CH₄.

El capítulo 5 se centró en la síntesis de una nueva clase de redes poliméricas porosas a partir de diferentes construcciones aromáticas rígidas y voluminosas unidas mediante entrecruzantes que incorporan grupos funcionales con afinidad al CO₂ en la estructura de la red. La idea era utilizar estos materiales porosos como cargas que presentan buena compatibilidad con matrices poliméricas específicas para aumentar, en separaciones de CO₂, la permeabilidad al gas sin sacrificar la selectividad. Por otro lado, la naturaleza altamente microporosa de estos materiales condujo al estudio de su potencial aplicación como adsorbentes para la separación selectiva de CO₂ a partir de mezclas gaseosas CO₂/N₂ y CO₂/CH₄.

Para ello, se prepararon POPs altamente microporosos a partir de monómeros rígidos aromáticos tetra- (SBF) y trifuncionales (TPB, TMB, TBB y TR) que se combinaron (o no) con monómeros aromáticos bifuncionales (denominados Ho-POPs, cuando no se utilizó un monómero difuncional, o Co-POPs, cuando se empleó un monómero difuncional) utilizando tres cetonas activadas diferentes (I, MI y TF) como entrecruzantes. Todos los POPs se obtuvieron con rendimiento cuantitativo utilizando una metodología factible de bajo costo.

Las propiedades texturales de los POPs mostraron una fuerte dependencia de la estructura química. Así, la superficie específica, S_{BET} , de los Ho-POPs osciló entre 577 y 1033 mmol g⁻¹, excepto en el caso de TMB-TF que fue inesperadamente baja (28 mg g⁻¹), mientras que en la mayoría de los Co-POPs fue muy baja (osciló entre 0 y 101 mg g⁻¹), excepto para TR/BP-I y TPB/BP-I que mostraron valores comparables a los de los Ho-POPs. A pesar de los bajos valores de S_{BET} de algunos POPs, las medidas de isothermas de adsorción de CO₂ a baja presión a 0 °C revelaron que estos POPs eran materiales microporosos. Así, no se encontró una relación clara entre el S_{BET} y el volumen de microporos estrechos (V_{nmicro}), ya que algunos POPs con valores de S_{BET} muy diferentes presentaban V_{nmicro} similares.

A partir de los datos obtenidos de las isotermas de adsorción de CO₂ a baja presión, a 0 °C, la estructura de los POPs puede visualizarse como materiales con cadenas macromoleculares empaquetadas, que forman poros con diferentes tamaños de cavidad y tamaños de entrada que oscilan entre 5 - 8 Å, excepto para los Co-POPs que contienen DMHEA que tienen cavidades más pequeñas con tamaños de entrada entre 4 - 5 Å, lo que se apoyó en la nula adsorción de N₂ a -196 °C.

Para los entrecruzantes I y MI, los POPs formados a partir de TR y TPB mostraron las mejores absorciones de CO₂ (5,42 - 2,94 mmol g⁻¹ a 0 °C y 1 bar), mientras que los de SBF mostraron menores adsorciones (2,75 - 2,11 mmol g⁻¹ a 0 °C y 1bar) debido presumiblemente a un mayor entrecruzamiento de las cadenas macromoleculares. Los POPs que contienen el entrecruzante TF mostraron las menores adsorciones de CO₂ (2,12 - 0,89 mmol g⁻¹ a 0 °C y 1 bar). Por otro lado, la incorporación de BP y DMHEA en las redes produjo Co-POPs con buenas adsorciones de CO₂ (3,61 - 2,10 mmol g⁻¹ a 0 °C y 1 bar) en comparación con los Ho-POPs análogos.

Los POPs basados en TR mostraron el mejor rendimiento de separación de CO₂ a partir de mezclas binarias de CO₂/N₂ (15/85) y CO₂/CH₄ (50/50) a 25 °C y 1 bar, comparable a otros polímeros orgánicos porosos reportados en la bibliografía. Sin embargo, todos los Co-POPs mostraron una menor capacidad de adsorción de CO₂, pero buenas selectividades, comparables a las mejores selectividades observadas para materiales en la bibliografía, para cada mezcla de gases ensayada. Además, la separación de CO₂ sobre CH₄ mejoró a la presión de 10 bar, en contraste con la separación de CO₂ sobre N₂ donde la selectividad disminuyó al aumentar la presión debido a la saturación de gas en el material. Las buenas selectividades junto con las excelentes estabilidades térmicas y la fácil regeneración de estos POPs (liberación del gas adsorbido empleando vacío sin temperatura) los convirtieron en candidatos potenciales para su uso como tamices moleculares en procesos de separación de gases mediante el uso de tecnologías PSA.

Por último, el capítulo 6 presenta dos estrategias para suprimir la plastificación por CO₂ en membranas de poliimida de alta FFV. La primera se centró en la preparación de membranas entrecruzadas según los resultados obtenidos en el Capítulo 4. Así, se prepararon dos copoliimidias basadas en 6FDA-TMPD, una con un porcentaje de DABA del 20% por mol (PI*20) y otra con la misma cantidad de DABA y un porcentaje de PEO del 1% por mol (PI*20EO1). La eliminación selectiva del PEO se llevó a cabo mediante un tratamiento térmico seleccionado con buen criterio. La presencia de grupos carboxilo

procedentes de las moléculas de DABA en la estructura polimérica fue esencial para crear enlaces entrecruzados eficaces entre las cadenas poliméricas durante el tratamiento térmico. Este proceso de entrecruzamiento bloqueó eficazmente el volumen libre creado por la eliminación del PEO en la membrana (la FFV aumentó aproximadamente un 25 % con respecto a la membrana de referencia, 6FDA-TMPD o PI*), al tiempo que suprimió la plastificación.

Sin embargo, las membranas no mostraron un rendimiento de separación mejorado en relación con la membrana de referencia. Por lo tanto, se propuso una estrategia para preparar membranas de matriz mixta, MMMs, añadiendo un 20 % en peso de un POP de triptíceno-isatina, que era una de las redes poliméricas microporosas obtenidas en el capítulo 5, a las matrices de copoliimida entrecruzada (PI*20POP y PI*20EO1POP). Todas las membranas presentaron una dispersión homogénea del relleno, una excelente compatibilidad entre la matriz y el relleno, y buenas propiedades mecánicas. Las MMMs tratadas térmicamente, PI*20POP-TT y PI*20EO1POP-TT, mostraron un comportamiento opuesto en cuanto a permeabilidad al gas en relación con las membranas precursoras. En particular, la membrana PI*20EO1POP-TT mostró el mejor rendimiento de selectividad-permeabilidad, con un aumento de la permeabilidad de aproximadamente 1,6 veces para todos los gases, sin tener una disminución de la selectividad, en relación con PI*. Además, el tratamiento térmico mejoró significativamente la resistencia a la plastificación tanto de las membranas puras como de las MMMs tras la exposición a CO₂ hasta 30 atm, excepto en el caso de PI*20EO1POP, que no mostró ningún proceso de plastificación incluso antes del tratamiento térmico, probablemente debido a la presencia de una interacción de enlace de hidrógeno entre los segmentos PEO y los grupos lactama del POP. Por último, también se observó que la incorporación de POP disminuía la tendencia al envejecimiento físico de las membranas en el caso de PI*20EO1POP.

Como conclusión de esta tesis doctoral, la estrategia de entrecruzamiento térmico desarrollada fue muy eficaz para mejorar la estabilidad a largo plazo de las membranas y menos eficaz para mejorar el rendimiento de separación de gases en relación con las membranas de referencia. Sin embargo, cuando esta estrategia se aplicó a MMMs, que incorporaban POP de alta estabilidad térmica, se observó una mejora sustancial de la permeabilidad a los gases, aunque la mejora de la selectividad no fue alta. Se están llevando a cabo investigaciones para subsanar esta deficiencia. Una gran ventaja del enfoque propuesto es que puede extenderse a otros materiales poliméricos, lo que

constituye un punto clave para suprimir la plastificación y mejorar simultáneamente la permeabilidad y la selectividad. En el futuro habrá que investigar cómo se pueden fabricar membranas compuestas de película fina sin defectos a partir de estos materiales, lo que constituiría un paso necesario para extender este enfoque a procesos de separación industrial y a gran escala.

Appendix 1

INDEX

Section 1.1. Synthesis and characterization of PEO-containing copolyimides (PI-PEOs)

Section 1.2. Gas transport properties of PI_x and PI_xEO_y copolyimides

Section 1.3. Characterization of PI_x/PI_xEO_y(z/1) polymer blends

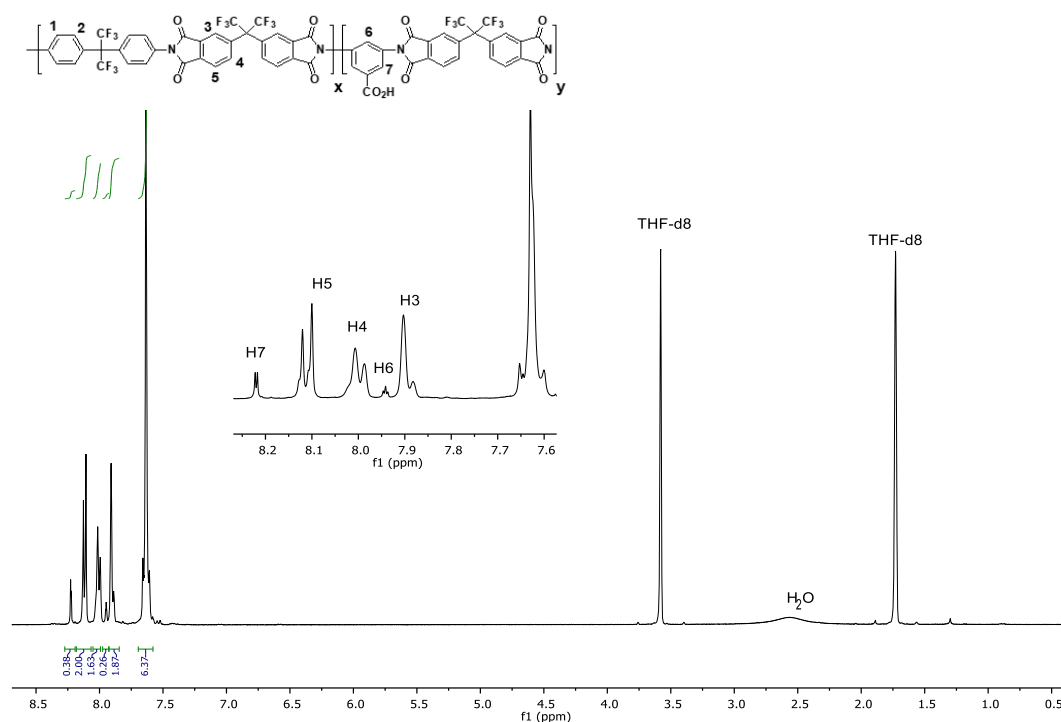
Section 1.4. Gas transport properties of PI₁₀/PI₁₀EO_y(z/1) polymer blends

Section 1.1. Synthesis and characterization of PEO-containing copolyimides

Table S1.1. Solubility^a of copolyimides

Polymers	Solvents					
	CHCl ₃	DMF	THF	DMAc	NMP	DMF
PI	++	++	++	++	++	++
PI10	++	++	++	++	++	++
PI20	++	++	++	++	++	++
PI10EO(1/1)	+-	++	++	++	++	++
PI10EO(1/2)	+-	++	++	++	++	++
PI10EO(1/4)	+-	++	++	++	++	++
PI20EO(1/1)	+-	++	++	++	++	++
PI20EO(1/2)	+-	++	++	++	++	++
PI20EO(1/4)	+-	++	++	++	++	++

^a Solubility test was performed by adding 1 o 2 mg of copolyimide to 1 mL of solvent, followed by stirring at room temperature for 24 h. When the sample was insoluble at that temperature, it was heated near the boiling point of the solvent until its complete dissolution and, then, the solution was allowed to cool to room temperature to see if the sample precipitated.

Figure S1.1. ¹H NMR spectrum of PI20 (y/x=0.2) in THF-d₈

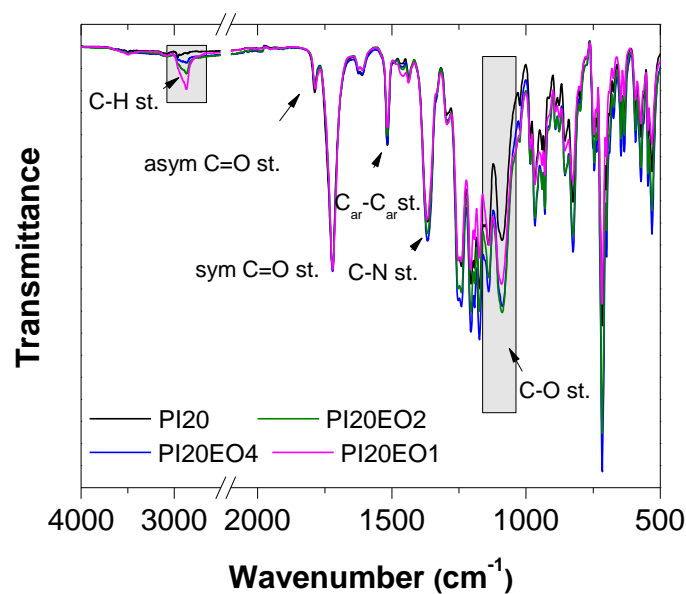


Figure S1.2. ATR-FTIR spectra of PI20 and PI20EO_y copolyimides. The FTIR spectra were normalized to the band at 1720 cm⁻¹ (sym C=O st.).

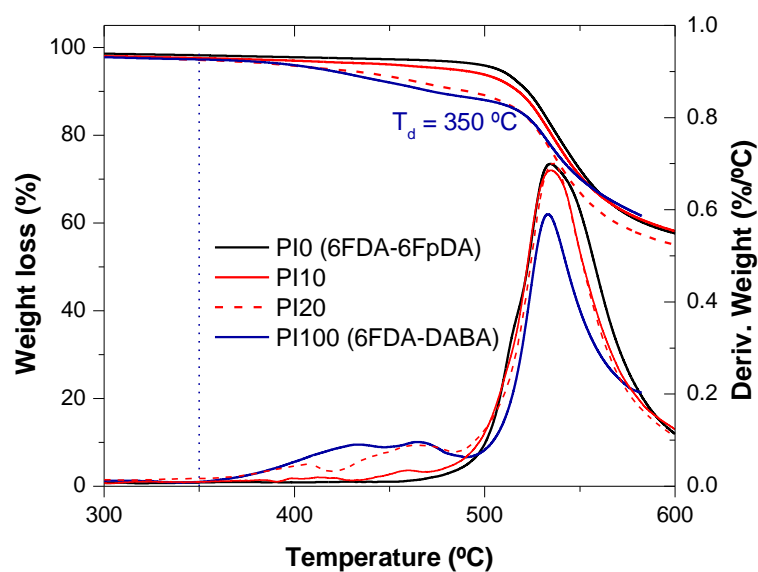


Figure S1.3 Hi-Res TGA scans of 6FDA-6FpDA (PI0) and 6FDA-DABA (PI100) polyimides in a nitrogen atmosphere (60 mL/min). Hi-Res parameters: 20 °C/min, sensitivity 1 and resolution 4. The value indicated corresponds to the onset degradation temperature.

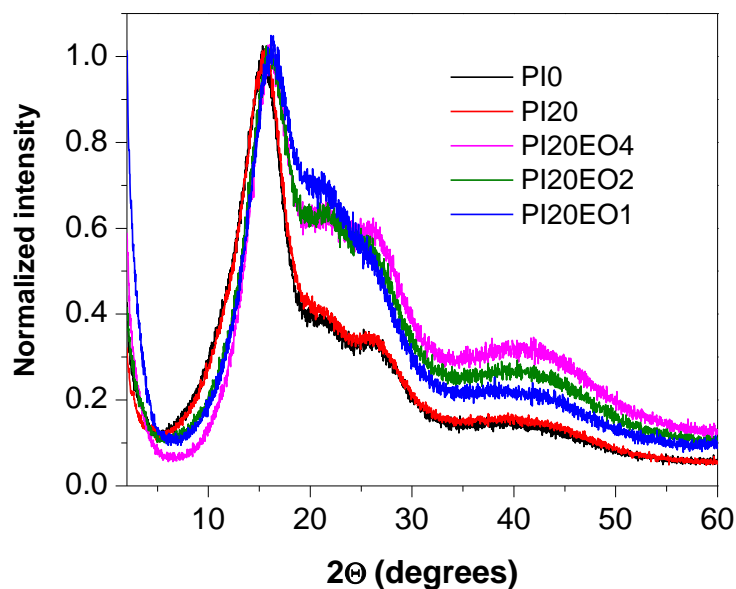


Figure S1.4. WAXS patterns of PI0, PI20, and PI20EOy. For comparative purposes, the patterns were normalized to the intensity of the large scattering peak around 15.5° (2θ).

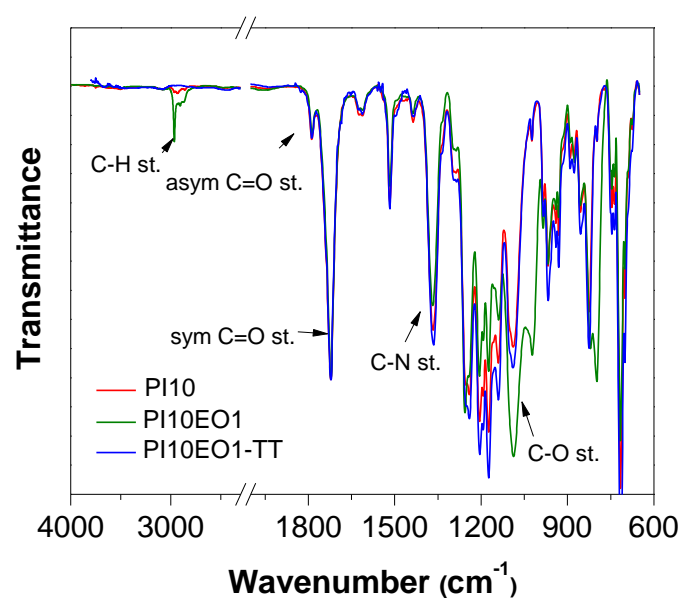


Figure S1.5. ATR-FTIR spectra of PI10, PI10EO1, and PI10EO1-TT. The spectra were normalized to the band at 1720 cm⁻¹ (sym C=O st.).

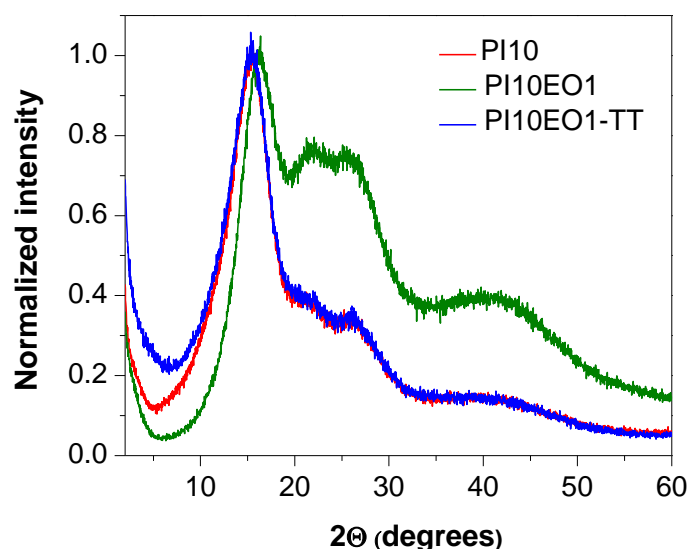


Figure S1.6. WAXS patterns of PI0, PI10EO1, and PI10EO1-TT. For comparative purposes, the patterns were normalized to the intensity of the large scattering peak around 15.5° (2 θ).

Table S1.2. Mechanical properties of the membranes before (PIxEOy) and after thermal treatment (PIxEOy-TT)^{a,b}.

Membranes	Young's Modulus (GPa)	Tensile Strength (MPa)	Elongation at break (%)
PI0	1.8±0.2	88±3	12±3
PI10EO4	1.9±0.2	90±4	11±2
PI10EO4-TT	1.4±0.1	93±5	13±3
PI10EO2	2.0±0.1	85±6	7±1
PI10EO2-TT	1.6±0.2	100±9	11±1
PI10EO1	1.6±0.3	71±11	7±2
PI20EO4	1.9±0.2	102±2	7±1
PI20EO4-TT	1.4±0.2	70±14	6.8±0.4
PI20EO2	1.7±0.2	90±10	10±3
PI20EO1	1.0±0.1	65±6	5.3±0.5

^a PI10EO1-TT, PI20EO2-TT, and PI20EO1-TT could not be accurately measured due to their poor mechanical properties. ^b The standard deviation in the Young's modulus, tensile strength, and deformation at break were calculated by measuring, at least, five samples.

Section 1.2. Gas transport properties of PIx and PIxEOy copolyimides

Table S1.3. Permeability coefficients of copolyimides, before and after (TT) thermal treatment, at 35 °C and 3 bar

Membrane	Permeability (barrer) ^a					Ideal selectivity	
	He	O ₂	N ₂	CH ₄	CO ₂	O ₂ /N ₂	CO ₂ /CH ₄
PI0	125±2	14.3±0.3	2.97±0.07	1.42±0.04	63±2	4.8±0.2	44±1
PI10	80±4	7.8±0.3	1.61±0.05	0.82±0.03	31±1	4.8±0.2	38±2
PI10-TT	91±3	11.1±0.4	2.5±0.1	1.26±0.05	46±2	4.4±0.2	37±2
PI20	62±2	5.8±0.2	1.19±0.04	0.60±0.02	25±1	4.9±0.2	42±2
PI20-TT	160±6	19±1	3.97±0.2	1.73±0.08	80±3	4.8±0.3	46±3
PI10EO4	48±2	4.6±0.2	0.88±0.04	0.59±0.03	21±1	5.2±0.3	36±3
PI10EO4-TT	215±8	23.1±0.8	4.8±0.2	2.3±0.1	95±4	4.8±0.3	41±2
PI10EO2	23±1	1.47±0.05	0.32±0.01	0.240±0.008	8.5±0.3	4.6±0.2	35±2
PI10EO2-TT	184±6	19.0±0.6	3.9±0.1	1.75±0.06	78±3	4.9±0.2	45±2
PI10EO1	10.4±0	1.13±0.04	0.27±0.01	0.23±0.01	8.9±0.4	4.2±0.2	39±3
PI10EO1-TT	116±5	12.2±0.5	2.5±0.1	1.07±0.04	51±2	4.9±0.3	48±3
PI20EO4	41±2	3.5±0.1	0.71±0.03	0.45±0.02	18.2±0.8	4.9±0.3	40±2
PI20EO4-TT	97±3	8.9±0.3	1.73±0.06	0.83±0.03	39±1	5.1±0.2	47±2
PI20EO2	14.3±0	1.15±0.05	0.26±0.01	0.187±0.008	6.1±0.3	4.4±0.3	33±2
PI20EO1	6.5±0	0.38±0.02	0.079±0.005	0.080±0.006	3.0±0.2	4.8±0.4	38±4

^a 1Barrer= 10⁻¹⁰ (cm³(STP) cm cm⁻² s⁻¹ cmHg⁻¹)

Section 1.3. Characterization of PIx/PIxEOy(z/1) polymer blends

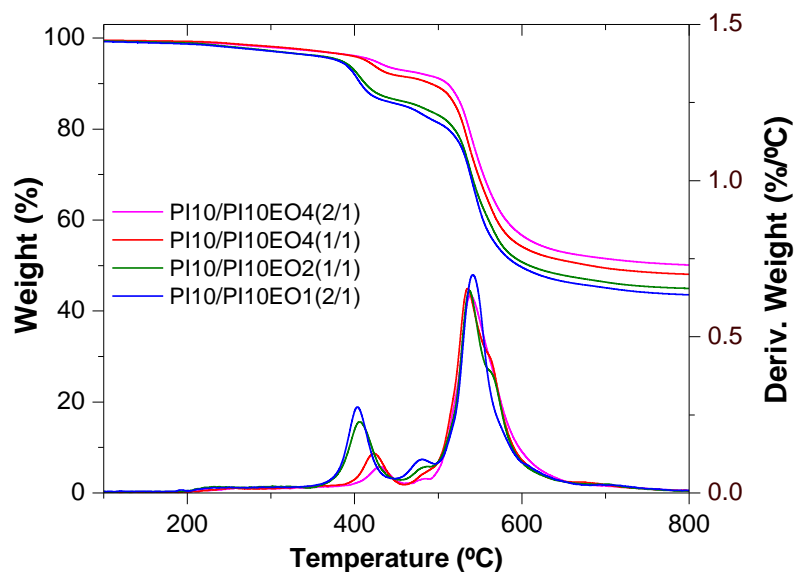


Figure S1.7 Hi-Res TGA scans of PI10/PI10EOy(z/1) blends in a nitrogen atmosphere (60 mL/min). Hi-Res parameters: 20 °C/min, sensitivity 1 and resolution 4.

Table S1.4. Weight loss of PEO and gel fraction of PI10/PI10EOy(z/1)-TT

Sample PI10/PI10EOy(z/1)-TT ^a	PEO weight loss ^b (wt.%)	Gel fraction (%)
PI10/PI10EO4(2/1)-TT	3.40 (3.22)	92
PI10/PI10EO4(1/1)-TT	5.06 (4.83)	95
PI10/PI10EO2(1/1)-TT	9.54 (8.60)	96
PI10/PI10EO1(2/1)-TT	10.5 (9.50)	98

^a (z/1) is the weight ratio between PI10 and PI10EOy; ^b experimental weight loss of PEO (%) after thermal treatment by TGA.

Section 1.4. Gas transport properties of PI10/PI10EOy(z/1) polymer blends

Table S.1.5. *Permeability coefficients of blends (PIx/PIxEOy(1/z)), before and after (TT) thermal treatment, at 30 °C and 3 bar*

Membrane	Permeability (barrer) ^a					Ideal selectivity	
	He	O ₂	N ₂	CH ₄	CO ₂	O ₂ /N ₂	CO ₂ /CH ₄
PI10/PI10EO4(2/1)	58±2	5.4±0.2	1.11±0.04	0.54±0.02	25±1	4.9±0.3	46±3
PI10/PI10EO4(2/1)-TT	124±4	14.4±0.5	3.0±0.1	1.34±0.05	63±2	4.8±0.2	47±2
PI10/PI10EO4(1/1)	79±3	6.5±0.2	1.29±0.05	0.70±0.03	31±1	5.0±0.2	44±2
PI10/PI10EO4(1/1)-TT	200±7	21.6±0.7	4.4±0.2	1.99±0.07	88±3	4.9±0.3	44±2
PI10/PI10EO2(1/1)	41±2	3.6±0.2	0.74±0.04	0.48±0.06	15.9±0.7	4.9±0.4	33±4
PI10/PI10EO2(1/1)-TT	133±5	13.3±0.5	2.8±0.1	1.16±0.05	57±2	4.8±0.3	49±3
PI10/PI10EO1(2/1)	51±2	4.4±0.2	0.92±0.03	0.58±0.02	26±1	4.8±0.3	45±2
PI10/PI10EO1(2/1)-TT	190±7	18.5±0.7	4.7±0.2	1.65±0.06	79±3	3.9±0.2	48±3

^a 1Barrer= 10^{-10} (cm³(STP) cm cm⁻² s⁻¹ cmHg⁻¹)

Appendix 2

INDEX

S2.1. Synthesis and spectroscopic characterization of monomers

S2.1.1. *Spectroscopic characterization of 9,9'-spirobifluorene (SBF).*

S2.1.2. *Spectroscopic characterization of 9,10-dimethyl-9,10-dihydro-9,10-ethanoanthracene (DMHEA).*

S2.1.3. *Spectroscopic characterization of 1,3,5-tri-(2-methylphenyl)benzene (TMB).*

S2.1.4. *Spectroscopic characterization of 1,3,5-tri-(biphenyl)benzene (TBB).*

S2.1.5. *Spectroscopic characterization of 1-methylindoline-2,3-dione (MeIs).*

S2.2. Crystal data and refinement structure for 9,10-Dimethyl-9,10-dihydro-9,10-ethanoanthracene.

S2.3. Molecular modeling of 9,10-Dimethyl-9,10-dihydro-9,10-ethanoanthracene.

S2.4. Synthesis optimization of porous organic polymers.

S2.4.1. *Low-pressure N₂ adsorption/desorption isotherms of POPs.*

S2.4.2. *Porosity parameters of POPs.*

S2.5. Acronyms of POPs

S2.6. Characterization of POPs

S2.6.1 *Wide-angle X-ray scattering (WAXS)*

S2.7. Thermal Properties of POPs

S2.8. Textural properties of POPs

S2.9. *High-pressure CO₂, CH₄, and N₂ uptakes*

S2.1. Spectroscopy characterization of monomers

S2.1.1. 9,9'-spirobifluorene (SBF)

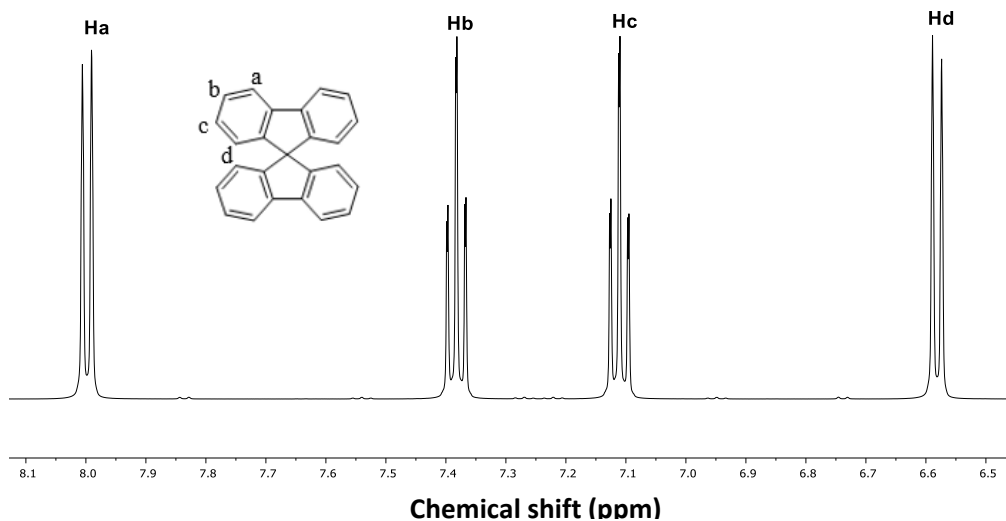


Figure S2.1. ^1H -NMR spectrum (500.13 MHz, DMSO-d_6) of 9,9'-spirobifluorene. $\delta_{\text{H}}(\text{ppm})$: 8.00 (dd, $J = 7.6$ Hz, $J = 1.1$ Hz, 4H); 7.38 (ddd, $J = 7.5$ Hz, $J = 7.5$ Hz and $J = 1.1$ Hz, 4H); 7.11 (ddd, $J = 7.5$ Hz, $J = 7.5$ Hz and $J = 1.1$ Hz, 4H); 6.58 (dd, $J = 7.6$ Hz and $J = 1.1$ Hz, 4H).

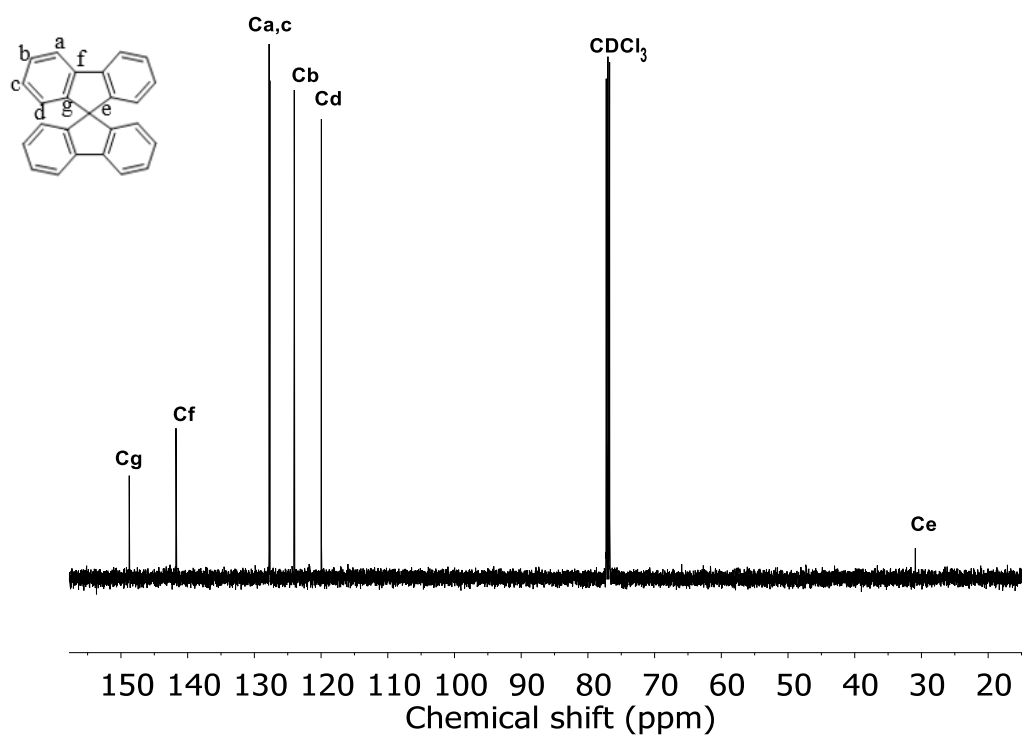


Figure S2.2. ^{13}C -NMR spectrum (125.78 MHz, CDCl_3) of 9,9'-spirobifluorene; $\delta_{\text{C}}(\text{ppm})$: 148.8, 141.8, 127.8, 127.7, 124.0, 119.9, 31.06

S2.1.2. Synthesis of 9,10-Dimethyl-9,10-dihydro-9,10-ethanoanthracene monomer (DMHEA)

S2.1.2.1 Synthesis of 2,5-diphenylhexane-2,5-diol

The ^1H -NMR spectrum evidenced the presence of two diastereoisomers: diastereoisomer I (meso compound) and diastereoisomer II (enantiomers pair), in an approximate ratio of 1:1. Each diastereoisomer showed a singlet for methyl protons (H_f , at 1.47 and 1.52 ppm), and for hydroxyl protons (H_g , at 2.36 and 2.52 ppm), and an AA'BB' spin systems for ethylene protons (H_h), centered at 1.80 ppm.

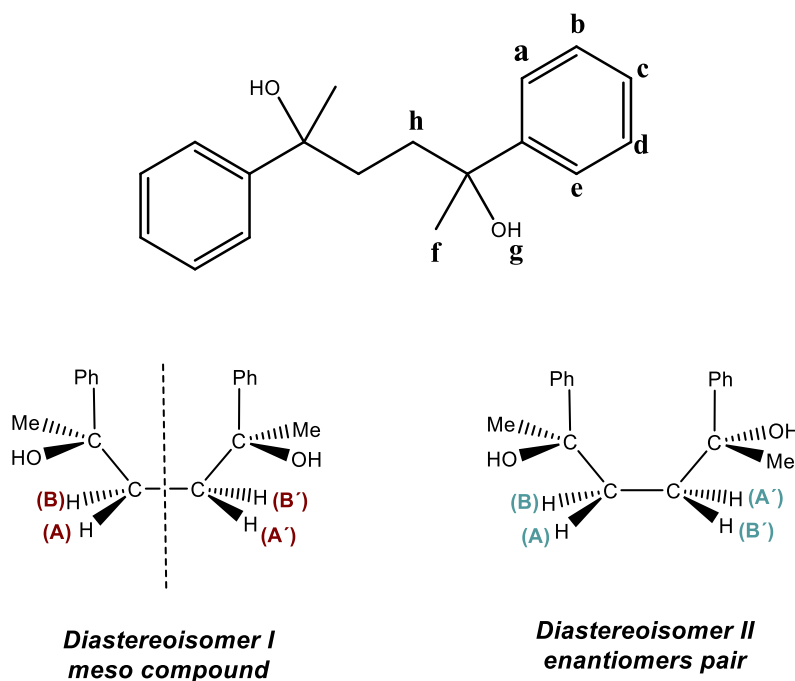


Figure S2.3. Scheme of diastereoisomers of 2,5-diphenylhexane-2,5-diol

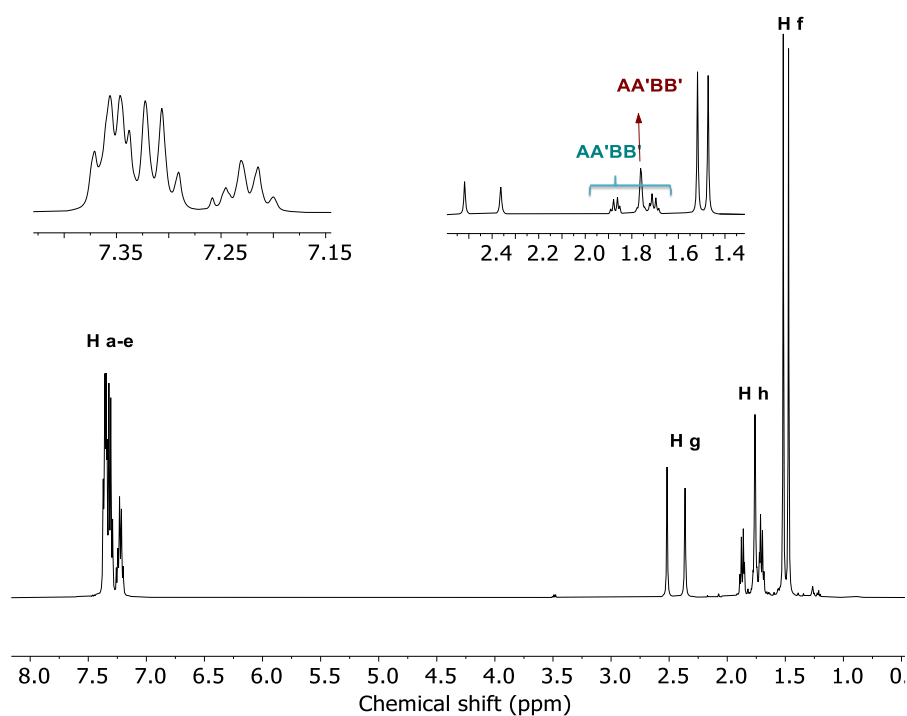


Figure S2.4. ^1H -NMR spectrum (500.13 MHz, CDCl_3) of 2,5-diphenylhexane-2,5-diol. $\delta_{\text{H}}(\text{ppm})$: 7.39 – 7.19 (m, 10H), 2.52 (s broad, 2H), 2.36 (s broad, 2H), 1.90-1.84 (m, 2H), 1.79-1.73 (m, 4H), 1.73-1.67 (m, 2H), 1.52 (s, 6H), 1.47 (s, 6H).

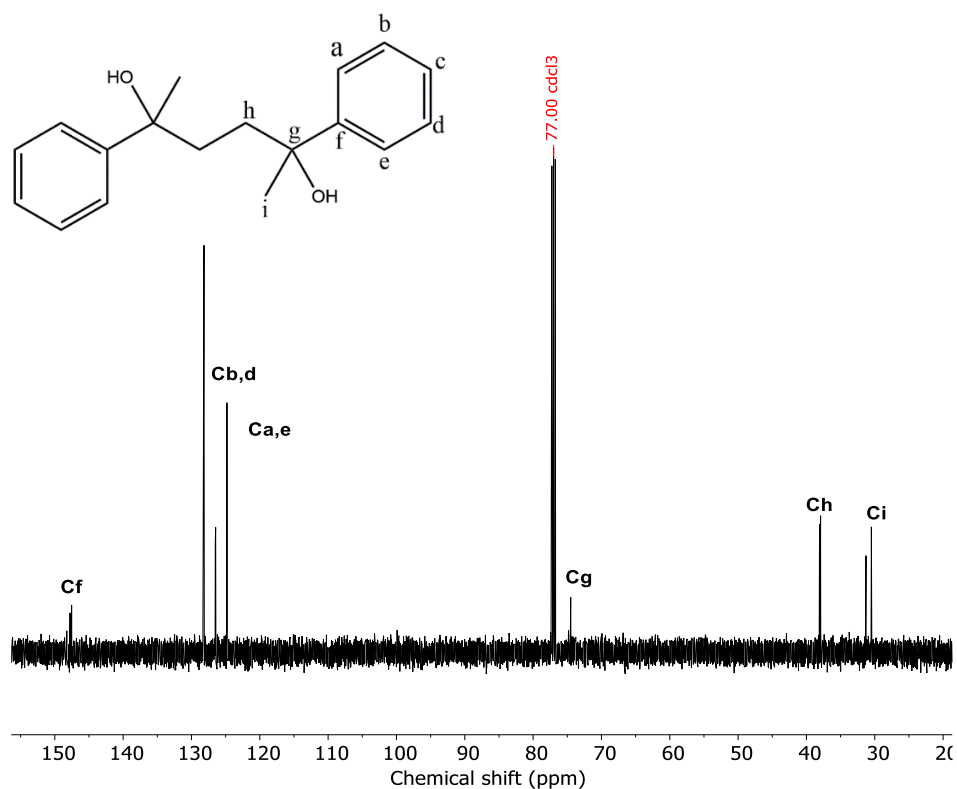


Figure S2.5. ^{13}C -NMR (125.78 MHz, CDCl_3) of 2,5-diphenylhexane-2,5-diol: $\delta_{\text{C}}(\text{ppm})$ = 147.7, 128.2, 126.5, 126.4, 124.8, 124.7, 74.5, 74.4, 38.1, 37.9, 31.3, 30.9.

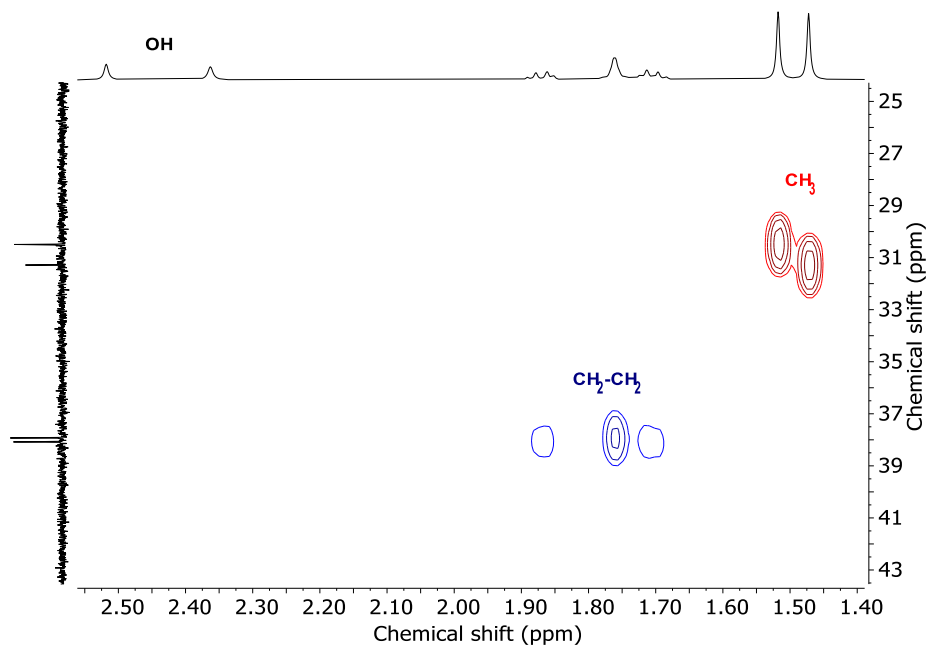


Figure S2.6. Aliphatic C-H bonds in the ^1H - ^{13}C -HSQC spectrum of 2,5-diphenylhexane-2,5-diol.

S2.1.2.2 Synthesis 9,10-dimethyl-9,10-dihydro-9,10-ethanoanthracene

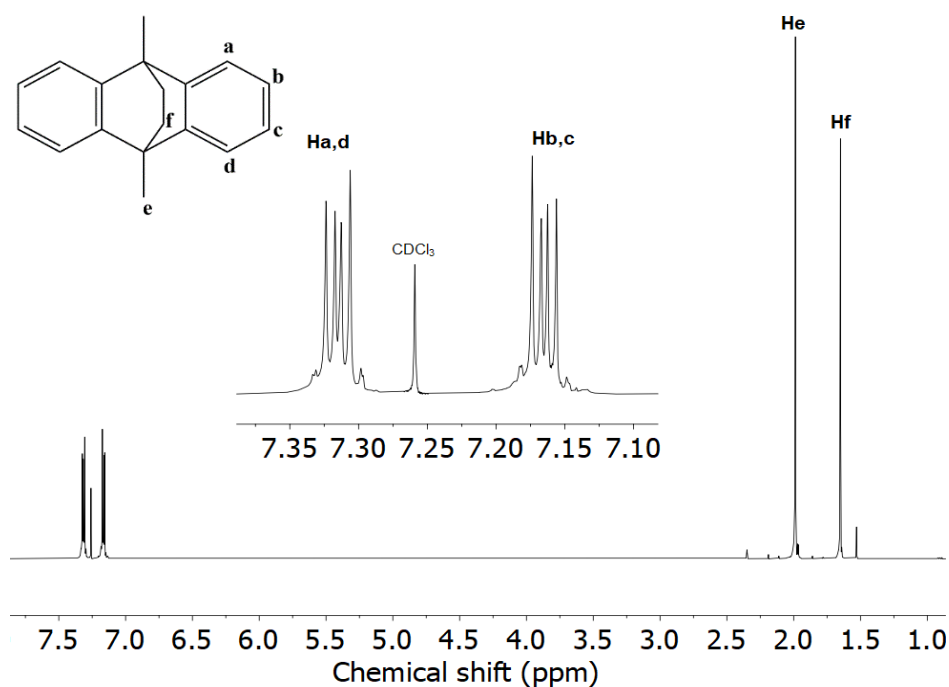


Figure S2.7. ^1H -NMR spectrum (500.13 MHz, CDCl_3) of 9,10-dimethyl-9,10-dihydro-9,10-ethanoanthracene. δ_{H} (ppm): 7.35-7.29 (m, 4H), 7.19- 7.14 (m, 4H) 1.99 (s, 6H), 1.65 (s, 4H)

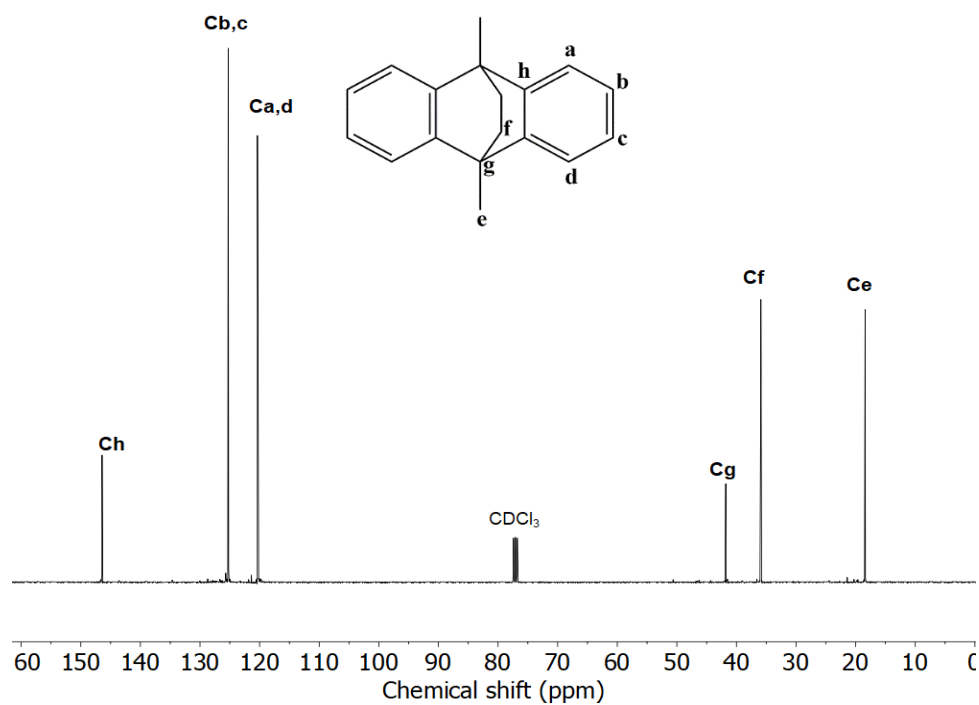


Figure S2.8. ^{13}C -NMR spectrum (125.78 MHz, CDCl_3) of 9,10-dimethyl-9,10-dihydro-9,10-ethanoanthracene. $\delta_{\text{c}}(\text{ppm}) = 146.4, 125.2, 120.3, 41.8, 35.7, 18.4$.

S2.1.3. 1,3,5-tri-(2-methylphenyl)benzene (135TMB)

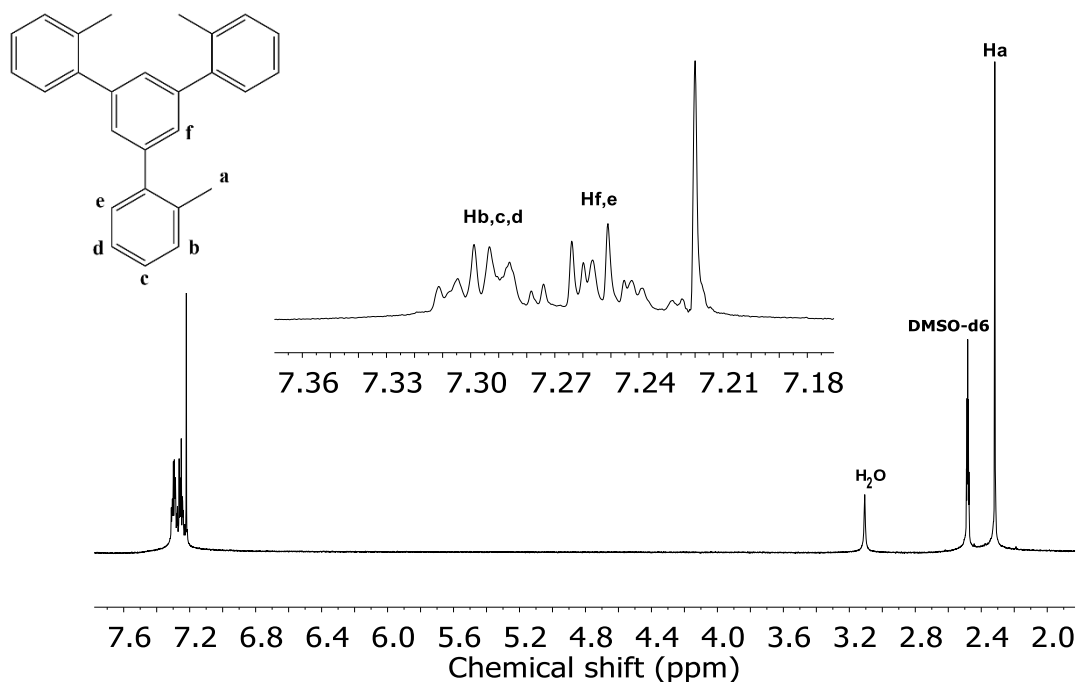


Figure S2.9. ^1H -NMR spectrum (500.13 MHz, DMSO-d_6) of 1,3,5-tri-(methyl phenyl)benzene. $\delta_{\text{H}}(\text{ppm})$: 7.30-7.25 (m, 2H), 7.25-7.22 (m, 2H), 2.30 (s, 3H)

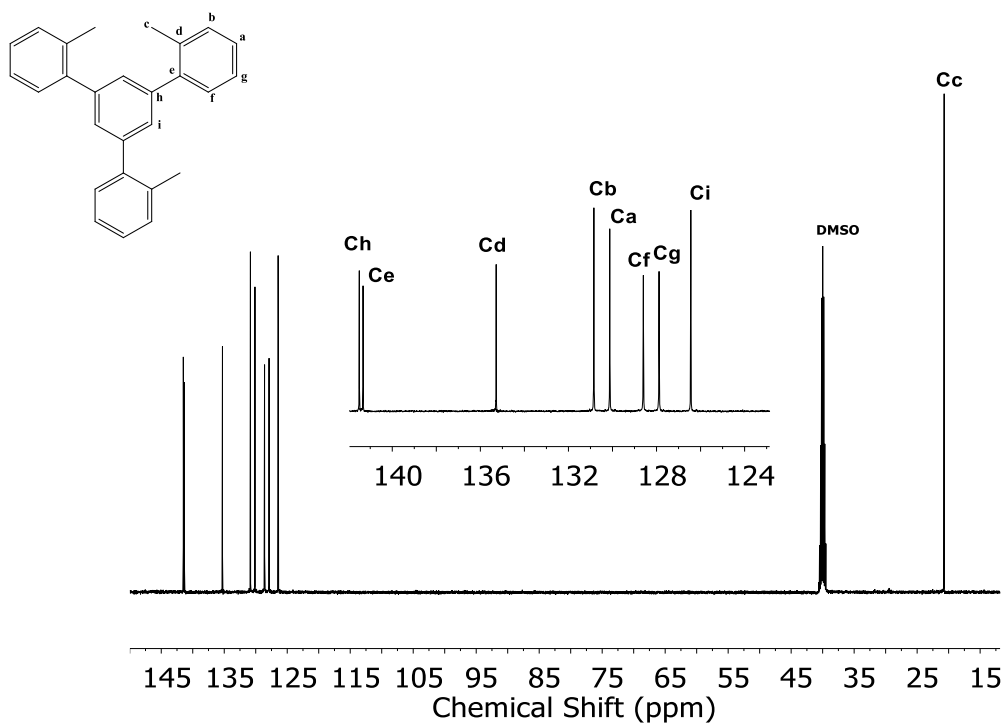


Figure S2.10. ^{13}C -NMR spectrum (125.78 MHz, CDCl_3) of 1,3,5-tri-(methylphenyl)benzene. $\delta_{\text{C}}(\text{ppm})$: 141.50, 141.33, 135.28, 130.84, 130.12, 128.60, 127.88, 126.44, 20.71.

S2.1.4. 1,3,5-tri-(4-biphenyl)benzene (TBB)

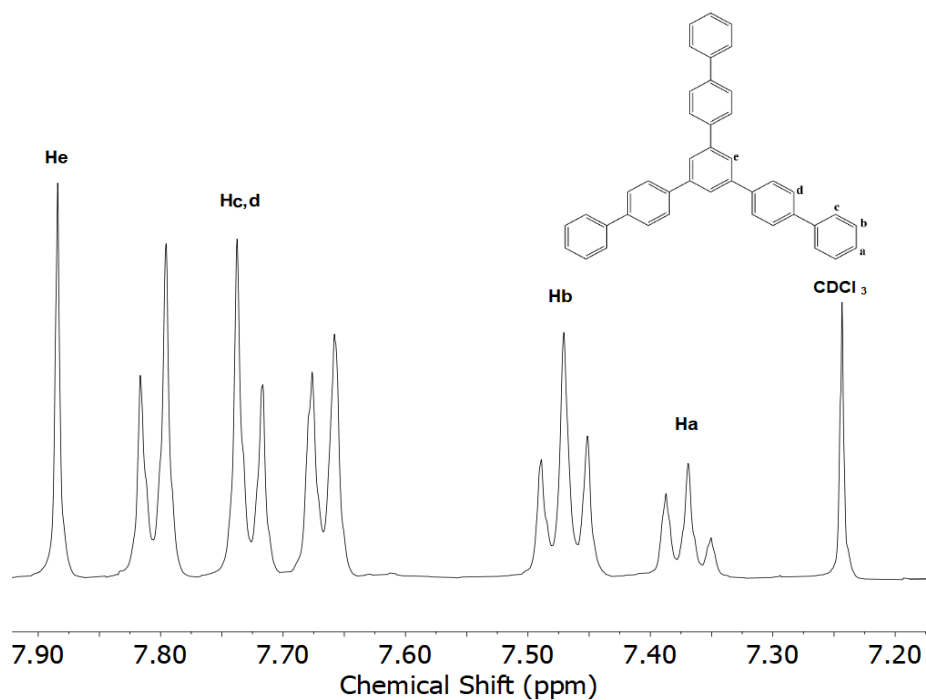


Figure S2.11. ^1H -NMR spectrum (500.13 MHz, CDCl_3) of 1,3,5-tri-(biphenyl)benzene. $\delta_{\text{H}}(\text{ppm})$: 7.88 (s, 3H), 7.81 (d, 6H), 7.73 (d, 6H)-7.67 (d, 6H), 7.47 (m, 6H), 7.37 (m, 3H).

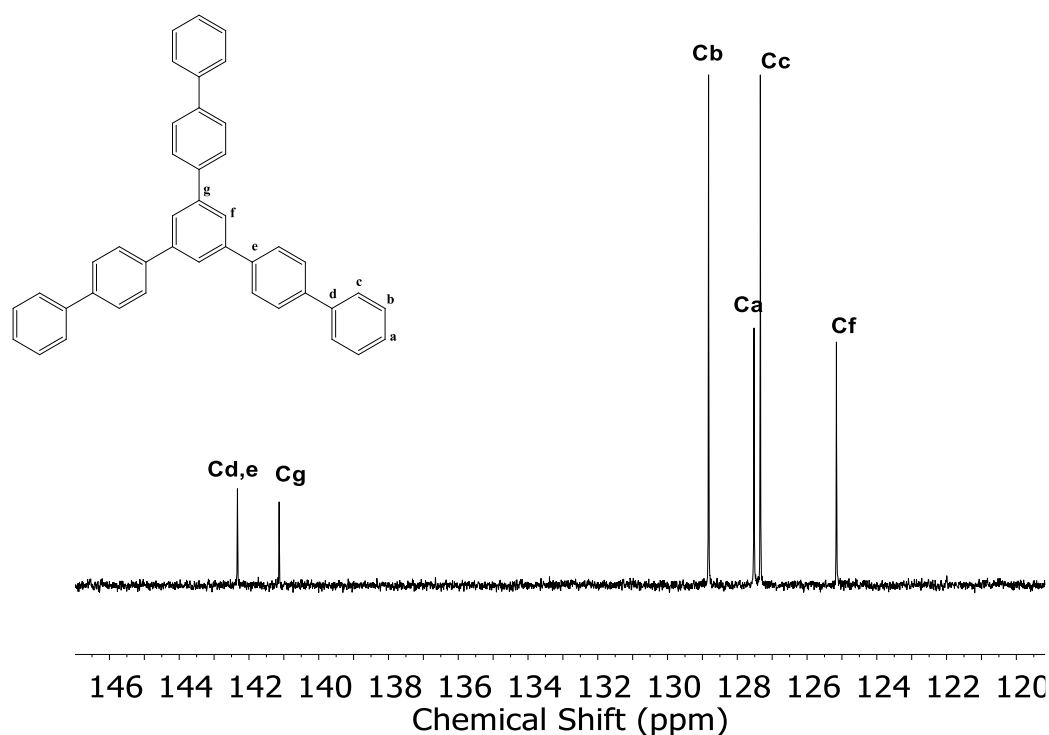


Figure S2.12. ^{13}C -NMR spectrum (125.78 MHz, CDCl_3) of 1,3,5-tri-(biphenyl)benzene. $\delta_{\text{H}}(\text{ppm})$: 142.33, 141.13, 128.82, 127.52, 127.34, 125.16.

S2.1.5. 1-methylindoline-2,3-dione (MI)

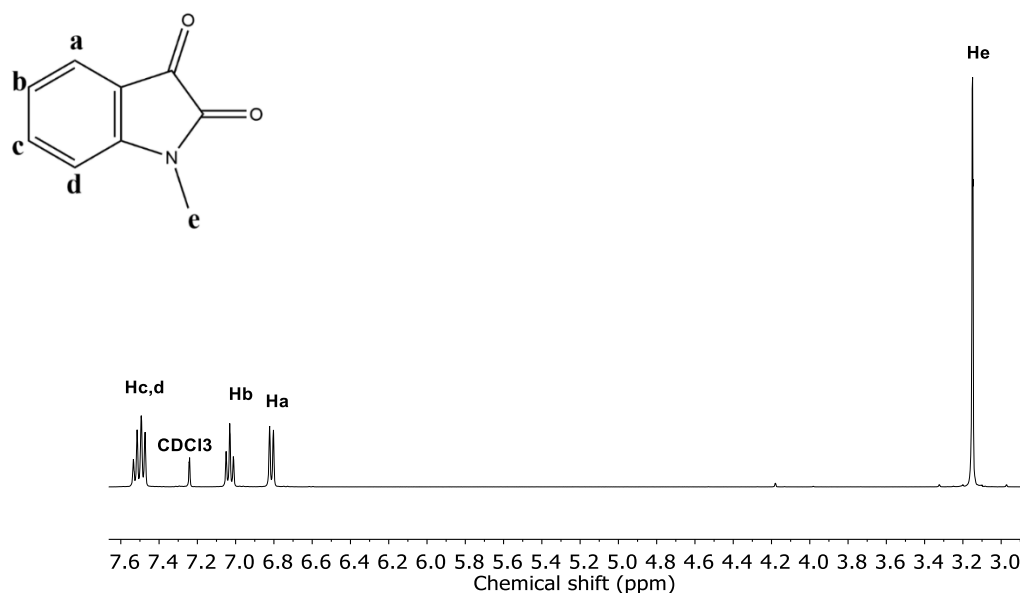


Figure S2.13. ^1H -NMR spectrum (500.13 MHz, CDCl_3) of 1-methylindoline-2,3-dione (N-methylisatin). $\delta_{\text{H}}(\text{ppm})$: 7.67-7.34 (m, 2H), 7.03 (M, 1H), 6.91-6.70 (D, 1H), 3.28-3.00 (s, 3H)

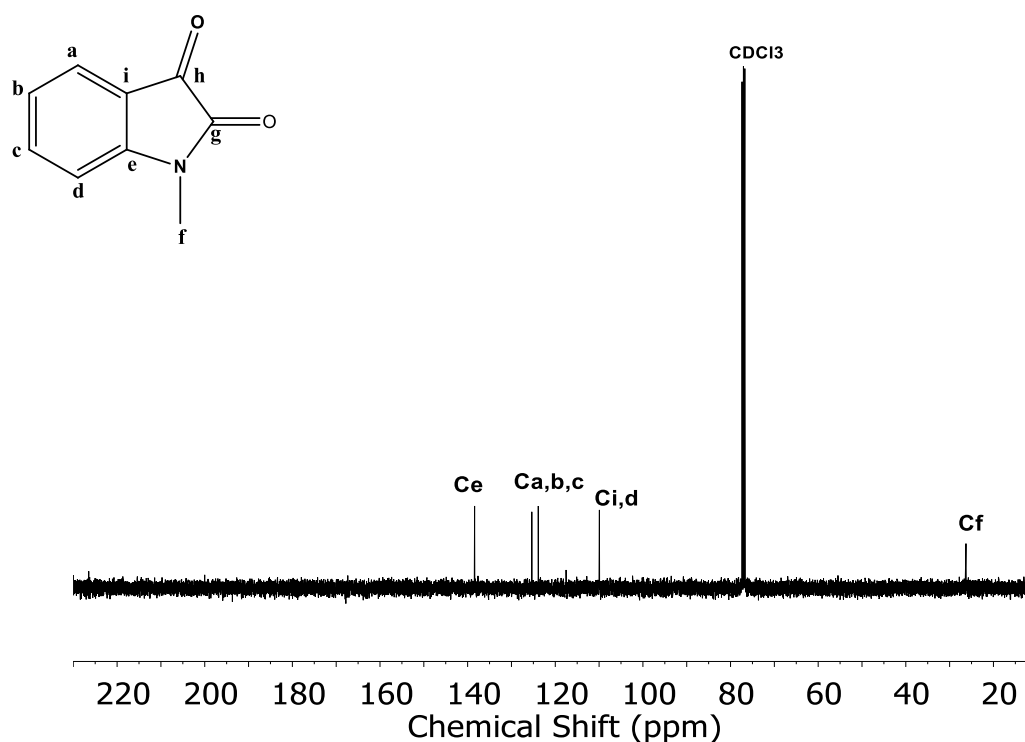
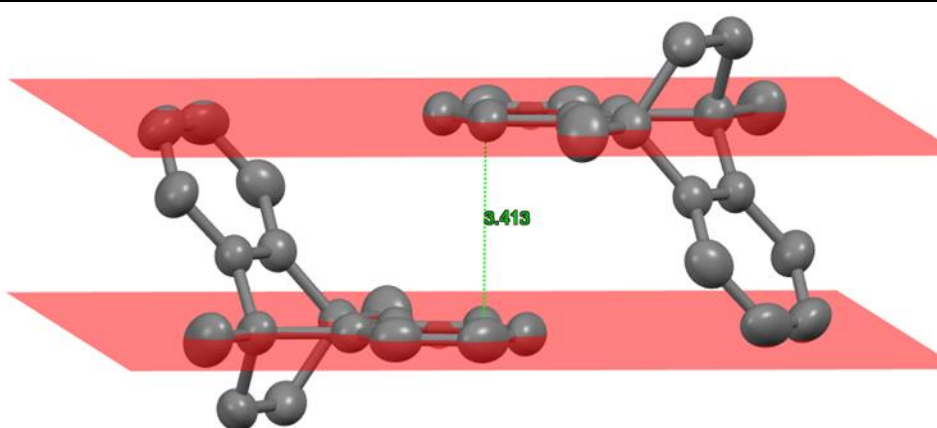


Figure S2.14. ¹³C-NMR spectrum (125.78 MHz, CDCl₃) of 1-methylindoline-2,3-dione (N-methylisatin). $\delta_{\text{H}}(\text{ppm})$: δ 138.41, 125.36, 123.88, 109.93, 26.27.

S2.2. Crystal data and refinement structure for 9,10-Dimethyl-9,10-dihydro-9,10-ethanoanthracene.

A single crystal of DMHEA was mounted onto a glass fiber and examined at 273 K (25 °C) on an Agilent Supernova diffractometer equipped with an Atlas CCD area detector using Cu-K α ($\lambda = 1.54184 \text{ \AA}$) radiation. Data integration, scaling, and empirical absorption correction were carried out using the CrysAlisPro program package [204]. The structure was solved using direct methods and refined by full-matrix-least-squares procedures against F^2 with the SHELXL programⁱ through the OLEX2 interface. The non-hydrogen atoms were refined anisotropically, and the hydrogen atoms were placed at idealized positions and refined with a riding model. Experimental data are listed in Table S2.1

Table S2.1. Crystal data and structure refinement for DMHEA


Empirical formula	C ₁₈ H ₁₈
Formula weight	234.32
Temperature (K)	293
Wavelength (Å)	1.54184
Crystal system	orthorhombic
Space group	Pccn
Unit cell dimensions	$a=14.5957(3)$ Å $\alpha=90^\circ$ $b=20.9859(4)$ Å $\beta=90^\circ$ $c=8.5677(2)$ Å $\gamma=90^\circ$
Volume (Å ³), Z	2624.32(10), 8
Crystal size (mm ³)	0.294 × 0.199 × 0.148
Density (calculated) (g/cm ³)	1.186
Absorption coefficient (mm ⁻¹)	0.497
$F(000)$	1008.0
2 θ range for data collection (°)	7.378 to 149.92
Limiting indices	$-18 \leq h \leq 17$, $-26 \leq k \leq 25$, $-10 \leq l \leq 7$
Reflections collected	13064
Independent reflections	2635 [$R_{\text{int}} = 0.0262$, $R_{\text{sigma}} = 0.0164$]
Data/restraints/parameters	2635/0/165
Goodness-of-fit on F^2	1.053
Final R indexes [$I \geq 2\sigma(I)$]	$R_1 = 0.0452$, $wR_2 = 0.1212$
Final R indexes [all data]	$R_1 = 0.0553$, $wR_2 = 0.1316$
Largest diff. peak/hole [e Å ⁻³]	0.13/-0.15

S2.3. Molecular modelling of 9,10-Dimethyl-9,10-dihydro-9,10-ethanoanthracene

Computer simulation of DMHEA carried out by first optimizing the molecule at the AM1 level of theory [73]. The optimized structure and electronic energy were calculated by Density Functional Theory (DFT), without any geometrical constraint (use of Opt

keyword) for models using Becke's three-parameter hybrid function [205] with the 6-31G(d, p) basis set (B3LYP/6-31G(d, p)) [206] employing the Gaussian 09 program [207]. Molecular depictions were created using the Arguslab 4.0.1 freeware program [208] and the GaussView program (Figure S2.15) [209].

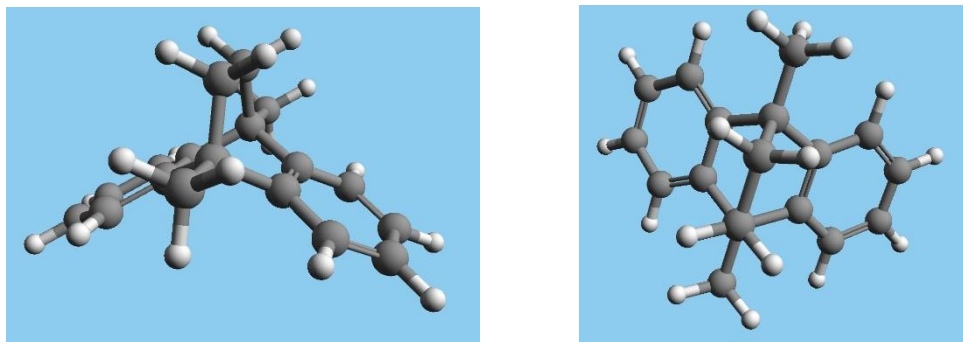


Figure S2.15. DFT modelling of DMHEA monomer

S2.4. Optimization of POPs syntheses

S2.4.1. low-pressure N₂ adsorption/desorption isotherms of POPs

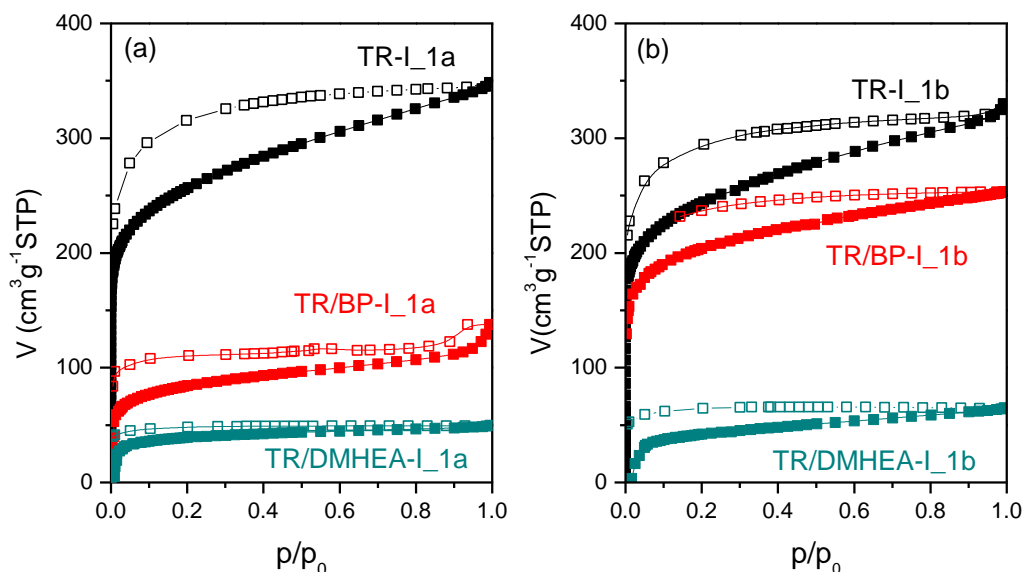


Figure S2.16. Low-pressure N₂ adsorption/desorption isotherms at -196 °C of TR-based POPs prepared by using a TFSA/CHCl₃ (2/1) mixture following: (a) the method 1a (heating at room temperature for 120 h) and (b) the method 1b (heating at room temperature for 1h, and at 60 °C for 96 h).

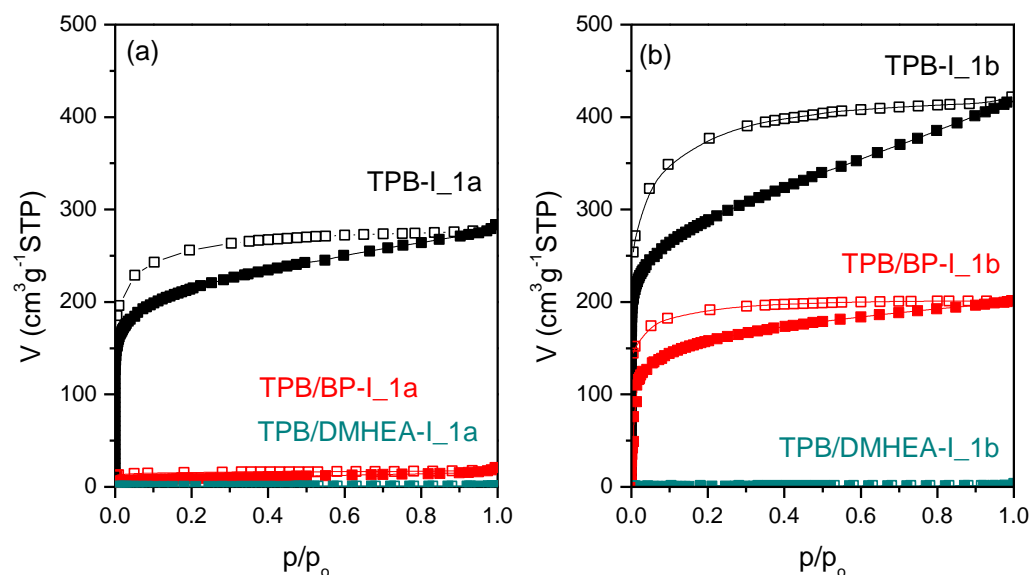


Figure S2.17. Low-pressure N₂ adsorption/desorption isotherms at -196 °C of TPB-based POPs prepared using a TFSA/CHCl₃ mixture (2/1) following: (a) the method 1a (heating at room temperature for 120 h) and (b) the method 1b (heating at room temperature for 1h, and at 60 °C for 96 h).

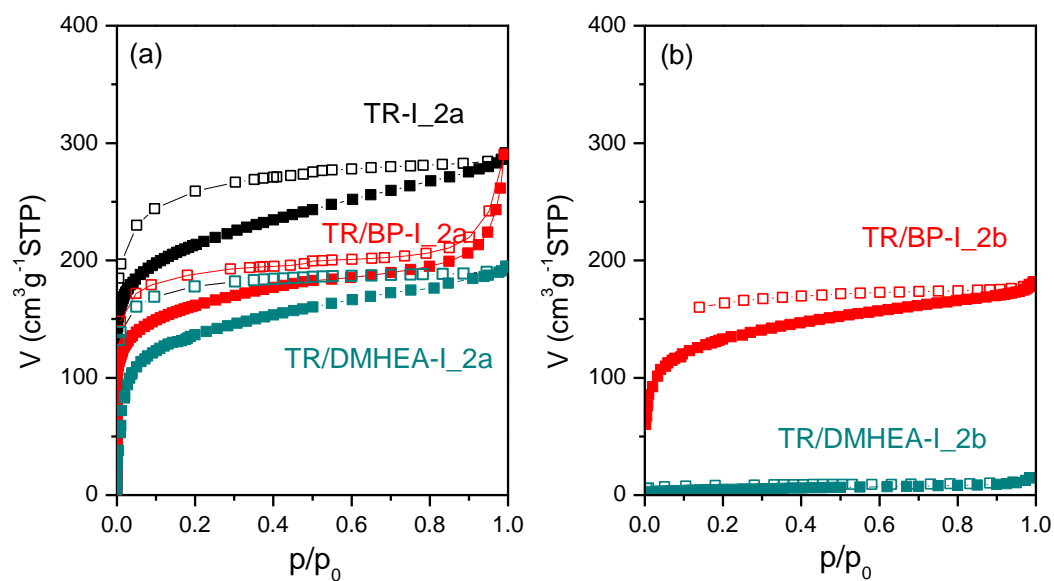


Figure S2.18. Low-pressure N₂ adsorption/desorption isotherms at -196 °C of TR-based POPs prepared using a TFSA/MSA (2/3) mixture following: (a) the method 2a (heating at room temperature for 120 h) and (b) the method 2b (heating at room temperature for 1h, and at 60 °C for 96 h).

S2.4.2. Textural parameters of POPs

Table S2.2. Reaction yield and porous textural parameters, obtained from N_2 adsorption isotherms at $-196\text{ }^\circ\text{C}$, of POPs derived from TR and 135TPB using TFSA/ $HC\text{Cl}_3$ (2/1) as the reaction medium.

Acronym_method ^a	Yield ^b	S_{BET}^c	V_{total}^d	V_{micro}^e
Ho_POPs				
TR-I_1a	97	919	0.53	0.33
TR-I_1b	>95	867	0.50	0.31
TPB-I_1a	95	775	0.43	0.28
TPB-I_1b	>95	1033	0.64	0.37
Co-POPs				
TR/BP-I_1a	>99	304	0.19	0.11
TR/BP-I_1b	>95	738	0.39	0.26
TR/DMHEA-I_1a	98	144	0.08	0.05
TR/DMHEA-I_1b	>95	151	0.10	0.05
TPB/BP-I_1a	96	32	0.03	0.01
TPB/BP-I_1b	93	542	0.31	0.19
TPB/DMHEA-I_1a	96	2	0.00	0.00
TPB/DMHEA-I_1b	>95	2	0.00	0.00

^a 1a: TFSA/ $HC\text{Cl}_3$ (2/1) at RT for 120 h and 1b: TFSA/ $HC\text{Cl}_3$ (2/1) at RT for 1 h and $60\text{ }^\circ\text{C}$ for 96 h; ^b reaction yield (%) and ^c specific surface area ($\text{m}^2\text{ g}^{-1}$); ^d total pore volume ($\text{cm}^3\text{ g}^{-1}$) calculated from single point measurement at $P/P_0 = 0.975$ and ^e micropore volume ($\text{cm}^3\text{ g}^{-1}$).

Table S2.3. Reaction yield and porous textural parameters, obtained from N_2 adsorption isotherms at $-196\text{ }^{\circ}\text{C}$, of PPNs derived from TR and 135TPB using TFSA/MSA (3/2) as the reaction medium.

Acronym_method ^a	Yield ^b	$S_{\text{BET}}^{\text{c}}$	$V_{\text{total}}^{\text{d}}$	$V_{\text{micro}}^{\text{e}}$
Ho-POPs				
TR-I_2a	98	771	0.47	0.27
Co-POPs				
TR/BP-I_2a	74	589	0.39	0.21
TR/BP-I_2b	94	480	0.27	0.17
TR/DMHEA-I_2a	73	511	0.29	0.18
TR/DMHEA-I_2b	23	17	0.02	0.01

^a 2a: TFSA/MSA (3/2) at RT for 120 h and 2b: TFSA/MSA (3/2) at RT for 1 h and 60 $^{\circ}\text{C}$ for 96 h; ^b reaction yield (%); ^c surface area ($\text{m}^2\text{ g}^{-1}$); ^d total pore volume ($\text{cm}^3\text{ g}^{-1}$) calculated from single point measurement at $P/P_0 = 0.975$; ^e micropore volume ($\text{cm}^3\text{ g}^{-1}$).

S2.5. Acronyms of POPs

Table S2.4. Acronyms of POPs, starting monomers employed for the preparation of POPs using a TFSA/CHCl₃ (2/1) mixture at 60 °C (according to method 1b), and reaction yields.

Acronym	Nucleophilic monomers		Cross-linker	Yield ^f	
	N-functional				
	Tetra-	Tri-	Bi-		
Ho-POPs					
TPB-I		TPB ^a	Isatin	>95	
TMB-I		TTB ^b	Isatin	83	
TBB-I		TBB ^c	Isatin	>95	
TR-I		Triptycene	Isatin	>95	
SBF-I	SBF ^d		Isatin	>95	
TPB-MI		TPB ^a	Methyl isatin	>95	
TMB-MI		TTB ^b	Methyl isatin	95	
TBB-MI		TBB ^c	Methyl isatin	80	
TR-MI		Triptycene	Methyl isatin	>95	
SBF-MI	SBF ^d		Methyl isatin	>95	
TPB-TF		TPB ^a	Trifluoroacetophenone	>95	
TMB-TF		TTB ^b	Trifluoroacetophenone	>95	
TBB-TF		TBB ^c	Trifluoroacetophenone	94	
TR-TF		Triptycene	Trifluoroacetophenone	>95	
SBF-TF	SBF ^d		Trifluoroacetophenone	>95	
Co-POPs					
TR/BP-I		Triptycene	Biphenyl	Isatin	>95
TPB/BP-I		TPB ^a	Biphenyl	Isatin	93
SBF/BP-I	SBF ^d		Biphenyl	Isatin	>95
TR/DMHEA		Triptycene	DMHEA ^e	Isatin	>95
TPB/DMHE		TPB ^a	DMHEA ^e	Isatin	>95
SBF/DMHE	SBF ^d		DMHEA ^e	Isatin	>95

^a 1,3,5-triphenylbenzene; ^b 1,3,5-tri-(2-methylphenyl)benzene; ^c 1,3,5-tri-(biphenyl)benzene; ^d 9,9'-spirobifluorene; ^e 9,10-dimethyl-9,10-dihydro-9,10-ethanoanthracene; ^f reaction yield (%)

S2.6. Characterization of POPs

S2.6.1 Wide-angle X-ray scattering (WAXS)

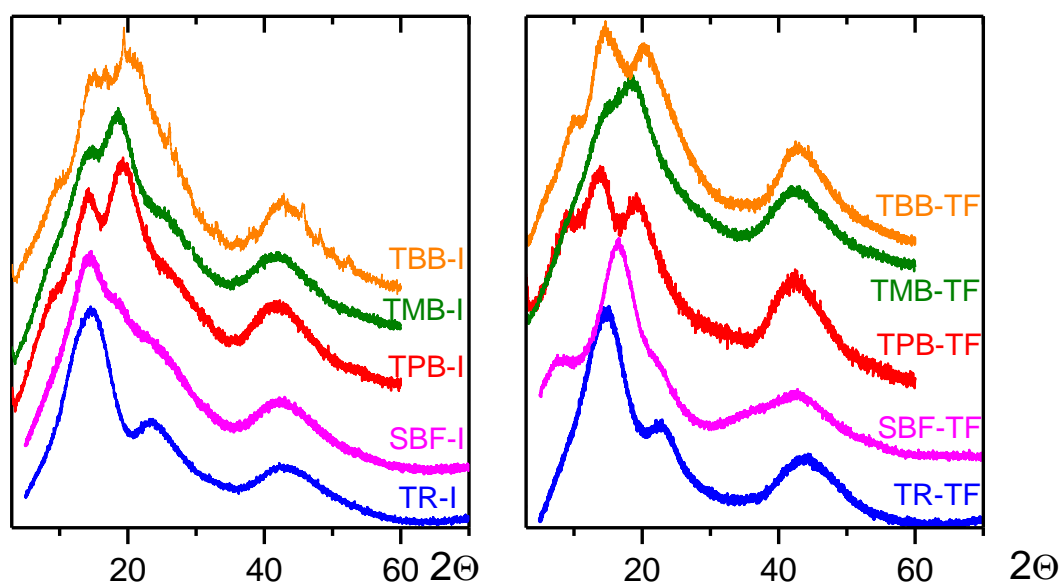


Figure S2.19. WAXS patterns of Ho-POPs containing isatin (left) and TFAP (right). The patterns were normalized to the intensity maximum at about 15° and shifted for clarity's sake.

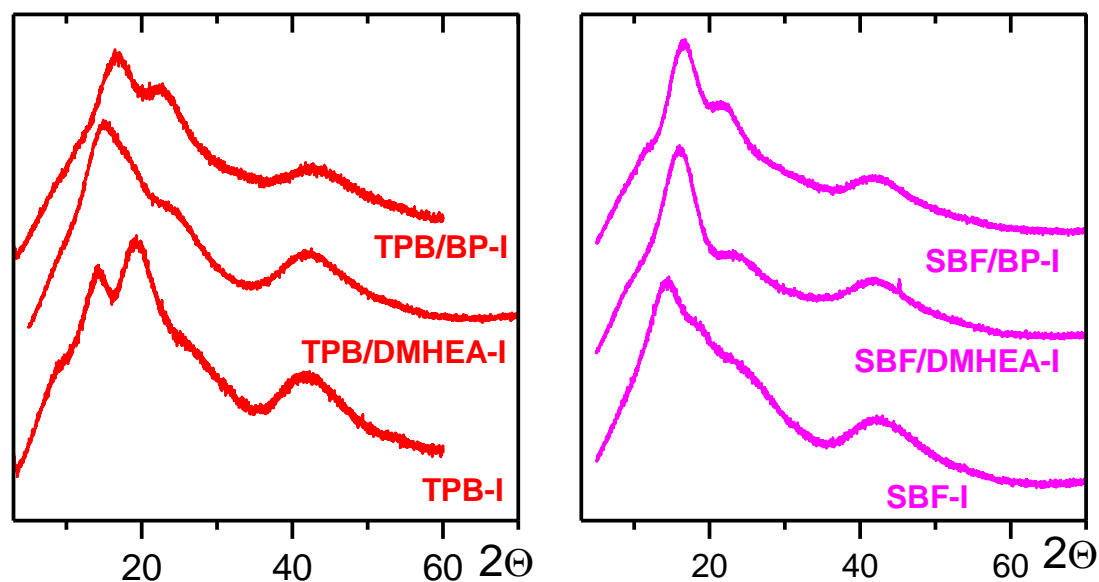


Figure S2.20. WAXS patterns of TPB-based POPs (left) and SBF-based POPs (right). The patterns were normalized to the intensity maximum at about 15° and shifted for clarity's sake.

S2.7. Thermal Properties of POPs**Table S2.5.** *Thermal stability of POPs: degradation onset temperature (T_d) and char yield at 800 °C (R^{800}).*

Acronyms	T _d (°C)		R ⁸⁰⁰ (%)
	Ho-POPs		
TPB-I		565	77
TMB-I		540	67
TBB-I		545	80
TR-I		565	75
SBF-I		515	78
TPB-MI		563	73
TMB-MI		532	59
TBB-MI		552	75
TR-MI		565	68
SBF-MI		552	76
TPB-TF		482	76
TMB-TF		505	59
TBB-TF		500	80
TR-TF		498	74
SBF-TF		480	74
Co-POPs			
TPB/BP-I		560	71
TR/BP-I		556	67
SBF/BP-I		555	74
TPB/DMHEA-I	310	482	70
TR/DMHEA-I	312	515	57
SBF/DMHEA-I	308	511	73

S2.8. Textural properties of POPs

Table S2.6. Porous textural parameters obtained from N_2 and CO_2 adsorption isotherms at $-196\text{ }^\circ\text{C}$, and $0\text{ }^\circ\text{C}$, respectively.

Acronyms	Low-pressure adsorption isotherms						
	N_2 at $-196\text{ }^\circ\text{C}$			CO_2 at $0\text{ }^\circ\text{C}$			
	S_{BET}^a	V_{total}	V_{micro}^c	V_{nmicro}	$V_{\text{nmicro}}/V_{\text{total}}^e$	d_p^f	Uptake ^g
Ho-POPs							
TPB-I	1033	0.64	0.37	0.38	60	5.86	4.10
TMB-I	195	0.11	0.07	0.17	100	5.85	1.98
TBB-I	772	0.45	0.27	0.29	64	5.85	3.11
TR-I	867	0.50	0.31	0.42	84	4.91	5.42
SBF-I	744	0.42	0.26	0.23	55	5.60	2.75
TPB-MI	906	0.55	0.32	0.28	51	5.99	2.94
TMB-MI	754	0.48	0.27	0.25	52	5.60	2.74
TBB-MI	845	0.56	0.30	0.28	50	5.73	3.11
TR-MI	886	0.55	0.31	0.32	58	4.69	3.90
SBF-MI	682	0.40	0.24	0.23	58	5.13	2.67
TPB-TF	580	0.34	0.24	0.24	70	6.12	1.72
TMB-TF	28	0.02	0.01	0.10	100	6.26	0.89
TBB-TF	722	0.46	0.26	0.23	50	6.19	2.12
TR-TF	655	0.43	0.25	0.24	56	5.85	1.89
SBF-TF	856	0.56	0.30	0.21	38	6.26	2.11
Co-POPs							
TPB/BP-I	542	0.31	0.19	0.24	77	5.42	2.78
TR/BP-I	738	0.39	0.26	0.29	74	4.80	3.61
SBF/BP-I	101	0.07	0.04	0.21	100	5.13	2.54
TPB/DMHEA-I	2	0.00	0.00	0.18	100	5.24	2.10
TR/DMHEA-I	151	0.10	0.05	0.21	100	4.91	2.61
SBF/DMHEA-I	0	0.00	0.00	0.18	100	5.13	2.24

^a Specific surface area ($\text{m}^2\text{ g}^{-1}$); ^b total pore volume ($\text{cm}^3\text{ g}^{-1}$) calculated from single point measurement at $P/P_0 = 0.975$; and ^c micropore volume ($\text{cm}^3\text{ g}^{-1}$) obtained from N_2 adsorption isotherms. ^d Narrow micropore volume ($\text{cm}^3\text{ g}^{-1}$); ^e percentage of narrow microporosity; ^f average pore diameter (\AA) and ^g CO_2 uptake (mmol g^{-1}) at p/p_0 of 0.03 obtained from CO_2 adsorption isotherms.

S2.9. High-pressure CO₂, CH₄, and N₂ uptakes**Table S2.7.** CO₂, N₂ and CH₄ uptakes and isosteric CO₂ adsorptions heats of POPs

Acronyms	CO ₂ at 1 bar ^a			CO ₂ ^b	N ₂ ^b	CH ₄ ^b
	0 °C	25 °C	Q _{st} ^c	25 °C, 30 bar		
Ho-POPs						
TPB-I	180	101	32.2	466	59	70
TMB-I	87	53	31.5	241	26	37
TBB-I	137	94	24.9	348	41	49
TR-I	239	159	34.2	384	49	62
SBF-I	132	83	31.4	350	48	52
TPB-MI	129	78	27.0	352	48	57
TMB-MI	121	70	30.7	197	42	52
TBB-MI	137	79	31.2	381	43	56
TR-MI	171	108	35.2	362	50	60
SBF-MI	117	71	32.7	262	36	40
TPB-TF	76	40	29.2	248	34	40
TMB-TF	39	22	25.5	143	13	20
TBB-TF	93	69	17.8	326	40	44
TR-TF	83	46	29.5	252	34	37
SBF-TF	93	52	27.5	325	41	47
Co-POPs						
TPB/BP-I	122	77	32.1	292	36	41
TR/BP-I	159	104	32.0	367	51	56
SBF/BP-I	112	70	31.3	272	28	38
TPB/DMHEA-I	93	59	35.3	226	26	35
TR/DMHEA-I	115	76	36.4	280	39	41
SBF/DMHEA-I	99	62	35.1	226	29	31

^a Gas uptake (mg g⁻¹); ^b Excess gas uptake (mg g⁻¹); ^c isosteric enthalpy of adsorption (kJ mol⁻¹)

Appendix 3

INDEX

Section S3.1. Characterization of polymers

S3.1.1 Solubility of polymers

S3.1.2 ^1H -NMR spectra of polymers

Section S3.2. Characterization of the porous organic polymer (POP)

S3.2.1 CP/MAS ^{13}C NMR spectrum of POP

S3.2.2 Textural characterization of POP

Section S3.3. Characterization of mixed matrix membranes (MMMs)

S3.3.1 ATR-FTIR spectra of mixed matrix membranes

S3.3.2 Hi-Res TGA of MMMs

S3.3.3. WAXS of MMMs

Section S3.4. Mechanical properties of the neat membranes and MMMs before and after thermal treatment

Section S3.5. Conditioning treatment of membranes

Section S3.6. Gas separation properties of neat membranes and their corresponding MMMs before and after thermal treatment

Section S3.7. CO_2 permeability plotted as a function of fugacity

Section S3.8. Effect of thermal treatment on the temperature dependence of CO_2 gas permeation

Section S3.9. Computer simulation

S3.9.1. Molecular picture of the adduct geometry between an isatin-model and a PEO-model

Section S3.1. Characterization of polymers.

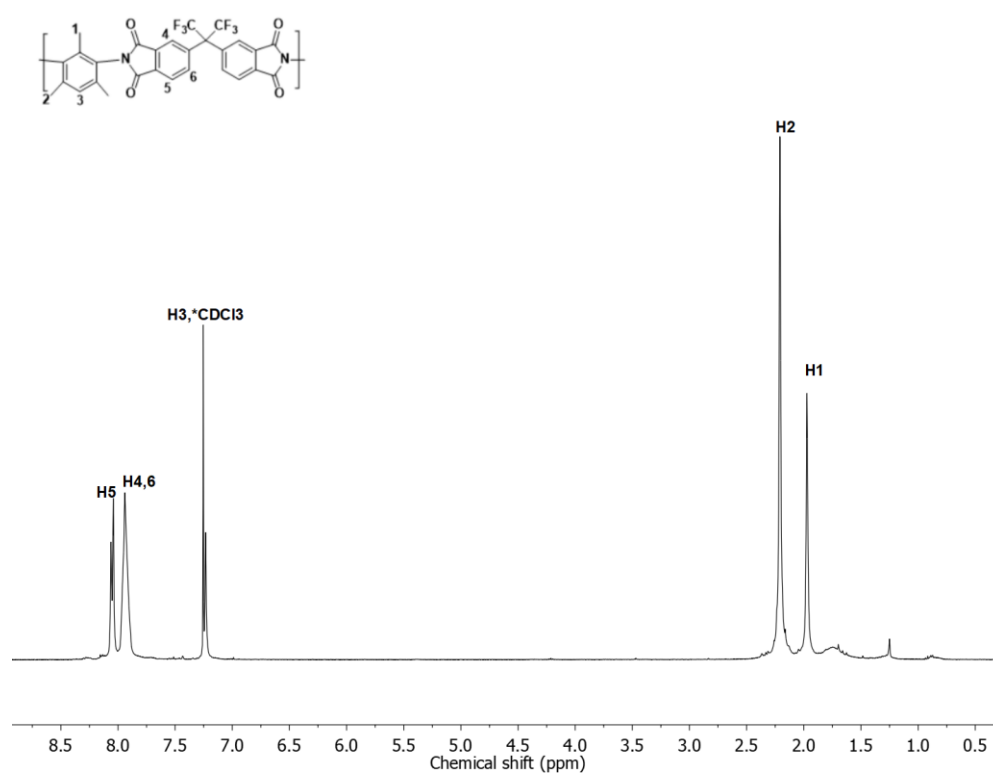
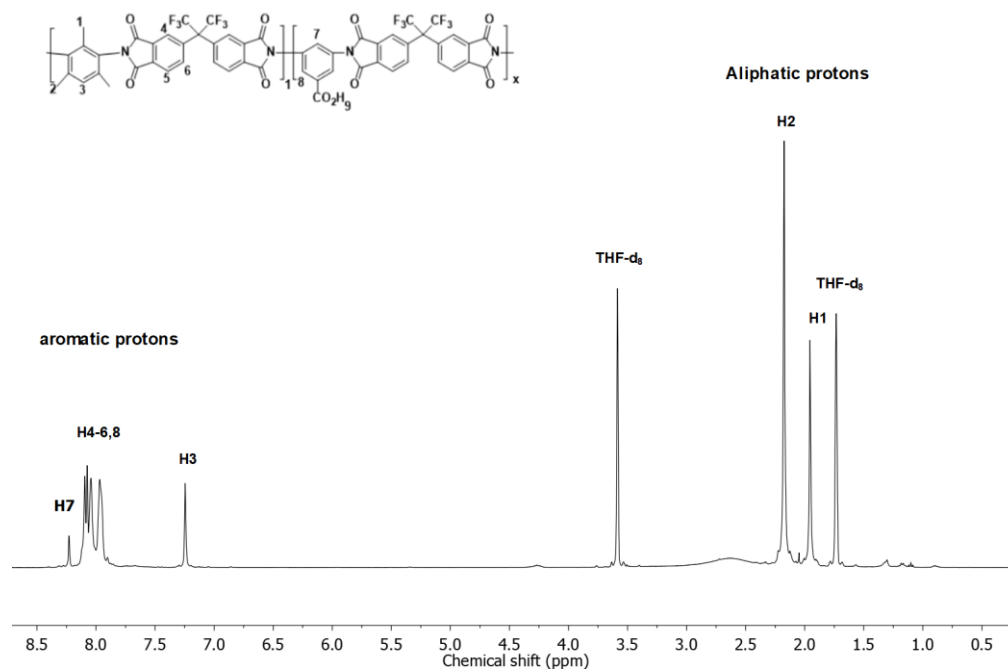
S3.1.1 Solubility of polymers

The three neat polymers (PI*, PI*20 and PI*20EO1) were soluble in polar aprotic solvents such as dimethylsulfoxide (DMSO), N,N-dimethylacetamide (DMAc), N-methyl-2-pyrrolidinone (NMP), and N,N-dimethylformamide (DMF), as well as solvents such as chloroform (CHCl₃) and tetrahydrofuran (THF). However, it should be noted that the solubility of PI*20EO1 was lower in CHCl₃ and THF, when compared with PI* and PI*20, requiring heating of the sample to the boiling temperature of the solvent to fully dissolve. The solubility results were used to choose the best solvents for the membrane processing process.

Table S1. Solubility of PI*, PI*20, and PI*20EO1.

	PI*	PI*20	PI*20EO1
DMSO	+	+	+
THF	++	++	+
CHCl₃	++	++	+
DMF	++	++	++
DMAc	++	++	++
NMP	++	++	++

++ : soluble at room temperature; + : soluble after heating

S3.1.2 ^1H -NMR spectra of polymersFigure S3.1. ^1H -NMR spectrum of PI* in deuterated CHCl_3 Figure S3.2. ^1H -NMR spectrum of PI*20 in deuterated THF (THF-d_8)

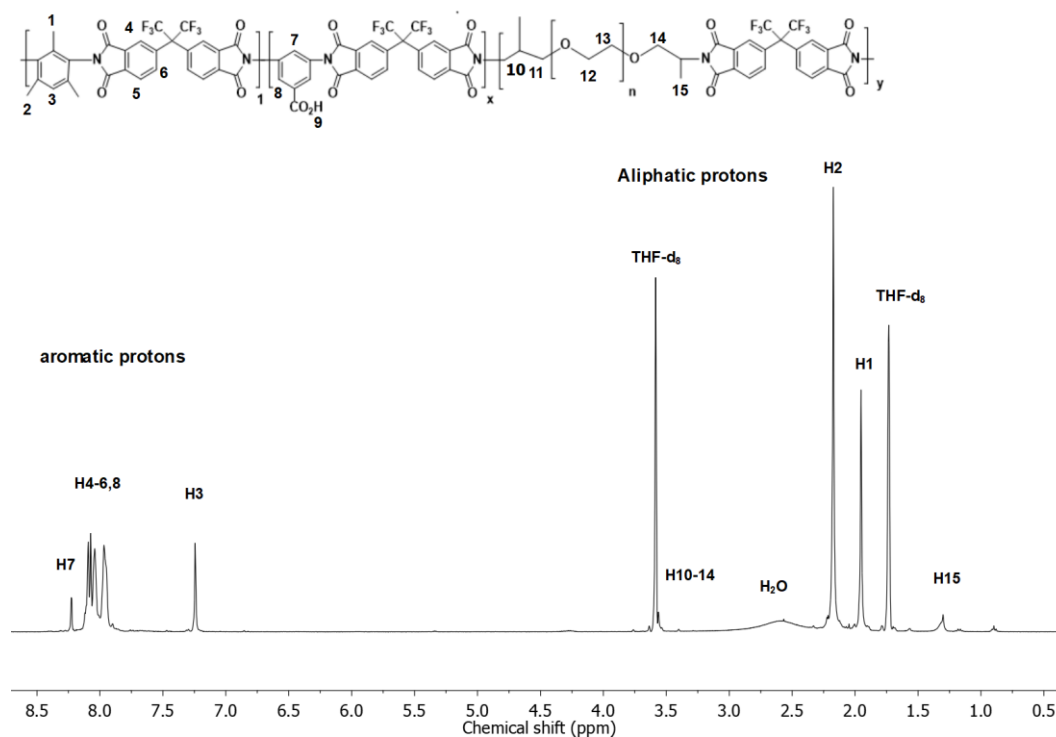


Figure S3.3. ^1H NMR spectrum of PI*20EO1 in THF- d_8 .

Section S3.2 Characterization of the porous organic polymer

S3.2.1 Solid-state CP/MAS ^{13}C NMR spectrum of POP

The spectrum of POP is shown in Figure S4 and the peaks were identified based on its structure.

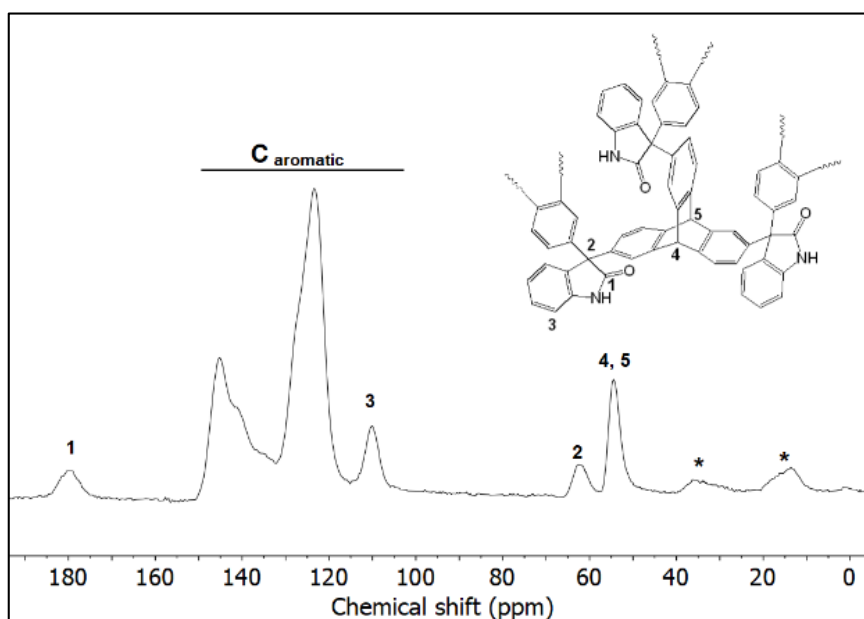


Figure S3.4. Solid-state CP/MAS ^{13}C -NMR spectrum of POP. Asterisks denote spinning side bands.

S3.2.2 Textural characterization of POP

The low-pressure N₂ adsorption/desorption isotherms are shown in Figure S3.5. The adsorption branch of the isotherm was used to obtain: (1) the apparent surface area (S_{BET}) by applying the Brunauer–Elmnett–Teller method (BET) in the 0.01 to 0.2 p/p_0 range, and (2), the micropore volume (V_{micro}) using the Dubinin–Radushkevich (DR) equation in the 0.001 to 0.2 p/p_0 range. The total pore volume (V_{total}) was considered as the volume of liquid nitrogen adsorbed at 0.975 p/p_0 . These results are summarized in Table S3.2.

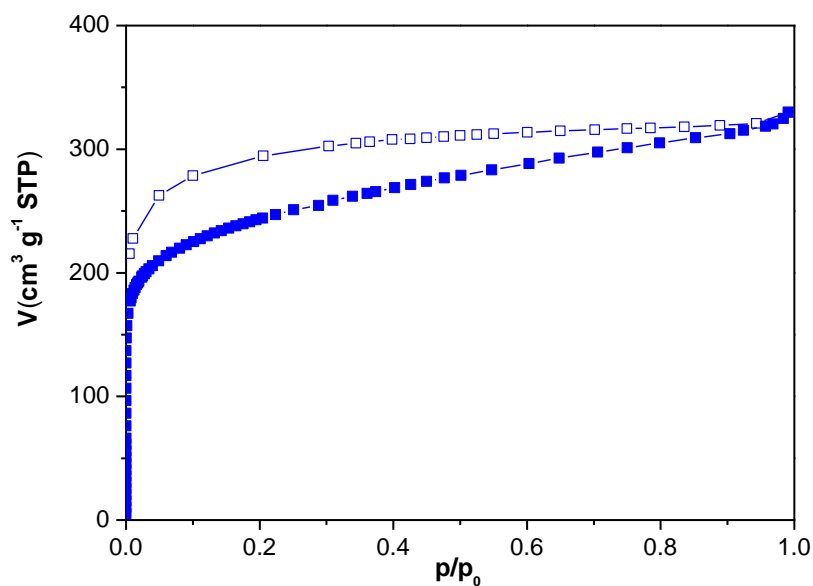


Figure S3.5. N₂ adsorption (solid symbols)–desorption (hollow symbols) isotherms measured at $-196\text{ }^{\circ}\text{C}$ for POP.

Table S3.2. Textural parameters of POP

Acronyms	$S_{\text{BET}}^{\text{a}}$	$V_{\text{total}}^{\text{b}}$	$V_{\text{micro}}^{\text{b}}$	Microporosity ^c
TR-IS: POP	867	0.50	0.31	62

^a $\text{m}^2 \text{g}^{-1}$; ^b $\text{cm}^3 \text{g}^{-1}$; ^c $\text{Microporosity} = 100 \times (V_{\text{micro}}/V_{\text{total}})\%$

Section S3.3. Characterization of membranes

S3.3.1 ATR-FTIR spectra of MMMs

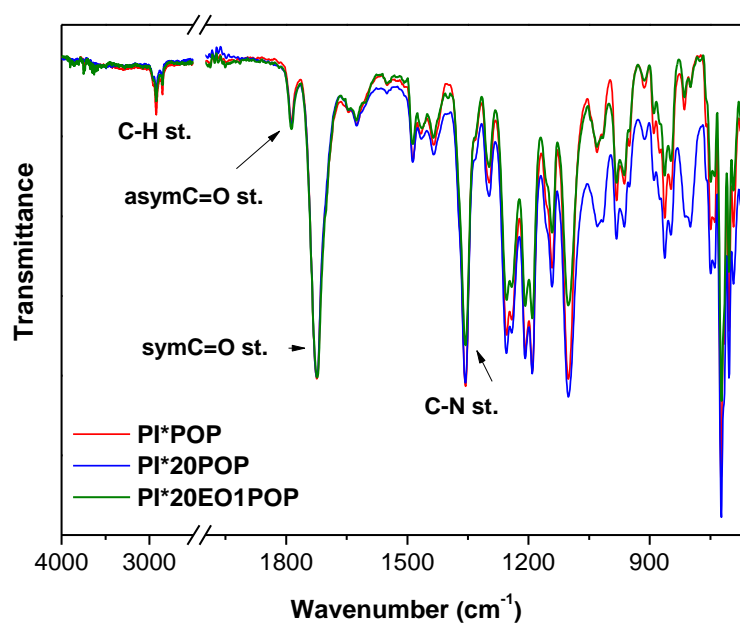


Figure S3.6. ATR-FTIR spectra of MMMs. Spectra were normalized to intensity of the peak at 1725 cm⁻¹

S3.3.2 Thermogravimetric analysis (TGA) of MMMs

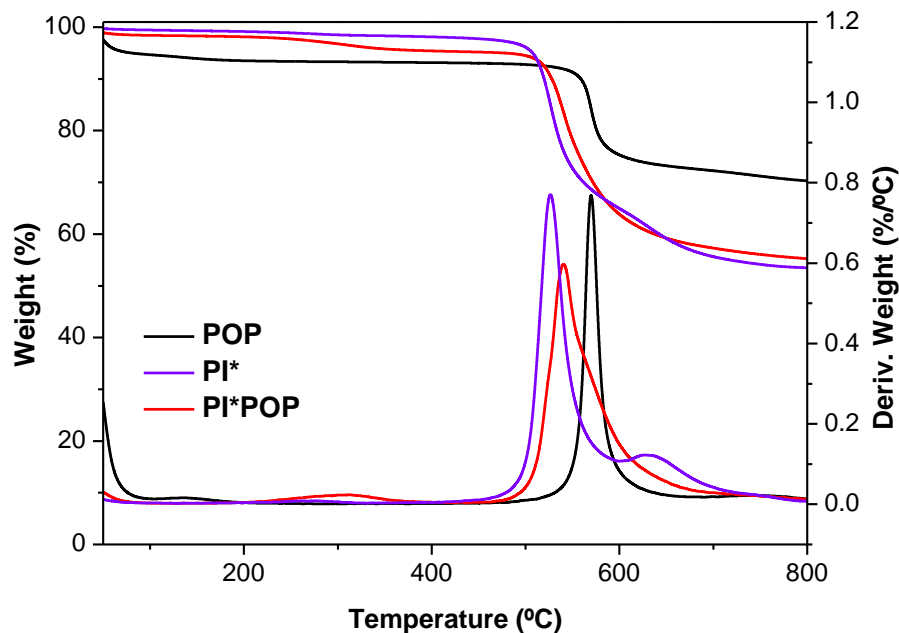


Figure S3.7. TGA thermograms of POP, PI* and PI*POP

S3.3.3. WAXS of MMMs

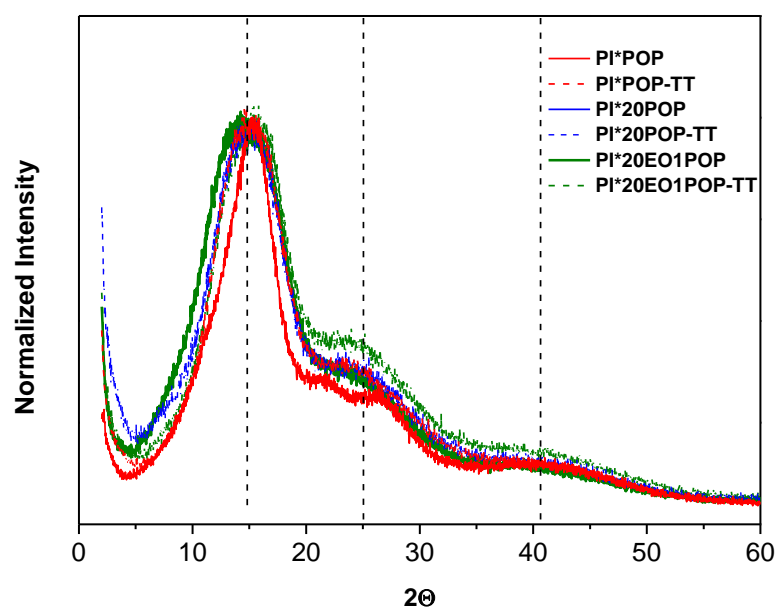


Figure S3.8. Normalized WAXS patterns of MMMs before and after thermal treatment.

Section S3.4. Mechanical properties of the neat membranes and MMMs before and after thermal treatment

Table S3.3: *Mechanical properties of neat membranes and MMMs before and after thermal treatment*

Matrix membranes			
	Young's Modulus (GPa)	Tensile strength (MPa)	Elongation at break (%)
PI*	1.3 ± 0.2	56 ± 5	6.5 ± 1
PI*20	1.3 ± 0.3	78 ± 13	8.3 ± 2.0
PI*20-TT	1.7 ± 0.2	58 ± 4	2.4 ± 1.2
PI*20EO1	1.5 ± 0.1	77 ± 5	7.3 ± 0.9
PI*20EO1-TT	1.2 ± 0.2	58 ± 18	7 ± 2
MMMs			
PI*20POP	1.4 ± 0.1	38 ± 6	3.7 ± 0.7
PI*20POP-TT	1.7 ± 0.1	42 ± 11	2.7 ± 0.8
PI*20EO1POP	1.1 ± 0.1	40 ± 7	3.9 ± 0.7
PI*20EO1POP-TT	1.8 ± 0.3	61 ± 11	3.1 ± 0.9

Section S3.5. Physical aging after conditioning in methanol

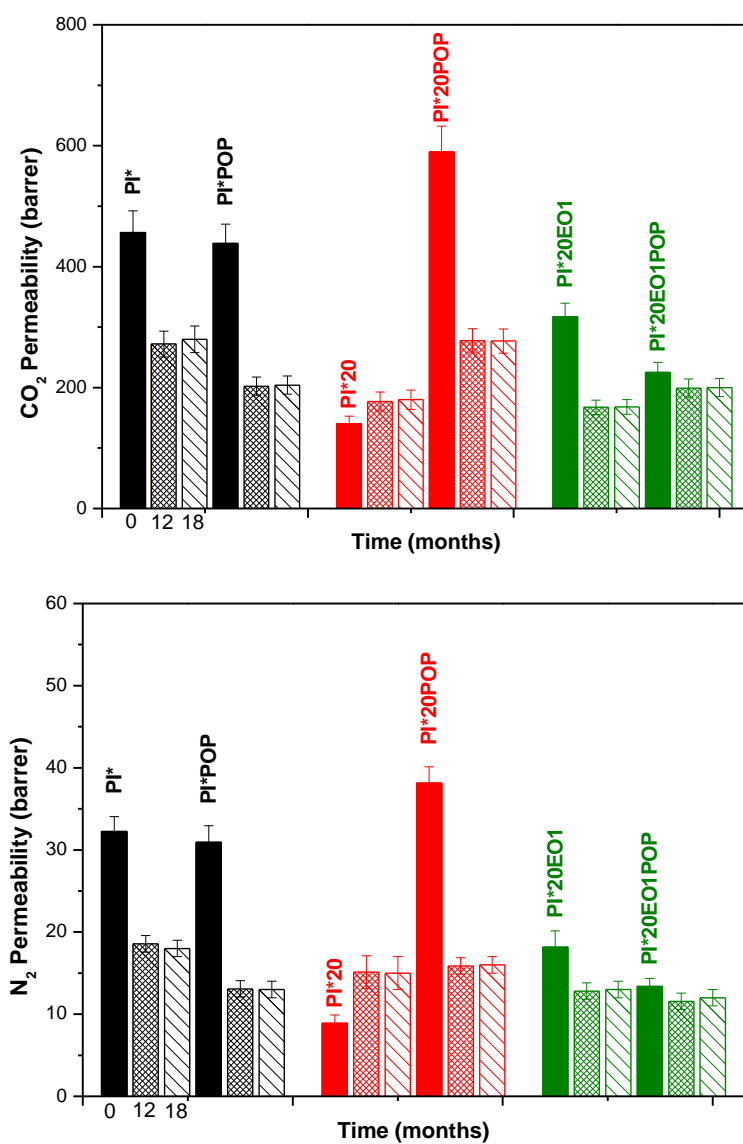


Figure S3.9. Comparison of CO₂ (up) and N₂ (bottom) permeabilities for the membranes aged for 0, 12, and 18 months, measured at 3 bar and 35 °C.

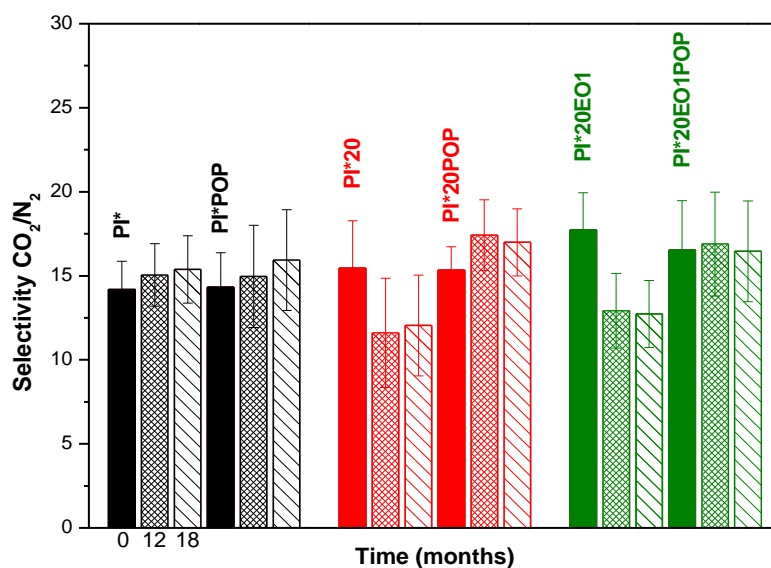


Figure S3.10. Comparison of CO₂/N₂ selectivity for the membranes aged for 0, 12, and 18 months, measured at 3 bar and 35 °C.

Section S3.6. Gas separation properties of neat membranes and their corresponding MMMs before and after thermal treatment.

Table S3.4. Gas permeability (Barrer^a) of neat membranes and their corresponding MMMs before and after thermal treatment.

Permeability	He	O ₂	N ₂	CH ₄	CO ₂	O ₂ /N ₂	CO ₂ /CH ₄
PI*	255±20	67±5	18±1	16±1	280±22	3.7±0.4	18±2
PI*POP	190±12	50±4	13±1	11±1	204±15	3.8±0.5	18±2
PI20*	205±15	47±4	15±2	10±1	180±16	3.1±0.5	18±3
PI*20TT	246±15	62±5	16±1	12±1	256±20	3.9±0.4	21±2
PI*20POP	252±15	64±6	16±2	14±1	277±20	4.0±0.6	20±2
PI*20POP-TT	146±10	29±2	6.9±0.5	5.5±0.4	126±9	4.2±0.4	23±2
PI*20EO1	159±14	56±4	13±1	8.2±0.6	168±12	4.3±0.4	20±2
PI*20EO1-TT	238±12	61±5	16±1	12±1	232±17	3.80±0.4	19±2
PI*20EO1POP	189±13	46±4	12±1	8.9±0.8	200±15	3.8±0.5	22±3
PI*20EO1POPTT	340±30	111±8	30±2	25±2	450±30	3.7±0.4	18±2

^a 1 barrer = 10⁻¹⁰ cm³ (STP) cm cm⁻² s⁻¹ cmHg⁻¹

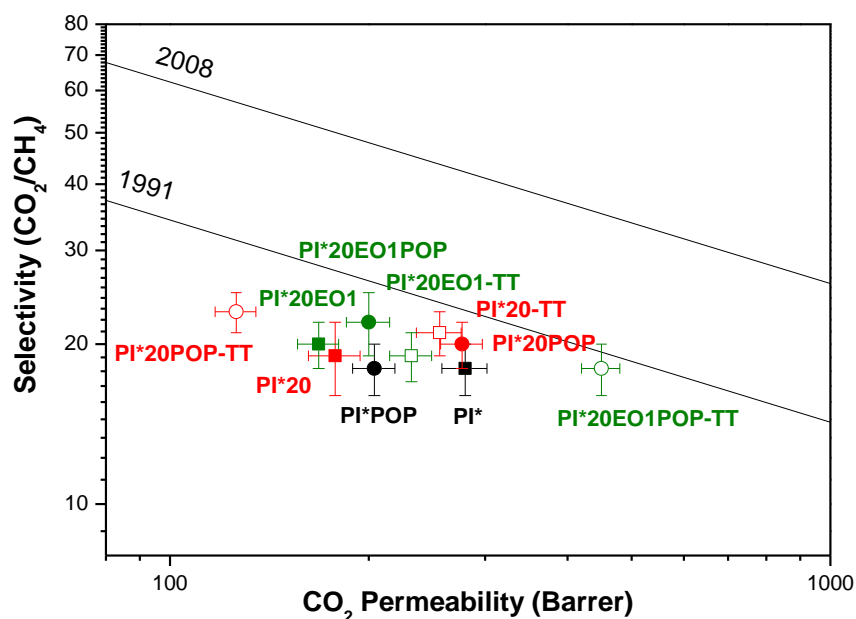


Figure S3.11. CO₂/CH₄ Robeson diagrams for neat PI*, PI*20, and PI*20EO1 membranes and the corresponding MMMs before and after thermal treatment (-TT). The standard deviations from permeability and selectivity values are shown as error bars. Solid lines correspond to the 1991 and 2008 upper bound limits [26,27].

Table S3.5. Diffusivity coefficients ($D \times 10^8$, cm² s⁻¹) of the neat membranes and their corresponding MMMs before and after thermal treatment

Diffusivity	O ₂	N ₂	CH ₄	CO ₂	O ₂ /N ₂	CO ₂ /CH ₄
PI*	26±3	10±1	2.4±0.2	11±1	2.6±0.4	4.6±0.6
PI*POP	17±2	5.7±0.6	1.3±0.2	7.5±0.8	3.0±0.5	6±1
PI*20	29±4	13±2	2.2±0.3	10±1	2.2±0.5	4.5±0.8
PI*20-TT	33±4	14±1	2.3±0.2	11±1	2.4±0.2	4.8±0.6
PI*20POP	31±4	9±1	1.9±0.2	11±1	3.4±0.6	5.8±0.8
PI*20POPTT	21±2	5.3±0.5	1.1±0.1	6.2±0.6	4.0±0.5	5.6±0.7
PI*20EO1	26±3	7.9±0.8	2.3±0.2	7.1±0.7	3.3±0.5	3.1±0.4
PI*20EO1-TT	23±3	8.6±0.8	1.9±0.2	9.4±0.8	2.7±0.4	4.9±0.7
PI20*EO1POP	17±2	5.7±0.6	1.1±0.1	7.4±0.7	3.0±0.5	6.7±0.9
PI*20EO1POP-TT	37±4	13±1	3.3±0.4	17±2	2.8±0.4	5.1±0.9

Table S3.6. Solubility coefficients ($S \times 10^2$, cm^3 (STP) cm^{-3} cmHg^{-1}) of the neat PI*, PI*20, and PI*20EO8 membranes and the corresponding MMMs before and after thermal treatment.

Solubility	O ₂	N ₂	CH ₄	CO ₂	O ₂ /N ₂	CO ₂ /CH ₄
PI*	2.6±0.3	1.8±0.2	6.7±0.7	25±3	1.4±0.2	3.7±0.6
PI*POP	2.9±0.4	2.3±0.3	8±1	27±4	1.3±0.2	3.4±0.6
PI*20	1.6±0.3	1.1±0.2	4.5±0.8	18±2	1.4±0.4	4.0±0.8
PI*20-TT	1.9±0.3	1.1±0.1	5.2±0.6	23±3	1.7±0.3	4.4±0.8
PI*20POP	2.0±0.3	1.8±0.3	7.4±0.9	25±3	1.1±0.2	3.4±0.6
PI*20POPTT	1.4±0.2	1.3±0.1	5.0±0.6	20±2	1.1±0.2	4.0±0.6
PI*20EO1	2.1±0.3	1.6±0.2	3.6±0.4	24±3	1.3±0.2	7±1
PI*20EO1-TT	2.6±0.4	1.9±0.2	6.3±0.8	25±3	1.4±0.2	4.0±0.7
PI*20EO1POP	2.7±0.4	2.1±0.3	8±1	27±3	1.3±0.3	3.4±0.6
PI*20EO1POP-TT	3.0±0.4	2.3±0.2	8±1	26±4	1.3±0.2	3.0±0.6

S3.7. Non-ideal behavior of CO₂ permeability plotted as a function of fugacity.

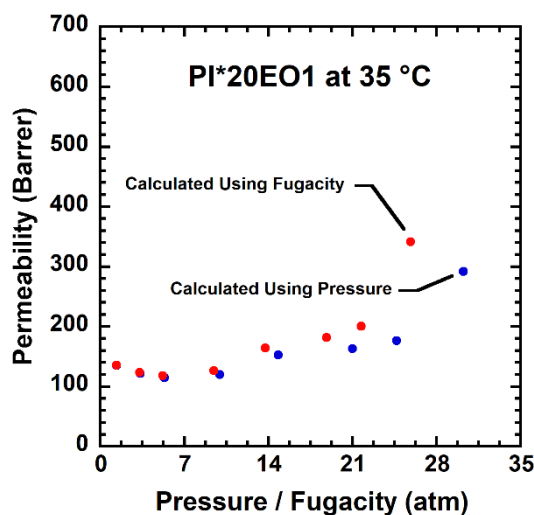


Figure S3.12. CO₂ permeability from 1-30 atm (in Barrer) plotted as a function of both pressure (blue) and fugacity (red) for PI*20EO1 at 35 °C.

Section S3.8. Effect of thermal treatment on the temperature dependence of CO₂ gas permeation.

CO₂ permeability at 1 atm for PI*20EO1, as well as its thermally treated counterpart, PI*20EO1TT were fit to an Arrhenius relationship to determine the permeation activation energy:

$$P = P_0 \times e^{-\frac{E_p}{RT}}$$

where P is the permeability in units of Barrer, P_0 is the pre-exponential factor, T is the temperature in units of K, R is the universal gas constant ($8.314 \text{ E-}03 \frac{\text{kJ}}{\text{mol K}}$), and E_p is the permeation activation energy ($\frac{\text{kJ}}{\text{mol}}$). Plotting $\ln(P)$ vs. $1/T$, as shown in Figure S16, a linear relationship was obtained, whose slope is proportional to E_p .

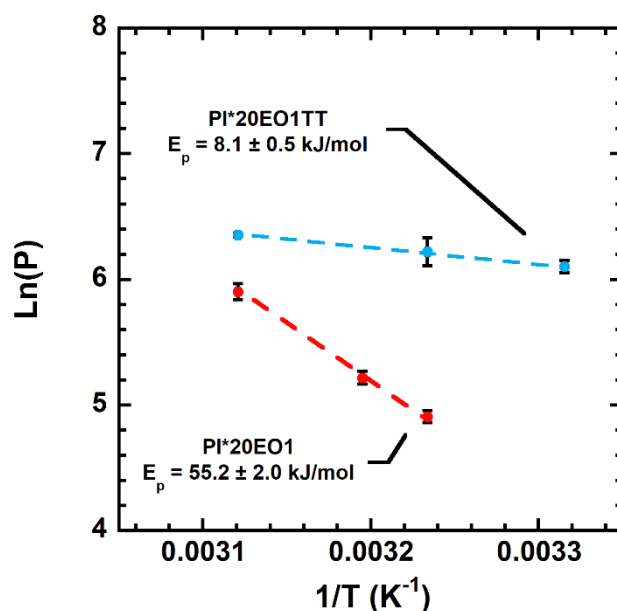


Figure S3.13. Logarithm of CO₂ permeability at 1 atm (in Barrer) plotted as a function of the reciprocal of the absolute temperature (in K) for PI*20EO1 and PI*20EO1TT. The linear best fit line for PI*20EO1TT $\{-6644x + 26.5, R^2 = 0.999\}$ and PI*20EO1 $\{y = -970x + 9.4, R^2 = 0.996\}$ are shown. Uncertainty was determined using linear error propagation.

Section S3.9. Computer simulation

Computer simulations of models: POP-model and PEO (Figure S3.14) model were carried out by first optimizing the molecules at the AM1 level of theory [73]. Afterward, optimized structures and electronic energies were calculated by Density Functional Theory (DFT)[210], without any geometrical constraint (use of Opt keyword) for both

models using the Becke's three-parameter hybrid function [205,211] with the 6-31G (d, p) basis set (B3LYP/6-31G(d, p)) [212,213] using the Gaussian 09 program [214]. Subsequently, the POP-model and PEO-model (Figure S3.14) were conveniently placed, and they were optimized to give the POP-PEO adduct geometry (Figure S3.14). The resulting optimized geometries were analyzed by determining the difference in electronic energy between the POP-PEO adduct and the sum of the electronic energies of the corresponding models (POP-model, and PEO-model), as shown in Table S3.7. Molecular depictions of the interaction adduct were created using the GaussView program [215], and it is seen in Figure S3.17.

Table S3.7. *Electronic energy of the models and the corresponding adduct as calculated by DFT quantum-mechanical method.*

Molecule	DFT Electronic energy (Hartree)	DFT Interaction electronic energy (Hartree)	DFT Interaction electronic energy (kcal mol⁻¹)
PEO-model	-308.8683803	-0.01593389	10.0
POP-Model	-901.1810128		
POP-PEO adduct	-1210.065327		

S3.9.1. Molecular picture of the adduct geometry between an isatin-model and a PEO-model

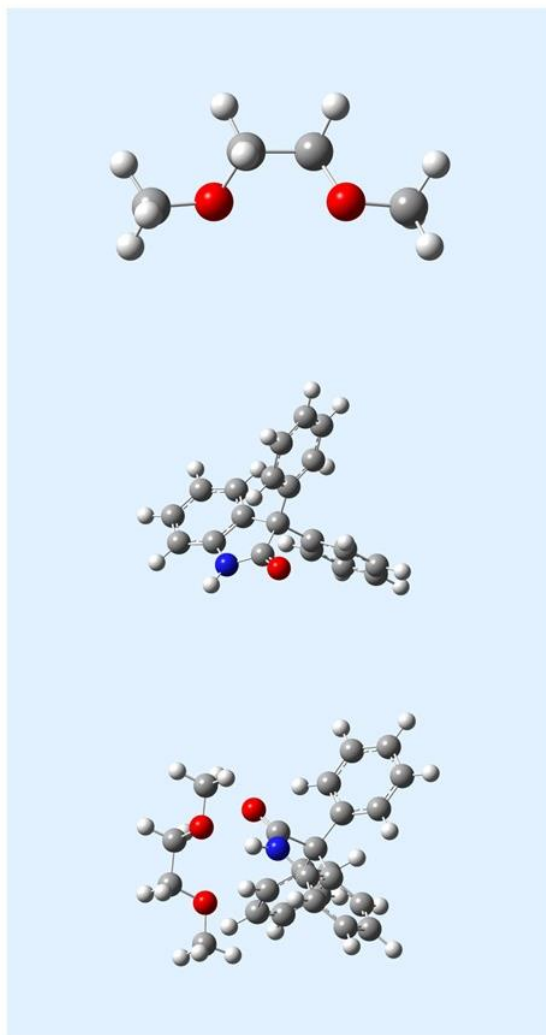


Figure S3.14. Molecular picture of the interaction between an isatin-model and a PEO-model. Top; PEO model, middle; Isatin model; bottom; Optimized geometry of the adduct of isatin-model and PEO-model

Chapter 8

8. References

- [1] J. Houghton, Global warming, *Reports Prog. Phys.* 68 (2005) 1343–1403. <https://doi.org/10.1088/0034-4885/68/6/R02>.
- [2] Greenhouse gases continued to increase rapidly in 2022 | National Oceanic and Atmospheric Administration, (n.d.). <https://www.noaa.gov/news-release/greenhouse-gases-continued-to-increase-rapidly-in-2022> (accessed October 31, 2023).
- [3] Causas del cambio climático, (n.d.). https://climate.ec.europa.eu/climate-change/causes-climate-change_es (accessed October 31, 2023).
- [4] COP27: Delivering for people and the planet | United Nations, (n.d.). <https://www.un.org/en/climatechange/cop27> (accessed October 31, 2023).
- [5] Key aspects of the Paris Agreement | UNFCCC, (n.d.). <https://unfccc.int/most-requested/key-aspects-of-the-paris-agreement> (accessed October 31, 2023).
- [6] A. Gulzar, A. Gulzar, M.B. Ansari, F. He, S. Gai, P. Yang, Carbon dioxide utilization: A paradigm shift with CO₂ economy, *Chem. Eng. J. Adv.* 3 (2020) 100013. <https://doi.org/10.1016/j.cej.2020.100013>.
- [7] BP, BP Statistical Review of World Energy 2022,(71st edition), <https://www.bp.com/content/dam/bp/business-sites/en/global/corporate/pdfs/energy-economics/statistical-review/bp-stats-review-2022-full-report.pdf>. (2022) 1–60. <https://www.bp.com/content/dam/bp/business-sites/en/global/corporate/pdfs/energy-economics/statistical-review/bp-stats-review-2022-full-report.pdf>.
- [8] E. Liu, X. Lu, D. Wang, A Systematic Review of Carbon Capture, Utilization and Storage: Status, Progress and Challenges, *Energies*. 16 (2023) 2865. <https://doi.org/10.3390/en16062865>.
- [9] J. Sleeman, Transport of Coal., *Min. Technol.* 58 (1976) 665.
- [10] A. Reyes-Lua, Y. Arellano, I. Treu Roe, L. Rycroft, T. Wildenborg, K. Jordal, CO₂ ship transport: Benefits for early movers and aspects to consider 4th Report of the Thematic Working Group on: CO₂ Transport, Storage, and Networks, (2021) 33. [https://www.ccusnetwork.eu/sites/default/files/TG3_Briefing-CO₂-ship-transport-Benefits-for-early-movers-and-aspects-to-consider.pdf](https://www.ccusnetwork.eu/sites/default/files/TG3_Briefing-CO2-ship-transport-Benefits-for-early-movers-and-aspects-to-consider.pdf).
- [11] L. Fu, Z. Ren, W. Si, Q. Ma, W. Huang, K. Liao, Z. Huang, Y. Wang, J. Li, P. Xu, Research progress on CO₂ capture and utilization technology, *J. CO₂ Util.* 66 (2022) 102260.

- <https://doi.org/10.1016/j.jcou.2022.102260>.
- [12] C. Hepburn, E. Adlen, J. Beddington, E.A. Carter, S. Fuss, N. Mac Dowell, J.C. Minx, P. Smith, C.K. Williams, The technological and economic prospects for CO₂ utilization and removal, *Nature*. 575 (2019) 87–97. <https://doi.org/10.1038/s41586-019-1681-6>.
 - [13] R. Chauvy, G. De Weireld, CO₂ Utilization Technologies in Europe: A Short Review, *Energy Technol.* 8 (2020) 12. <https://doi.org/10.1002/ente.202000627>.
 - [14] R. Gholami, A. Raza, S. Iglauer, Leakage risk assessment of a CO₂ storage site: A review, *Earth-Science Rev.* 223 (2021) 103849. <https://doi.org/10.1016/j.earscirev.2021.103849>.
 - [15] A.I. Osman, M. Hefny, M.I.A. Abdel Maksoud, A.M. Elgarahy, D.W. Rooney, Recent advances in carbon capture storage and utilisation technologies: a review, *Environ. Chem. Lett.* 19 (2021) 797–849. <https://doi.org/10.1007/s10311-020-01133-3>.
 - [16] T.A. Jimoh, F.O. Omoarukhe, E.I. Epelle, P.U. Okoye, E. Oke Olusola, A. Mukherjee, J.A. Okolie, *Introduction to Carbon Capture by Solvent-based Technologies*, Elsevier Ltd., 2023. <https://doi.org/10.1016/b978-0-323-93940-9.00003-7>.
 - [17] F.O. Ochedi, J. Yu, H. Yu, Y. Liu, A. Hussain, *Carbon dioxide capture using liquid absorption methods: a review*, Springer International Publishing, 19 (2021) 77–109. <https://doi.org/10.1007/s10311-020-01093-8>.
 - [18] M. Galizia, W.S. Chi, Z.P. Smith, T.C. Merkel, R.W. Baker, B.D. Freeman, 50th Anniversary Perspective : Polymers and Mixed Matrix Membranes for Gas and Vapor Separation: A Review and Prospective Opportunities, *Macromolecules*. 50 (2017) 7809–7843. <https://doi.org/10.1021/acs.macromol.7b01718>.
 - [19] R.W. Baker, Future directions of membrane gas separation technology, *Ind. Eng. Chem. Res.* 41 (2002) 1393–1411. <https://doi.org/10.1021/ie0108088>.
 - [20] R. Sidhikku Kandath Valappil, N. Ghasem, M. Al-Marzouqi, Current and future trends in polymer membrane-based gas separation technology: A comprehensive review, *J. Ind. Eng. Chem.* 98 (2021) 103–129. <https://doi.org/10.1016/j.jiec.2021.03.030>.
 - [21] Y. Ding, Perspective on Gas Separation Membrane Materials from Process Economics Point of View, *Ind. Eng. Chem. Res.* 59 (2020) 556–568. <https://doi.org/10.1021/acs.iecr.9b05975>.
 - [22] M. Mulder, *Basic Principle of Membrane Technology*; Springer-Science+Business Media, 110 (1991) 1689–1699.
 - [23] B.D. Freeman, I. Pinnau, *Gas and Liquid Separations Using Membranes: An Overview*,

- in: 2004: pp. 1–23. <https://doi.org/10.1021/bk-2004-0876.ch001>.
- [24] M. Sarbolouki, Advanced materials for membrane separations, Volume 876, ACS Symposium Series. Edited by I Pinnau and BD Freeman. American Chemical Society, Washington, DC, 2004, Polym. Int. 54 (2005) 614–614. <https://doi.org/10.1002/pi.1716>.
 - [25] M. Calle, C. García, A.E. Lozano, J.G. De la Campa, J. De Abajo, C. Álvarez, Local chain mobility dependence on molecular structure in polyimides with bulky side groups: Correlation with gas separation properties, J. Memb. Sci. 434 (2013) 121–129. <https://doi.org/10.1016/j.memsci.2013.01.054>.
 - [26] L.M. Robeson, Correlation of separation factor versus permeability for polymeric membranes, J. Memb. Sci. 62 (1991) 165–185. [https://doi.org/10.1016/0376-7388\(91\)80060-J](https://doi.org/10.1016/0376-7388(91)80060-J).
 - [27] L.M. Robeson, The upper bound revisited, J. Memb. Sci. 320 (2008) 390–400. <https://doi.org/10.1016/j.memsci.2008.04.030>.
 - [28] R. Swaidan, B. Ghanem, I. Pinnau, Fine-Tuned Intrinsically Ultramicroporous Polymers Redefine the Permeability/Selectivity Upper Bounds of Membrane-Based Air and Hydrogen Separations, ACS Macro Lett. 4 (2015) 947–951. <https://doi.org/10.1021/acsmacrolett.5b00512>.
 - [29] B. Comesaña-Gándara, J. Chen, C.G. Bezzu, M. Carta, I. Rose, M.C. Ferrari, E. Esposito, A. Fuoco, J.C. Jansen, N.B. McKeown, Redefining the Robeson upper bounds for CO₂/CH₄ and CO₂/N₂ separations using a series of ultrapermeable benzotriptycene-based polymers of intrinsic microporosity, Energy Environ. Sci. 12 (2019) 2733–2740. <https://doi.org/10.1039/c9ee01384a>.
 - [30] B.D. Freeman, Basis of Permeability/Selectivity Tradeoff Relations in Polymeric Gas Separation Membranes, Macromolecules. 32 (1999) 375–380. <https://doi.org/10.1021/ma9814548>.
 - [31] L.M. Robeson, Z.P. Smith, B.D. Freeman, D.R. Paul, Contributions of diffusion and solubility selectivity to the upper bound analysis for glassy gas separation membranes, J. Memb. Sci. 453 (2014) 71–83. <https://doi.org/10.1016/j.memsci.2013.10.066>.
 - [32] Y. Wang, B.S. Ghanem, Y. Han, I. Pinnau, State-of-the-art polymers of intrinsic microporosity for high-performance gas separation membranes, Curr. Opin. Chem. Eng. 35 (2022) 100755. <https://doi.org/10.1016/j.coche.2021.100755>.
 - [33] S. Bandehali, A. Ebadi Amooghin, H. Sanaeepur, R. Ahmadi, A. Fuoco, J.C. Jansen, S. Shirazian, Polymers of intrinsic microporosity and thermally rearranged polymer

- membranes for highly efficient gas separation, *Sep. Purif. Technol.* 278 (2021) 119513. <https://doi.org/10.1016/j.seppur.2021.119513>.
- [34] H. Sanaeepur, A. Ebadi Amooghin, S. Bandehali, A. Moghadassi, T. Matsuura, B. Van der Bruggen, Polyimides in membrane gas separation: Monomer's molecular design and structural engineering, *Prog. Polym. Sci.* 91 (2019) 80–125. <https://doi.org/10.1016/j.progpolymsci.2019.02.001>.
- [35] F. Kadir Khan, P.S. Goh, A.F. Ismail, W.N.F. Wan Mustapa, M.H.M. Halim, W.K. Soh, S.Y. Yeo, Recent Advances of Polymeric Membranes in Tackling Plasticization and Aging for Practical Industrial CO₂/CH₄ Applications—A Review, *Membranes*. 12 (2022) 71. <https://doi.org/10.3390/membranes12010071>.
- [36] M.M. Merrick, R. Sujanani, B.D. Freeman, Glassy polymers: Historical findings, membrane applications, and unresolved questions regarding physical aging, *Polymer*. 211 (2020) 123176. <https://doi.org/10.1016/j.polymer.2020.123176>.
- [37] J.K. Adewole, A.L. Ahmad, Polymeric membrane materials selection for high-pressure CO₂ removal from natural gas, *J. Polym. Res.* 24 (2017) 70. <https://doi.org/10.1007/s10965-017-1231-6>.
- [38] A. Bos, I.G.M. Pünt, M. Wessling, H. Strathmann, CO₂-induced plasticization phenomena in glassy polymers, *J. Memb. Sci.* 155 (1999) 67–78. [https://doi.org/10.1016/S0376-7388\(98\)00299-3](https://doi.org/10.1016/S0376-7388(98)00299-3).
- [39] R. Swaidan, B. Ghanem, E. Litwiller, I. Pinnau, Physical Aging, Plasticization and Their Effects on Gas Permeation in “Rigid” Polymers of Intrinsic Microporosity, *Macromolecules*. 48 (2015) 6553–6561. <https://doi.org/10.1021/acs.macromol.5b01581>.
- [40] K.L. Gleason, Z.P. Smith, Q. Liu, D.R. Paul, B.D. Freeman, Pure- and mixed-gas permeation of CO₂ and CH₄ in thermally rearranged polymers based on 3,3'-dihydroxy-4,4'-diamino-biphenyl (HAB) and 2,2'-bis-(3,4-dicarboxyphenyl) hexafluoropropane dianhydride (6FDA), *J. Memb. Sci.* 475 (2015) 204–214. <https://doi.org/10.1016/j.memsci.2014.10.014>.
- [41] J.M. Hutchinson, Physical aging of polymers, *Prog. Polym. Sci.* 20 (1995) 703–760. [https://doi.org/10.1016/0079-6700\(94\)00001-I](https://doi.org/10.1016/0079-6700(94)00001-I).
- [42] M.S. McCaig, D.R. Paul, Effect of film thickness on the changes in gas permeability of a glassy polyarylate due to physical aging: Part I. Experimental observations, *Polymer*. 41 (2000) 629–637. [https://doi.org/10.1016/S0032-3861\(99\)00172-X](https://doi.org/10.1016/S0032-3861(99)00172-X).
- [43] H. Furukawa, K.E. Cordova, M. O'Keeffe, O.M. Yaghi, *The Chemistry and Applications*

- of Metal-Organic Frameworks, *Science* 341 (2013) 6149. <https://doi.org/10.1126/science.1230444>.
- [44] H.B. Park, J. Kamcev, L.M. Robeson, M. Elimelech, B.D. Freeman, Maximizing the right stuff: The trade-off between membrane permeability and selectivity, *Science*. 356 (2017) 1138–1148. <https://doi.org/10.1126/science.aab0530>.
- [45] C. Casado-Coterillo, Mixed Matrix Membranes, *Membranes*. 9 (2019) 149. <https://doi.org/10.3390/membranes9110149>.
- [46] J. Dechnik, J. Gascon, C.J. Doonan, C. Janiak, C.J. Sumby, Mixed-Matrix Membranes, *Angew. Chemie Int. Ed.* 56 (2017) 9292–9310. <https://doi.org/10.1002/anie.201701109>.
- [47] A.R. Kamble, C.M. Patel, Z.V.P. Murthy, A review on the recent advances in mixed matrix membranes for gas separation processes, *Renew. Sustain. Energy Rev.* 145 (2021) 111062. <https://doi.org/10.1016/j.rser.2021.111062>.
- [48] M.I.F. Zainuddin, A.L. Ahmad, Mixed matrix membrane development progress and prospect of using 2D nanosheet filler for CO₂ separation and capture, *J. CO₂ Util.* 62 (2022) 102094. <https://doi.org/10.1016/j.jcou.2022.102094>.
- [49] T.T. Moore, W.J. Koros, Non-ideal effects in organic–inorganic materials for gas separation membranes, *J. Mol. Struct.* 739 (2005) 87–98. <https://doi.org/10.1016/j.molstruc.2004.05.043>.
- [50] S. Das, P. Heasman, T. Ben, S. Qiu, Porous Organic Materials: Strategic Design and Structure–Function Correlation, *Chem. Rev.* 117 (2017) 1515–1563. <https://doi.org/10.1021/acs.chemrev.6b00439>.
- [51] Z. Xiang, D. Cao, Porous covalent–organic materials: synthesis, clean energy application and design, *J. Mater. Chem. A*. 1 (2013) 2691–2718. <https://doi.org/10.1039/C2TA00063F>.
- [52] G. Ji, Y. Zhao, Z. Liu, Design of porous organic polymer catalysts for transformation of carbon dioxide, *Green Chem. Eng.* 3 (2022) 96–110. <https://doi.org/10.1016/j.gce.2021.11.011>.
- [53] N. Taheri, M. Dinari, M. Asgari, Recent Applications of Porous Organic Polymers Prepared via Friedel-Crafts Reaction under the Catalysis of AlCl₃: A Review, *ACS Appl. Polym. Mater.* 4 (2022) 6288–6302. <https://doi.org/10.1021/acsapm.2c00927>.
- [54] Y. Wang, Y. Yang, Q. Deng, W. Chen, Y. Zhang, Y. Zhou, Z. Zou, Recent Progress of Amorphous Porous Organic Polymers as Heterogeneous Photocatalysts for Organic

- Synthesis, Adv. Funct. Mater. 2307179 (2023) 1–40.
<https://doi.org/10.1002/adfm.202307179>.
- [55] A. Giri, Y. Khakre, G. Shreeraj, T.K. Dutta, S. Kundu, A. Patra, The order-disorder conundrum: a trade-off between crystalline and amorphous porous organic polymers for task-specific applications, J. Mater. Chem. A. 10 (2022) 17077–17121.
<https://doi.org/10.1039/d2ta01546c>.
- [56] S. Ramakrishnan, Condensation polymerization, Resonance. 22 (2017) 355–368.
<https://doi.org/10.1007/s12045-017-0475-0>.
- [57] W.H. Carothers, Polymerization., Chem. Rev. 8 (1931) 353–426.
<https://doi.org/10.1021/cr60031a001>.
- [58] W.H. Carothers, Polymers and polyfunctionality, Trans. Faraday Soc. 32 (1936) 39.
<https://doi.org/10.1039/tf9363200039>.
- [59] P.M. S. Wilson, H.D.; Hergenrother, Book Reviews, J. Soc. Welf. Fam. Law. 13 (1991) 522–524. <https://doi.org/10.1080/09649069108413580>.
- [60] A.E. Lozano, J. de Abajo, J.G. de la Campa, Synthesis of Aromatic Polyisophthalamides by in Situ Silylation of Aromatic Diamines, Macromolecules. 30 (1997) 2507–2508.
<https://doi.org/10.1021/ma961543p>.
- [61] D.M. Muñoz, M. Calle, J.G.J.G. de La Campa, J. de Abajo, A.E. Lozano, D.M. Munoz, M. Calle, J.G.J.G. de La Campa, J. de Abajo, A.E. Lozano, An Improved Method for Preparing Very High Molecular Weight Polyimides, Macromolecules. 42 (2009) 5892–5894. <https://doi.org/10.1021/ma9005268>.
- [62] D.M. Muñoz, J.G. De La Campa, J. De Abajo, A.E. Lozano, Experimental and theoretical study of an improved activated polycondensation method for aromatic polyimides, Macromolecules. 40 (2007) 8225–8232. <https://doi.org/10.1021/ma070842j>.
- [63] B. Lopez-Iglesias, F. Suárez-García, C. Aguilar-Lugo, A. González Ortega, C. Bartolomé, J.M. Martínez-Ilarduya, J.G. De La Campa, Á.E. Lozano, C. Álvarez, Microporous Polymer Networks for Carbon Capture Applications, ACS Appl. Mater. Interfaces. 10 (2018) 26195–26205. <https://doi.org/10.1021/acsami.8b05854>.
- [64] S. Yuan, B. Dorney, D. White, S. Kirklin, P. Zapol, L. Yu, D.J. Liu, Microporous polyphenylenes with tunable pore size for hydrogen storage, Chem. Commun. 46 (2010) 4547–4549. <https://doi.org/10.1039/c0cc00235f>.
- [65] Z. ALOthman, A Review: Fundamental Aspects of Silicate Mesoporous Materials,

- Materials. 5 (2012) 2874–2902. <https://doi.org/10.3390/ma5122874>.
- [66] M.E. Verde Sesto, Nuevos polímeros porosos como soportadores para catalizadores. Tesis Doctoral, (2014) 256. https://repositorio.uam.es/bitstream/handle/10486/660494/verde_sesto_mariaester.pdf?sequence=1.
- [67] B.J. Butler, D.O. Muhleman, M.A. Slade, M.S. Rice, S.E. Wood, A.R. Vasavada, D.A. Paige, S.E. Wood, D.M. Hunten, K. Ladders, J. Ulrichs, D.E. Shemansky, R.M. Killen, G.J. Taylor, B.G. Bills, D.A. Paige, L. Jorda, J.A.M. Bleeker, J. Geiss, M. Huber, J. Veverka, D.R. Davis, W.K. Hartmann, M.J. Gaffey, R.P. Binzel, T. Gehrels, M.S. Matthews, An Efficient Polymer Molecular Sieve for Membrane Gas Separations, *Science* 80. (2013) 303–307.
- [68] L. Matesanz-Niño, C. Aguilar-Lugo, P. Prádanos, A. Hernandez, C. Bartolomé, J.G. de la Campa, L. Palacio, A. González-Ortega, M. Galizia, C. Álvarez, Á.E. Lozano, Gas separation membranes obtained by partial pyrolysis of polyimides exhibiting polyethylene oxide moieties, *Polymer*. 247 (2022) 124789. <https://doi.org/10.1016/j.polymer.2022.124789>.
- [69] A. Brunetti, M. Cersosimo, G. Dong, K.T. Woo, J. Lee, J.S. Kim, Y.M. Lee, E. Drioli, G. Barbieri, In situ restoring of aged thermally rearranged gas separation membranes, *J. Memb. Sci.* 520 (2016) 671–678. <https://doi.org/10.1016/j.memsci.2016.07.030>.
- [70] A.J. Hill, S.J. Pas, T.J. Bastow, M.I. Burgar, K. Nagai, L.G. Toy, B.D. Freeman, Influence of methanol conditioning and physical aging on carbon spin-lattice relaxation times of poly(1-trimethylsilyl-1-propyne), *J. Memb. Sci.* 243 (2004) 37–44. <https://doi.org/10.1016/j.memsci.2004.06.007>.
- [71] A. Fuoco, B. Satilmis, T. Uyar, M. Monteleone, E. Esposito, C. Muzzi, E. Tocci, M. Longo, M.P. De Santo, M. Lanč, K. Friess, O. Vopička, P. Izák, J.C. Jansen, Comparison of pure and mixed gas permeation of the highly fluorinated polymer of intrinsic microporosity PIM-2 under dry and humid conditions: Experiment and modelling, *J. Memb. Sci.* 594 (2020) 6149. <https://doi.org/10.1016/j.memsci.2019.117460>.
- [72] Z.X. Low, P.M. Budd, N.B. McKeown, D.A. Patterson, Gas Permeation Properties, Physical Aging, and Its Mitigation in High Free Volume Glassy Polymers, *Chem. Rev.* 118 (2018) 5871–5911. <https://doi.org/10.1021/acs.chemrev.7b00629>.
- [73] M.J.S. Dewar, E.G. Zebisch, E.F. Healy, J.J.P. Stewart, Development and use of quantum mechanical molecular models. 76. AM1: a new general purpose quantum mechanical

- molecular model, *J. Am. Chem. Soc.* 107 (1985) 3902–3909. <https://doi.org/10.1021/ja00299a024>.
- [74] M.J.S. Dewar, E.G. Zoebisch, E.F. Healy, J.J.P. Stewart, Development and use of quantum mechanical molecular models. 76. AM1: a new general purpose quantum mechanical molecular model, *J. Am. Chem. Soc.* 107 (1985) 3902–3909. <https://doi.org/10.1021/ja00299a024>.
- [75] D.H. Everett, *Manual of Symbols and Terminology for Physicochemical Quantities and Units*, Appendix II: Definitions, Terminology and Symbols in Colloid and Surface Chemistry, *Pure Appl. Chem.* 31 (1972) 577–638. <https://doi.org/10.1351/pac197231040577>.
- [76] J. Rouquerol, D. Avnir, C.W. Fairbridge, D.H. Everett, J.M. Haynes, N. Pernicone, J.D.F. Ramsay, K.S.W. Sing, K.K. Unger, Recommendations for the characterization of porous solids (Technical Report), *Pure Appl. Chem.* 66 (1994) 1739–1758. <https://doi.org/10.1351/pac199466081739>.
- [77] R.V.R.A. Rios, J. Silvestre-Albero, A. Sepúlveda-Escribano, M. Molina-Sabio, F. Rodríguez-Reinoso, Kinetic Restrictions in the Characterization of Narrow Microporosity in Carbon Materials, *J. Phys. Chem. C* 111 (2007) 3803–3805. <https://doi.org/10.1021/jp0701486>.
- [78] J.M. Martín Martínez, *Porosidad de Carbones II Teoría de Polanyi - Dubinin*, 1990.
- [79] J. Jagiello, Stable Numerical Solution of the Adsorption Integral Equation Using Splines, *Langmuir*. 10 (1994) 2778–2785. <https://doi.org/10.1021/la00020a045>.
- [80] A.L. Myers, J.M. Prausnitz, Thermodynamics of mixed-gas adsorption, *AIChE J.* 11 (1965) 121–127. <https://doi.org/10.1002/aic.690110125>.
- [81] S. Bartholdy, M.G. Bjørner, E. Solbraa, A. Shapiro, G.M. Kontogeorgis, Capabilities and Limitations of Predictive Engineering Theories for Multicomponent Adsorption, *Ind. Eng. Chem. Res.* 52 (2013) 11552–11563. <https://doi.org/10.1021/ie400593b>.
- [82] C.M. Simon, B. Smit, M. Haranczyk, PyIAST: Ideal adsorbed solution theory (IAST) Python package, *Comput. Phys. Commun.* 200 (2016) 364–380. <https://doi.org/10.1016/j.cpc.2015.11.016>.
- [83] D.S. Scholl, R.P. Lively, Seven chemical separations to change the World, *Nature*. 532 (2016) 435–437.
- [84] H. Lin, Integrated membrane material and process development for gas separation, *Curr.*

- Opin. Chem. Eng. 4 (2014) 54–61. <https://doi.org/10.1016/j.coche.2014.01.010>.
- [85] M.E. Boot-Handford, J.C. Abanades, E.J. Anthony, M.J. Blunt, S. Brandani, N. Mac Dowell, J.R. Fernández, M.-C. Ferrari, R. Gross, J.P. Hallett, R.S. Haszeldine, P. Heptonstall, A. Lyngfelt, Z. Makuch, E. Mangano, R.T.J. Porter, M. Pourkashanian, G.T. Rochelle, N. Shah, J.G. Yao, P.S. Fennell, Carbon capture and storage update, *Energy Environ. Sci.* 7 (2014) 130–189. <https://doi.org/10.1039/C3EE42350F>.
- [86] P. Bernardo, E. Drioli, G. Golemme, Membrane Gas Separation: A Review/State of the Art, *Ind. Eng. Chem. Res.* 48 (2009) 4638–4663. <https://doi.org/10.1021/ie8019032>.
- [87] T.C. Merkel, H. Lin, X. Wei, R. Baker, Power plant post-combustion carbon dioxide capture: An opportunity for membranes, *J. Memb. Sci.* 359 (2010) 126–139. <https://doi.org/10.1016/j.memsci.2009.10.041>.
- [88] P. Luis, T. Van Gerven, B. Van der Bruggen, Recent developments in membrane-based technologies for CO₂ capture, *Prog. Energy Combust. Sci.* 38 (2012) 419–448. <https://doi.org/10.1016/j.pecs.2012.01.004>.
- [89] D.F. Sanders, Z.P. Smith, R. Guo, L.M. Robeson, J.E. McGrath, D.R. Paul, B.D. Freeman, Energy-efficient polymeric gas separation membranes for a sustainable future: A review, *Polymer*. 54 (2013) 4729–4761. <https://doi.org/10.1016/j.polymer.2013.05.075>.
- [90] R.W. Baker, B.T. Low, Gas separation membrane materials: A perspective, *Macromolecules*. 47 (2014) 6999–7013. <https://doi.org/10.1021/ma501488s>.
- [91] Y. Yampolskii, Polymeric gas separation membranes, *Macromolecules*. 45 (2012) 3298–3311. <https://doi.org/10.1021/ma300213b>.
- [92] M. Reza kazemi, M. Sadrzadeh, T. Matsuura, Thermally stable polymers for advanced high-performance gas separation membranes, *Prog. Energy Combust. Sci.* 66 (2018) 1–41. <https://doi.org/10.1016/j.pecs.2017.11.002>.
- [93] J. Deng, Z. Huang, B.J. Sundell, D.J. Harrigan, S.A. Sharber, K. Zhang, R. Guo, M. Galizia, State of the art and prospects of chemically and thermally aggressive membrane gas separations: Insights from polymer science, *Polymer*. 229 (2021) 123988. <https://doi.org/10.1016/j.polymer.2021.123988>.
- [94] L.M. Robeson, Q. Liu, B.D. Freeman, D.R. Paul, Comparison of transport properties of rubbery and glassy polymers and the relevance to the upper bound relationship, *J. Memb. Sci.* 476 (2015) 421–431. <https://doi.org/10.1016/j.memsci.2014.11.058>.
- [95] M. Minelli, G.C. Sarti, Elementary prediction of gas permeability in glassy polymers, *J.*

- Memb. Sci. 521 (2017) 73–83. <https://doi.org/10.1016/j.memsci.2016.09.001>.
- [96] B.D. Freeman, Basis of permeability/selectivity tradeoff relations in polymeric gas separation membranes, *Macromolecules*. 32 (1999) 375–380. <https://doi.org/10.1021/ma9814548>.
- [97] C. Álvarez, A.E. Lozano, J.G. de la Campa, High-productivity gas separation membranes derived from pyromellitic dianhydride and nonlinear diamines, *J. Memb. Sci.* 501 (2016) 191–198. <https://doi.org/10.1016/j.memsci.2015.11.039>.
- [98] P.M. Budd, N.B. McKeown, Highly permeable polymers for gas separation membranes, *Polym. Chem.* 1 (2010) 63. <https://doi.org/10.1039/b9py00319c>.
- [99] I. Rose, C.G. Bezzu, M. Carta, B. Comesaña-Gándara, E. Lasseuguette, M.C. Ferrari, P. Bernardo, G. Clarizia, A. Fuoco, J.C. Jansen, K.E. Hart, T.P. Liyana-Arachchi, C.M. Colina, N.B. McKeown, Polymer ultrapermeability from the inefficient packing of 2D chains, *Nat. Mater.* 16 (2017) 932–937. <https://doi.org/10.1038/nmat4939>.
- [100] Y. Okamoto, H.-C. Chiang, M. Fang, M. Galizia, T. Merkel, M. Yavari, H. Nguyen, H. Lin, Perfluorodioxolane Polymers for Gas Separation Membrane Applications, *Membranes*. 10 (2020) 394. <https://doi.org/10.3390/membranes10120394>.
- [101] M. Yavari, M. Fang, H. Nguyen, T.C. Merkel, H. Lin, Y. Okamoto, Dioxolane-Based Perfluoropolymers with Superior Membrane Gas Separation Properties, *Macromolecules*. 51 (2018) 2489–2497. <https://doi.org/10.1021/acs.macromol.8b00273>.
- [102] L.M. Robeson, M.E. Dose, B.D. Freeman, D.R. Paul, Analysis of the transport properties of thermally rearranged (TR) polymers and polymers of intrinsic microporosity (PIM) relative to upper bound performance, *J. Memb. Sci.* 525 (2017) 18–24. <https://doi.org/10.1016/j.memsci.2016.11.085>.
- [103] D. Cangialosi, V.M. Boucher, A. Alegría, J. Colmenero, Physical aging in polymers and polymer nanocomposites: recent results and open questions, *Soft Matter*. 9 (2013) 8619. <https://doi.org/10.1039/c3sm51077h>.
- [104] Y. Xiao, B.T. Low, S.S. Hosseini, T.S. Chung, D.R. Paul, The strategies of molecular architecture and modification of polyimide-based membranes for CO₂ removal from natural gas—A review, *Prog. Polym. Sci.* 34 (2009) 561–580. <https://doi.org/10.1016/j.progpolymsci.2008.12.004>.
- [105] A. Bos, I. Pünt, H. Strathmann, M. Wessling, I. Pünt, H. Strathmann, M. Wessling, Suppression of gas separation membrane plasticization by homogeneous polymer blending, *AIChE J.* 47 (2001) 1088–1093. <https://doi.org/10.1002/aic.690470515>.

- [106] S. Mazinani, R. Ramezani, G.F. Molelekwa, S. Darvishmanesh, R. Di Felice, B. Van der Bruggen, Plasticization suppression and CO₂ separation enhancement of Matrimid through homogeneous blending with a new high performance polymer, *J. Memb. Sci.* 574 (2019) 318–324. <https://doi.org/10.1016/j.memsci.2018.12.060>.
- [107] W.F. Yong, F.Y. Li, T.S. Chung, Y.W. Tong, Molecular interaction, gas transport properties and plasticization behavior of cPIM-1/Torlon blend membranes, *J. Memb. Sci.* 462 (2014) 119–130. <https://doi.org/10.1016/j.memsci.2014.03.046>.
- [108] K. Vanherck, G. Koeckelberghs, I.F.J. Vankelecom, Crosslinking polyimides for membrane applications: A review, *Prog. Polym. Sci.* 38 (2013) 874–896. <https://doi.org/10.1016/j.progpolymsci.2012.11.001>.
- [109] S.D. Kelman, B.W. Rowe, C.W. Bielawski, S.J. Pas, A.J. Hill, D.R. Paul, B.D. Freeman, Crosslinking poly[1-(trimethylsilyl)-1-propyne] and its effect on physical stability, *J. Memb. Sci.* 320 (2008) 123–134. <https://doi.org/10.1016/j.memsci.2008.03.064>.
- [110] H. Eguchi, D.J. Kim, W.J. Koros, Chemically cross-linkable polyimide membranes for improved transport plasticization resistance for natural gas separation, *Polymer*. 58 (2015) 121–129. <https://doi.org/10.1016/j.polymer.2014.12.064>.
- [111] W.F. Yong, K.H.A. Kwek, K.-S. Liao, T.-S. Chung, Suppression of aging and plasticization in highly permeable polymers, *Polymer*. 77 (2015) 377–386. <https://doi.org/10.1016/j.polymer.2015.09.075>.
- [112] M. Puertas-Bartolomé, M.E. Dose, P. Bosch, B.D. Freeman, J.E. McGrath, J.S. Riffle, A.E. Lozano, J.G. De La Campa, C. Álvarez, Aromatic poly(ether ether ketone)s capable of crosslinking via UV irradiation to improve gas separation performance, *RSC Adv.* 7 (2017) 55371–55381. <https://doi.org/10.1039/c7ra11018a>.
- [113] M. Askari, T.-S. Chung, Natural gas purification and olefin/paraffin separation using thermal cross-linkable co-polyimide/ZIF-8 mixed matrix membranes, *J. Memb. Sci.* 444 (2013) 173–183. <https://doi.org/10.1016/j.memsci.2013.05.016>.
- [114] H. Li, Y. Liu, A review of polymer-derived carbon molecular sieve membranes for gas separation, *New Carbon Mater.* 37 (2022) 484–507. [https://doi.org/10.1016/S1872-5805\(22\)60613-9](https://doi.org/10.1016/S1872-5805(22)60613-9).
- [115] K.M. Steel, W.J. Koros, An investigation of the effects of pyrolysis parameters on gas separation properties of carbon materials, *Carbon N. Y.* 43 (2005) 1843–1856. <https://doi.org/10.1016/j.carbon.2005.02.028>.
- [116] M. Kiyono, P.J. Williams, W.J. Koros, Effect of polymer precursors on carbon molecular

- sieve structure and separation performance properties, *Carbon N. Y.* 48 (2010) 4432–4441. <https://doi.org/10.1016/j.carbon.2010.08.002>.
- [117] J.S. Adams, A.K. Itta, C. Zhang, G.B. Wenz, O. Sanyal, W.J. Koros, New insights into structural evolution in carbon molecular sieve membranes during pyrolysis, *Carbon N. Y.* 141 (2019) 238–246. <https://doi.org/10.1016/j.carbon.2018.09.039>.
- [118] M.E. Rezac, E. Todd Sorensen, H.W. Beckham, Transport properties of crosslinkable polyimide blends, *J. Memb. Sci.* 136 (1997) 249–259. [https://doi.org/10.1016/S0376-7388\(97\)00170-1](https://doi.org/10.1016/S0376-7388(97)00170-1).
- [119] Y.J. Fu, C.C. Hu, D.W. Lin, H.A. Tsai, S.H. Huang, W.S. Hung, K.R. Lee, J.Y. Lai, Adjustable microstructure carbon molecular sieve membranes derived from thermally stable polyetherimide/polyimide blends for gas separation, *Carbon N. Y.* 113 (2017) 10–17. <https://doi.org/10.1016/j.carbon.2016.11.026>.
- [120] L. Escorial, M. de la Viuda, S. Rodríguez, A. Tena, A. Marcos, L. Palacio, P. Prádanos, A.E. Lozano, A. Hernández, Partially pyrolyzed gas-separation membranes made from blends of copolyetherimides and polyimides, *Eur. Polym. J.* 103 (2018) 390–399. <https://doi.org/10.1016/j.eurpolymj.2018.04.031>.
- [121] E.M. Maya, A. Tena, J. de Abajo, J.G. de la Campa, A.E. Lozano, Partially pyrolyzed membranes (PPMs) derived from copolyimides having carboxylic acid groups. Preparation and gas transport properties, *J. Memb. Sci.* 349 (2010) 385–392. <https://doi.org/10.1016/j.memsci.2009.12.001>.
- [122] A.M. Kratochvil, W.J. Koros, Decarboxylation-Induced Cross-Linking of a Polyimide for Enhanced CO₂ Plasticization Resistance, *Macromolecules.* 41 (2008) 7920–7927. <https://doi.org/10.1021/ma801586f>.
- [123] C. Zhang, P. Li, B. Cao, Decarboxylation crosslinking of polyimides with high CO₂/CH₄ separation performance and plasticization resistance, *J. Memb. Sci.* 528 (2017) 206–216. <https://doi.org/10.1016/j.memsci.2017.01.008>.
- [124] C. Staudt-Bickel, W. J. Koros, Improvement of CO₂/CH₄ separation characteristics of polyimides by chemical crosslinking, *J. Memb. Sci.* 155 (1999) 145–154. [https://doi.org/10.1016/S0376-7388\(98\)00306-8](https://doi.org/10.1016/S0376-7388(98)00306-8).
- [125] M. Saberi, A.A. Dadkhah, S.A. Hashemifard, Modeling of simultaneous competitive mixed gas permeation and CO₂ induced plasticization in glassy polymers, *J. Memb. Sci.* 499 (2016) 164–171. <https://doi.org/10.1016/j.memsci.2015.09.044>.
- [126] IPCC, Climate Change 2022 - Mitigation of Climate Change - Full Report, 2022.

- [127] X. Wang, F. Zhang, L. Li, H. Zhang, S. Deng, Carbon dioxide capture, *Advances in Chemical Engineering*. 58 (2021) 297–348. <https://doi.org/10.1016/bs.ache.2021.10.005>.
- [128] F.M. Santos, A.L. Gonçalves, J.C.M. Pires, Negative emission technologies, *Bioenergy with Carbon Capture Storage Using Nat. Resour. Sustain. Dev.* (2019) 1–13. <https://doi.org/10.1016/B978-0-12-816229-3.00001-6>.
- [129] M. Bui, C.S. Adjiman, A. Bardow, E.J. Anthony, A. Boston, S. Brown, P.S. Fennell, S. Fuss, A. Galindo, L.A. Hackett, J.P. Hallett, H.J. Herzog, G. Jackson, J. Kemper, S. Krevor, G.C. Maitland, M. Matuszewski, I.S. Metcalfe, C. Petit, G. Puxty, J. Reimer, D.M. Reiner, E.S. Rubin, S.A. Scott, N. Shah, B. Smit, J.P.M. Trusler, P. Webley, J. Wilcox, N. Mac Dowell, Carbon capture and storage (CCS): the way forward, *Energy Environ. Sci.* 11 (2018) 1062–1176. <https://doi.org/10.1039/C7EE02342A>.
- [130] J.C.M. Pires, F.G. Martins, M.C.M. Alvim-Ferraz, M. Simões, Recent developments on carbon capture and storage: An overview, *Chem. Eng. Res. Des.* 89 (2011) 1446–1460. <https://doi.org/10.1016/j.cherd.2011.01.028>.
- [131] B.P. Spigarelli, S.K. Kawatra, Opportunities and challenges in carbon dioxide capture, *J. CO₂ Util.* 1 (2013) 69–87. <https://doi.org/10.1016/j.jcou.2013.03.002>.
- [132] R.S. Haszeldine, Carbon Capture and Storage: *Energy Environ Science* 325 (2009) 1647–1652. <https://doi.org/10.1126/science.1172246>.
- [133] R. Dawson, A.I. Cooper, D.J. Adams, Nanoporous organic polymer networks, *Prog. Polym. Sci.* 37 (2012) 530–563. <https://doi.org/10.1016/j.progpolymsci.2011.09.002>.
- [134] L. Zou, Y. Sun, S. Che, X. Yang, X. Wang, M. Bosch, Q. Wang, H. Li, M. Smith, S. Yuan, Z. Perry, H. Zhou, Porous Organic Polymers for Post-Combustion Carbon Capture, *Adv. Mater.* 29 (2017) 1700229. <https://doi.org/10.1002/adma.201700229>.
- [135] P. Puthiaraj, W.-S. Ahn, CO₂ Capture by Porous Hyper-Cross-Linked Aromatic Polymers Synthesized Using Tetrahedral Precursors, *Ind. Eng. Chem. Res.* 55 (2016) 7917–7923. <https://doi.org/10.1021/acs.iecr.5b03963>.
- [136] P. Ramirez-Vidal, F. Suárez-García, R.L.S. Canevesi, A. Castro-Muñoz, P. Gadonneix, J.I. Paredes, A. Celzard, V. Fierro, Irreversible deformation of hyper-crosslinked polymers after hydrogen adsorption, *J. Colloid Interface Sci.* 605 (2022) 513–527. <https://doi.org/10.1016/j.jcis.2021.07.104>.
- [137] K.J. Msayib, N.B. McKeown, Inexpensive polyphenylene network polymers with enhanced microporosity, *J. Mater. Chem. A*. 4 (2016) 10110–10113. <https://doi.org/10.1039/C6TA03257E>.

- [138] L. Li, H. Ren, Y. Yuan, G. Yu, G. Zhu, Construction and adsorption properties of porous aromatic frameworks via AlCl_3 -triggered coupling polymerization, *J. Mater. Chem. A*. 2 (2014) 11091–11098. <https://doi.org/10.1039/c4ta01252f>.
- [139] L. Li, K. Cai, P. Wang, H. Ren, G. Zhu, Construction of Sole Benzene Ring Porous Aromatic Frameworks and Their High Adsorption Properties, *ACS Appl. Mater. Interfaces*. 7 (2015) 201–208. <https://doi.org/10.1021/am505697f>.
- [140] H. Zhou, C. Rayer, A.R. Antonangelo, N. Hawkins, M. Carta, Adjustable Functionalization of Hyper-Cross-Linked Polymers of Intrinsic Microporosity for Enhanced CO_2 Adsorption and Selectivity over N_2 and CH_4 , *ACS Appl. Mater. Interfaces*. 14 (2022) 20997–21006. <https://doi.org/10.1021/acsami.2c02604>.
- [141] P. Arab, M.G. Rabbani, A.K. Sekizkardes, T. İslamoğlu, H.M. El-Kaderi, Copper(I)-Catalyzed Synthesis of Nanoporous Azo-Linked Polymers: Impact of Textural Properties on Gas Storage and Selective Carbon Dioxide Capture, *Chem. Mater.* 26 (2014) 1385–1392. <https://doi.org/10.1021/cm403161e>.
- [142] M.G. Rabbani, H.M. El-Kaderi, Synthesis and Characterization of Porous Benzimidazole-Linked Polymers and Their Performance in Small Gas Storage and Selective Uptake, *Chem. Mater.* 24 (2012) 1511–1517. <https://doi.org/10.1021/cm300407h>.
- [143] A.K. Sekizkardes, T. İslamoğlu, Z. Kahveci, H.M. El-Kaderi, Application of pyrene-derived benzimidazole-linked polymers to CO_2 separation under pressure and vacuum swing adsorption settings, *J. Mater. Chem. A*. 2 (2014) 12492–12500. <https://doi.org/10.1039/c4ta01281j>.
- [144] Y.-C. Zhao, Q.-Y. Cheng, D. Zhou, T. Wang, B.-H. Han, Preparation and characterization of triptycene-based microporous poly(benzimidazole) networks, *J. Mater. Chem.* 22 (2012) 11509. <https://doi.org/10.1039/c2jm31187a>.
- [145] M.G. Rabbani, T. Islamoglu, H.M. El-Kaderi, Benzothiazole- and benzoxazole-linked porous polymers for carbon dioxide storage and separation, *J. Mater. Chem. A*. 5 (2017) 258–265. <https://doi.org/10.1039/C6TA06342J>.
- [146] A.G. Slater, A.I. Cooper, Function-led design of new porous materials, *Science*. 348 (2015) 8075. <https://doi.org/10.1126/science.aaa8075>.
- [147] N. Chaoui, M. Trunk, R. Dawson, J. Schmidt, A. Thomas, Trends and challenges for microporous polymers, *Chem. Soc. Rev.* 46 (2017) 3302–3321. <https://doi.org/10.1039/c7cs00071e>.
- [148] B. Lopez-Iglesias, F. Suárez-García, C. Aguilar-Lugo, A. González Ortega, C. Bartolomé,

- J.M. Martínez-Ilarduya, J.G. de la Campa, Á.E. Lozano, C. Álvarez, Microporous Polymer Networks for Carbon Capture Applications, *ACS Appl. Mater. Interfaces*. 10 (2018) 26195–26205. <https://doi.org/10.1021/acsami.8b05854>.
- [149] C. Aguilar-Lugo, F. Suárez-García, A. Hernández, J.A. Miguel, Á.E. Lozano, J.G. De La Campa, C. Álvarez, New Materials for Gas Separation Applications: Mixed Matrix Membranes Made from Linear Polyimides and Porous Polymer Networks Having Lactam Groups, *Ind. Eng. Chem. Res.* 58 (2019) 9585–9595. <https://doi.org/10.1021/acs.iecr.9b01402>.
- [150] C. Aguilar-Lugo, W.H. Lee, J.A. Miguel, J.G. De La Campa, P. Prádanos, J.Y. Bae, Y.M. Lee, C. Álvarez, Á.E. Lozano, Highly Permeable Mixed Matrix Membranes of Thermally Rearranged Polymers and Porous Polymer Networks for Gas Separations, *ACS Appl. Polym. Mater.* 3 (2021) 5224–5235. <https://doi.org/10.1021/acsapm.1c01012>.
- [151] S. Rico-Martínez, C. Álvarez, A. Hernández, J.A. Miguel, Á.E. Lozano, Mixed Matrix Membranes Loaded with a Porous Organic Polymer Having Bipyridine Moieties, *Membranes*. 12 (2022) 1–19. <https://doi.org/10.3390/membranes12060547>.
- [152] L. Matesanz-Niño, N. Esteban, M.T. Webb, A. Martínez-Gómez, F. Suárez-García, A. González-Ortega, J.A. Miguel, L. Palacio, M. Galizia, C. Álvarez, Á.E. Lozano, Polymer materials derived from the SEAr reaction for gas separation applications, *Polymer*. 267 (2022) 125647. <https://doi.org/10.1016/j.polymer.2022.125647>.
- [153] N. Esteban, M.L. Ferrer, C.O. Ania, J.G. de la Campa, Á.E. Lozano, C. Álvarez, J.A. Miguel, Porous Organic Polymers Containing Active Metal Centers for Suzuki–Miyaura Heterocoupling Reactions, *ACS Appl. Mater. Interfaces*. 12 (2020) 56974–56986. <https://doi.org/10.1021/acsami.0c16184>.
- [154] E.L. Vargas, N. Esteban, J. Cencerrero, V. Francés, C. Álvarez, J.A. Miguel, A. Gallardo, A.E. Lozano, M.B. Cid, Pyrrolidine-based catalytic microporous polymers in sustainable C[dbnd]N and C[dbnd]C bond formation via iminium and enamine activation, *Mater. Today Chem.* 24 (2022) 2468–5194. <https://doi.org/10.1016/j.mtchem.2022.100966>.
- [155] P.J.M. Carrott, R.A. Roberts, K.S.W. Sing, Adsorption of nitrogen by porous and non-porous carbons, *Carbon* N. Y. 25 (1987) 59–68. [https://doi.org/10.1016/0008-6223\(87\)90040-6](https://doi.org/10.1016/0008-6223(87)90040-6).
- [156] M. Thommes, K. Kaneko, A. V. Neimark, J.P. Olivier, F. Rodríguez-Reinoso, J. Rouquerol, K.S.W. Sing, Physisorption of gases, with special reference to the evaluation of surface area and pore size distribution (IUPAC Technical Report), *Pure Appl. Chem.*

- 87 (2015) 1051–1069. <https://doi.org/10.1515/pac-2014-1117>.
- [157] J. Silvestre-Albero, A. Silvestre-Albero, F. Rodríguez-Reinoso, M. Thommes, Physical characterization of activated carbons with narrow microporosity by nitrogen (77.4 K), carbon dioxide (273 K) and argon (87.3 K) adsorption in combination with immersion calorimetry, *Carbon* N. Y. 50 (2012) 3128–3133. <https://doi.org/10.1016/j.carbon.2011.09.005>.
- [158] A.K. Sekizkardes, S. Altarawneh, Z. Kahveci, T. İslamoğlu, H.M. El-Kaderi, Highly Selective CO₂ Capture by Triazine-Based Benzimidazole-Linked Polymers, *Macromolecules*. 47 (2014) 8328–8334. <https://doi.org/10.1021/ma502071w>.
- [159] S. Mondal, N. Das, Triptycene based 1,2,3-triazole linked network polymers (TNP s): Small gas storage and selective CO₂ capture, *J. Mater. Chem. A*. 3 (2015) 23577–23586. <https://doi.org/10.1039/c5ta06939d>.
- [160] C. Zhang, Y. Liu, B. Li, B. Tan, C.F. Chen, H.B. Xu, X.L. Yang, Triptycene-based microporous polymers: Synthesis and their gas storage properties, *ACS Macro Lett.* 1 (2012) 190–193. <https://doi.org/10.1021/mz200076c>.
- [161] H. Gao, Q. Li, S. Ren, Progress on CO₂ capture by porous organic polymers, *Curr. Opin. Green Sustain. Chem.* 16 (2019) 33–38. <https://doi.org/10.1016/j.cogsc.2018.11.015>.
- [162] F. Bauer, T. Persson, C. Hulteberg, D. Tamm, Biogas upgrading - technology overview, comparison and perspectives for the future, *Biofuels, Bioprod. Biorefining*. 7 (2013) 499–511. <https://doi.org/10.1002/bbb.1423>.
- [163] O.W. Awe, Y. Zhao, A. Nzihou, D.P. Minh, N. Lyczko, A Review of Biogas Utilisation, Purification and Upgrading Technologies, *Waste and Biomass Valorization*. 8 (2017) 267–283. <https://doi.org/10.1007/s12649-016-9826-4>.
- [164] T. İslamoğlu, M. Gulam Rabbani, H.M. El-Kaderi, Impact of post-synthesis modification of nanoporous organic frameworks on small gas uptake and selective CO₂ capture, *J. Mater. Chem. A*. 1 (2013) 10259–10266. <https://doi.org/10.1039/c3ta12305g>.
- [165] M. Rong, L. Yang, C. Yang, J. Yu, H. Liu, Tetraphenyladamantane-based microporous polyaminals for efficient adsorption of CO₂, H₂ and organic vapors, *Microporous Mesoporous Mater.* 323 (2021) 111206. <https://doi.org/10.1016/j.micromeso.2021.111206>.
- [166] A. Roozitalab, F. Hamidavi, A. Kargari, A review of membrane material for biogas and natural gas upgrading, *Gas Sci. Eng.* 114 (2023) 204969. <https://doi.org/10.1016/j.jgsce.2023.204969>.

- [167] C. a. Scholes, G.W. Stevens, S.E. Kentish, Membrane gas separation applications in natural gas processing, *Fuel*. 96 (2012) 15–28. <https://doi.org/10.1016/j.fuel.2011.12.074>.
- [168] E.P. Favvas, F.K. Katsaros, S.K. Papageorgiou, A.A. Sapalidis, A.C. Mitropoulos, A review of the latest development of polyimide based membranes for CO₂ separations, *React. Funct. Polym.* 120 (2017) 104–130. <https://doi.org/10.1016/j.reactfunctpolym.2017.09.002>.
- [169] R.H. Vora, K.S.Y. Lau, High-performance aromatic polyimides, fluoropolyimides, and other high-temperature-resistant thermoset polymers, *Handbook of Thermoset Plastics INC*, (2021) 263-265. <https://doi.org/10.1016/B978-0-12-821632-3.00024-5>.
- [170] A. Hayek, G.O. Yahaya, A. Alsamah, S.K. Panda, Fluorinated copolyimide membranes for sour mixed-gas upgrading, *J. Appl. Polym. Sci.* 137 (2020) 1–13. <https://doi.org/10.1002/app.48336>.
- [171] G.M. Iyer, L. Liu, C. Zhang, Hydrocarbon separations by glassy polymer membranes, *J. Polym. Sci.* (2020) pol.20200128. <https://doi.org/10.1002/pol.20200128>.
- [172] N. Esteban, M. Juan-y-Seva, C. Aguilar-Lugo, J.A. Miguel, C. Staudt, J.G. de la Campa, C. Álvarez, Á.E. Lozano, Aromatic Polyimide Membranes with tert-Butyl and Carboxylic Side Groups for Gas Separation Applications?Covalent Crosslinking Study, *Polymers*. 14 (2022) 5517. <https://doi.org/10.3390/polym14245517>.
- [173] M. Wessling, S. Schoeman, T. van der Boomgaard, C.A. Smolders, Plasticization of gas separation membranes, *Gas Sep. Purif.* 5 (1991) 222–228. [https://doi.org/10.1016/0950-4214\(91\)80028-4](https://doi.org/10.1016/0950-4214(91)80028-4).
- [174] Y. Huang, D.R. Paul, Physical aging of thin glassy polymer films monitored by gas permeability, *Polymer*. 45 (2004) 8377–8393. <https://doi.org/10.1016/j.polymer.2004.10.019>.
- [175] J.D. Wind, S.M. Sirard, D.R. Paul, P.F. Green, K.P. Johnston, W.J. Koros, Carbon Dioxide-Induced Plasticization of Polyimide Membranes: Pseudo-Equilibrium Relationships of Diffusion, Sorption, and Swelling, *Macromolecules*. 36 (2003) 6433–6441. <https://doi.org/10.1021/ma0343582>.
- [176] N. Alaslai, B. Ghanem, F. Alghunaimi, E. Litwiller, I. Pinnau, Pure- and mixed-gas permeation properties of highly selective and plasticization resistant hydroxyl-diamine-based 6FDA polyimides for CO₂/CH₄ separation, *J. Memb. Sci.* 505 (2016) 100–107. <https://doi.org/10.1016/j.memsci.2015.12.053>.
- [177] K.P. Bye, V. Loianno, T.N. Pham, R. Liu, J.S. Riffle, M. Galizia, Pure and mixed fluid

- sorption and transport in Celazole® polybenzimidazole: Effect of plasticization, *J. Memb. Sci.* 580 (2019) 235–247. <https://doi.org/10.1016/j.memsci.2019.03.031>.
- [178] J.D. Wind, C. Staudt-Bickel, D.R. Paul, W.J. Koros, The effects of crosslinking chemistry on CO₂ plasticization of polyimide gas separation membranes, *Ind. Eng. Chem. Res.* 41 (2002) 6139–6148. <https://doi.org/10.1021/ie0204639>.
- [179] M. Zhang, L. Deng, D. Xiang, B. Cao, S.S. Hosseini, P. Li, Approaches to suppress CO₂-induced plasticization of polyimide membranes in gas separation applications, 2019. <https://doi.org/10.3390/pr7010051>.
- [180] M. Houben, J. Kloos, M. van Essen, K. Nijmeijer, Z. Borneman, Systematic investigation of methods to suppress membrane plasticization during CO₂ permeation at supercritical conditions, *J. Memb. Sci.* 647 (2022) 120292. <https://doi.org/10.1016/j.memsci.2022.120292>.
- [181] S.M. Jordan, W.J. Koros, J.K. Beasley, Characterization of CO₂-induced conditioning of polycarbonate films using penetrants with different solubilities, *J. Memb. Sci.* 43 (1989) 103–120. [https://doi.org/10.1016/S0376-7388\(00\)82356-X](https://doi.org/10.1016/S0376-7388(00)82356-X).
- [182] Q. Liu, A.T. Shaver, Y. Chen, G. Miller, D.R. Paul, J.S. Riffle, J.E. McGrath, B.D. Freeman, Effect of UV irradiation and physical aging on O₂ and N₂ transport properties of thin glassy poly(arylene ether ketone) copolymer films based on tetramethyl bisphenol A and 4,4'-difluorobenzophenone, *Polymer.* 87 (2016) 202–214. <https://doi.org/10.1016/j.polymer.2016.01.075>.
- [183] F. Moghadam, T.H. Lee, I. Park, H.B. Park, Thermally annealed polyimide-based mixed matrix membrane containing ZIF-67 decorated porous graphene oxide nanosheets with enhanced propylene/propane selectivity, *J. Memb. Sci.* 603 (2020) 118019. <https://doi.org/10.1016/j.memsci.2020.118019>.
- [184] R. Hou, S. Wang, L. Wang, C. Li, H. Wang, Y. Xu, C. Wang, Y. Pan, W. Xing, Enhanced CO₂ separation performance by incorporating KAUST-8 nanosheets into crosslinked poly(ethylene oxide) membrane, *Sep. Purif. Technol.* 309 (2023) 123057. <https://doi.org/10.1016/j.seppur.2022.123057>.
- [185] H. Wang, K. Zhang, J.P. Ho Li, J. Huang, B. Yuan, C. Zhang, Y. Yu, Y. Yang, Y. Lee, T. Li, Engineering plasticization resistant gas separation membranes using metal-organic nanocapsules, *Chem. Sci.* 11 (2020) 4687–4694. <https://doi.org/10.1039/d0sc01498b>.
- [186] D. Muñoz, E. Maya, J. De Abajo, J. De la Campa, A.E. Lozano, Thermal treatment of poly(ethylene oxide)-segmented copolyimide based membranes: An effective way to

- improve the gas separation properties, *J. Memb. Sci.* 323 (2008) 53–59. <https://doi.org/10.1016/j.memsci.2008.06.036>.
- [187] L. Escorial, M. de la Viuda, S. Rodríguez, A. Tena, A. Marcos, L. Palacio, P. Prádanos, A.E. Lozano, A. Hernández, Partially pyrolyzed gas-separation membranes made from blends of copolyetherimides and polyimides, *Eur. Polym. J.* 103 (2018) 390–399. <https://doi.org/10.1016/j.eurpolymj.2018.04.031>.
- [188] L. Cui, W. Qiu, D.R. Paul, W.J. Koros, Physical aging of 6FDA-based polyimide membranes monitored by gas permeability, *Polymer*. 52 (2011) 3374–3380. <https://doi.org/10.1016/j.polymer.2011.05.052>.
- [189] S.H. Goh, H.S. Lau, W.F. Yong, Metal–Organic Frameworks (MOFs)-Based Mixed Matrix Membranes (MMMs) for Gas Separation: A Review on Advanced Materials in Harsh Environmental Applications, *Small*. 18 (2022) 1–24. <https://doi.org/10.1002/sml.202107536>.
- [190] Y. Cheng, Z. Wang, D. Zhao, Mixed Matrix Membranes for Natural Gas Upgrading: Current Status and Opportunities, *Ind. Eng. Chem. Res.* 57 (2018) 4139–4169. <https://doi.org/10.1021/acs.iecr.7b04796>.
- [191] R.M. Huertas, A. Tena, A.E. Lozano, J. de Abajo, J.G. de la Campa, E.M. Maya, Thermal degradation of crosslinked copolyimide membranes to obtain productive gas separation membranes, *Polym. Degrad. Stab.* 98 (2013) 743–750. <https://doi.org/10.1016/j.polymdegradstab.2012.12.017>.
- [192] G.S. Sur, H.L. Sun, S.G. Lyu, J.E. Mark, Synthesis, structure, mechanical properties, and thermal stability of some polysulfone/organoclay nanocomposites, *Polymer*. 42 (2001) 9783–9789. [https://doi.org/10.1016/S0032-3861\(01\)00527-4](https://doi.org/10.1016/S0032-3861(01)00527-4).
- [193] Y. Zhang, I.H. Musselman, J.P. Ferraris, K.J. Balkus, Gas permeability properties of Matrimid® membranes containing the metal-organic framework Cu–BPY–HFS, *J. Memb. Sci.* 313 (2008) 170–181. <https://doi.org/10.1016/j.memsci.2008.01.005>.
- [194] A.C. Puleo, D.R. Paul, S.S. Kelley, The effect of degree of acetylation on gas sorption and transport behavior in cellulose acetate, *J. Memb. Sci.* 47 (1989) 301–332. [https://doi.org/10.1016/S0376-7388\(00\)83083-5](https://doi.org/10.1016/S0376-7388(00)83083-5).
- [195] Q. Liu, D.R. Paul, B.D. Freeman, Gas permeation and mechanical properties of thermally rearranged (TR) copolyimides, *Polymer*. 82 (2016) 378–391. <https://doi.org/10.1016/j.polymer.2015.11.051>.
- [196] B. Comesaña-Gándara, M. Calle, H.J. Jo, A. Hernández, J.G. de la Campa, J. de Abajo,

- A.E. Lozano, Y.M. Lee, Thermally rearranged polybenzoxazoles membranes with biphenyl moieties: Monomer isomeric effect, *J. Memb. Sci.* 450 (2014) 369–379. <https://doi.org/10.1016/j.memsci.2013.09.010>.
- [197] M. Minelli, G. Sarti, Gas Transport in Glassy Polymers: Prediction of Diffusional Time Lag, *Membranes*. 8 (2018) 8. <https://doi.org/10.3390/membranes8010008>.
- [198] M. Galizia, K.A. Stevens, Z.P. Smith, D.R. Paul, B.D. Freeman, Nonequilibrium Lattice Fluid Modeling of Gas Solubility in HAB-6FDA Polyimide and Its Thermally Rearranged Analogues, *Macromolecules*. 49 (2016) 8768–8779. <https://doi.org/10.1021/acs.macromol.6b01479>.
- [199] K.A. Stevens, Z.P. Smith, K.L. Gleason, M. Galizia, D.R. Paul, B.D. Freeman, Influence of temperature on gas solubility in thermally rearranged (TR) polymers, *J. Memb. Sci.* 533 (2017) 75–83. <https://doi.org/10.1016/j.memsci.2017.03.005>.
- [200] V. Loianno, K.P. Bye, M. Galizia, P. Musto, Plasticization mechanism in polybenzimidazole membranes for organic solvent nanofiltration: Molecular insights from in situ FTIR spectroscopy, *J. Polym. Sci.* 58 (2020) 2547–2560. <https://doi.org/10.1002/pol.20200151>.
- [201] H. Lin, B.D. Freeman, Gas permeation and diffusion in cross-linked poly(ethylene glycol diacrylate), *Macromolecules*. 39 (2006) 3568–3580. <https://doi.org/10.1021/ma051686o>.
- [202] V. Loianno, S. Luo, Q. Zhang, R. Guo, M. Galizia, Gas and water vapor sorption and diffusion in a triptycene-based polybenzoxazole: effect of temperature and pressure and predicting of mixed gas sorption, *J. Memb. Sci.* 574 (2019) 100–111. <https://doi.org/10.1016/j.memsci.2018.12.054>.
- [203] W.J. Box, Z. Huang, R. Guo, M. Galizia, The mechanism of light gas transport through configurational free volume in glassy polymers, *J. Memb. Sci.* 656 (2022) 120608. <https://doi.org/10.1016/j.memsci.2022.120608>.
- [204] Agilent, CrysAlisPro Data Collection and Processing Software for Agilent X-ray Diffractometers, Technol. UK Ltd, Yarnton, Oxford, UK. 44 (2014) 1–53.
- [205] A.D. Becke, Density-functional thermochemistry. III. The role of exact exchange, *J. Chem. Phys.* 98 (1993) 5648–5652. <https://doi.org/10.1063/1.464913>.
- [206] C. Lee, W. Yang, R.G. Parr, Development of the Colle-Salvetti correlation-energy formula into a functional of the electron density, *Phys. Rev. B.* 37 (1988) 785–789. <https://doi.org/10.1103/PhysRevB.37.785>.

- [207] H.B. Schlegel, G.E. Scuseria, M.A. Robb, J.R. Cheeseman, G. Scalmani, V. Barone, B. Mennucci, G.A. Petersson, H. Nakatsuji, M. Caricato, X. Li, H.P. Hratchian, A.F. Izmaylov, J. Bloino, G. Zheng, J.L. Sonnenberg, M. Hada, M. Ehara, K. Toyota, R. Fukuda, J. Hasegawa, M. Ishida, T. Nakajima, Y. Honda, O. Kitao, T. Nakai, T. Vreven, J.A. Montgomery Jr., J.E. Peralta, F. Ogliaro, M. Bearpark, J.J. Heyd, E. Brothers, K.N. Kudin, V.N. Staroverov, R. Kobayashi, J. Normand, K. Raghavachari, A. Rendell, J.C. Burant, S.S. Iyengar, J. Tomasi, M. Cossi, N. Rega, J.M. Millam, M. Klene, J.E. Knox, J.B. Cross, V. Bakken, C. Adamo, J. Jaramillo, R. Gomperts, R.E. Stratmann, O. Yazyev, A.J. Austin, R. Cammi, C. Pomelli, J.W. Ochterski, R.L. Martin, K. Morokuma, V.G. Zakrzewski, G.A. Voth, P. Salvador, J.J. Dannenberg, S. Dapprich, A.D. Daniels, O. Farkas, J.B. Foresman, J. V. Ortiz, J. Cioslowski, D.J. Fox, Gaussian 09, revision A.02, Gaussian, Inc., Wallingford CT, 2009. 37 (1988).
- [208] M.A. Thompson, ArgusLab 4.0.1, Planaria Software LLC, Seattle, WA. (n.d.).
- [209] J. Dennington, R.; Keith, T.; Millam, GaussView (Version 5), Semichem Inc., Shawnee Mission. KS. (2009).
- [210] J.B. Foresman, A. Frisch, Exploring Chemistry With Electronic Structure Methods, Gaussian, Inc. Pittsburgh, PA. 1996.
- [211] P. Verma, D.G. Truhlar, Status and Challenges of Density Functional Theory, Trends Chem. 2 (2020) 302–318. <https://doi.org/10.1016/j.trechm.2020.02.005>.
- [212] F. Neese, Prediction of molecular properties and molecular spectroscopy with density functional theory: From fundamental theory to exchange-coupling, Coord. Chem. Rev. 253 (2009) 526–563. <https://doi.org/10.1016/J.CCR.2008.05.014>.
- [213] S.K. Ghosh, P.K. Chattaraj, eds., Concepts and Methods in Modern Theoretical Chemistry, Two Volume Set, CRC Press, 2020. <https://doi.org/10.1201/b15083>.
- [214] G.A.P. M. J. Frisch, G. W. Trucks, H. B. Schlegel, G. E. Scuseria, M. A. Robb, J. R. Cheeseman, G. Scalmani, V. Barone, Gaussian 09, Revision A.02, Gaussian 09, Revis. A.02. (2009).
- [215] R. Dennington, T. Keith, J. Millam, GaussView, Version 5., Semichem Inc. , Shawnee Mission. KS. (2009).